Development of original solutions for the 3D integration of RF and millimeter-wave devices based on carbon nanotubes

Joseph de Saxce

Ph.D. Thesis

Université de Limoges

University of Limoges

ED 610 - Sciences et Ingénierie des Systèmes, Mathématiques, Informatique (SISMI)

Xlim

A thesis submitted to University of Limoges
in partial fulfillment of the requirements of the degree of

Doctor of Philosophy

Electroniques des Hautes Fréquences, Photoniques et Systèmes

Presented and defensed by

Joseph DE SAXCE

On January 6, 2022

Development of Original Solutions for the 3D Integration of RF and Millimeter-wave Devices Based on Carbon Nanotubes

Thesis supervisor: Dominique BAILLARGEAT and Stéphane BILA

JURY:

President of the jury
M. Philippe COQUET, Professeur des universités, IRL CINTRA, Université de Lille

Reporters
M. Christian PERSON, Professeur des universités, LABSTICC, IMT-Atlantique
M. Gaëtan PRIGENT, Maître de conférences, LAAS-CNRS, INPT-ENSEEIHT

Examiners
Mme. Florence PODEVIN, Maître de Conférences, RFIC Lab, Grenoble INP
M. Stéphane PIOTROWICZ, Ingénieur, III-V Lab, Thales
Mrs. Dunlin TAN, Engineer, Thales Solution Asia, Thales
M. Dominique Baillargeat, Professeur des universités, Xlim, Université de Limoges
M. Stéphane Bila, Professeur des universités, Xlim, Université de Limoges

À ma famille,

… un auteur ne nuit jamais tant à ses lecteurs que quand il dissimule une difficulté.
Evariste Galois

Acknowledgements

Je tiens dans un premier temps à remercier le professeur Dominique Baillargeat, mon principal directeur de thèse, qui m'a proposé ce sujet de thèse et a su me guider avec pédagogie pendant ces trois années de thèse. Ses connaissances scientifiques et sa grande expérience du milieu de la recherche ont été cruciaux dans l'aboutissement de ce doctorat. Je voudrais remercier au même titre le professeur Philippe Coquet, qui, bien qu'il n'ait pas été mon encadrant officiel, m'a suivi de près tout au long de celle-ci et a joué un rôle prédominant dans mon encadrement. Je tiens aussi à remercier le professeur Stéphane Bila pour son soutien et ses conseils tout au long de ma thèse.

Je remercie les membres permanents de l'équipe MACAO (Olivier Tantot, Aurélien Périgaud, Kamel Frigui et Nicolas Delhote), qui ont toujours été disponibles pour partager leur immense culture scientifique avec moi. Je ne peux pas oublier Marie-Claude Lerouge qui a toujours été présente pour m'aider lors de mes différentes démarches administratives. Merci aussi à Françoise Mérigaud pour son aide.

Je remercie les ingénieurs de la plateforme PLATINOM (Cyril Guines, Damien Passerieux et Clément Hallepee) qui m'ont été d'une aide précieuse pour la fabrication et les mesures de mes dispositifs.

Je remercie l'Agence Nationale de la Recherche d'avoir financé ces recherches et tous les membres du projets ANR TRiCOT qui ont su partager leurs connaissances du domaine tout au long de ces trois dernières années ; merci à Stéphane Piotrowicz, Didier Floriot, Stéphanie Bohbot, Florence Podevin, Philippe Ferrari, Emmanuel Pistono, Beng Kang Tay, Jianxiong Wang, Simon Goh, Chong Wei, Edwin Teo.

A special thanks to Chun Fei Siah, not only because all the results in this manuscript are a direct consequence of his manufacturing skills, but also because of his kindness and willingness throughout my whole PhD. In general, I thank all the team in Singapore led by professor Tay for their care all along these last years.

Enfin et surtout, je remercie ma famille et mes amis pour leur soutien tout au long de cette aventure. Un merci tout particulier aux membres de l'open space qui ont fait de cette thèse une expérience inoubliable de partage tant dans les moments difficiles que joyeux. Merci à Julien, l'âme de l'open space ces dernières années, pour « ses » gâteaux, son amitié et son mentorat sans lequel je n'aurais pas été à l'abri de bien des épreuves. J'aurais tant aimé être à la hauteur de l'esprit d'équipe que tu incarnes, chef de meute, j'y travaille chaque jour mais j'ai déjà beaucoup appris avec toi. Je te souhaite toute la réussite possible dans ta nouvelle vie, tu le mérites. Thank you Andrés, you have been an unwavering beacon of happiness in the grey skies of Limoges, for that I will be in debt always. Your work and social skills will never cease to amaze me, keep on being who you are; you should be able to achieve anything. Merci à Thibault pour son entrain à partager et discuter de nos résultats scientifiques (et de vélo de temps en temps, mais si peu). Merci à Etienne, qui m'a fait me sentir un membre de l'équipe à part entière et qui a su être l'idéal indétrônable du doctorant parfait même après avoir quitté l'équipe ; l'ultime échelon sur l'échelle d'Olivier à l'aune duquel tous les doctorants sont mesurés. Depuis ton départ le grand squelette d'Olivier erre dans les couloirs afin de trouver un moyen de soulager sa peine immense, heureusement que tu l'appelles de temps en temps. Etre comparé au quotidien avec toi m'aura permis de me surpasser. Merci à Oualid pour son amitié mais surtout pour ses talents footballistiques sans lesquels nous n'aurions sans doute pas gagné la ligue. Merci à Chaimaa d'avoir su garder son calme (la plupart du temps) dans

cette open-space rempli de doctorants parfois lourdauds. Je te souhaite de trouver un travail dans lequel tu pourras t'épanouir pleinement, afin de faire profiter au monde de tes qualités certaines. Enfin, merci à tous les autres que j'ai croisé au cours de ma thèse et qui m'ont aidé dans ce périple, Anthony, Johann, Ali, Dali, Aarefa, Roua, Amal et Philippe. Je vous souhaite à tous plein de réussite.

Rights

Table of Contents

List of Figures

List of Tables

Introduction

On the sixteenth of August 1858, the first official telegraphic message crosses the Atlantic; queen Victoria of the United Kingdom congratulates the newly elected American president, James Buchanan. After four years of research, hundreds of thousands of pounds and a series of failed expeditions, the first transatlantic telegraph cable is finally achieved. The Telegraph Construction and Maintenance Company, led by Cyrus W. Field, finally prevailed on the Atlantic sea. An undersea telegraph cable now links Newfoundland and Ireland. The cable is in itself 3500 km long, and is made of at least 600 tons of copper and 200 tons gutta-percha, a natural polymer similar to rubber allowing its isolation in water. In order to unfold this gigantic cable, the two biggest ships of the United Kingdom and the United States, the Agamemnon and the Niagara, have been requisitioned. Unfortunately, the cable only works for three weeks and the New World will have to wait six more years before being permanently linked with Europe. If Stefan Zweig decided to dedicate one of his twelve short stories from his work "Decisive Moments in History" to this particular moment, it is because for the first time in history, all the continents inhabited by humanity can communicate almost instantly, thus creating some sort of "universal conscience".

Since then, numerous breakthrough innovations in telecommunications, from the use of electromagnetic waves for wireless telegraph by Marconi, to the internet and the different generations of mobile networks (1G to 4G), led to the internet, as we know it today. In January 2021, the estimated number of people connected to the Internet was of 4.66 billion, and 92.6% of that number through mobile devices [1].

The next step in the evolution of telecommunications is the fifth generation of mobile networks (5G). The three main objectives of this new generation are higher data rates, lower latency and the Internet of Things (IoT). Between 4G and 5G, the average data rates would go from 20 Mbps to 100 Mbps and the latency would decrease from 50 ms to 1 ms. The IoT consists in connecting an important number of objects that can transfer data over a wireless network without human intervention. The opportunities that arise from such possibilities are endless.

However, to attain such objectives there are some technological difficulties to overcome. For example, to have better data rates, it is necessary to use higher frequency bands because of the overcrowded lower ones. Yet, the size of devices is directly linked to their working frequency, meaning new fabrication processes are necessary. Moreover, the increasing number of connected devices comes with an increasing number of hardware pieces. Unfortunately, this hardware is mainly made from metals which become scarcer and more difficult to extract [2]. What Cyrus W. Field did in the 19th century is not possible today anymore:

> *Entire mines of iron and copper were depleted to make this single rope, entire forests of rubber trees were bled to produce the envelope of gutta-percha intended to cover such a gigantic length.*

Nonetheless, just as much as the discovery of gutta-percha allowed for isolated undersea cables, new materials discovered in the 90s could solve both problems mentioned above: new fabrication processes for higher frequencies and available resources. These new materials are the nanomaterials derived from Carbon, one of the most abundant and easily accessible element on earth.

Graphene and carbon nanotubes (CNTs) received a lot of attention in the past decades, for their exceptional properties. In 2010, A.K. Geim and K.S. Novoselov received the Nobel price in Physics only six years after physically isolating Graphene. In 2013, the European Union has set up a research initiative, the Graphene Flagship, which will receive 1 billion euros in 10 years to investigate new applications of graphene and other 2D materials.

In this work, we will investigate the possible use of CNTs for Radio Frequency (RF) and millimeter-wave (mm-wave) devices. In particular, we will study the possibility of creating a new type of heterogeneous integration fabrication process for mm-wave devices using bundles of CNTs.

The research reported in this thesis was funded by the Agence Nationale de la Recherche (ANR) as part of the project TRiCOT (Emerging Technology for RF and Millimeter-wave Circuits based on Carbon Nanotubes). This project was in the context of ultra-compact millimeter-wave systems manufacturing and in particular we planned to develop E-band demonstrators (71-86 GHz). An original concept of functionalized interposer has been proposed, in particular by integrating a beamforming circuit (Butler matrix), which was based on two innovations from previous work of the partners : the design of slow-wave waveguides and a technology of carbon nanotubes growth and transfer, compatible with CMOS technology.

There are four partners to the project. I was attached to Xlim, a joint CNRS-Université de Limoges research institute (UMR 7252) where I spent the three years of my PhD. Xlim gathers 460 researchers, staff and PhD students divided in six different axis studying different domains from Mathematics to Electromagnetism. I was attached to the team MACAO (Advanced Methods for Computer Aided Design) in the axis System-RF. In the project, Xlim was responsible for the design and measurements of the fabricated devices. CINTRA (CNRS International-NTU-Thales Research Alliance) is a CNRS Mixt International Unit (UMI 3288) with academic NTU (Nanyang Technological University) and industrial (THALES) partners, located in Singapore on NTU's campus. CINTRA was responsible for the fabrication of the devices. RFIC Lab is a research laboratory, which belongs both to the University Grenoble Alpes (UGA), Grenoble INP, USMB and to the CNRS. With a staff of 170 persons, –RFIC Lab is one of France's top micro and nanotechnology research centers. In the project, RFIC Lab was responsible for the simulation and design of the slow-wave devices. III-V Lab is an industrial research laboratory under the guidance of Nokia, Thales and CEA Leti. III-V Lab conducts R&D activities in the field of micro/nano-electronics and photonics semiconductor components for different application: telecoms, defense, security, safety, space etc. In the project III-V Lab was responsible for the test of the devices robustness.

This PhD thesis is organized as follows :

In the first chapter, the basic notions about CNTs and Vertically Aligned CNTs (VACNTs) are presented. From the properties of single CNTs to the fabrication process and characterization methods.

The three next chapters treat three different aspects of the CNT based functionnalized interposer.

In the second chapter, the possibility of guiding electromagnetic (EM) waves using an air filled Surface Integrated Waveguide (SIW) with lateral walls of VACNT is studied. The devices are simulated, fabricated and measured. Different fabrication processes are tested as well as different designs.

In the third chapter, the potential slow-wave properties of VACNTs are investigated.

In the fourth chapter, the performances of interconnects made of VACNTs are studied.

Finally, a conclusion and perspectives are proposed in a last part.

Chapter 1: Carbon Nanotubes and Nanopackaging

Since Feynman's famous lecture "There is plenty of room at the bottom" at California Institute of Technology in 1960 [3], researchers and engineers have pushed the dimensions of systems further and further into the infinitely small. This allowed for an increase in calculus speed and number of functions in an ever-decreasing space. In May of 2021, IBM announced the first chip with transistors 2 nm wide (that is smaller than the width of a strand of DNA), allowing for an improvement of performances by 45% or of energy consumption by 75%, compared to today's 7 nm transistor chips [4]. More than that, it has been possible for a few decades now to manipulate matter atom by atom, making atomic scale devices possible. This technology is of particular interest in fields as important as quantum computing [5] – where recent results published by Google AI already show the utmost potential [6], [7] – or artificial molecular machines [8]. However, in order to have a new generation of atomic scale systems, one must think of ways to package them. Indeed, the conditions for these circuits to work (Ultra High Vacuum (UHV) and surface quality) make it difficult to have a standalone chip [9]. Furthermore, the scale of these devices raises the issue of filling the gap between the atomic scale and the rest of the components linked to it, typically at the millimeter or micron scale.

These issues are tackled by nanopackaging, the field of research that is defined as "the packaging of devices and systems with nanoscale materials and processes for improved performance, functionality, reliability and cost" [10]. There are many different subsections to this field: the use of DNA and its assembling properties to make nano-scale assembly [11], [12], atomic scale surface preparation to host atomic scale circuitry [9], material engineering using nanomaterials to tune dielectric properties [13] or for better soldering performances [14], [15], graphene nanoribbon interconnects [16], [17], to cite a few.

The focus of this work will be on a particular subsection: nanopackaging for millimeter-wave (mm-wave) devices[1] using CNTs. This field of research stemmed from the observations below.

The global demand for higher data rates and the overcrowded lower frequency bands has led communicating devices to work at higher frequencies. Because higher frequencies mean smaller dimensions and because of the demand for more functions in a smaller space, RF devices have shrunk considerably. The smaller dimensions combined with the physical phenomena at higher frequencies has led to packaging issues. Indeed, the parasitic effects that could be neglected at lower frequencies now become limiting [18]. To overcome these limitations, one of the solutions is to use nanomaterials, such as Carbon Nano Tubes (CNTs), for they have exceptional properties and are becoming more and more accessible. Their unique properties allow to overcome unwanted physical phenomena and their scale permits easy integration in small mm-wave devices.

Because this work is focused on the use of CNTs for nanopackaging of mm-wave devices, this first chapter will consist of a presentation of CNTs and Vertical Aligned CNT (VACNT) bundles, followed by a state of the art of VACNT bundles nanopackaging in the mm-wave band. In the first part, we will present CNTs and their properties, their fabrication process, their characterization methods and the modelization tools to model them. In the second part, we will present the following applications for CNTs in mm-wave packaging: thermal management, electromagnetic EM shielding, antennas and level 0 interconnects.

[1] Millimeter-wave devices are devices that operate at frequencies above 30 GHz, which is equivalent to a wavelength below 10mm, hence the name mm-wave devices.

1.1. From Graphene to CNTs

Due to the impact their discovery had on the research of the 20th century, the paternity of CNTs is subject to debate [19]. However, we can safely say that it is in 1991, with Ijima's article [20], that the research community really started to investigate CNTs and their numerous applications. Since then, numerous articles have been published, some that show through theory and experience the exceptional properties of CNTs, and others, which find innovative ways to use their properties. We will give in this section a description of CNTs so as to be able to understand their properties.

The most common way to describe CNTs is to say they are a rolled-up sheet of graphene, only a few nanometers in diameter. This presupposes the knowledge of what graphene is. In this section we will describe graphene and its properties and from there give a more complete description of CNTs.

1.1.1. The Allotropes of Carbon and Graphene

Carbon has six electrons and its electronic structure is 1s2 2s2 2p2. When it is excited (by absorbing energy), one of its 2s electron is promoted into the 2p sublevel (Figure 1a). This explains why carbon usually makes four covalent bonds[2]. However, for example, we know the four covalent bonds of methane (CH_4) to be equivalent. Yet, the s orbitals and p orbitals are not of the same shape as shown in Figure 1b. It is in order to solve the apparent problem that Linus Pauling developed the theory of hybridization.

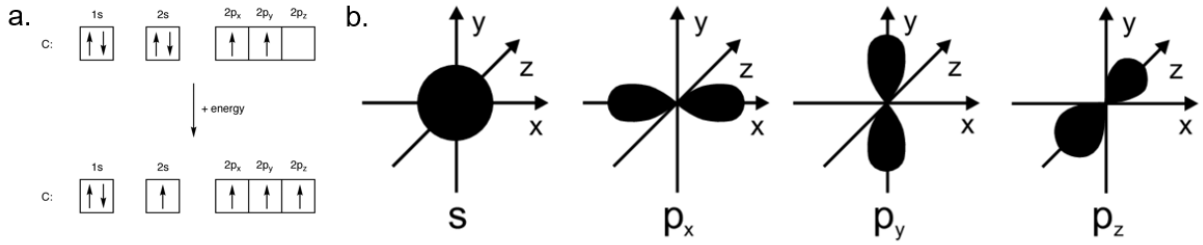

Figure 1 : a. Electronic structure of carbon and excited carbon [19], b. Shape of the s orbital and the p orbitals (probability of presence of the electron) [20]

In this theory, electrons from the s sublevel and p sublevel can make a hybrid sublevel called sp, sp2 or sp3 depending on the number of bonds needed. In Figure 2, the different types of hybridization are shown for carbon, as well as the associated orbital shapes. We can say that for sp3 hybridization, the orbitals are a mix of 25% s shape and 75% p shape, for sp2 33% and 66% and for sp 50% and 50%, which explains the different shapes. For different molecules, carbon will behave differently, for CH_4 the hybridization will be sp3, for ethylene (C_2H_4) it will be sp2 and for carbon dioxide (CO_2) it will be sp. Note that carbon always shares four electrons, which means certain covalent bonds are doubled in organic chemistry, this is what is explained by hybridization theory.

[2] A covalent bond happens when two atoms share one electron each to make a shared doublet. There is an overlap of two orbitals, one from each atom.

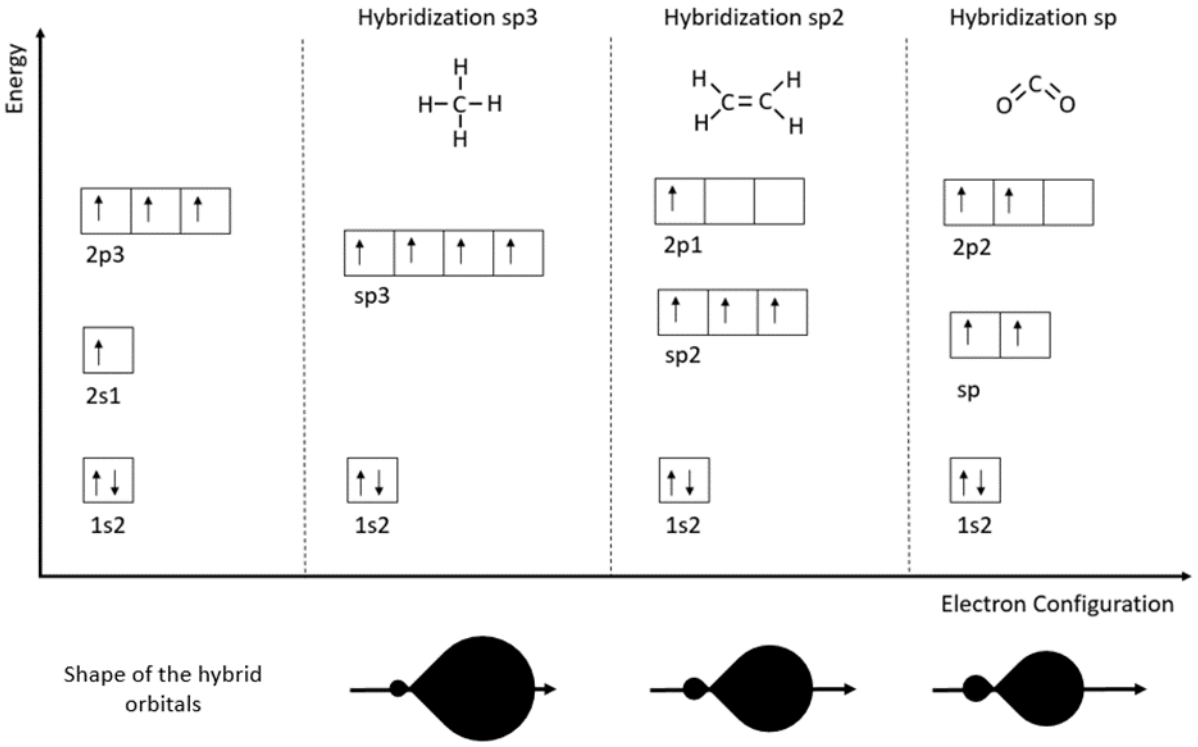

Figure 2 : Hybridizations of Carbon

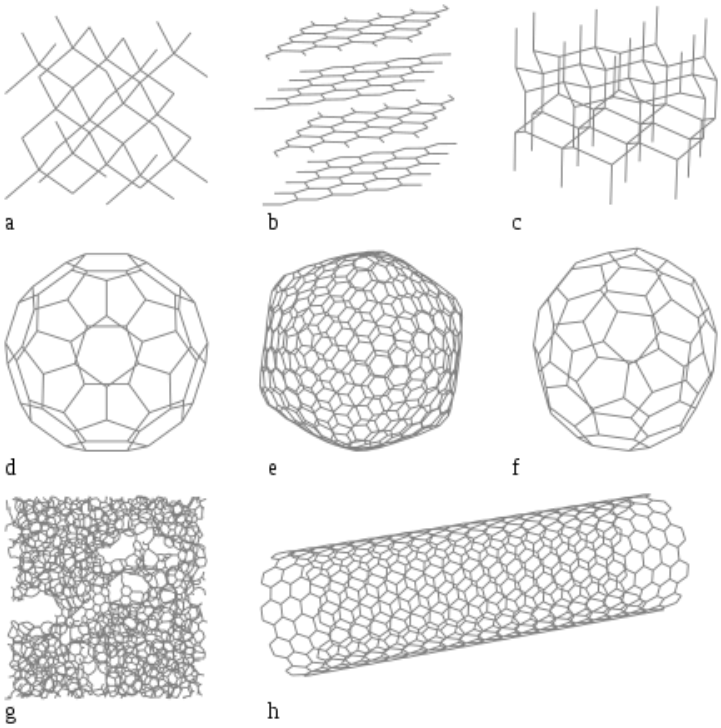

Figure 3 [21]: Allotropes of Carbon: (a) diamond, (b) lonsdaleite, (c) several sheets of graphene forming graphite, (d) C_{60} buckminsterfullerene, (e) C_{540} fullerite, (f) C_{70} fullerene, (g) amorphous carbon, (h)zig-zag single walled carbon nanotube

It is partially due to the different hybridization possible (i.e. possible number of bonds) that carbon allotropes[3] are numerous, some of them are shown in Figure 3. In particular, in graphene ((h) in Figure 3), we can see that each atom of carbon makes three covalent bonds, which means, the electronic structure of carbon is sp2 hybridized. For each carbon atom, there are three σ-bonds from the direct overlap of the sp2 orbitals and one π-bond made from the overlap of the p orbital, this is shown in Figure 4.

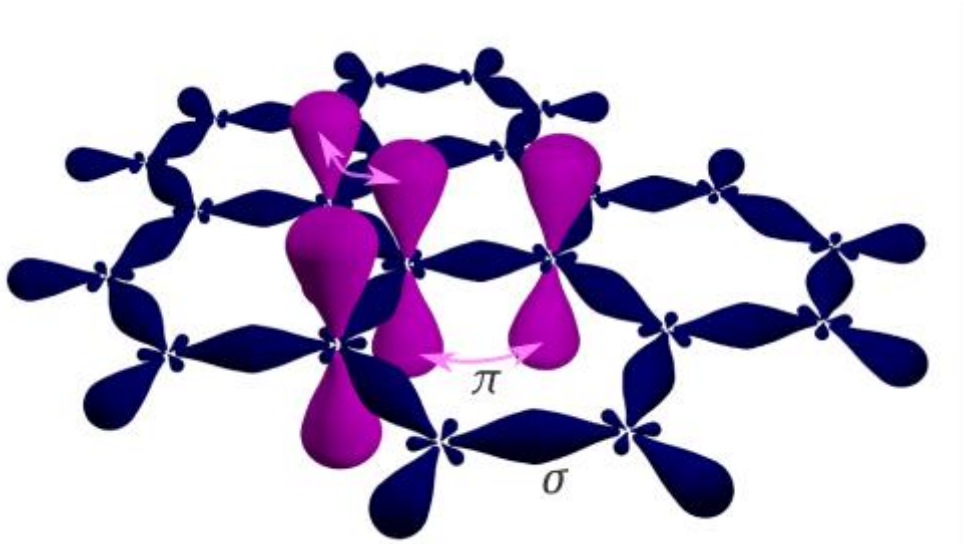

Figure 4 [22]: Carbon covalent bonds in a hexagonal/sp2 geometry

When two π-bonds overlap, which is the case here, the p orbital of each atom overlaps the p orbital of the three neighboring atoms; the π-bonds are called delocalized. These delocalized π-bonds (electrons moving freely above and below the nuclei lattice) can give a first understanding of carbon nanotube properties.

1.1.2. Electronic Properties of Graphene

To describe graphene's electronic properties, we will start by calculating the band diagram. We begin by defining the Bravais net and the first Brillouin zone of the honeycomb structure of graphene in Figure 5.

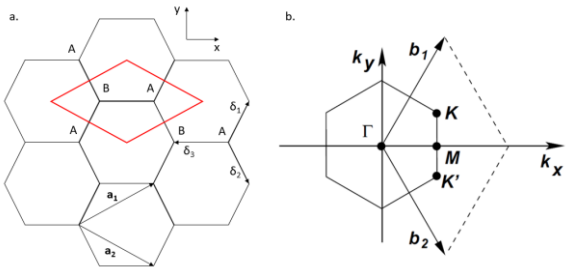

Figure 5 : a. Definition of graphene's Bravais lattice, b. Representation of the first Brillouin zone [23]

[3] Different physical forms in which an element can exist; molecules made of the only element, arranged in different shapes.

Two atoms are sufficient to describe entirely the structure, we name them A and B. We obtain the full net by translating the red zone along the $\mathbf{a_1}$ and $\mathbf{a_2}$ vectors. δ_1, δ_2 and δ_3 are the vectors giving the three nearest B atoms from an A atom.

We have,

$$\boldsymbol{a_1} = \frac{a}{2}\begin{pmatrix} 3 \\ \sqrt{3} \end{pmatrix}$$

$$\boldsymbol{a_2} = \frac{a}{2}\begin{pmatrix} 3 \\ -\sqrt{3} \end{pmatrix}$$

And,

$$\boldsymbol{\delta_1} = \frac{a}{2}\begin{pmatrix} 1 \\ \sqrt{3} \end{pmatrix},\ \boldsymbol{\delta_2} = \frac{a}{2}\begin{pmatrix} 1 \\ -\sqrt{3} \end{pmatrix},\ \boldsymbol{\delta_3} = -a\begin{pmatrix} 1 \\ 0 \end{pmatrix}$$

The vectors $\mathbf{b_1}$ and $\mathbf{b_2}$ defining the reciprocal lattice, are defined by:

$$\mathrm{a_i}.\mathrm{b_j} = 2\pi\delta_{\mathrm{ij}}$$

With δ_{ij}, the Kronecker operator[4].

This leads to,

$$\boldsymbol{b_1} = \frac{2\pi}{3a}\begin{pmatrix} 1 \\ \sqrt{3} \end{pmatrix}$$

$$\boldsymbol{b_2} = \frac{2\pi}{3a}\begin{pmatrix} 1 \\ -\sqrt{3} \end{pmatrix}$$

As we have seen in 1.1.1, the relevant atomic orbital to consider is the p one forming π bonds, which is in the perpendicular direction of the lattice. In a tight-binding representation, we have, the following Hamiltonian [24] (Hamiltonian of tight binding with the nearest neighbors, with obvious notations):

$$\hat{\mathrm{H}}_{\mathrm{TB},n.n.} = -t \sum_{\substack{ij=n.n. \\ \sigma}} \left(a_{i\sigma}^{\dagger} b_{j\sigma} + \mathrm{H.\,c.}\right)$$

Where, t is the integral overlap between two p orbitals (2.7 eV [25]), *i* and *j* the indices of the nearest neighbors, σ the spin of the electron equal to ±1, $a_{i\sigma}$ (and its conjugate $a_{i\sigma}^{\dagger}$) the annihilation (creation, respectively) operator for electrons on site A, $b_{j\sigma}$ (and its conjugate $b_{j\sigma}^{\dagger}$) the annihilation (creation, respectively) operator for electrons on site B and $\mathrm{H.\,c.}$ the Hermitian conjugate.

We also know that, because the potential is periodic (net of carbon atoms), we can use Bloch's theorem. The wave functions ψ solution of Heisenberg equations (eigenvalues of the Hamiltonian) are of the form:

$$\psi(\boldsymbol{r}) = e^{i\boldsymbol{k}.\boldsymbol{r}} u(\boldsymbol{r})$$

With, $\boldsymbol{r}$ the position, $\boldsymbol{k}$ the wave vector and u has the same periodicity as the structure of the crystal.

[4] It is equal to one if i=j, it is zero otherwise.

This leads to the Hamiltonian in function of $\boldsymbol{k}$ [30]:

$$\hat{\mathrm{H}}_k = \begin{pmatrix} 0 & \Delta_k \\ \Delta_k^* & 0 \end{pmatrix} \qquad \Delta_k \equiv -t \sum_{l=1}^{3} \exp i\mathbf{k} \cdot \boldsymbol{\delta_l}$$

To find the energy bands equations in function of $\boldsymbol{k}$, the last step is to determine the eigenvalues of $\hat{\mathrm{H}}_k$:

$$E_{\pm}(\mathbf{k}) = \pm t \left(1 + 4\cos\frac{3k_x a}{2}\cos\frac{\sqrt{3}k_y a}{2} + 4\cos^2\frac{\sqrt{3}k_y a}{2}\right)^{\frac{1}{2}}$$

This allows us to plot the band diagram in Figure 6:

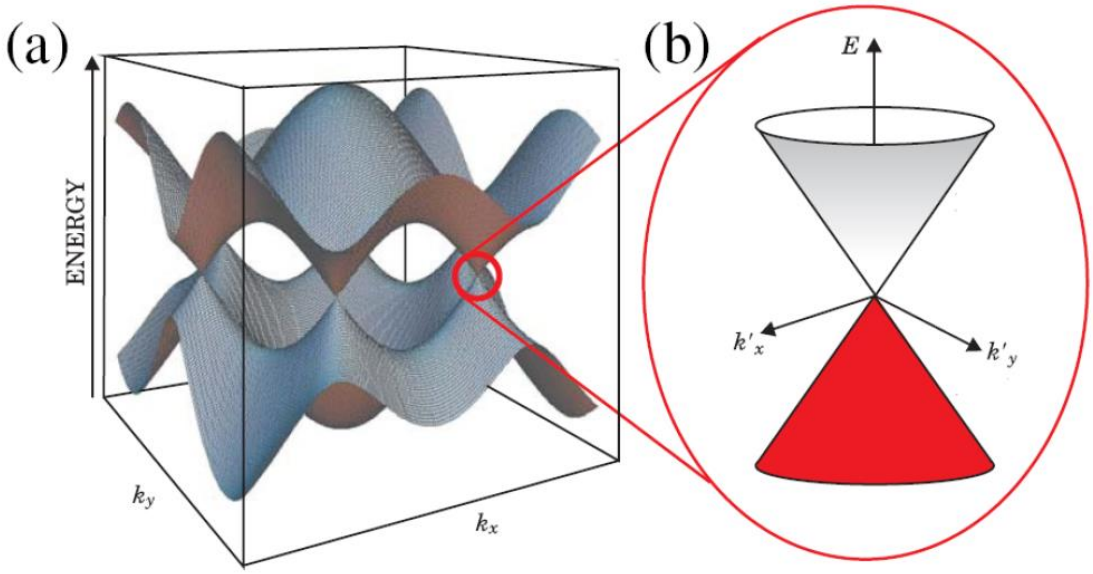

Figure 6 : (a) Representation of the conduction and valence band in the first zone of Brillouin (b) Zoom in on a Dirac cone [26]

We can note that there are particular values for which $E_{\pm}(\mathbf{k})$ is equal to zero. This happens exactly in the two points K and K' from Figure 8. These points are called Dirac points. We have what we call a degenerate band, graphene is a perfect semi-metal, a semi-conductor with a gap equal to 0.

By performing a linear approximation around these points [27], we can extract particular properties of the electrons. If we take $\mathbf{k} = \mathbf{K} + \boldsymbol{\delta}\mathbf{k}$, with $|\boldsymbol{\delta}\mathbf{k}| << |\mathbf{K}|$ we have :

$$E_{\pm}(\delta\mathbf{k}) = \pm\hbar\delta k v_F$$

With, $\hbar$, Planck's constant divide by 2π and v_F, Fermi's velocity equal to $\frac{3\gamma_0 a}{2\hbar} \simeq 1 \times 10^6\ \mathrm{m.s^{-1}}$.The dispersion equation is linear unlike the usual cases of 2D gases for which the relation is quadratic [26]. The effective mass is thus equal to zero and the charges behave like relativist particles with speed v_F that does not depend on their energy. However, there are limits to this approximation, because there are interactions with the defaults in the graphene

net. In that case we also need to have $E_C < \gamma_0$ where $E_C = \hbar\delta k_C v_F$ is the energy of the charge carriers, in order to have the aforementioned properties [28].

To go further, in [23] the band diagram is determined while also taking into account the interaction with the second nearest neighbors. The equation remains the same, only a second term with lower γ_0 for tight binding with the further neighbors, is added. The band diagram is shown in Figure 7. It is no longer symmetric with respect to the Fermi level, but the properties stay true around the Dirac points.

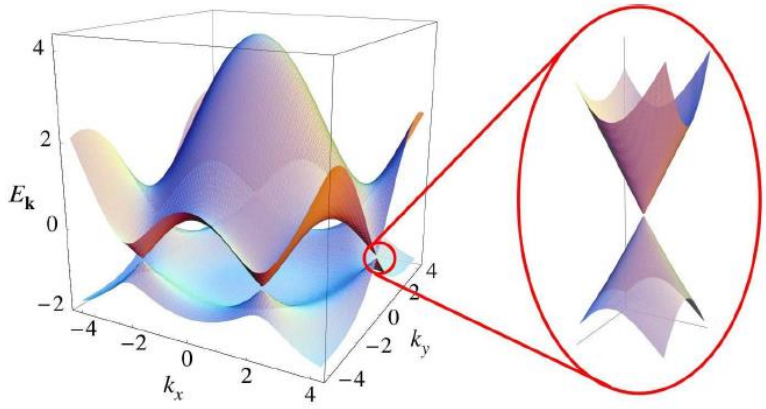

Figure 7 : On the left the diagram with the second nearest neighbors taken into consideration, On the right, a zoom on one of Dirac point.

Now that we have the electronic properties of graphene, we can properly determine those of CNTs. First, let us describe CNTs.

1.1.3. Different CNTs and Chirality

Single wall CNTs (SWCNT) are described, mathematically and physically, as a rolled-up sheet of graphene. To define the different types of CNTs, and because it will have an impact on their properties, we define the chiral vector Figure 8. This vector, $\mathbf{C_v}$ defines the winding of the sheet of graphene to form a SWCNT. The properties of the CNT will depend on it. The vector $\boldsymbol{C_v}$ is defined using the base vectors ($\boldsymbol{a_1}$, $\boldsymbol{a_2}$) of the graphene sheet, and a couple of scalars (n,m):

$$\boldsymbol{C_v} = n\boldsymbol{a_1} + m\boldsymbol{a_2}$$

We can then define the translation vector $\boldsymbol{T}$ as:

$$\boldsymbol{T} = t_1\boldsymbol{a_1} + t_2\boldsymbol{a_2}$$

With,

$$t_1 = \frac{2m+n}{d_R},$$

$$t_2 = -\frac{2n+m}{d_R},$$

$$d_R = \mathrm{GCD\ of}\ (2m+n)\ \mathrm{and}\ (2n+m)$$

The length of $\boldsymbol{C_v}$ defines the diameter of the CNT, while the length of $\boldsymbol{T}$ defines the distance from which the CNT will repeat itself, (CNTs being periodic structures). If we define *a* as the distance between two carbon atoms (a=0.142 nm), we have:

$$||\boldsymbol{C_v}|| = \sqrt{3}a\sqrt{n^2 + m^2 + mn}$$

$$||\boldsymbol{T}|| = \frac{\sqrt{3}a}{2}\sqrt{3(t_1^2 + t_2^2) + 4t_1 t_2}$$

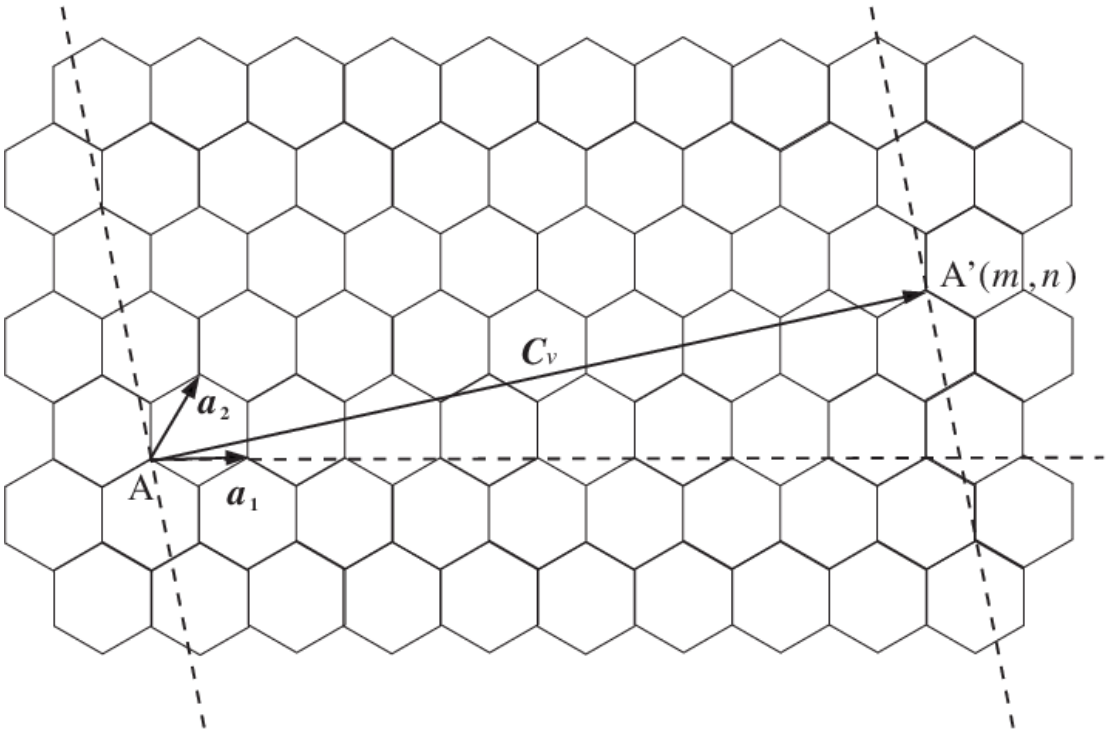

Figure 8 [29]: Schematic of $\mathbf{C_v}$, chiral vector

From the couple of scalars (n,m), we can define the following three different types of configuration shown in Figure 9:

- If m=0, the configuration is called “zig-zag”
- If n=m, the configuration is called “armchair”
- In all the other cases, the configuration is said to be “chiral”

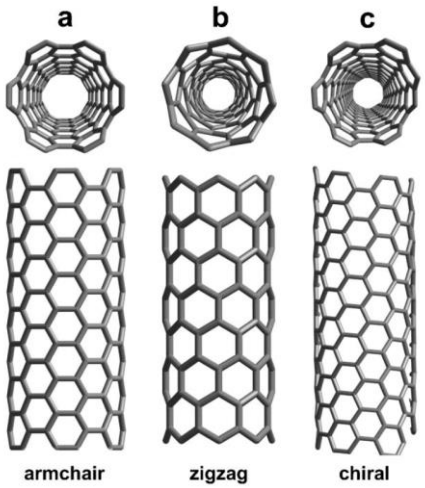

Figure 9 [30]: Molecular models of SWCNTs exhibiting different chiralities: (*a*) armchair configuration, (*b*) zig-zag arrangement, and (*c*) chiral conformation

These different conformations will give the CNTs different properties. While armchair tubes are always metallic, others can be semi conducting or metallic (see I.2.1). More precisely, if n=m the tube will be metallic, if n-m is a multiple of three and n≠m, the tube will be quasi-metallic with a very small band-gap[5], and in all other cases the nanotube is a moderate semi-conductor.

We can note that controlling the chirality of the CNTs during the fabrication process is of crucial importance, because it will determine their behavior. Many works have been published on this subject [31], [32], however, to this date, the growth processes used do not permit it. That being said, if the chirality of the CNTs is random, the probability for a CNT to be metallic is approximately 1/3rd.

1.1.4. Multiwall CNTs

Multiwall Carbon Nanotubes usually have bigger dimensions, their diameters are bigger and they are longer. They consist of multiple SWCNTs sharing the same axis, each of them called a shell, as shown in Figure 10.

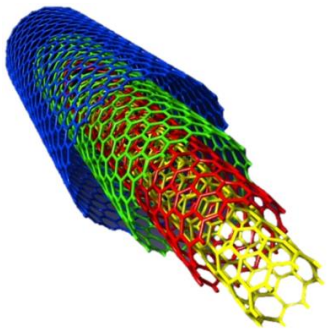

Figure 10 [33]: Multiwall carbon nanotube

[5] Energy gap between the valence electrons and the conduction electrons in a material. With that energy electrons can go from the valence band to the conduction one. This makes the material conductive.

Even though it is not the case in Figure 10, the inner shells can have their own chirality. What does not vary is the distance between each shell, that we shall name d, that is equal to Van Der Walls length (0.34 nm).

1.2. CNT Properties

Because CNTs are directly derived from graphene, we can deduce CNT electronic properties from the ones of graphene. That is why, using the knowledge of the previous section, we will deduce the properties of CNTs.

1.2.1. SWCNT Band Diagram

As we have said earlier, CNTs are conductive or semi-conductor, depending on their chirality. We will try here to explain this particularity. Though we will mainly focus on the metallic properties of CNTs in this thesis, it is important to understand the semi-conductor behavior of SWCNT, for they are part of MWCNTs, the type of CNTs we will be using for our devices.

Because CNTs are rolled up sheets of graphene, the boundary conditions on the circumference are periodic. This means the wave vector is quantified [34]:

$$\boldsymbol{C_v} \cdot \mathbf{k} = 2\pi \cdot i$$

Where i is an integer.

We can deduce the electronic band structure of a CNT from the one of graphene. The quantization condition is reflected in Figure 11. Slices cut out of the band structure of the first Brillouin zone, indicated by the solid lines in Figure 11a.

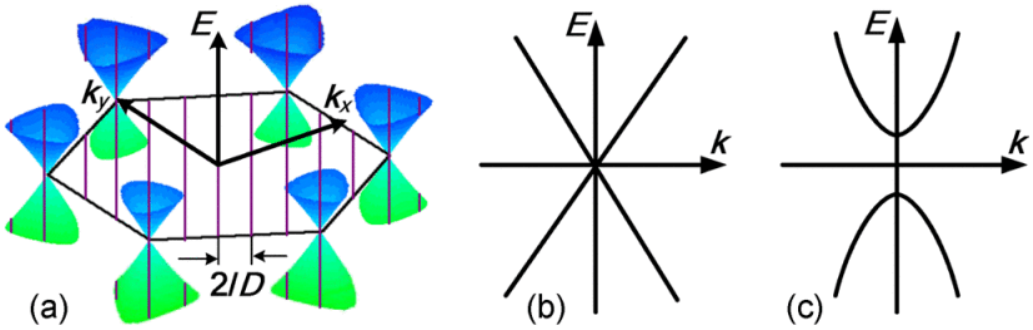

Figure 11 : (a) Band structure of graphene (b) metallic CNT or (c) semiconducting CNT

The locations of the cross section of the cut lines in k-space with the Dirac cones determine whether the resulting band structure is Figure 11. (b) Metallic or Figure 11. (c) Semi-conducting. The condition for a CNT to be metallic is for one of the slice to cut one of the cones at the apex, indeed, the band gap will be equal to zero.

To obtain the band diagram of a CNT, we simply superimpose each of the lone-dimensional curves obtained from the cuts, as in Figure 12.

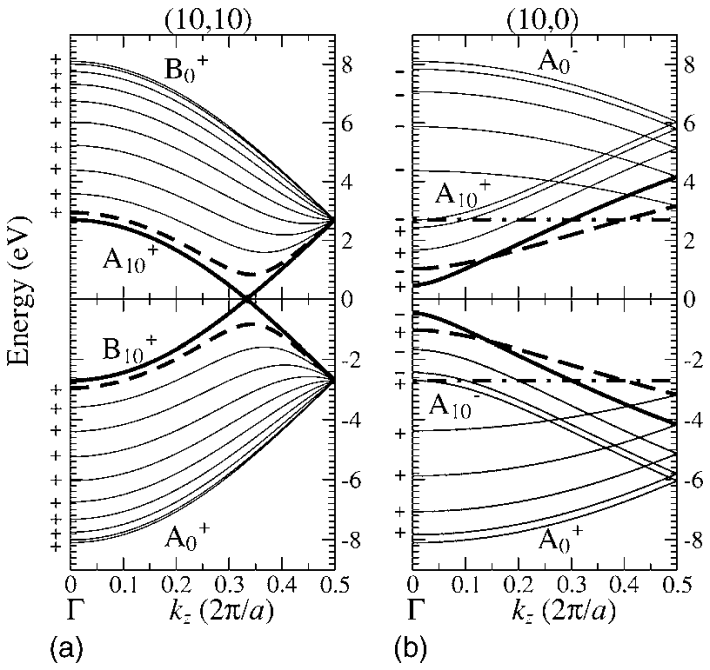

Figure 12: Band structure of an (a) (10,10) armchair and (b) (10,0) zigzag nanotube [35]

Let us note [34] that the orientation of the slices depend on the chirality of the CNT and that the distance between two slices is:

$$2\pi/\left||C_v|\right| = 2/D$$

We define $\boldsymbol{T_r}$ and $\boldsymbol{C_r}$ as the reciprocal vectors of $\boldsymbol{T}$ and $\boldsymbol{C_v}$. The condition for a slice to cut through the apex of the cone in K, is that the distance between X (the orthogonal projection of K on **T**) and K is a multiple of $\left||C_r|\right|$ (cf. Figure 13).

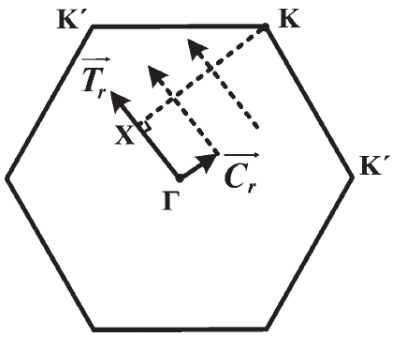

Figure 13: First Brillouin zone of graphene on which $\boldsymbol{T_r}$, $\boldsymbol{C_r}$ and X are drawed

It is shown in [36] that we have:

$$||\overrightarrow{XK}|| = \frac{2n+m}{3}||\boldsymbol{C_r}||$$

Meaning, that the CNTs are metallic if 2n+m is a multiple of three. A good approximation, given the hypothesis we made, of what we said in 1.1.3.

1.2.2. Band gap of the semiconducting CNTs

In order to calculate the band gap between the valence band and the conduction band, E_g, in semiconducting SWCNT, we can use the equation as a first approximation [37]:

$$\mathrm{E}_g = \frac{2\gamma_0 a}{D}$$

As we can see, the more the diameter increases, the more the gap decreases. With diameters important enough, at ambient temperature, the gap (between Fermi's level and the conduction band) is smaller than the energy given to the electrons by heat, E_h:

$$\mathrm{E_h}=\mathrm{k_B T}$$

With, k_B Boltzman constant in J.K^{-1}, and T, the temperature in K.

The electrons can go from the valence band to the conduction band, and the CNT behaves as a conductor.

Other models have been developed to calculate the energy gap, more precisely [38], [39].

1.2.3. Electronic Properties of Metallic SWCNTs

At the nanoscale, Ohm's law is no longer true, because conduction becomes quantized. In a CNT an electron can propagate on a finite number of channels. For a SWCNT, the number of channels is equal to two. Since a channel of conduction stems from the crossing of the conduction band and the valence band, and since those two cross only at the Dirac points K and K', the number of channel is indeed equal to two [40].

One of the more important characteristics of metallic CNTs when it comes to their conduction properties is the Mean Free Path (MFP). The MFP is the mean distance a charge carrier will travel without collisions with another particle. The longer the MFP, the lower the resistance. As we have seen in 1.2.1, an electron, or a hole, in a metallic SWCNT will behave as a Fermion. It will behave as a relativist particle, with a half integer spin, respecting Dirac's equation. Its speed will be v_F. That is why we say charge propagation in CNT sis ballistic and not diffusive (Figure 14). The MFP has been studied and determined in [41] :

$$\mathrm{MFP} = \frac{2\sqrt{3}\pi t^2 r}{2\sigma_E^2 + 9\sigma_t^2}$$

With σ_E and σ_t the variances of the local energy, t the jump energy to the nearest neighbor and r the radius of the CNT, t was determined to be 2.8 eV in [42].

Even though much approximatively, the formula below is also used:

$$\mathrm{MFP} \approx 1000D$$

With D, the diameter of the CNT. The MFP increases with the diameter.

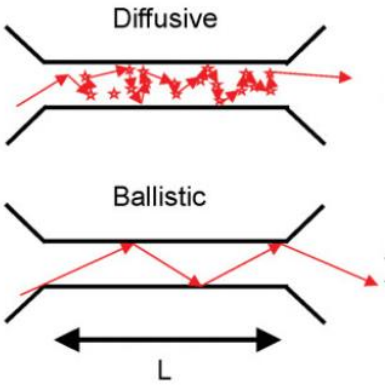

Figure 14: Above, diffusive conduction of charges, below, ballistic conduction of charges.

1.2.4. Electronic Properties of MWCNTs

As we said earlier, MWCNTs are composed of multiple SWCNTs sharing the same axis. We also showed earlier that there is roughly a probability 1/3rd for a SWCNT to be metallic. Thus, a simple statistical calculus, leads us to think that MWCNT generally be metallic. Indeed, for a MWCNT with more than three shells, the probability for one shell to be metallic is very high (0.7 for three shells). And, if one shell is metallic, the whole CNT is metallic, provided you have contact with all the inner shells i.e. that the CNTs are not closed (cf. 1.3 Fabrication).

Defaults can exist in SWCNT, and they usually are present. They can arise from topological exceptions, wrong hybridization, missing bonds or even doping from other materials than carbon. These defaults, reduce the MFP of the charge carriers, and increase the resistance. It is worthy to note that for MWCNTs, these defaults affect the inner shells less because the outer wall shields them. This makes MWCNTs more likely to conduct. The outer wall itself is just as prone to defaults as a SWCNT.

Finally, the most important factor that makes MWCNTs “metallic” is its diameter. Indeed, its diameter is usually much bigger than for SWCNTs. This means that even if some shells are semi-conducting, because their diameter is big, the energy gap is small. As we saw in 1.2.2, at ambient temperature, the energy given to the electrons can allow them to jump from the valence band to the conduction band. For a temperature of 300K, a simple numerical application gives a minimum diameter of 20nm, if we want $k_B T$ to be bigger than the gap between Fermi’s level and the conduction band. Furthermore, even if the diameter is not quite 20 nm, the electrons still have a reasonable probability (f_i) to appear on Fermi’s level, following Fermi-Dirac distribution:

$$f_i = \frac{1}{\exp\left(\frac{|E_i - E_F|}{k_B T}\right) + 1}$$

Where E_i is the energy level of the valence band just below E_F or the conduction band just above.

Because, there are an important number of sub-bands in a shell with a big diameter (1.2.2, number of slices proportional to D), their cumulative effect on the probability imply there can be numerous conductive channels. By consequent, a MWCNT with a lot of large shells can be a good conductor.

The exact number of conductive channels in a shell can be calculated by adding the probabilities:

$$N_{channel/shell} = \sum_{sub\ bands} \frac{1}{\exp\left(\frac{|E_i - E_F|}{k_B T}\right) + 1}$$

For a MWCNT, the total number of channels is the sum of each number of channels per shells.

But the usually used formula stems from [43] approximation:

$$N_{canaux/paroi}(D) \approx \begin{cases} a \cdot D + b, & D > 3\ \text{nm} \\ \frac{2}{3}, & D < 6\ \text{nm} \end{cases}$$

With D the diameter of the shell, $a = 0.0612\ \text{nm}^{-1}$ and $b = 0.425$. The error of this model is below 15% compared to the formula above. Because we know the internal diameter of a MWCNT is half the outer one [44], we have:

$$N_{channels/MWCNT} = \sum_{i=1}^{p} a \cdot D_i + b$$

With D_i, the diameter of the shell number i.

In [45], they explain the exceptional inductance they found, using the formula above. Ballistic conduction was proved in [44], where they found a MFP of 25um for a single MWCNT.

1.2.5. Other CNT Properties

In this section, we will do a brief list of the CNTs properties that have been reported in the literature.

CNTs can have huge aspect ratio, meaning their length can be considerably greater than their diameter (between 1 nm and 100 nm). In [46], growth of CNTs a few decimeters long has been reported, and in [47] an aspect ratio of 132,000,000:1 was measured.

CNTs have excellent strength. In [48], Young's modulus[6] ranging between 100 GPa and 263 GPa have been measured, while 63 GPa is the value reported in [49]. As a comparison, Young's modulus of diamond is 1 TPa and for steel 200 GPa. Furthermore, CNTs are also extremely flexible [50], [51], they can bend with a 45° angle and still be in the elastic deformation domain and up to 110° without irreversible fracture.

CNTs have exceptional thermal conductivity. Numerous results have been published on thermal conductivity of CNTs at room temperature [52]–[58]. Values range between 1750 and 5800 W/mK. Other materials used in electronics for their thermal properties, such as copper or aluminium, have thermal conductivity of 400 W/mK and 239 W/mK. The gap of performance is due to the difference in the mechanisms of heat propagation between metals and CNTs. In metals, mainly electrons propagate heat. In CNTs, thermal waves propagate through the vibration of each carbon atom; it is called phonon heat propagation. This has led to many studies regarding the possible use of CNTs in heat dissipation for electronics [59].

CNTs can withhold extreme current densities, up to 10^9 A.cm^{-2} (10^5 A.cm^{-2} for copper) and their conductivity can be as high as six fold the one of gold [60]. It is due to the ballistic transport

[6] Ratio between the axial force applied and the material deformation.

of charges. It makes them ideal for micron scale interconnects, because other conventional bulk materials are not as efficient due to electromigration, as we will see in Chapter 4.

Finally, CNTs have useful optical properties, mainly due to their narrow selectivity of the wavelength [61]. For example, they can be used as optically controlled switches [62], or as light emitting diodes (LEDs) [63] and photo detectors [64].

1.3. Fabrication Processes

There are different methods to fabricate CNTs. Depending on the application, research teams or firms, tend to use one or the other. Indeed, if, a transistor (or a nano-needle) is a few nm in dimensions, in mm-wave packaging applications, the dimensions range from a few tens of microns to a few millimeters. This means the scale of production is very different; while one CNT is sufficient for a transistor application; in our case, we will need much more to do a 50x50x50 um bump interconnect, for example. Fortunately, manufacturing methods, allow the fabrication of single CNTs as well as billions of them in parallel. Furthermore, the length of CNTs and the other parameters of importance can be controlled through fabrication.

In this section, we will mainly describe the Chemical Vapor Deposition (CVD) growth processes. Because, the temperature of this process is around 700°C, it is not compatible with typical mm-wave devices. That is why we will explain the different ways we can incorporate CNTs in mm-wave devices, with a focus on the transfer process (the process we will use to fabricate our devices).

In this work, all the CNTs used for fabrication and characterization were grown by our partner in Singapore, CINTRA (special thanks to Simon Goh and Chun Fei Siah).

1.3.1. Arc Discharge and LASER Ablation

1.3.1.1. Arc Discharge

In Ijima's founding article [20], the CNTs were fabricated using the arc discharge technique. The method is quite simple to implement and was the most used in the premises of CNT based works.

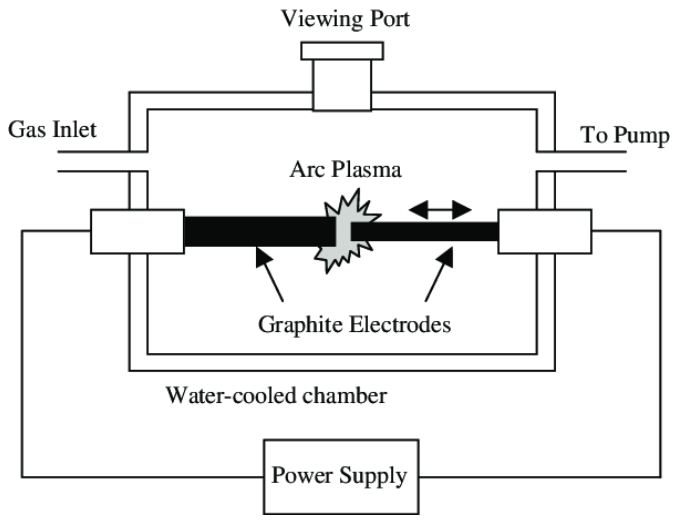

Figure 15: Arc Discharge Method Setup [65]

The setup (Figure 15) consists of two electrodes (an anode and a cathode) placed in a chamber filled by Helium at low pressure (between 200 and 900 mBar [66]). Both electrodes are separated by approximately one millimeter. The anode is made of a metal containing carbon, and the anode of graphite. A current is applied and sent through the two electrodes. The arc discharges created will heat both anode and cathode surfaces, and temperatures of 4,000 K and 3,500 K will be reached on the anode and cathode, respectively. The carbon in the anode will evaporate to the cathode and form carbon nanotubes structure on it.

We can note that a direct current (DC) is better than an alternative current (AC) to obtain CNTs of good quality (less defaults) and that an anode made of graphite will give MWCNT (in opposition to SWCNT for an anode made of metal containing carbon) [51]. This method gives CNTs of good quality and is efficient to produce them in large numbers. However, the CNTs produced are all different in length and diameter.

1.3.1.2. LASER Ablation

Though LASER ablation was used before, R.E Smalley group was the first to use LASER ablation for the fabrication of CNTs in 1995 [67].

The setup is shown in Figure 16. It consists of a LASER, a furnace with a graphite (or metal containing carbon) target inside and a copper collector. To produce CNTs, the furnace has its temperature set to 1,500 K and a high energy pulsed beam (few hundred Joules) is sent on the target. The Laser beam scans the surface of the target to get a uniform temperature and carbon nanotubes stem from the target. Argon is sent in the chamber with a continuous flow in order to carry the carbon particles to the cooled copper collector, where they can be collected.

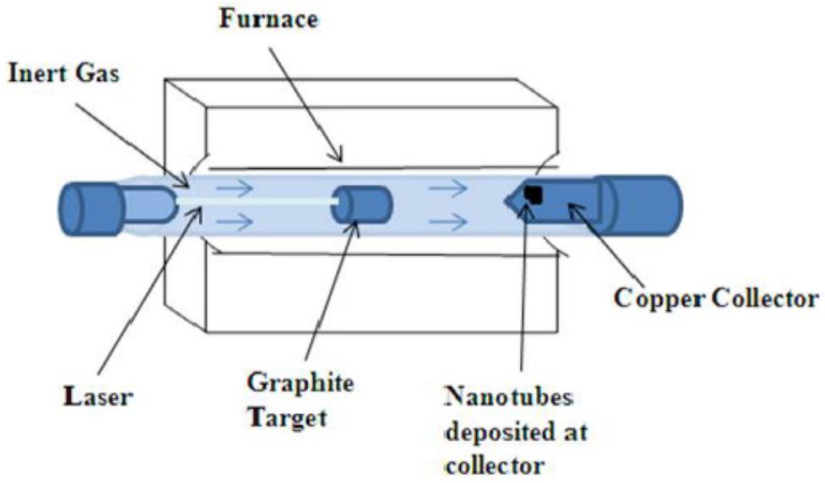

Figure 16 : Schematic diagram of Laser ablation set-up for CNT synthesis [68]

The CNTs obtained with this method are mostly SWCNTs. They arrive on the collector agglomerated in bundles due to the Van Der Walls force. This process allows for excellent quality CNTs (purity up to 90% [69]). Unfortunately, because this process is very expensive, not efficient for large-scale production, and the fact that the CNTs are disparate and in bundles (not aligned), it will not be used in our work.

1.3.2. CVD Growth

CVD is a fabrication process that consists in depositing layers of chemical (in opposition to Physical Vapor Deposition (E beam evaporation)) on a surface using the reaction that happens between the volatile compound and the surface material. This process is often used in the industry to produce thin films.

For the fabrication of CNTs using CVD, the reaction taking place at the surface of the material is of the Vapor-Liquid-Solidification (VLS) type.

In this section, we will start by explaining the VLS mechanism, in order to describe the Thermal CVD (TCVD) and Plasma Enhanced CVD (PECVD) processes.

1.3.2.1. VLS Principle and Equations

The VLS method is a way to grow a crystal on a surface through direct adsorption of a gas phase. We will base what follows on the concrete example of CNTs, yet other crystal can grow using VLS, such as silicon nanowires [70].

The objectif is to grow a CNT on a silicon substrate. If we were to take the substrate and put it in a chamber with a flow of carbonous gas and wait for the carbon atoms of the gas to precipitate in silicon to grow out of it as a CNT, we would not have results. The VLS simply proposes to add in the equation a little droplet of liquid gold (or alloy in general) typically a few nm in diameter. Though what happens is not fully understood yet [71], the carbon atoms from the gas will precipitate in the droplet and oversaturate it. Once there is no more room for the new coming atoms, those push out of the droplet the ones already there. When the carbon atoms are pushed out, they arrange themselves to form a CNT (if it is silicon atoms in the gas, they form Silicon crystals). There is a schematic of the process in Figure 17. This process is called VLS, because we have the three states in the reaction, vapour for the gas, liquid for the alloy and solid for the crystal.

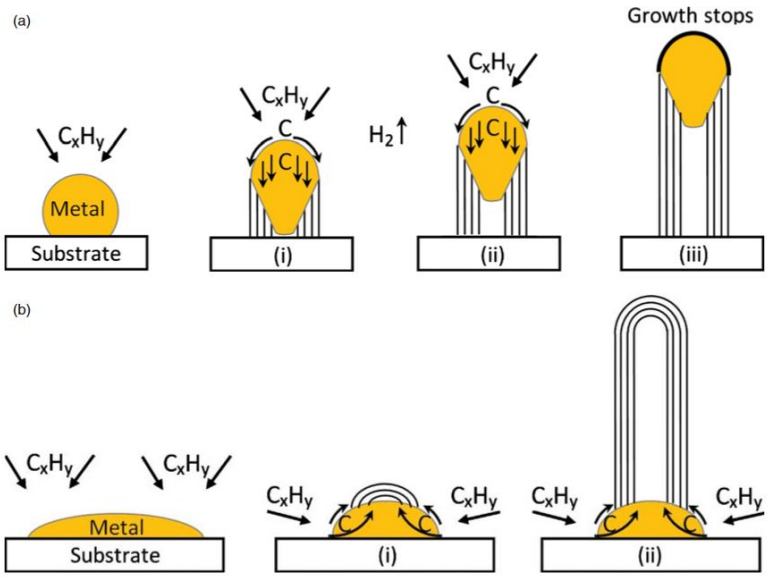

Figure 17 : Widely-accepted growth mechanisms for CNTs: (a) tip-growth model, (b) base-growth model [72]

Here are a few equations ruling the VLS mechanism [73], [74]:

- The radius of the nanostructure (R) is given in function of the seed radius (r) by:

$$\mathrm{R} = r\sqrt{1 - (\frac{\sigma_{ls}}{\sigma_{lv}})^2}$$

With, σ_{ls} and σ_{lv} , the liquid-solid and liquid-vapor interfaces tension energies. As expected, we have R smaller than r.

- The flux of adsorbed atoms in the droplet (Φ_{ads}) is given by:

$$\Phi_{ads} = \alpha \frac{P_G}{\sqrt{2\pi m_G k_B T_G}}$$

With, α the effective adsorption coefficient, P_G the partial pressure of the gas, m_G the mass of the gas molecule, k_B Boltzmann's constant and T_G the temperature of the gas.

- The flux of desorbed atoms (Φ_{des}) is given by:

$$\Phi_{des} = \alpha \frac{P(r)}{\sqrt{2\pi m_G k_B T_G}}$$

With,

$$\mathrm{P(r)} = P_\infty e^{\frac{2\Omega_l \sigma_{lv}}{r k_B T_G}}$$

With, P_∞ the vapour tension for an infinite diameter seed and $\Omega_l$the seed volume.

To have growth, we need to have:

$$\Phi_{ads} > \Phi_{des}$$

Which gives a minimal seed radius:

$$r_{min} = \frac{2\Omega_l \sigma_{lv}}{k_B T ln(\frac{P}{P_\infty})} \Phi_{des}$$

These equations allow us to better understand how we can tweak the growth parameters in order to obtain the geometry of CNT we want.

1.3.2.2. TCVD Growth

The steps of TCVD for CNT growth are as follows: catalyst preparation, growth of the CNTs and end of growth.

On the substrate (silicon wafer), we deposit the barrier and catalyst layer. The catalyst layer is a few nm in thickness of the wanted metal (iron for example). The barrier layer is made of alumina (Al2O3), for example. We then put the catalyst and substrate in the furnace and heat it. It ensues the formation of droplets of alloy, due to the difference of CTE coefficient between the silicon substrate and the catalyst. The barrier layer is here to ensure the formation of the seed by avoiding diffusion of the alloy in the substrate. We now have a substrate with multiple seeds of the wanted dimensions (it depends on the catalyst thickness and temperature) as seen in Figure 18.

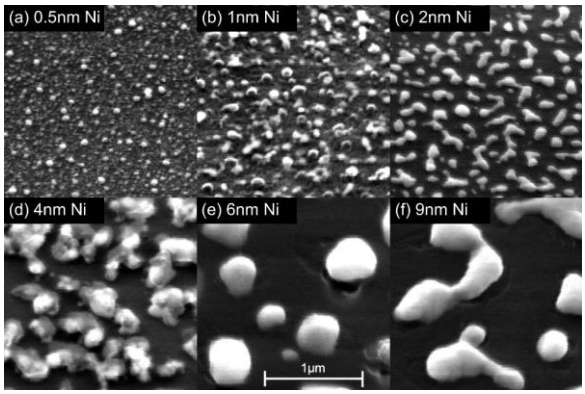

Figure 18 : SEM imaging of the catalyst after heating for different thicknesses

We then increase the temperature (between 550°C and 1200°C) and start the flow of gas inside the chamber. Carbon precipitates in the droplets and carbon nanotubes start forming. Different studies on different parameters show experimentally that:

- The different precursors [75]–[79] impact the produced CNTs morphology [80]
- The alloys that work best for CNT growth are Fe, Co and Ni [81]
- The temperature affects the CNT structure [76]
- The catalyst can also be solid [81]

The growth stops either when the gas flow is cut or when the droplets cannot adsorb the carbon atoms anymore. This happens when a layer of carbon is totally covering its surface (Figure 19).

It is worthy to note that we can add a vapor to augment the quality of our CNTs [82]. For example, if ethanol or water is added during the growth, it increases the quality by eliminating amorphous carbon. It also allows for longer CNTs, because the layer of carbon that can cover the seed is eliminated [83]. A schematic is shown in Figure 19, to summarize the process.

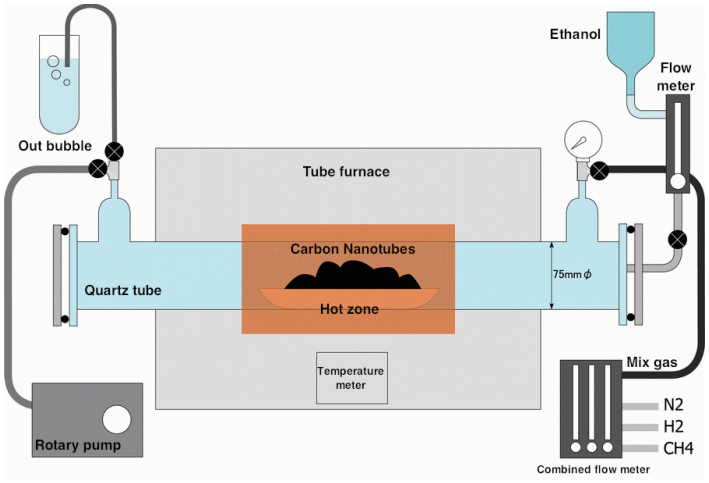

Figure 19 : Chemical Vapor Deposition (CVD) process principle. The central tube, which is surrounded by a furnace, is the CNT growth location [84]

TCVD will be the method used to grow the CNTs that we will consider in this PhD work for the fabrication of the studied devices. The CNTs produced are what we call VACNT bundles (or CNT forest), an SEM picture is shown in Figure 20. It consists of multiple CNTs in parallel, each stemming from a seed. This new material has particular properties that will be described later in this work.

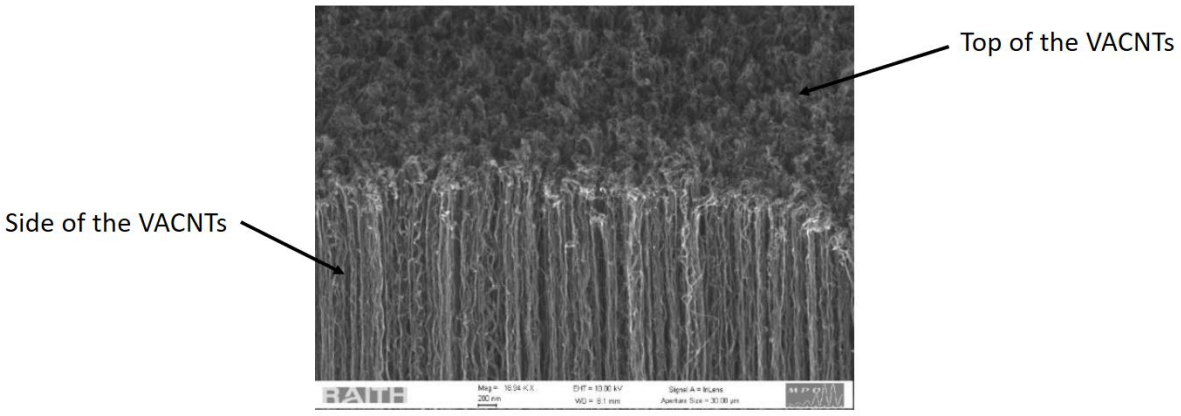

Figure 20 : SEM picture, from the side, of the VACNT forest grown by TCVD

1.3.2.3. PECVD Growth

PECVD consists in the same steps than a TCVD with an added plasma during the growth. The setup is as shown in Figure 21.

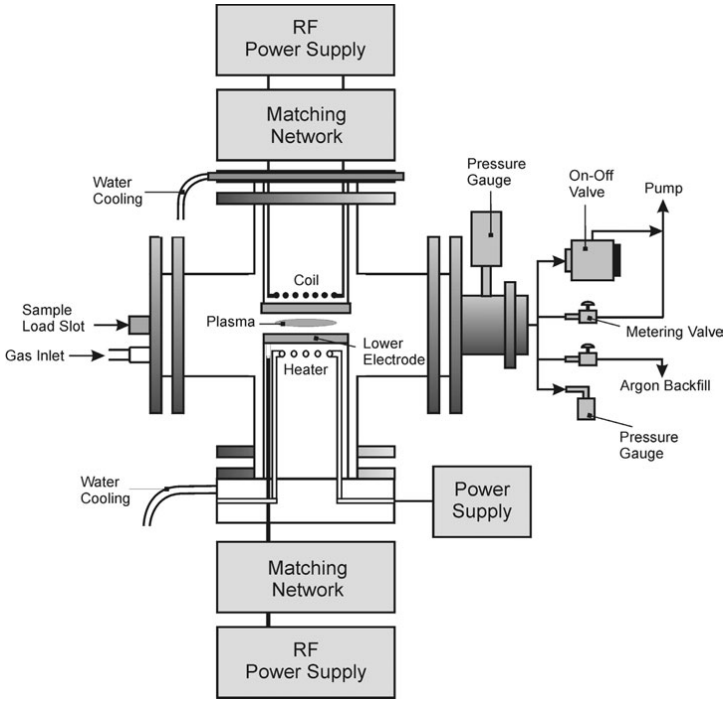

Figure 21 : Schematic of a PECVD setup [85]

The plasma allows for lower temperatures, less dense forest and orientation of the CNTs [85].It also allows for self-standing CNTs as opposed to wavy CNTs from TCVD. As we have seen the temperatures of the TCVD process range between (550°C and 1200°C), which is not compatible with CMOS technology for example (400°C). The direction of the current in the plasma will be collinear to the axis of the CNTs. Finally, we can note that less dense forests can be useful if there is a need for single CNT measurement, where TCVD samples are two tightly packed.

1.3.3. Transfer Process

Due to the very high temperature processes we cannot grow our CNTs directly on our devices using TCVD [86]. Due to the lower density, and possible ionizing of the circuit [81] we also chose not to use PECVD, though previous results have been obtained by this method [87]. The only remaining solutions is to grow separately our VACNT with CVD and find a way to transfer them on our devices using compatible temperature processes.

Some research teams use spray-coating [88], brushing [89] or even inkjet printing [90] but the resulting structure is fundamentally different then VACNT. Indeed, the CNT are oriented in a random order, this is what we call CNT Buckypaper.

Fortunately, there is a possibility to take the separately grown VACNTs bundles and bond them to a receiving substrate. Various methods of bonding have been investigated in the literature [91]–[93]. A schematic of the process is shown in Figure 22. The steps are: growth of the VACNT bundles by TCVD on a separate substrate, preparation of the receiving substrate, assembly of the two parts, bonding of the CNTs to the receiving substrate and mechanical removal of the growth substrate.

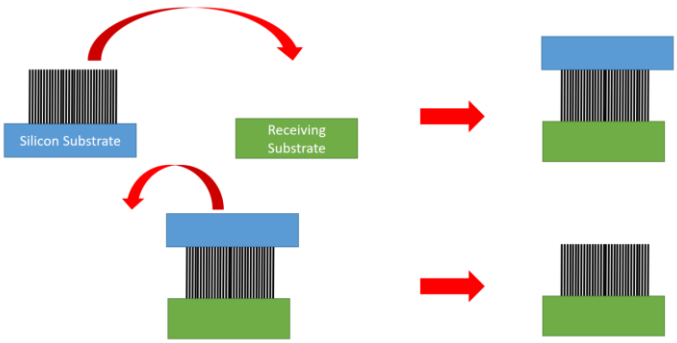

Figure 22 : Schematic of transfer of VACNTs

As long as the bonding between the receiving substrate and the CNTs is stronger than the one with the growth substrate, we can simply pull away the two parts and the CNTs will be transferred.

Given the fact that we can grow CNTs in pattern using TCVD by simply patterning the catalyst [94], we can transfer the shape we want. The resolution of the catalyst patterning is the one of classical photolithography process. That means we can have transferred VACNTs bundles almost as small as we wish, the theoretical limit is the size of a single CNT. It is this fabrication process that has been used throughout this thesis, the process will be described more precisely in Chapter 2.

1.4. Modellization of VACNT bundles

A full quantum mechanical treatment would be the most accurate method to model our VACNT bundles. It can be applied using Density Functionnal Theory but it is not applicable in our case because of the too great difference of dimension between a single CNT and the rest of the mm-wave device (a few mm). Another solution, but still limited to the nanoscopic scale, is the joint solving of electromagnetic and quantum equations. We face one of the most common problem when trying to use nanomaterials at the bigger scale, the modellization of billions of elements.

In this section, we will start by developing the simple CNT circuit model in DC, and then develop circuit models in RF for SWCNT, MWCNTs and MWCNT arrays. We will conclude by presenting the bulk equivalent model from [95] for VACNT bundles.

1.4.1. CNT DC circuit model

In the case of DC, a CNT behaves as a resistance. Its resistance is decomposed as three types of resistances in series:

- The contact resistance R_c
- The quantum resistance R_q
- The CNT resistance R_{CNT}

In this section, we will define and describe each of these resistances.

1.4.1.1. The contact resistance R_c

This resistance models the difficulty with which the electrons can go from the CNT to the material in contact with it. This contact resistance has mainly been studied for metals.

As we can expect, it depends on the contact surface (roughness, etc.) and the material. It varies between a few kΩ and a few MΩ [96]–[101].

We can add that the contact resistance depends on the shape of the end of the CNT. If it is closed (Figure 17) and only the outer shell is in contact with the surface, the resistance will be higher. If it is open, and the contact is made with the inner shells as well, the resistance will be lower [102].

Finally, the study in [101] shows contact resistance decreases with CNT diameter.

1.4.1.2. The quantum resistance R_q

The quantum resistance stems from the fact that electron propagation is CNTs is quantized (cf. I.2.1). There is a limited number of channels of conduction in a CNT, and only two spins can propagate in each. This limitation gives [103]:

$$R_Q = \frac{h}{N_{spin} N_{channel} e^2}$$

With, h Planck's constant, e the elementary electron charge, N_{spin} the number of electron spin for the channel and $N_{channel}$ the number of conducting channels.

For a SWCNT, there are only two conduction channels giving a resistance of 6.45 kΩ. This value is quite high. To remedy the high resistance, CNTs are usually used in bundles in DC

applications. Using MWCNT also reduces the resistance because the number of conducting channels is higher.

1.4.1.3. The Carbon Nanotube Resistance R_{CNT}

This resistance contrarily to the quantum resistance, depends on the length of the CNT, it is distributed. Because electron propagation in CNTs is ballistic, it only appears if its length is bigger than the MFP. This resistance was measured in [104], the formula is [103]:

$$R_{CNT} = R_Q \frac{l}{MFP}$$

CNTs with few defects will increase MFP and thus, decrease resistance.

We can now obtain the DC resistance of bundles of VAMWCNT, the formula is obtained by summing the resistances defined above for an individual CNT and consider multiple similar CNTs in parallel:

$$R_{bundle} = \frac{R_{C1} + R_{C2} + R_Q + R_{CNT}}{N_{CNT}}$$

With R_{C1} and R_{C2} the contact resistances at each CNT end and N_{CNT} the number of MWCNTs.

Though this formula is useful for Nanopackaging (DC interconnects in Chapter IV), we are mainly interested by the RF behavior of CNTs. We develop them in the next section.

1.4.2. RF circuit models

1.4.2.1. SWCNT RF circuit model

We will consider in this part the CNT to be “above a ground plane”, meaning the CNT is parallel to a theoretically infinite metallic plane. We can then use the model of the transmission line to describe the propagation of an EM wave along the CNT. The distributed parameters of the CNT line are shown in Figure 23:

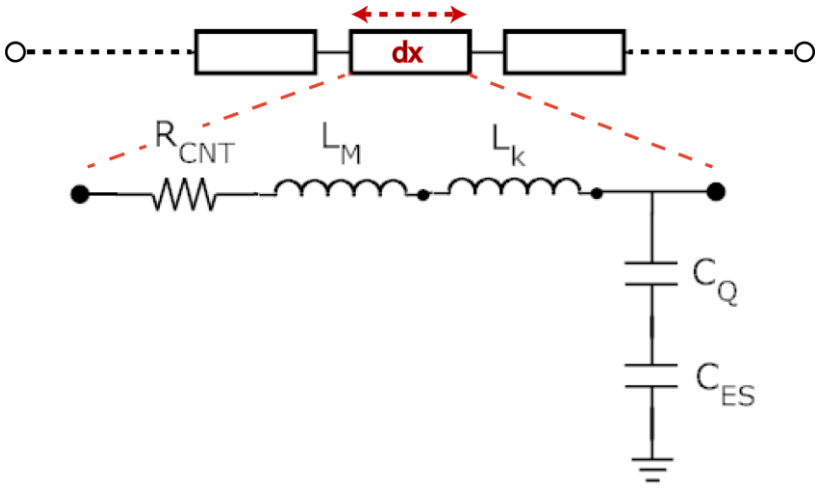

Figure 23 : Transmission line model of a SWCNT [84]

R_Q is also present but not distributed so not included in the RF transmission line model. There is no conductance because we consider the surrounding medium to be vacuum, which is lossless. The other five distributed components are thoroughly explained in [105], [106], and comes from Burke's article on Luttinger liquid theory applied to carbon nanotubes [107].

The magnetic inductance L_M and the electrostatic capacitance C_{ES} come from the classical electromagnetic equations for a conductive wire parallel to a ground plane:

$$L_M = \frac{\mu_0 l}{2\pi} arcosh(\frac{d}{a})$$

$$C_{ES} = \frac{2\pi\varepsilon_0 l}{arcosh(\frac{d}{a})}$$

With a the CNT radius, d the distance between the CNT and the ground plane (d>a), l the CNT length (dx) and ε_0 and μ_0 the vacuum constants.

The distributed resistance R_{CNT} and R_Q the quantum resistance remain the same because they depend on the number of channels, and it remains the same as in DC in RF, a priori.

The kinetic inductance L_K and quantum capacitance C_Q stem from the quantum effects of electron propagation in 1D conductors [refs]. The equations are:

$$C_{Q/channel} = \frac{4e^2}{hv_F}$$

$$L_{K/channel} = \frac{\mathrm{h}}{4e^2 v_F}$$

With h Planck's constant, e the elementary charge and v_F Fermi's velocity.

C_Q will be negligible compared to C_{ES} and L_M will be negligible compared to L_K, for small CNT diameters [87].

1.4.2.2. MWCNT RF circuit model

We will consider in this part the MWCNTs to be open-ended, and that the contact is made with all the shells. A circuit model for such a case has been developed in [106].

The quantum resistance is adjusted with the number of conducting channels in the MWCNT.

The outer shell is simulated just the same way as a SWCNT would be. The inner shells, all with different diameters have the same distributed elements as in the previous part to the exception of C_{ES}, which does not have the same expression anymore (no longer wire parallel to the ground, but coaxial transmission), and L_M, which is being considered to be 0.

Furthermore, different physical phenomena that were not happening for SWCNT need to be modelled, the tunneling conductance G_T between two shells and the mutual inductance between a shell and its two neighbors. The equations are:

$$C_{ES} = \frac{2\pi\varepsilon_0 l}{\ln(\frac{D_{out}}{D_{out} - 2d})}$$

$$G = \frac{1}{\sigma\pi D_{in}\mathrm{l}}$$

$$M_{shell} = \frac{\mu_0}{2\pi}(\ln\left(\frac{4l}{D_{out}}\right) - 1 + \frac{D_{out} + D_{in}}{\pi l}$$

With, d the distance between the two shells (Van Der Walls), D_{in} the diameter of the inner shell of the caxial structure, D_{out} the diameter of the outer shell and σ the tunneling conductivity between two shells. The circuit model is presented in Figure 24.

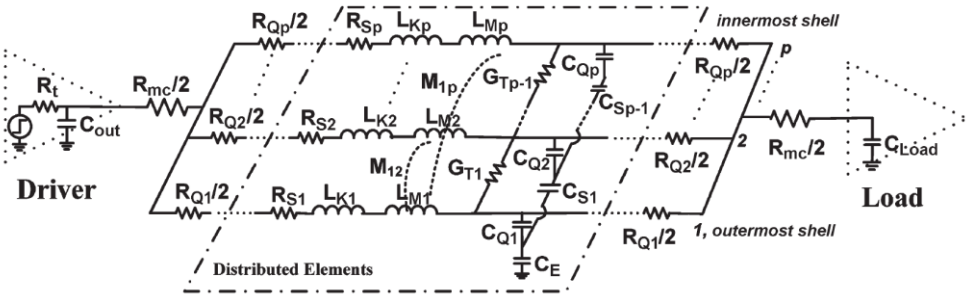

Figure 24 : MWCNT transmission line, equivalent circuit model

1.4.2.3. Bundle of MWCNT Circuit Model

If we were to do hybrid simulations, combining the use of the circuit software ADS to HFSS for example [81], the computer processor would not allow for billions of circuit lines in parallel each representing a CNT in a bundle. That is why we need to simplify the circuit first, by neglecting what can be neglected and sum what can be summed. To simplify the problem, we will consider every CNT to be the same if only for their position in space.

Mutual inductance, tunneling conductance and coupling capacitance are not considered, they were shown to be negligible in [108], [109].

The number of CNTs divides resistances and inductances in series, and capacitances in parallel are multiplied. We obtain, with the previous notations:

$$R_{Q/Bundle} = \frac{\mathrm{h}}{2e^2}\frac{1}{N_{channel}N_{CNT}}$$

$$R_{CNT/Bundle} = R_{Q/Bundle}\frac{\mathrm{l}}{\mathrm{MFP}}$$

$$L_{K/Bundle} = \frac{\mathrm{h}}{2v_F e^2}\frac{l}{N_{channel}N_{CNT}}$$

$$C_{Q/Bundle} = \frac{2e^2}{\mathrm{h}v_F} l N_{channel}N_{CNT}$$

$$C_{ES/Bundle} = \frac{2\pi\varepsilon_0}{\ln(\frac{d}{a} + \sqrt{\frac{d^2}{a^2} - 1})} l N_{CNT}$$

This model is a circuit one, though very useful for interconnect modelling, lacks to represent certain aspects of the CNT forest we will use for our devices in this work. For example, we

cannot model EM characteristics such as the reflection of an EM wave on a VACNT bundle, or the radiation pattern of an antenna, etc.

That is why an equivalent bulk model was developed previously in our research team [62] and we will briefly explain the equation behind it in the next section.

1.4.3. The Bulk Equivalent model

The complete development of the model is explained thoroughly in [62], [95]. The steps of obtention are as follows: we first model individual CNTs as hollow metallic tubes; we then find the equivalent nanowires; and finally, we determine the bulk equivalent model properties (Figure 25).

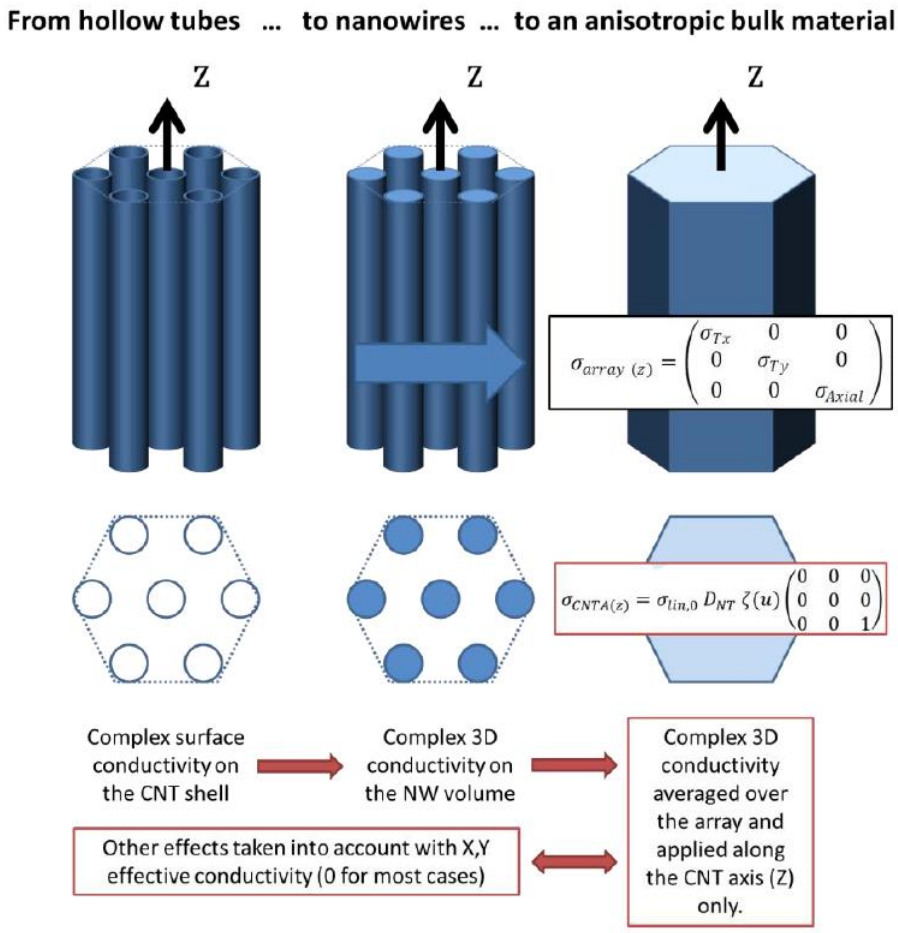

Figure 25 : Schematic illustration of the obtention of the anisotropic bulk model

Because, the diameter of the CNTs is very small (few nm) compared to the wavelength we are working at (mm-wave), we consider the use of a bulk equivalent model to be coherent.

Slepyan and Masimenko [110] model CNT quantum properties by an equivalent hollow tube with complex conductivity. The conductivity is obtained using the semi-classical approximation based on Boltzman kinetic equation and tight-binding theory [111]. We have:

$$\sigma_{CNT,surf} \simeq \frac{2e^2 v_F}{\pi^2 \hbar a(\nu + j\omega)}$$

With, e the elementary charge, v_F Fermi's velocity, $\hbar$ Planck's constant divided by 2π, ν is the relaxation frequency and ω the angular frequency.

This formula is valid for SWCNTs only, and for $\omega < \frac{3v_F}{a}$, or a frequency below a few tens of THz [112].

A bulk nanowire equivalent to this hollow tube is obtained by equalizing the impedances of the two types of tube (hollow, nanowire).

Finally, by averaging the conductivity of the nanowire bundle (bundle of vertically aligned nanowires in hexagonal geometry), we obtain the conductivity in the direction of the axis of the nanowires:

$$\sigma_{Axial} = \frac{8e^2 v_F}{h(\nu + j\omega)} D_{CNT}$$

With, D_{CNT} the density of CNTs in the bundle in number/area.

Also, by using the effective medium theory (Bruggeman), we have an expression linking the lateral conductivity of the equivalent material to the nanowire conductivity and the conductivity of the embedding medium (vacuum here). This leads to:

$$\sigma_{lateral} = 0$$

If,

$$\delta_r \geq 2\left(\sqrt{\frac{\pi}{\sqrt{3}}} - 1\right)a$$

With δ_r the distance between two nanowires, and a the radius of the nanowire. This is verified in TCVD grown forests were the density reaches 10^{15} CNTs/m^2 maximum [113].

To summarize, the bulk equivalent model for VACNT bundles conductivity is the following tensor:

$$\sum = \begin{bmatrix} \sigma_{lateral} & 0 & 0 \\ 0 & \sigma_{lateral} & 0 \\ 0 & 0 & \sigma_{Axial} \end{bmatrix}$$

This model has been developed for VASWCNT and has been compared to the circuit model from I.4.2.3 with good accordance [62] for interconnects. This model is the one we use in all the Finite Element Method (FEM) simulations of this manuscript.

Though the model was developed for VASWCNT arrays, it can still be used for bundles of MWCNT with good accordance with measurements results [81]. Indeed, this model shows two important things common to all bundles of nanowires: the conductivity is anisotropic (provided the distance between the wires is sufficient) and the conductivity depends on the density of the array. Numerical applications are presented in Table 1.

Table 1 : Values of Conductivity (in S/m) for Different Densities and Different Frequency

D_{CNT} (CNTs/m^2)	10GHz	20GHz	50GHz	80GHz	100GHz
10^{13}	2.95e3	2.68e3	1.62e3	9.34e2	6.72e2
10^{14}	2.95e4	2.68e4	1.62e4	9.34e3	6.72e3
10^{15}	2.95e5	2.68e5	1.62e5	9.34e4	6.72e4
10^{16}	2.95e6	2.68e6	1.62e6	9.34e5	6.72e5

1.5. Characterization of VACNT bundles

The previous paragraphs show that some parameters will change the way VACNT bundles behave, especially electrically. Whether it is the number of shells, the type of CNTs, their diameter, their quality or more importantly, the density, the conductivity will vary greatly depending on these parameters. Moreover, all these characteristics will also impact all the other properties; thermal, mechanical, optical, etc. Thus, it is critical to have ways to characterize the grown samples from TCVD.

VACNTs bundles is a difficult material to characterize for a least two reasons:

- The main difficulty resides in its definition: billions of CNTs in parallel. Indeed, for a few tens of microns square, the bundle is already composed of billions of CNTs and it is the properties of the individual CNTs that give the bundle its properties. We would need to have the characteristics of each CNT to have the exact behavior of the bundle. Yet characterizing one CNT takes time, let alone billions of them.
- The second difficulty is the limitations implied by the fabrication process, we cannot have samples of any dimension we want, the bundles are to be supported by a substrate, they have to be perpendicular to the substrate, etc.

In this section, we will present a few of the characterization methods we have used to characterize our samples. These methods go from the observation of one CNT to the overall DC conductivity of a bundle.

1.5.1. Characterization of the CNTs

To determine the structure of the individual CNTs , two methods are usually used. TEM allows for “direct observation” of the CNT, while Raman and XPs allow scanning an area with multiple CNTs and extracting the average characteristics of this area.

1.5.1.1. Tunneling Effect Microscope (TEM)

The tunneling effect microscope is actually the first tool used to observe CNTs, it is widely used in the domain of nanotechnologies. It consists of sending electrons in a sample and measure the transmitted electrons. Because of the known equations of the tunnel effect, in function of what is transmitted, an image can be artificially created. This method allows to see as little as individual atoms.

To observe the TCVD grown CNTs used in this PhD work, we must fabricate a sample thin enough to allow for the tunneling effect to happen. In order to do that, CNTs are diluted in water and then a sample is kept between two glass plates. A TEM image obtained using this

method is shown in Figure 26. We can see a MWCNT and determine its diameter and number of shells. We usually do several measurements and the mean gives the average CNT in the forest.

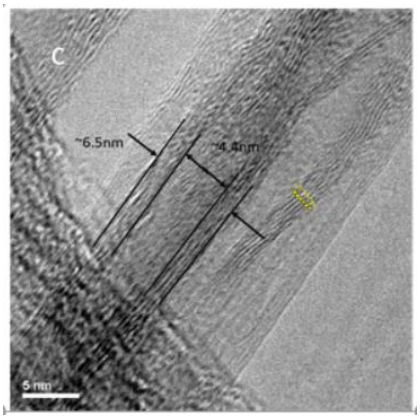

Figure 26 : TEM image of a Multiwall CNT in CINTRA

1.5.1.2. Raman and XPs

Raman and XPS are used not for determining the geometry of the CNTs but their structural quality (type of covalent bonds). Both are Spectroscopy method. For Raman, a beam is sent toward the sample and the reflected beam is measured with a CCD captor. For XPS an X-ray beam is sent on the sample and the emitted phonons of the sample are measured.

Depending on the electronic structure of the sample, the shift in frequency (Raman), or the wavelength of the emitted (photoelectrons) will give information.

In our case, it will give us the amount of sp2, sp3, CO, etc. bonds in the sample. The ratio between the number of sp2 bonds and the rest gives the quality of the CNTs (for a perfect CNT there are 75% of sp2 bonds (1.1.1)). For a high ratio of sp2 bonds, we can deduce a high number of CNTs compared to other possible carbon structures without sp2 bonds. Results for Raman and XPS of our samples are shown in Figure 27.

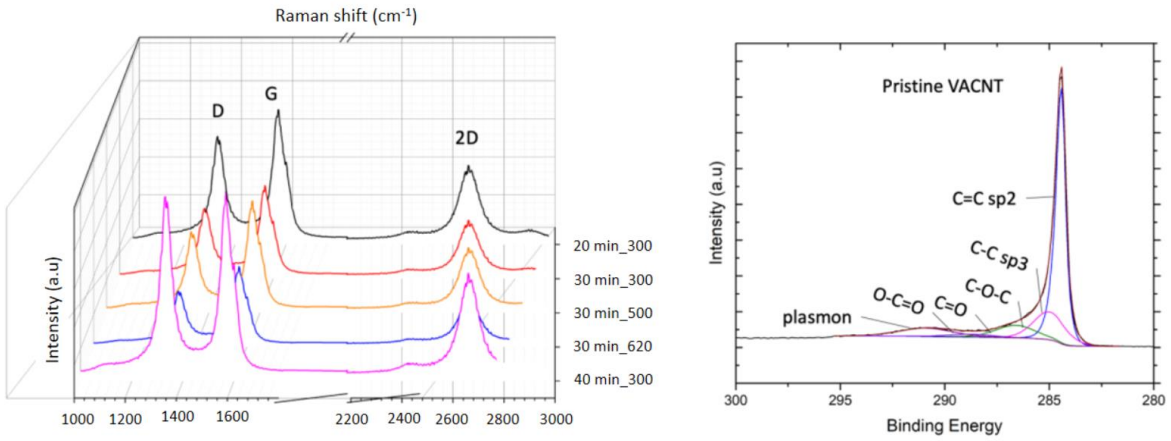

Figure 27 : Left Raman shift of our CNT samples, and Right, XPS spectrum

The different colors relate represent different growth processes tested in CINTRA. In the case of the Raman scan, the ratio between the two intensity peaks ID and IG is directly linked to the percentage of sp2 bonds. The smaller the ratio, the less defects will be present in the CNTs. For different growth times (black, red and pink curves), 20 minutes, 30 minutes and 40 minutes the ratios are 0.783, 0.783 and 0.971 respectively. Which means if the growth time is too long, the quantity of defects will increase. Yet, in order to achieve a certain height, the growth time has to be increased; one must find a compromise. The XPS spectrum on the right gives the binding energy spectrum of the samples. Different binding energies correspond to different types of bonds. By measuring the area below the curve, it is possible to obtain the different percentage of each bond in the sample. These measurements complete well the Raman scan, and are in accordance.

1.5.2. Density measurements

The most used method to calculate the density of VACNT bundles is the use of a microbalance, conjugated with TEM observations. TEM observations give the average of the dimensions of the CNTs outer and inner diameter R_{out} and R_{in}, the average weight is given by [114]:

$$m_{CNT} = V_{CNT} \rho_{graphite}$$

With, $V_{CNT} = \pi({R_{out}}^3 - {R_{in}}^3)$, the average volume of the CNT and $\rho_{graphite}$ the density of graphite.

By measuring the weight of the substrate before and after CNT growth, one can obtain the number of CNTs, by dividing the total weight by the weight of the average CNT.

However, this method does not take into account that not all structures in the forest are CNTs. There can be amorphous carbon, or other carbon oxygen composites, whose weight will be counted as CNT.

1.5.2.1. X-ray

In this section, we will explain the X-ray method developed by Hart's team in [115], [116]. This method is the most complete to determine accurately the CNT bundle density.

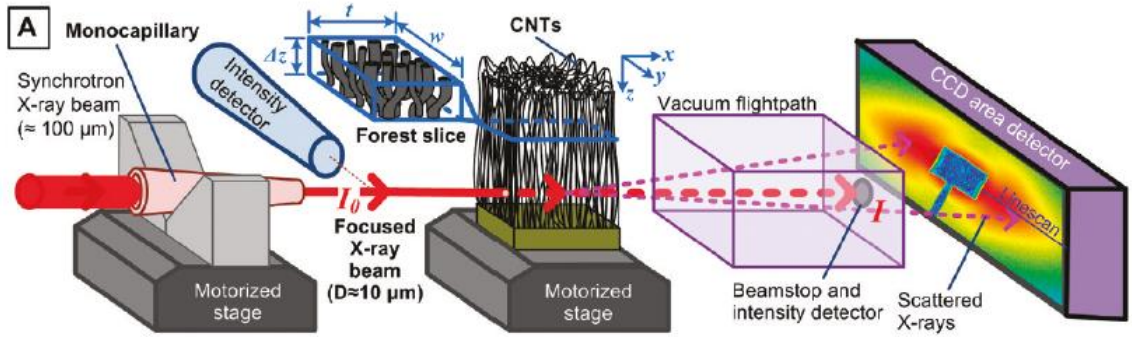

Figure 28 : Schematic of the X-ray characterization method [115]

As shown in Figure 28, here is how the outline of how the method works: an X-ray beam is generated and it goes through a forest of CNT, we then gather the scattering data on a screen behind the forest.

Here is how it works precisely step by step:

Step 1: We apply Beer-Lambert-Bouguer law. We calculate the ratio between the intensity before and after the sample and we can infer the volume mass of the slice we are lighting.

$$\rho_m = \frac{\ln(\frac{I_0}{I})}{t(\frac{\mu}{\rho})}$$

ρ_m is the local mass density, I_0 the intensity before going through the forest, I the intensity after the beam went through the forest, t the thickness of the forest (forest depth in the direction of the beam) and $\frac{\mu}{\rho}$ the total mass attenuation coefficient (3 cm^2/g for graphite for an X-ray energy of 10keV).

If we say all the CNTs are aligned, we can deduce their number directly from the mass density calculated above. We consider the tubes are hollow tubes with walls having the same density as graphite. We just need to know their radii, which can be done by TEM.

Unfortunately, the tubes are wavy. And, one tube takes more space if he is wavy than straight (Figure 29), the number of CNTs is an overestimate if we stick to the simple calculus. Plus, all the CNTs do not have the same diameter, we have to take an average of many measurements made by TEM (Figure 26) and it takes time.

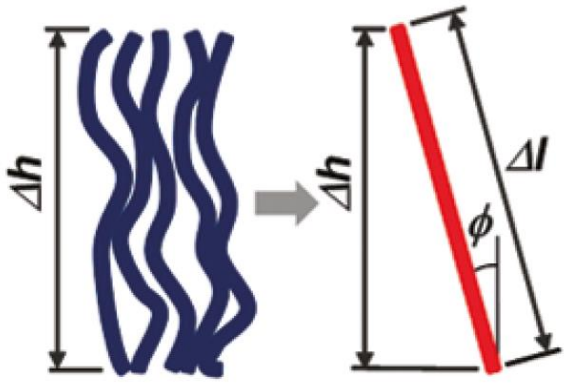

Figure 29: Schematic of the space taken by wavy CNTs, Source: [116]

With the X-ray method we are not only able to precisely determine the distribution of the diameters of the CNTs but also their waviness which allows us estimate very precisely the density of the forest.

Step 2: A series of scan for different distances to the top of the sample (middle of the focal spot to top) are then made. For each distance from the top of the forest, a scan is made, and the intensity in function of the scattering vector is plotted. In Figure 30, the scans are superimposed on the same graph. For each scan, the fitted model (explained below) is also plotted.

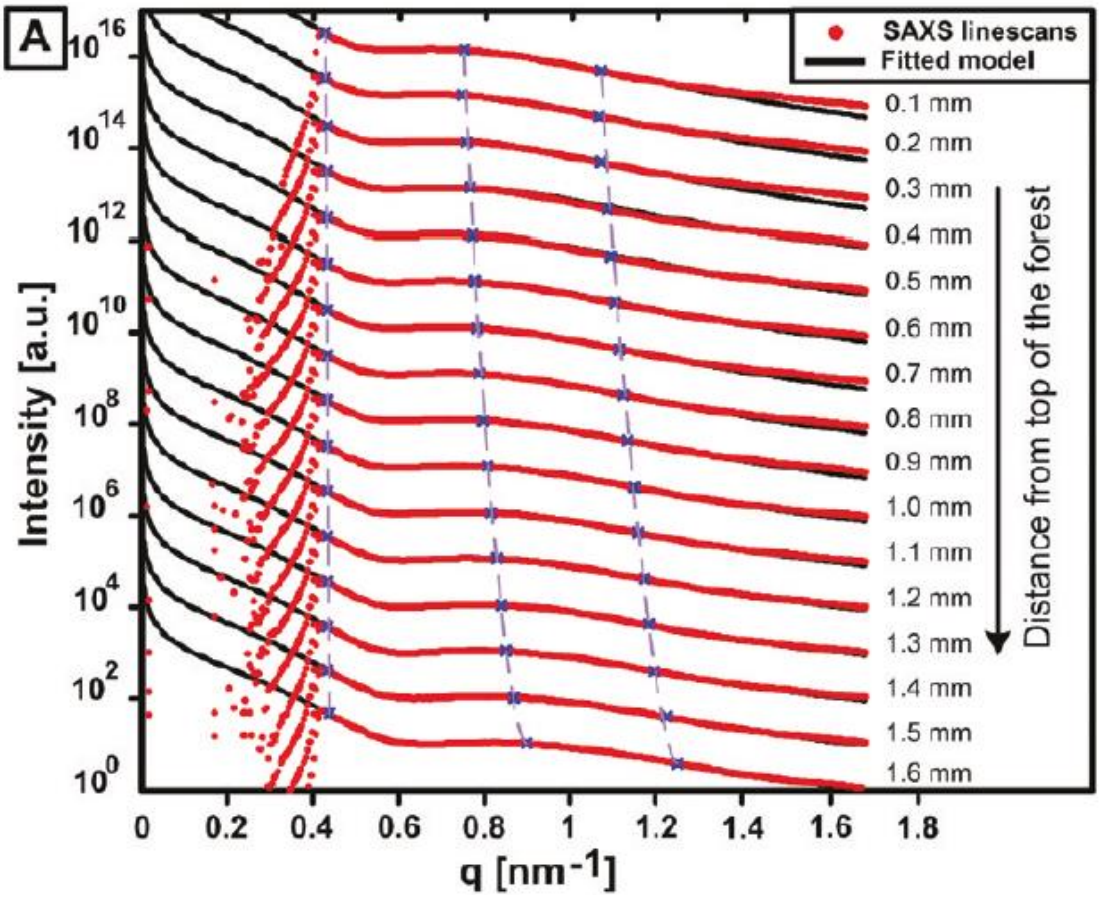

Figure 30: Measurements of the outcoming intensity function of the wavenumber for different heights [116]

We then try to fit those curves (for each distance from the top) with the following model:

First the repartition of CNT diameters in the forest is supposed to be Gaussian, the probability of a CNT to have a diameter R is given by P(R) below:

$$P(R) = \frac{1}{R\sigma\sqrt{2\pi}} \exp[\frac{-(\ln(R) - \mu)^2}{2\sigma^2}]$$

With,

$$\mu = \ln(\bar{R}) - \frac{1}{2}\ln(1 + \frac{{\sigma_R}^2}{\bar{R}^2})$$

And,

$$\sigma = \ln(1 + \frac{{\sigma_R}^2}{\bar{R}^2})$$

With $\bar{R}$ the mean diameter and σ_R the variance of the diameter.

The scattering model used is the one of the hollow tubes [117], it is described below:

$$I(q) = AF(q)S(q)$$

$S(q)$ is the factor due to particle-particle scattering, it is equal to one because there are no such phenomenons for Carbon-Carbon bonds for these wavenumbers.

$F(q)$ is the form factor, linking the scattering to the shape of the structures in the sample (hollow tubes in our case). It is given by the following equations:

$$F(q) = \frac{L\pi}{q} I_c(q)$$

$$I_c(q) = \frac{\int_0^\infty P(R) f^2(q,R,c) dR}{\int_0^\infty P(R) dR}$$

$$f(q,R,c) = \Delta\rho R \frac{2[J_1(Rq) - cJ_1(cRq)]}{qR(1-c^2)}$$

With L the length of the CNTs, c the ratio of the outer and inner diameters of the CNTs and J_1 the spherical Bessel function of the first kind.

We can vary $\bar{R}$, σ_R and c to fit the experimental results. Once we are fitting the experimental data we have the repartition of the CNT diameters in our sample and we can go to the next step, which is obtaining the waviness of our CNTs.

Step 3: In order to obtain the waviness (or the corrected height c.f. Figure 29), we scan for different angles between the beam and the forest, we rotate the sample around the z-axis (angle φ different than the one in figure 28). We then have the experimental data I(φ), for different azimuthal scans. We can extract from it the corrected height of our CNTs (waviness) [116].

The corrected height of our CNTs, $\Delta l = \Lambda \Delta z$, is given by:

$$\Lambda = \left(\frac{3}{2f+1}\right)^{\frac{1}{2}}$$

With,

$$f = \frac{1}{2}(3\langle cos^2\phi\rangle - 1)$$

And,

$$\langle cos^2\phi\rangle = \frac{\int_0^{\frac{\pi}{2}} (I(\phi) sin\phi cos^2\phi) d\phi}{\int_0^{\frac{\pi}{2}} (I(\phi)\sin(\phi)) d\phi}$$

From Step 2 and 3 we have the distribution of diameters and the corrected length respectively. Given that we have the volumic mass from Step 1, we can now determine the density of CNTs.

Measurements were made in CINTRA, by Chun Fei Siah, the PhD student of project TRiCOT working there, using the SWAXS Nanoinxider. The setup is shown in Figure 31.

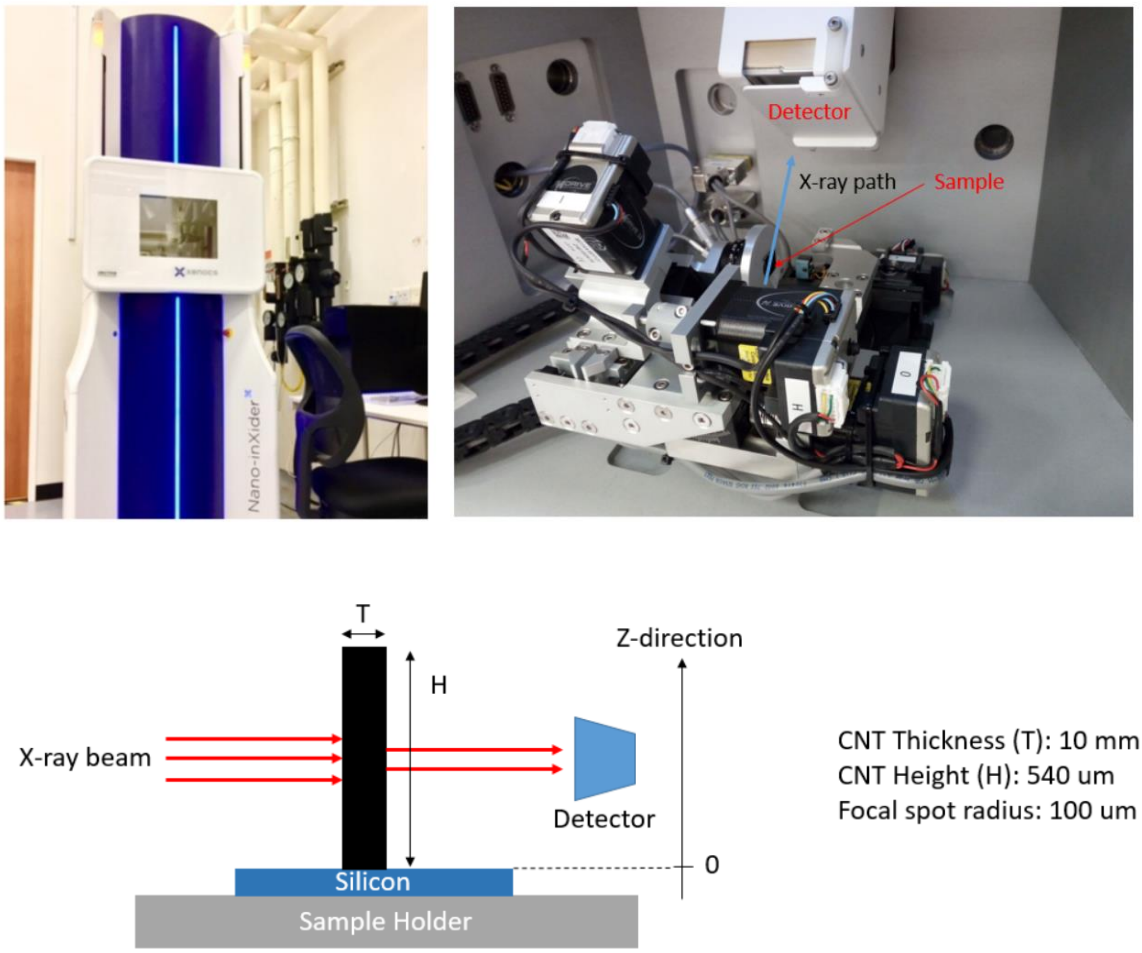

Figure 31 : Above, photo of the X-ray Measurement setup (by Chun Fei Siah), Below, Schematic of the sample position

The intensity measurements for different heights are plotted in Figure 32. As we can see, the measurements are not exploitable. The forest has a height of 500 um (measure with SEM), which means we should have the different steps in intensity:

- For Z between 0 and 0.2 mm, the beam is partially blocked by the silicon wafer (radius of 100 um), the intensity should increase but still be low.
- For Z between 0.2 and 0.4 mm, the beam is totally blocked by the CNT forest (height of 500 um), the measurements give the CNT density.
- For Z between 0.4 and 0.7mm, the beam is partially blocked by the CNT forest, the intensity should increase to its maximum, when nothing is in between the source and the receptor.

However, this is not what is observed in Figure 32. The noise in the measurements is too high to extract coherent values.

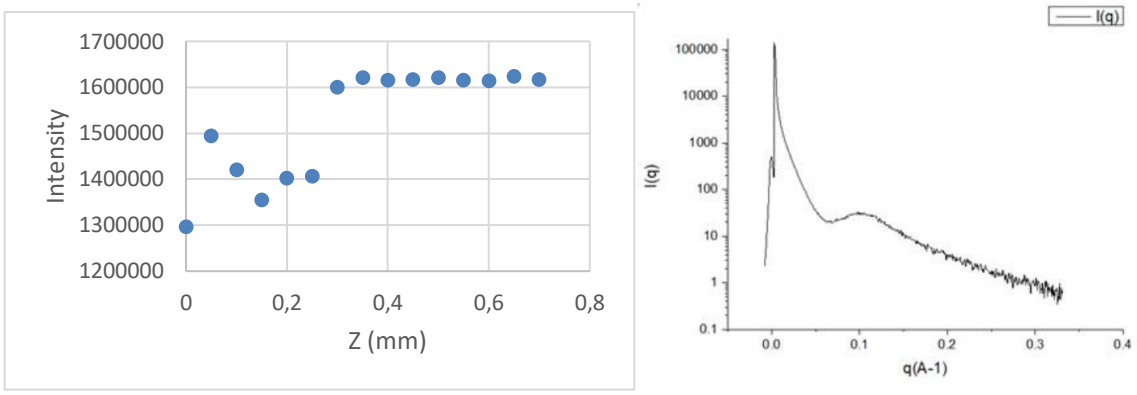

Figure 32 : Left, Intensity measurements for different Z (position of the beam relative to the top of the forest), Right, Scan for different wavenumbers for Z=0.4 mm

The size of the beam was t0o important compared to the height of the CNT forest, which implied scattering noise from the silicon supporting the forest. Indeed the beam size in Hart's article is 10 um in diameter, which is 20 times smaller than the one we can obtain with the X-ray machine in CINTRA. It is explained by the fact that Hart's team uses a synchrotron, an equipment to which, in this PhD work, we do not have access. Furthermore, the forest used in their article are a few millimeters high against a few hundred of microns in our case (the fabrication process we use aims for bigger density and we cannot achieve important heights).

If we consider the values between 0.3 mm and 0.4 mm to be correct, we can apply Beer-Lambert-Bouguer law. I_0 is taken to be the value of the measured intensity for Z=2mm, where the beam is well above the top of the CNT forest. Step 2 and Step 3 are skipped and we consider straight CNTs with a radius of 5 nm. The thickness of the forest is 10 mm. The calculus is explained below.

The volumic mass of the forest (ρ_m) is given by:

$$\rho_m = \frac{\ln(\frac{I_0}{I})}{t(\frac{\mu}{\rho})}$$

Numerical application :

$$\rho_m = \frac{\ln(\frac{1626090}{1599850})}{1 * 3} = 5.42 * 10^{-3}\ g/cm^3$$

The mass of a single CNT is given by:

$$m_{CNT} = \rho_{graphite} * V_{CNT}$$

With $\rho_{graphite}$ being the mass density of graphite and $V_{CNT} = \pi * \left({R_{out}}^2 - {R_{in}}^2\right) * h$ the volume of a CNT (hollow tube of height h, outer diameter R_{out} and inner diameter R_{in} (taken to be equal to half of R_{out}, c.f 1.1.4)).

Numerical application (height of 1 cm, R_{out} and R_{in}, 5 nm and 2.5 nm from TEM observation):

$$m_{CNT} = 2.26 * \pi * ((5e-9)^2 - (2.5e-9)^2) = 1.33 * 10^{-16}\ g$$

The number of CNTs in a given volume V is equal to:

$$N_{CNT} = \frac{\rho_m * V}{m_{CNT}}$$

Numerical application for 1 cm^3:

$$N_{CNT} = \frac{5.42*10^{-3}}{1.33*10^{-16}} = 4.07*10^{13}$$

This means that the density of CNTs is equal to $4.07*10^{17}$ CNTs/m^2.

The density values for different Z are given in Table 2.

Table 2 : Values of Conductivity (in S/m) for Different Densities and Different Frequency

$Z(mm)$	0.3	0.35	0.4
D_{CNT} (CNTs/m^2)	$4.07*10^{17}$	$8*10^{16}$	$1.7*10^{17}$

The values we find are one order of magnitude than the highest values reported in the literature for as-grown CNTs (non modified after growth) [82], [114]. However, the value we find is probably higher than the reality for two reasons. The first reason is that the size of the beam is quite bigger than in the reference, meaning there is probable reflection on the silicon wafer, leading to lower transmitted intensity and over evaluated density. The ratio of forest height to beam diameter is 40 times lower for our measurements than in the reference article [116]. The second reason is that the waviness of the CNT was not taken into account, thus reducing the effective volume occupied by a CNT, leading again to an over evaluation of the density.

Regarding the characterization set-up we used in Singapore, it would be possible to obtain results by opening the X-ray machine and use a diaphragm with the correct aperture, thus obtaining an available characterization method for the grown CNT forest. However, with this particular type of machine, the manufacturer does not allow the opening. It was decided to investigate other density measurements experimentations in order to cross the results with this set of measurements.

1.5.2.2. Densification

Another method that can be used for density measurement is densification. This method is interesting not only for the insight it gives on the density but also for the fabrication processes it gives way to.

The principle of the method is the following one:

Step 1: CNT shapes are grown, typically circular pillars or square ones.

Step 2: A liquid is dropped on them and, by capillarity; the CNTs will be drawn together. We assume the maximum density achieved after densification is the value given in [118].

Step 3: By measuring the ratio of the initial surface to the one after densification, we will have the density of the CNTs we have grown before densification. The surface ratio is equal to the density ratio (density before densification (the unknown) and after densification (known)).

SEM pictures of this method, from experimentation in CINTRA, are shown below in Figure 33:

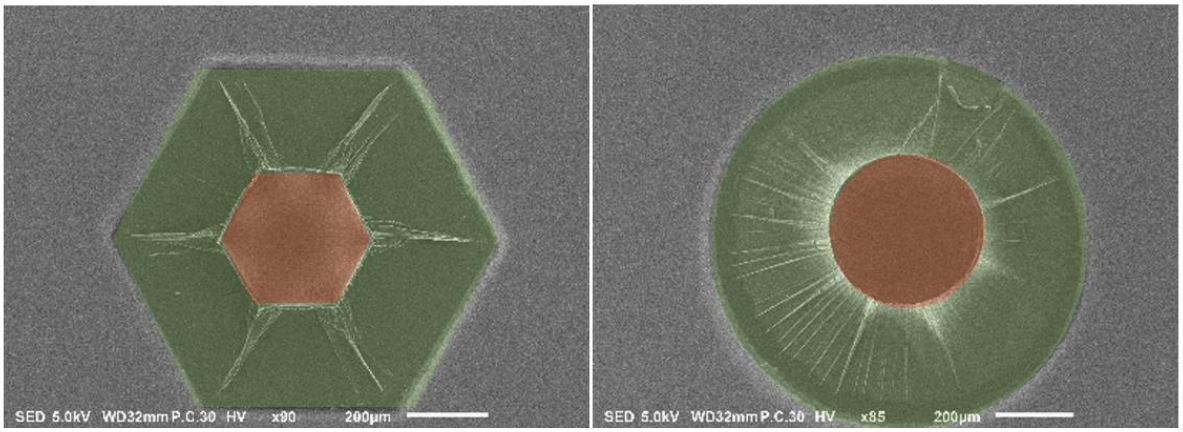

Figure 33 : SEM pictures of the densification method (CINTRA), in red area after densification, in green area before densification

Theoretically [118], after densification, the density is equal to the maximum density attainable for CNTs. After densification, the distance between each CNTs and its neighbors is equal to Van der Waals distance. This gives a density of 10^{17} CNTs/m^2. This density is a theoretical value for bundles of SWCNTs (3 nm diameter), supposing that all the CNTs are perfectly vertical, it does not account for waviness. Furthermore, we probably have a density a bit lower for MWCNTs (our case) due to their bigger diameter (5nm). However, with this value, for samples fabricated in CINTRA, we find densities of $2.5*10^{16}$ CNTs/m^2.

This value is coherent with the values reported in the literature [82]. Yet, it is one order of magnitude higher than the highest density reported in Hart's article [116] (X-ray characterization). It is probably partially due to the fact that the CNTs used in [116] are not high density CNTs. Indeed, in order to obtain consequent heights (a few millimeters) it is not possible to achieve very high density. But it is also probably due to the fact that, pretty much as the microbalance method, this characterization does not take into account the waviness of the CNTs.

Nevertheless, this densification process can be interesting if we want to engineer different types of shapes. Here are a few examples of how to use the densification process in order to make interesting shapes (Figures 34):

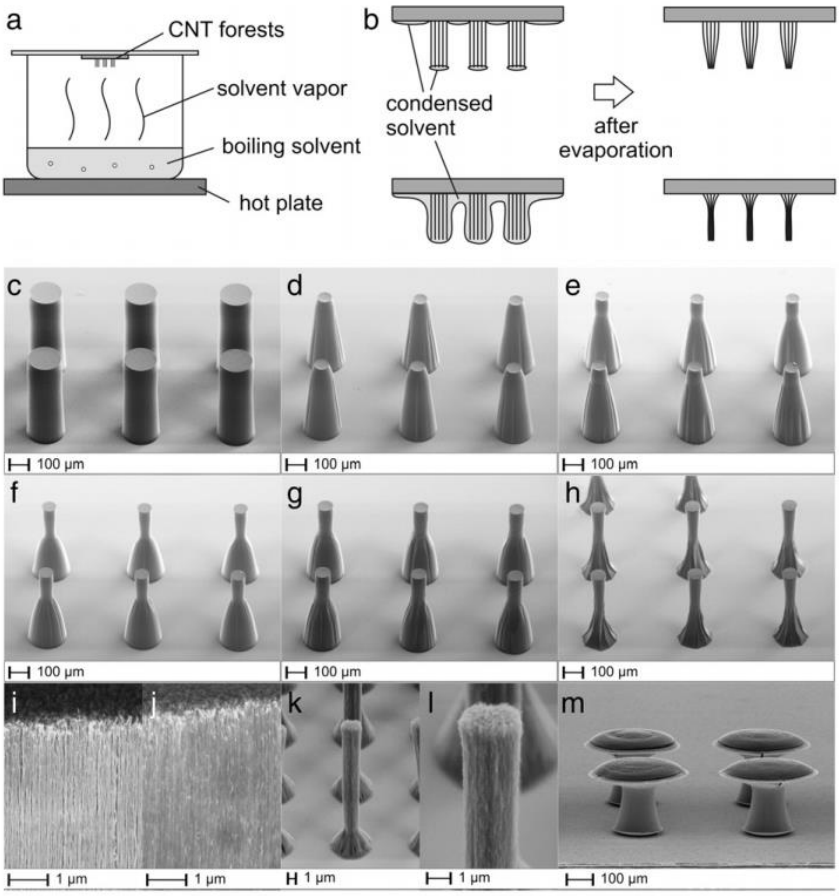

Figure 34 : (a) Illustration of the experimental setup of the vapor densification. The chip carrying CNT forests was placed on a lid above the boiling solvent, collecting controllable amount of solvent. (b) Illustration of the mechanism of the vapor densification. After collecting and evaporating different amounts of solvent, the CNT forests can be densified to different degrees. (c) Un-densified CNT forests. (d–h) CNT forests densified after exposing to the solvent vapor for 20 (d), 30 (e), 40 (f), 50 (g), and 60 (h) seconds. (i) Aligned CNTs in an un-densified forest. (j) Closely packed aligned CNTs in a densified forest. (k, l) A needle-like densified CNT forest with small dimension (~2 µm in diameter) and high aspect ratio (~10). (m) CNT forests made upside down by a transfer process, with densified parts on the bottom and un-densified parts on the top. Source: [119]

1.5.2.3. FIB-SEM-TEM blade

Because we could not use the X-ray method, and because we have doubts about the results obtained from the densification method, we decided to cross the previous results with another method. We came across the idea for this method due to an equipment that became newly available in Xlim during my PhD, we decided to call this method the FIB-SEM-TEM blade.

It consists in observing a TEM blade. This blade is of a different kind than in 5.1.1.Instead of diluting the CNTs in a liquid and then making the observation. The blade is cut out directly in the forest using a Focused Ion Beam (FIB). This is interesting because, we do not modify the way CNTs are arranged by diluting them. For example, if CNTs tend to intertwine themselves, forming ropes of several CNTs, we can observe it.

We decided implement this experimentation in Limoges. This experimentation relies on a FIB-SEM machine that was bought in common between XLIM and IRCER (a laboratory in Limoges researching on Ceramics). The engineers from XLIM (M. Rougier) and IRCER (M. Carles) in charge of this heavy equipment brought me their knowledge and competences, and realized the following steps of the process:

Step 1: We deposit a rectangle of platinum of 1um thickness on the top of the CNT forest (fabricated by CINTRA), in order to hold the CNTs together (Figure 35).

Step 2: We dig holes on each side of the deposited rectangle, in order to allow for the FIB to cut perpendicularly to the CNTs (Figure 35).

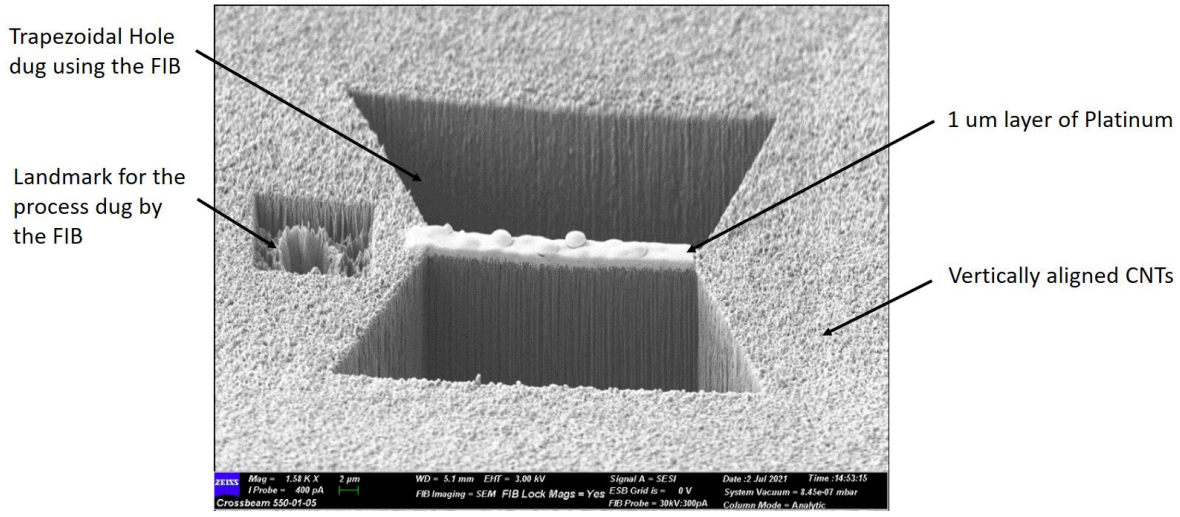

Figure 35 : SEM image of Step 1 and 2

Step 3: The FIB cuts the shape of the blade, while leaving a little support area (Figure 36).

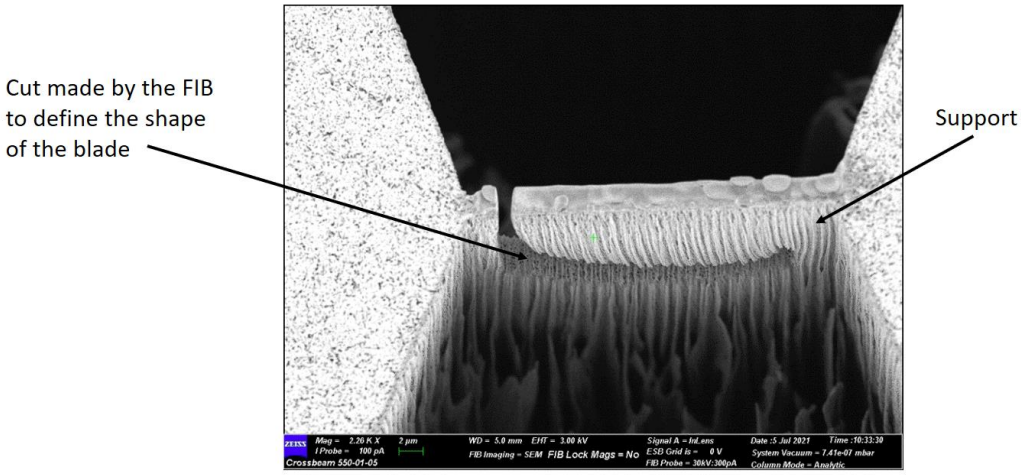

Figure 36 : FIB image of Step 3

Step 4 : A probe comes in and is soldered to the free end of the blade (Figure 37).

Step 5: The FIB cuts the last support of the blade (Figure 37).

Step 6: The blade is transported to a support fit for TEM observation (Figure 37).

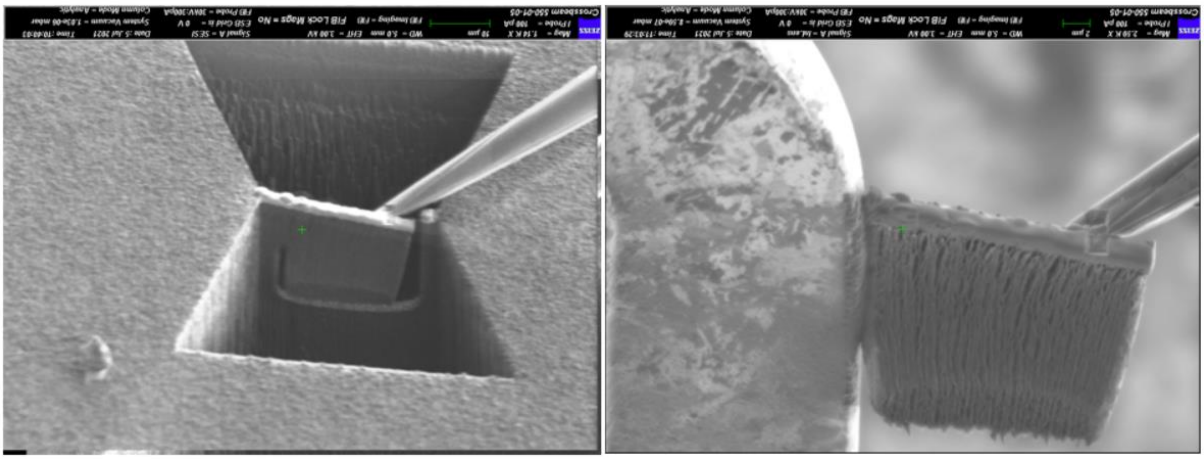

Figure 37 : SEM images of steps 4 to 6

Step 7: The blade is soldered to the support using platinum.

Step 8: The probe is cut off using FIB.

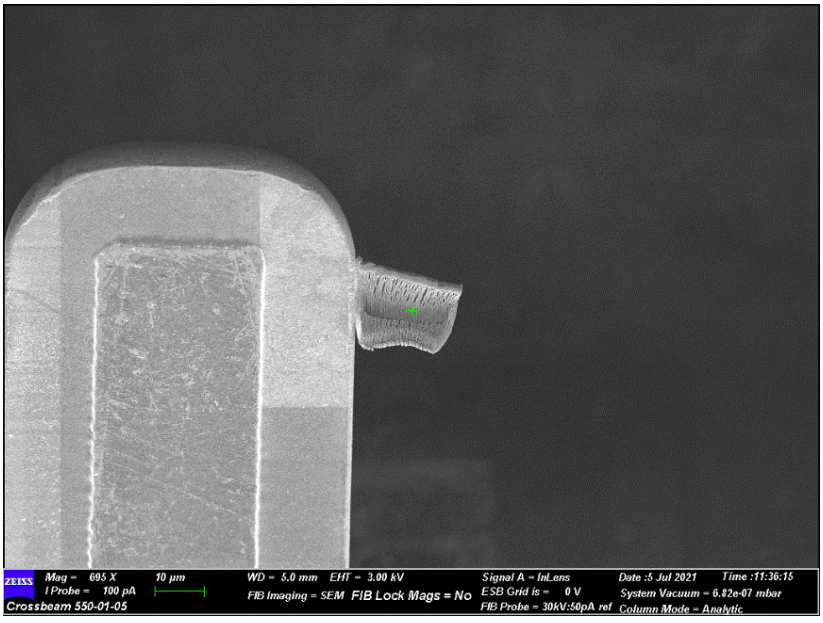

Figure 38 : SEM image of Step 8

Step 9: The blade is then thinned to 100nm thickness using the FIB, and observed with the TEM.

The TEM image of the blade is a projection of the slice into a plane. We observe the transmitted electrons. That means all the CNTs present in the blade will be projected on the plane of the image. Thus, we can count the number of CNTs present in a certain section of the blade. Given that we know the thickness of the blade (100 nm) and its width (width of the TEM image taken), we can deduce the number of CNTs per unit area. By analyzing different areas and different blades, we can have a mean estimate of the density. But more interestingly, we can see if CNTs are intertwined together (nanoropes).

Unfortunately, we encountered some problems, Due to the structure of TCVD grown CNTs, during step 3, the CNTs from the blade bend. It is because they are not hold by their bottom part anymore. As a result, only the upper half of the blade can be properly thinned and observed in the TEM. However, due to the thinning process (Step 9), a lot of platinum atoms deposit on the CNTs and since they are much heavier than carbon atoms, we cannot see the CNTs. Another longer blade will be fabricated for the defense in order to be able to observe the CNTs with TEM.

1.5.3. Conductive properties

The characterization processes we are trying to implement have one objective: determining the conductivity of our material, in order to provide an accurate model of the RF devices under consideration. Density measurements, give an estimate of the sample conductivity through the bulk equivalent model from 1.4.3. However, instead of determining the structure of the forest, to incorporate the values in an equivalent model, one can also try to experimentally measure its conductivity.

1.5.3.1. DC conduction

The measurement of VACNT bundle resistance grown by PECVD has been made in [84]. The CNTs are grown using PECVD, which allows for this type of measurement between two gold lines (Figure 39). Indeed, the CNTs are horizontally grown. The grown CNTs are Double Wall CNTs (DWCNTs).

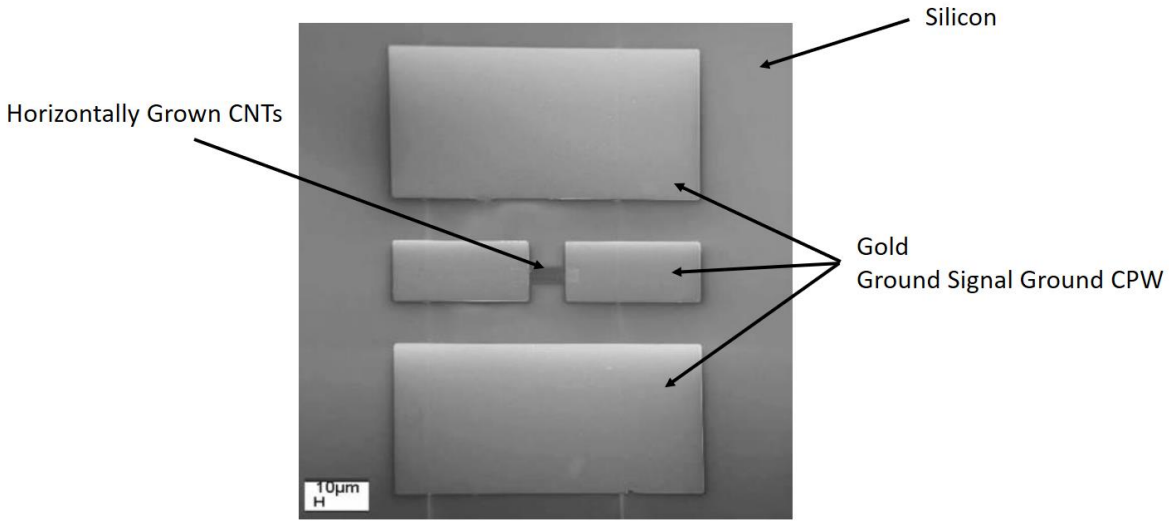

Figure 39 : Measurement Setup for DC and RF CNTs conductivity measurements [62]

The resistance of the CNT bundle was measured using DC probes on the signal of the CPW lines, and removing the resistance due to the gold portions.

By defining the conductivity σ as:

$$\sigma = \frac{L}{RS}$$

with, L the length of the bundle, R the resistance and S the cross-section, the authors obtain a conductivity of 10^4 S/m. This value is quite low, but the density of CNTs obtained for PECVD growth is quite lower than for TCVD

Because we do not choose the direction of growth in TCVD, we cannot use this method. We can think of methods if the possibility of transfer is taken into account, but the transfer method will induce a different behavior than directly grown CNT, with higher contact resistances.

1.5.3.2. RF conduction

The method from [84] (1.5.3.1), can also be used for RF measurement. The authors simply measured the S-parameters of the structure using GSG probes connected to a VNA on the CPW lines. The equivalent parameters of the transmission line for the CNT bundle have been extracted from the RF measurements and deembedding

The use of the resonant cavity method [120] is not applicable directly in our case. First, the area of the samples needed is too big for the fabrication utilities in CINTRA. Second, the anisotropy of the VACNTs does not allow for the usually used modes to appear. For detailed explanations, see Appendix 1.

To palliate this problem, we fabricated cavities using the transfer process (1.3.3). However, these measurements will strongly depend on the fabrication process, due to the assembly process, as we will see later in this work (see section 2.5).

To conclude, three different methods were investigated in order to evaluate the density of a CNT forest: X-ray measurements, densification, and FIB-SEM-TEM blade. Though we do not have definite results yet, we estimate the density to be around 10^{15} CNTs/m^2. By incorporating this estimate into P. Franck's model, we evaluate the axial conductivity of the CNTs that will be used in this work to be around $2*10^5$ S/m.

However, the CNTs conductivity can also be evaluated experimentally. To the knowledge of the author, no RF values have been reported in the literature, probably due to their uncommon anisotropic property and the restricting fabrication process. A process will be shown later in this work, but its results depend strongly on the fabrication process (see section 2.5).

1.6. VACNT Bundles Nanopackaging Applications

We will now give examples of how VACNT bundles have been used, in the industry and in research, for nanopackaging. We will focus on the three following fields: Thermal Management, EMI shielding and Antennas. There are other ways to use CNTs for Nanopackaging such as Interconnects but they are not presented in this section, either because we will have a particular focus on it in the other chapters, or because they are not known to the author, the number of CNT published research being simply too great.

1.6.1. Thermal Management

Of the different nanopackaging applications for VACNT bundles, thermal management is one of, if not the most, studied. With the downscaling of transistor circuitry and the increasing power needed for faster calculation [121], the power loss of chips has consequently increased. The excess power is mainly dissipated as heat, which increases chip temperatures, and becomes more and more critical as circuits are more and more 3D integrated. Indeed the stress induced by thermal variations will reduce the chips longevity, reliability and performances [121].

This evolution in electronic devices calls for better thermal management. Of the different solutions proposed, chip integration that allow for better heat dissipation are intensely studied, though other solutions such as processor architecture also give viable solutions. To reduce the temperature locally on the chip, one must transfer it first to a larger area than can itself be cooled via liquid or air convection. Thus many materials have been under scrutiny for their high thermal conductivity that allow for the quick transport of heat waves, mainly metals, but also VACNT bundles. We can note here that for thermal isolation, CNT buckypapers have shown very low thermal conductivity (74 W/mK at room temperature), meaning high isolation [122].

Not only do VACNTs bundles have theoretical exceptional thermal conductivity, they are also incredibly lightweight, and have interesting mechanical properties. This makes them ideal candidates for Thermal Interface Materials (TIMS) [123]. TIMs are used to improve heat transfer between the chip and the heat sink. The heat sink is the part that allows for dissipation of the heat in the surrounding medium. It usually is in the shape of multiple fins in parallel in order to maximize surface, for optimal convection, and in metal (e.g. copper). The problem is that if the contact is not good between the heat sink and the chip, the resulting thermal resistance will impact heat dissipation. That is why TIM materials are usually placed between the two, they have to fit the shape of the two surfaces in contact and are usually pastes. The topology of a chip with heat sink and thermal paste is presented in Figure 40.

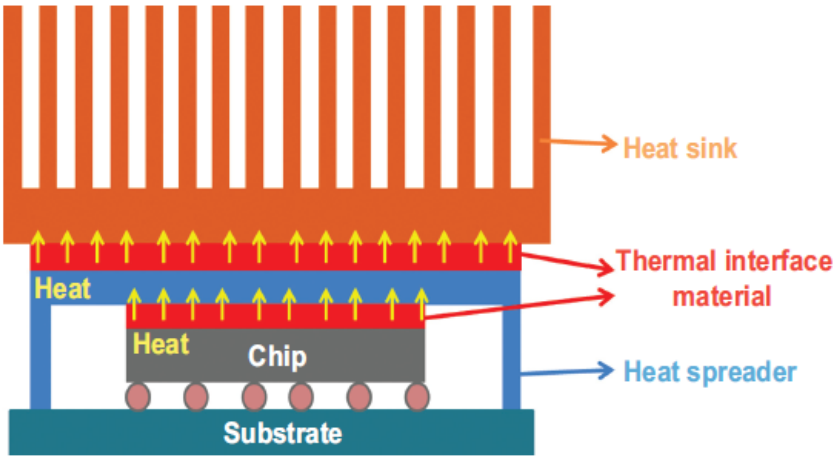

Figure 40 : Usual topology for heat dissipation of chips [123]

VACNTs bundles make ideal candidate for TIMs due to their mechanical and thermal properties. They can be used in three different ways, either, as is, or, embedded in a medium that can be a metal or a polymer, Figure 41.

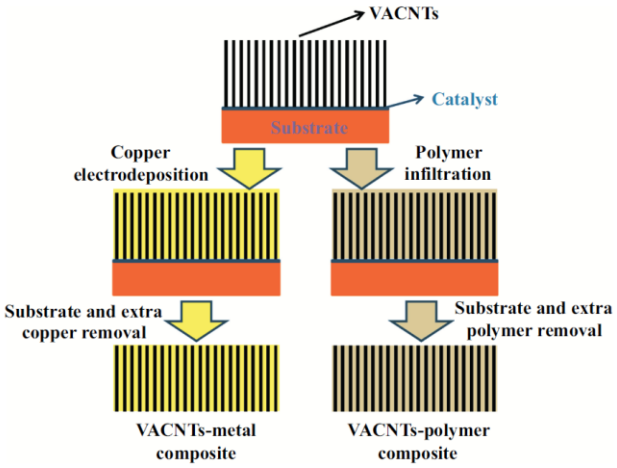

Figure 41 : Different TIMs materials using VACNT bundles [123]

The use of VACNT bundles as cannot happen through direct growth, for the temperature processes are too high. Different transfer processes have been studied and the most promising one (with the lower contact resistance) uses a layer of Indium, that penetrates a certain amount in the top of the CNT forest [124], the contact resistance was shown to decrease ten fold. However, because the conductivity of air is only 0.02 W/mK, the use of VACNT bundles will benefit greatly from an embedding medium with high thermal conductivity.

The first medium that was studied is copper [125]. It was inserted in the VACNT bundles using electrodeposition, and it was shown that the thermal conductivity increased. The problem is that it no longer was as flexible and could not fit the curves of the surfaces as well. Furthermore, it could not claim to be lightweight anymore.

This led to the study of different polymers as embedding media [126]–[128]. These materials show the best thermal conductivity of all the materials using CNTs. In [128] the thermal conductivity was measured to be 8.2 $Wm^{-1}K^{-1}$. Furthermore, these materials remain flexible.

Finally, it is worth to note that VACNTs can also be used directly as heat sinks due to their high aspect ratio as shown in [129] . The performances were as good as a copper heat sink with a noticeable weight reduction. The heat sink was machined from a VACNT forest using laser. A picture of the heat sink and its performances are presented in Figure 42.

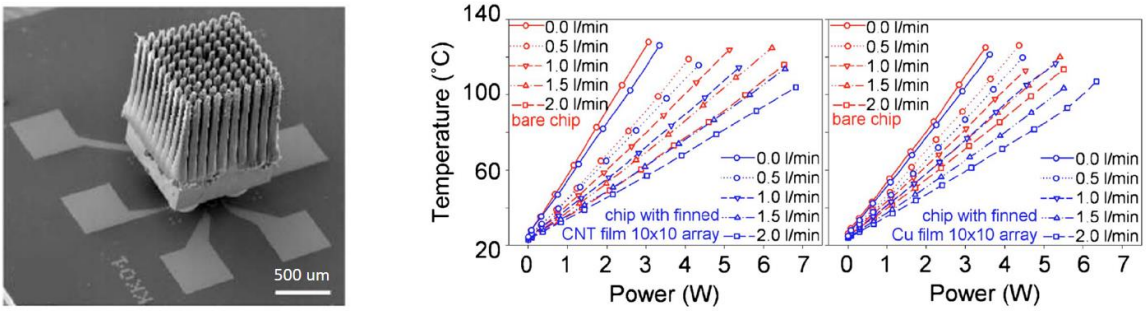

Figure 42 : Left, SEM picture of the chip and the CNT heat sink, Right, Performances for different H2 flows for VACNT heat sink and copper heat sink [129]

Figure 42, shows on the right the measured performances of the CNT fins compared to the same Copper fins for different H2 flows. As we can see, both types of fins have very similar performances, while copper is a bit better for higher H2 flows, VACNTs seem to be better for lower flows.

1.6.2. Antennas

With the scaling down of transistors (down to 7nm in today's processors) the limiting factor is no more the processing time but the communication between the chips (Multiple chips are put in parallel for faster calculations) [130]. The communication between the chips is done using classical interconnections, and the resulting delay becomes a limiting factor. In addition, as the number of transistors increases there will be less room for interconnects that will eventually interfere with one another. Furthermore, the size difference and the ensuing impedance mismatch, as well as the contact resistances are recurrent problems. It is because of this context that the idea of wireless interconnections is under particular scrutiny.

The idea is to replace interconnections by communicating antennas. An antenna working at a particular frequency, by having a given length, as shown in Figure 43, would replace each interconnection. Because the size of the antennas is inversely proportional to the working frequency, such interconnects would work in the 60 GHz to 100 GHz band [131]. It is also possible for two chips to communicate using a set of nano antennas on each of them replacing interconnects, as it has been shown in [132], for nano metallic dipole antennas up to 90 GHz.

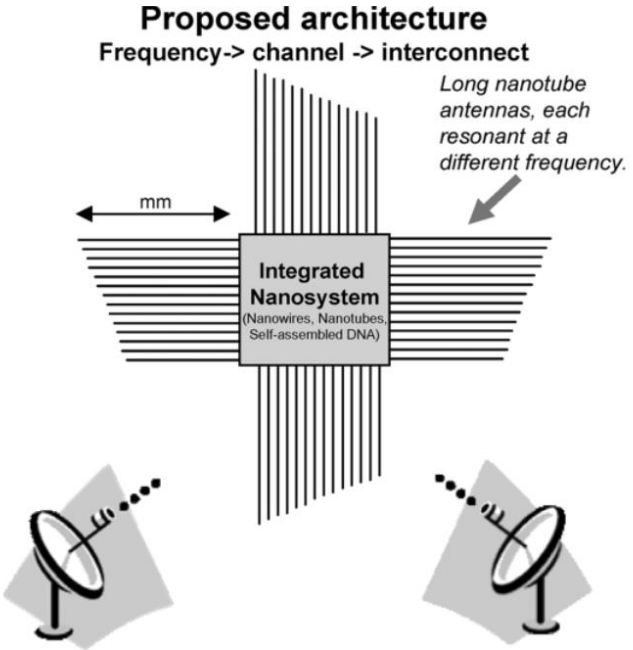

Figure 43 : Possible configuration of a system using CNT antennas [133]

CNTs as radiating elements have been particularly studied because of the possible size reduction of the antennas they could induce. On the one hand, studies show that the low speed of surface plasmons can shift the resonance frequency to the THz [134]–[136], and an antenna behavior of a bundle of MWCNTs has been observed in [137]. On the other hand, the following studies [133], [138], [139] show that due to the high kinetic inductance of CNTs, the speed of

electromagnetic waves is only 2% of the one in vacuum, which allows for a 50 fold size reduction. This result is applicable for frequencies lower than THz but above 53 GHz, as shown in [140], for a dipole antenna.

The main problem of single CNTs antennae is impedance mismatch, which is why use of bundled VACNTs monopole antennae has been studied in [62], [81], [141]. Different geometries (antenna with parabolic reflector, antenna array) at different frequencies (90 GHz and 300 GHz) have been studied, but experimental results have not yet shown great potential. The principal problem comes from the fabrication process, because the shapes with high aspect ratios (higher than 5) are difficult to transfer. In addition, the VACNT array should be particularly conductive (at least 10^6 S/m [62]) for good efficiency.

These antennas have been studied in XLIM before [81], [141], but fabrication problems were encountered. As of today, with the transfer process developed by CINTRA, it should become possible to fabricate and measure such structures.

1.6.3. EMI Shielding

With dwindling dimensions, the distance between circuits diminishes, and EM interferences become a growing concern. To protect signal integrity, the use of shielding techniques is often used. As of today, the different methods used are numerous [142]–[144] , via fencing, grounding, guard rings, metal casting, etc. The idea is to shield a circuit from another using materials or structures that reflect or absorb the incident EM waves.

CNTs are widely studied for this application; they are either embedded in a material, mixed with other composites or coated to increase shielding performances [145]–[148]. However, one of the most promising ways is to directly use densely packed VACNT arrays as walls [149]. In order, for this to work, one must first be able to transfer the CNTs on a via fence, which was accomplished in CINTRA in collaboration with XLIM. When coupled with a via fence to avoid coupling through the substrate, the footprint does not increase, and the weight of the material make it particularly interesting for applications in which weight matter, such as satellites. Though the material has a theoretical anisotropic conductivity, experimental results show an improvement in shielding of 10 dB as shown in Figure 44, equivalent to a kovar wall of the same dimensions. The comparison is made between the coupler without and with the CNT wall and with a kovar wall.

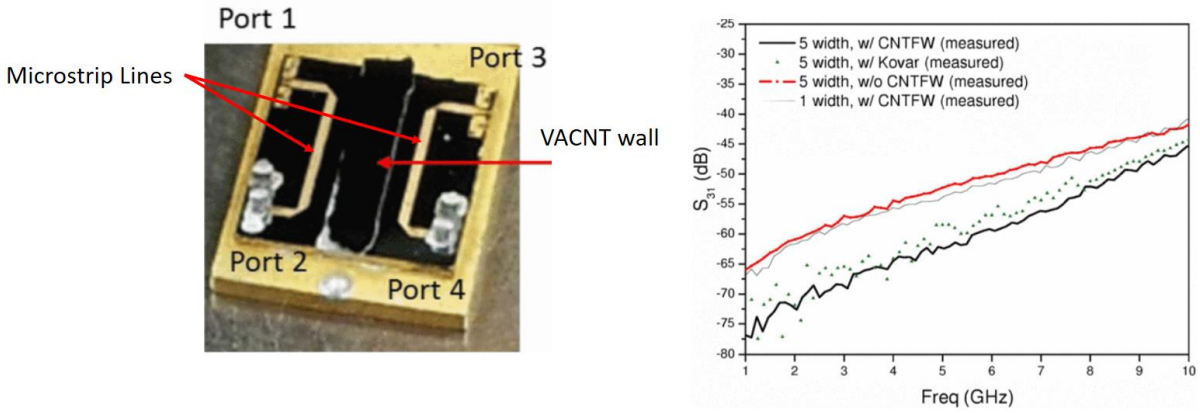

Figure 44 : Left, Photo of the coupler with the VACNT wall, and right, measurements of the isolation with Kovar, VACNTs or nothing on the via fence in the middle (of different widths) [149]

As we can see, the measurements with a kovar wall show approximately the same isolation than the measurements with the VACNT wall. Furthermore, the improvement in isolation is around 10 dB between the measurements without the VACNT wall and with the VACNT wall.

To improve isolation, the use of a Faraday cage has been studied [150]. But the problem of the electrical contact between the top plate and the top of the CNT walls is still being studied. This application seems promising and THALES Singapore has filed a patent [151].

1.7. Conclusion

We started this chapter by explaining what CNT were and what their properties were. We then explained the fabrication processes, thus describing what were VACNT bundles, the material we will be studying for different Nanopackaging applications. Because modeling and characterization are problems often faced when using nanomaterials at the bigger scale, we decided to present different ways to apprehend each of them. This allowed us to lay the foundations of VACNT Nanopackaging methods. We finished by presenting three different Nanopackaging applications used in the industry or still studied in research.

The next three chapters will each be focused on a different aspect to integrate VACNT bundles in mm-wave devices for packaging applications: air filled waveguides, slow-waves and interconnects. As we will see the three of them are constituent bricks of the idea developed in the TriCOT project, a functionalized interposer.

Chapter 2: CNT Smart Interposer: A butler Matrix as Proof of Concept

As time goes by, the demand for mm-wave modules up to 100 GHz keeps on growing. They are used in more and more fields, high-resolution sensors, THz imaging, radars for autonomous vehicle, etc. But if one field in particular represents the need for such modules, it is 5G, the fifth generation of mobile networks. Indeed, the promises of 5G: higher data rates (at least equal to the fiber optic ones 10 Gbit/s, if not more), and lower latency (from 40-60 ms in 4G to 1-10 ms in 5G [4G vs 5G how will next generation improve on the last]), have pushed wireless systems to work at higher frequencies, in the millimeter wave band.

However, this colonization of the mm-wave band, associated with the increasing number of functions and need for miniaturization, faces a few technological bottlenecks, one of them being packaging. Indeed, the smaller dimensions, the proximity of the chips, and new the no more negligible high frequency phenomena, raise a few problematics: 3D heterogeneous integration, high frequency interconnection, densification, functionalization, etc.

To solve these problems, we propose a new type of packaging i.e. a functionalized interposer based on VACNT forest. We can note that the thermal and shielding properties of VACNT forest are of interest in this application. This concept was developed in the ANR project TRiCOT.

Interposers were first developed by IBM and Bell Labs in the 80s to allow for better chip to chip performances [152]. As of today, interposers are used to minimize the footprint and increase performances of multiple chips modules [153], but none is functionalized, to the knowledge of the author. They consist of “substrates having through VIA interconnections at the same input-output (I/O) pitch as the chips on one of its sides (fine I/Os) and the same I/Os as of packages or boards on the other side (coarse I/Os compared to chips side)”. Their purpose is to reroute and adapt pitches of the different connections.

Before explaining further the principle of our CNT functionalized interposer, we will explain the application which we have used it for, as to have a concrete example for the figures.

Recent announcements related to the E-band (60-90 GHz), demonstrated that it could be used as a complementary spectrum band to the lower band for 5G communication. The [71-86 GHz] sub-band is arranged into two 5 GHz bands [71-76] and [81-86] to address 5G millimeter wave backhaul [154], [155]. Due to this need, the plan of TRICOT was to fabricate a phased array with a Butler Matrix in the [71-86] GHz band using the functionalized interposer technology. The realization of such a device would serve as a proof of concept for the packaging technology.

The phased array is composed of three distinct elements: a SP4T switch, the Butler matrix and the array of antennas. Because we want to do a mm-wave package consisting of a phased array, we considered that two elements could be found as integrated chips, the SP4T switch and the butler matrix; the antenna array is an array of patch antenna directly on the RF substrate.

For a classical interposer technology, the topology is presented in Figure 45. And, in Figure 46, we have a schematic of the same package but with the functionalized interposer in which we have the Butler matrix, and the antenna array on top of the interposer. We can see that there is improvement in the footprint. Though it is not shown in the 2D drawings, one can mentally visualize how the CNT interposer allows multiplying vias, just as any other interposer. Such a property will be better developed in Chapter 4.

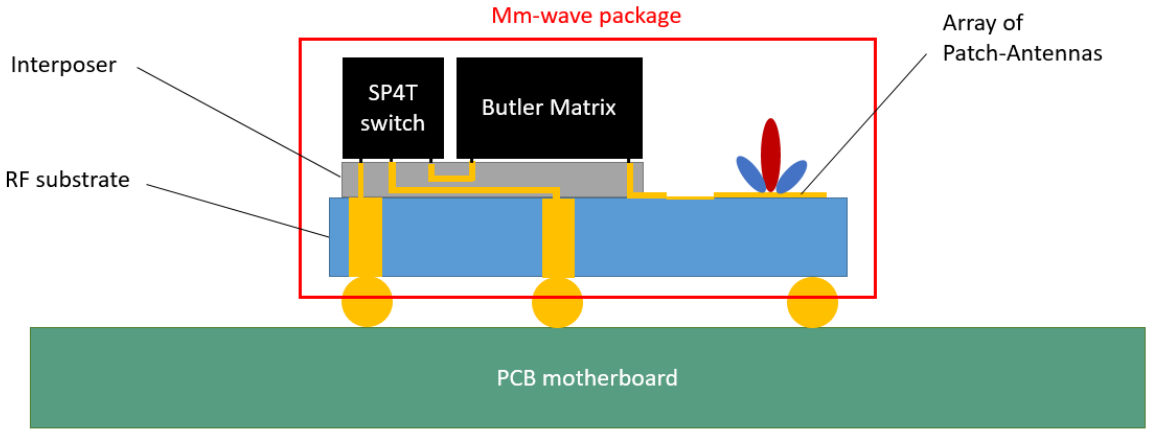

Figure 45 : Schematic of the topology for a classical interposer

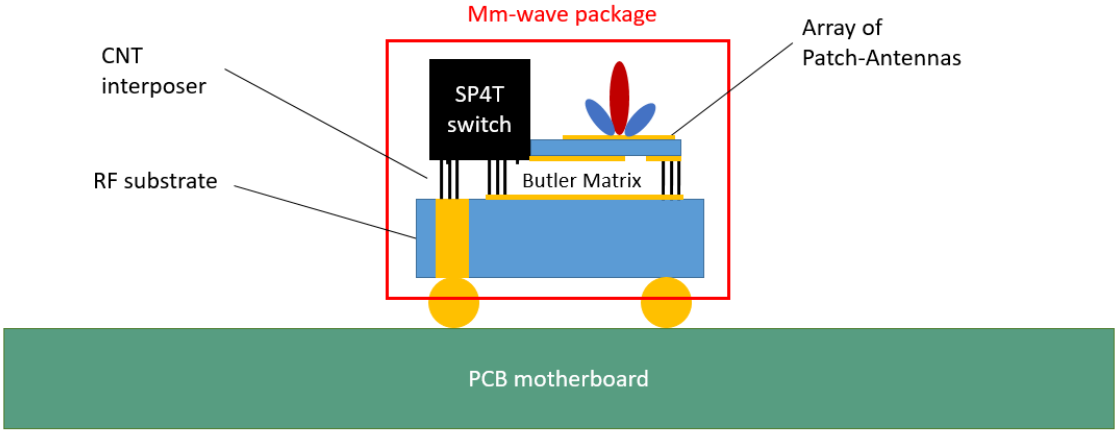

Figure 46 : Schematic of the topology for a CNT functionnalized interposer proposed in TRICOT

We will now explain exactly, how we manage to functionalize the CNT interposer so that it behaves as a Butler Matrix.

To understand how a Butler matrix can be formed into a VACNT forest, one must first admit that for some propagating modes, the VACNT forest acts as a metallic wall, even though its conductivity is anisotropic. We will go over this property of the VACNT later in this chapter.

If we define where CNTs are placed on the RF substrate, we can create an air filled designs (delay lines, couplers and crossovers) needed as elementary blocks to design the Butler Matrix. The ground below the top substrate forms the cover of the structure, the walls are made of VACNT, and the bottom is metal from the top of the RF substrate. This is illustrated in Figure 47.

Our partners at RFIC lab developed the same principle for an interposer in [156]. The interposer differs by using porous alumina membrane filled with vertically aligned metallic nanowires. Therefore, the resulting SIW structures are not air-filled. Interesting results were published during the course of this PhD in [157].

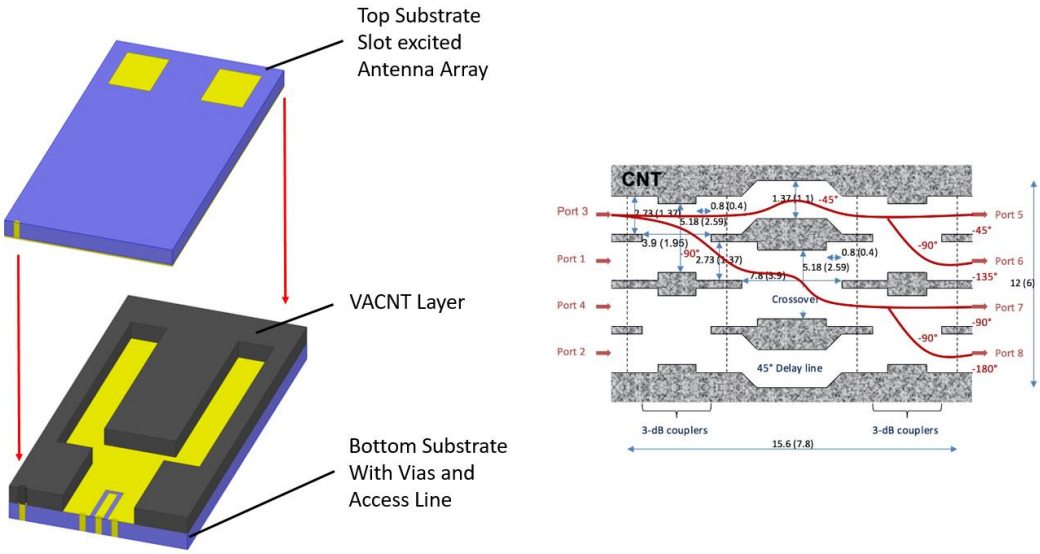

Figure 47 : Left, Schematic of the functionalized Interposer, Right, Topology of a Butler matrix with VACNTs seen from above.

In this section, we will have a particular focus on the realization of waveguide with VACNTs walls. It is the base of the Butler Matrix and if we can make a waveguide, the other functions will be easily made afterwards. Thus, we will begin by a state of the art mainly about guiding structures at high frequency, so that we can compare to our results. We will then develop from previously obtained results by M. Cometto (previous PhD student [86]), and the problems faced, to our last batch of devices measured.

2.1. State of the art of high frequency Butler Matrixes

When it comes to interposers, the review [153] offers a good insight on the problematics and promises of the technology. Three technologies share the attention of the research field, silicon, organic and glass with glass seaming to be the most viable one. These technologies can be functionalized using Through Silicon Vias (TSV) [158], [159].

In this section, we will focus our bibliography on Butler matrixes and wave guiding structures technologies for high frequency applications. [160] gives a more thorough study of the following state of the art and can be a good complement. A recapitulative table with the main values is given at the end of this section (2.1).

2.1.1. Beam Forming Networks and Butler Matrixes

At higher frequencies, attenuation is higher in air. This leads to a deterioration of the signal [161]. One solution to this problem is the use of high gain antennas. However, for None Line Of Sight communications, the signal needs to “find” the right direction. Thus, antennas that can scan a certain area, while having high gain, are of major importance. That is what led to the study of multi-beam antennas [162]. In order to achieve such an antenna (without servos, for speed related issues) one needs beam-forming networks, devices that rely on the constructive/destructive interferences of an array of “isotropic” antennas. By tuning the delay of the signal brought to each antenna, we can obtain different directivity.

There exist different types of beam-forming technologies that can be divided in two categories: active and passive. The search for passive beam-forming network (BFN) stems from the fact that component of BFNs are needed in large numbers, and consequently, should not be costly [163]. There are numerous topologies that can be used for BFNs: the Butler matrix, the Blass matrix [164], the Nolen matrix [165], Rotman's lens [166], the monopulse antenna [167], etc. Depending on the size of the antenna array or the specific needs of the application, these topologies can vary slightly between two devices [168], [169].

The Butler matrix is by far the most studied topology, due to its advantages over the other counterparts, such as perfect matching, isolation and equal power division that can be obtained at the same time [170], [171]. In addition, BM has a larger bandwidth, structural simplicity and lower losses.

The Butler matrix was first described by Jesse Butler and Ralph Lowe in [172]. A Butler matrix usually has N inputs and N outputs, with N being a power of two. We will consider as a convention for the signal to be on the inputs side and the antennas on the output ports though the BM is perfectly symmetric and can receive as much as emit. The topology of a 4x4 BM is shown in Figure 48.

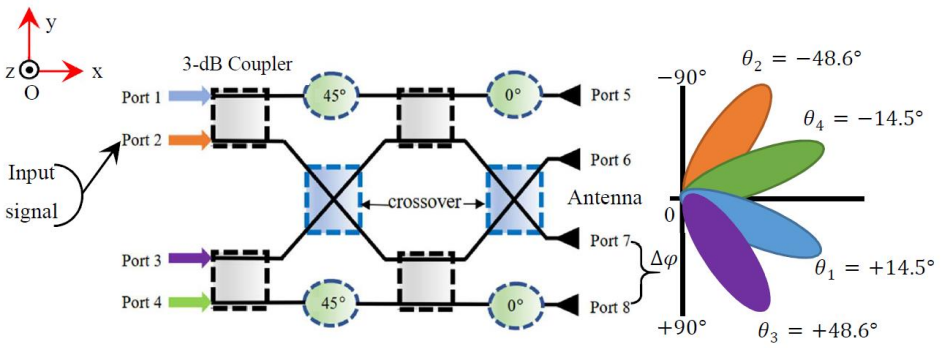

Figure 48 : Working Principle of a conventional 4x4 Butler matrix[160]

The input signal is divided into four sub signals each going to one of the output antennas. By going through different elements of the matrix for each, 3-dB coupler fixed phased delay lines and crossovers, each of them will have a different phase in the outputs. If the distance between two antennas is equal to $\frac{\lambda}{2}$ (with λ the wavelength in the propagating medium), depending on the port chosen for the input signal, the phase increment of the four antennas will be: 45° for port 1, 135° for port 2, 270° for port 3 and 315° for port 4. This results in four different beam directions in the xy plane, $\theta_1 = 14.5°$, $\theta_3 = 48.6°$ and their opposite due to the symmetry of the matrix. For 3D direction, one only needs to use two Butler matrixes for two antenna arrays perpendicular planes.

The three main focus on which researchers and industrials have worked regarding Butler matrixes are: reduction of the size of the structure, augmenting the bandwidth and reducing the side lobe level of the beam pattern [169]. The two main transmission technologies used for fabricating Butler matrixes are Microstrip line technology and Surface Integrated Waveguide (SIW) technology.

2.1.2. Microstrip Butler matrixes

This technology is probably the most used when it comes to Butler matrixes. It presents the advantages of being easy to fabricate as well as being well understood. A non-exhaustive list of Microstrip based structures is presented below in function of size reduction, bandwidth increase or side lobe reduction.

Because Butler matrixes have their size increase exponentially with the number of antennas (64x64 for MIMO in 5G has been reported in [173]) numerous research have been published on size reduction. One of the most conventional way to do so in Microstrip technology is to use meander lines as in [174], where a 34% size reduction has been reported in the 2.4GHz band. [175] uses back to back bilayer Microstrip in the 4GHz band in order to avoid 0 dB crossover so as to simplify the design and consequently reduce size for 8x8 Butler matrix. In [176], the use of stub loaded transmission lines allows for a 45% decrease in size at 2.4 GHz. In [177], at 1GHz, the use of slow-waves allows for the Butler matrix to as little as 5.8% of its original size.

To increase the bandwidth (up to 14% at 30 GHz) the idea is to avoid using branchline couplers which have a narrow bandwidth [169]. This results in multilayer structures using most of the time three section directional couplers, or coupled line couplers [178]–[183].

Some results about side lobe reduction have been obtained in [184]–[186]. The solutions rely on unequal split power.

Though the Microstrip technology can be used to make Butler matrixes in the mm-wave band [184], [187], [188], [189, p. 10] it is difficult to implement at these frequencies because of the higher radiation losses and manufacturing processes. Much more often, the SIW technology will be used.

2.1.3. SIW Butler Matrixes

Due to its lower insertion losses than planar structures, high quality factor, high power capability, low weight, etc. SIW has attracted a lot of interest for high frequency butler matrixes, ranging from 5G applications, to radars, and imaging systems [190], [191].

The reduction of size will be discussed in chapter 3. Basically, the methods used mainly rely on reducing the size of the SIW structure in itself [192] and multilayer topology [185], [193, p. 38], [194]–[196].

To increase the bandwidth, many different solutions were explored [197]–[207], such as increasing the order of the modes to TE20 [200], [201] or implementing multiple slots elements [202]–[204].

Finally, to reduce side lobes, [208] proposes to reduce the number of crossovers. Though not many works have been published for SIW matrixes, the techniques from Microstrip are also applicable.

2.1.4. Other Technologies for High Frequency Passive Components

While the two technologies afore mentioned make up for a lot of percentage of papers, other technologies can be used. Though all of the technologies we will present in what follows, have not necessarily yet been put to the test of a full Butler matrixes, high frequency devices were fabricated and nothing suggests the technology cannot be transposed to a BM.

First and foremost we have classical metallic volumic devices, such as [173], but as they are not really compatible with mm-wave packages (due to the dimensions attainable with the fabrication processes), and more often use for defense application, we chose not to develop.

The second technology is the groove-gap technology [209]. It consists of replacing the lateral walls of rectangular waveguides by “beds of nails”, thus making a metamaterial with a forbidden band, provided the dimensions are chosen correctly. It presents the advantage of not necessitating good contact between the cover and the top of the “bed of nails”, which is very interesting for high frequency applications where leakage current is a crucial matter. Groove gap Butler matrixes have been demonstrated for 5G applications [210] or higher frequencies [211, p. 3], [212]. The problem of this technology is again that it takes a lot of space if air filled. For higher frequencies groove gap can be substrate integrated [213], [214] and have a much smaller footprint.

There is also the air filled SIW technology, a technology well mastered by our partners in Grenoble RFIC Lab. This technology was reported in [215] by Ghiotto, who still works on this topic to this day at IMS Bordeaux. This technology consists of SIW for which the propagation zone is of air. The vias are still embedded in a substrate, but by stacking differently machine substrate, one can achieve such a feat. It has the advantages of enduring higher powers than classical SIW [216], and having low insertion losses [217]. Let us note that, because air is the propagating media, it has a higher footprint, which can be reduced using slow-wave [218].

Finally, additive micro manufacturing processes derived from MEMS, have allowed high frequency devices to be made. Since the original publication [219] by Blondy’s team in Limoges, other devices using the same fabrication process were made [220], [221]. The range of frequency is from 140GHz to 340GHz. It is due to the low attainable height by cleanroom electrolysis processes (200 um). However, one could apply this technology at lower frequencies, with slightly lower Q factors.

In Table 3 is a brief recap of the performances of the different technologies for 4x4 Butler matrixes. For more exhaustive recap tables, one may look at [160].

Table 3 : Recap of the performances of the different technologies at mm-wave

Ref.	Technology	Freq. (GHz)	Footprint (mm x mm)	BW (%)	Transmission (dB)	Phase Error (°)
[187]	Microstrip	30	20 x 20	14%	-7 dB	±2.5°
[195]	SIW	60	150 x 150	23%	-7.5dB	±1.4°
[210]	Groove Gap	26	200 x 200	10%	-4dB	NA
[196]	SIW	70	50 x 15	5%	-7dB	±5°

The difference in footprint and bandwidth between [190] and [191] is mainly due to the size reduction method implemented. Such methods will be described in Chapter 3.

2.2. Previous results

In this section, we will present the previous results obtained by M. Cometto [86] on air filled waveguides with VACNT lateral walls, and the issues encountered.

2.2.1. Guiding of EM waves using CNT walls

Let us consider the waveguide shown in Figure 49. The waveguide consists of two parallel metallic plates (3 um of gold layer supported by a silicon substrate) and two lateral walls made of VACNTs.

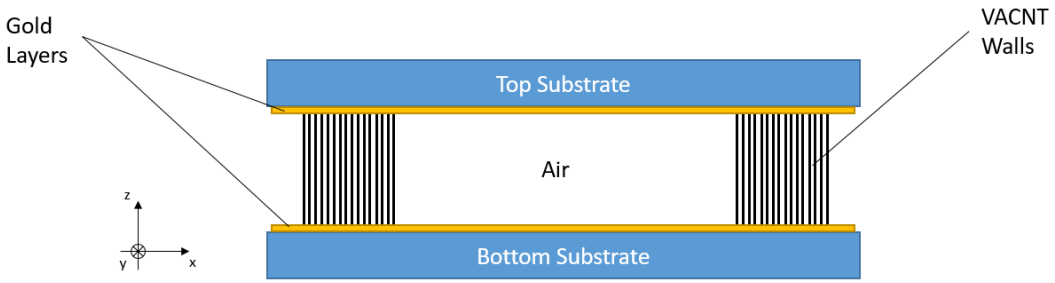

Figure 49 : Topology of the Waveguide, propagation direction in y

A full EM 3D simulation can be done by using Ansys HFSS, for the VACNT walls, the model of the anisotropic conductivity[7] (explained in I.4.3). The design is shown in Figure 50, without the top substrate in order to see the TE10 propagative mode. The dimensions of the waveguide are: 3 mm width and 0.5 mm height. For a classical rectangular waveguides (width of a and height of b) the cutoff frequency of the TE and TM modes are given by:

$$f_c = \frac{u'}{2}\sqrt{(\frac{m}{a})^2 + (\frac{n}{b})^2}$$

Where u' is the speed of light in the propagating medium, and (m,n) a couple of integers that cannot both be 0, the order of the mode. Visually, these m and n numbers represent the number of half periods of the standing electric wave (magnetic for TM) in the cross-section plane of the waveguide (m along the a-dimension, n along the b-dimension of the waveguide).

If a is bigger than b, the fundamental mode is the TE10. In that case, the width of the waveguide determines the cutoff. In our case a 3 mm width gives a cutoff at 50 GHz. The height of 0.5 mm does not impact the cutoff, it was chosen due to fabrication possibilities.

[7] HFSS solves Maxwell equations in each elements of the mesh and equalizes the continuity conditions at each frontier. In the case of an anisotropic material, Maxwell equations remain the same but with tensors for the material properties. Thus, HFSS allows having anisotropic materials in designs.

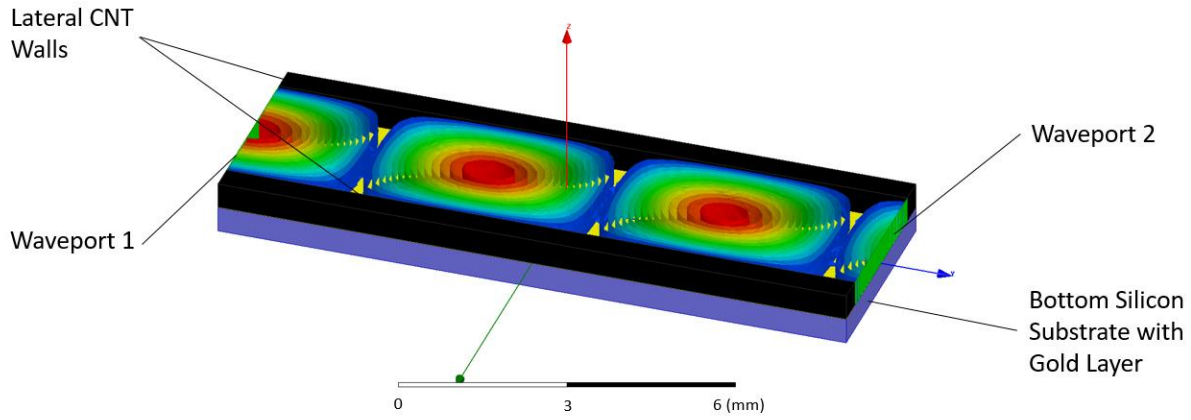

Figure 50 : HFSS E Field magnitude surfaces for the TE10 mode

3D EM simulation confirm that only Transverse Electric (TE) modes can propagate in such a structure. This is explained by the fact that the current in lateral walls is longitudinal for Transverse Magnetic (TM) modes, i.e. in the direction of propagation. Indeed, such a current cannot exist in our anisotropic walls, which conductivity is in the z direction (Ohm's law). For the same reasons, TE modes of the type TE0n, with n a non zero integer, do not propagate in this device, because the theoretical necessary current is not aligned with the CNTs direction.

Due to the strong similarity in behavior to SIW, this type of structure can be considered as Air-Filled SIW.

In Figure 51 we have plotted the transmission (S21) of such a waveguide between 40 GHz and 120 GHz . The transmission losses for a density of 10^{15} CNTs/m^2 are around 0.12dB in the passband for a length of 10 mm.

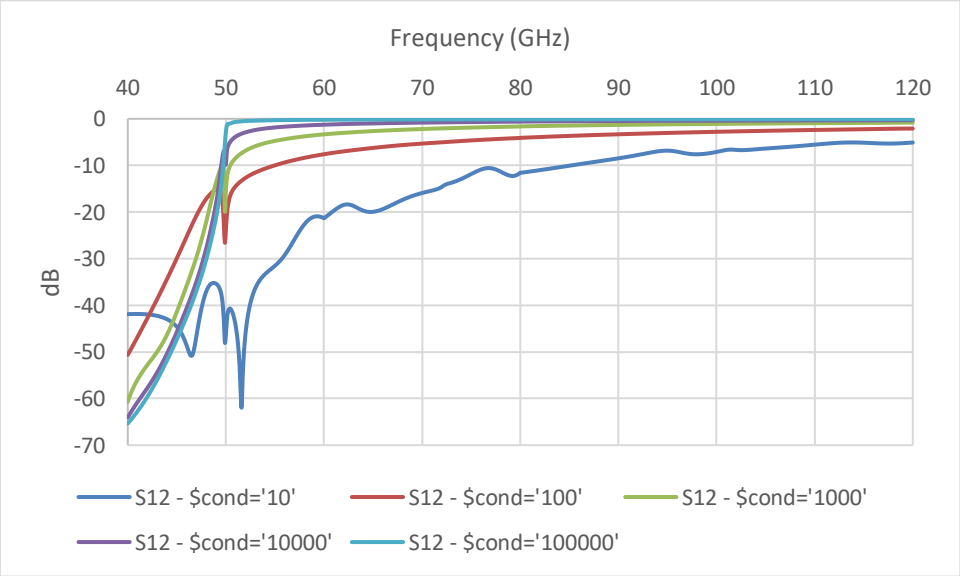

Figure 51 : Transmission of the VACNT Air Filled SIW without transitions, for different densities

The behavior of the waveguide in the whole E band is satisfactory, for a density above 10^{13} CNTs/m^2 (insertion losses above -1dB on the band). The bandwidth of the waveguide ranges approximately between propagation of the fundamental first mode TE10 (50 GHz) and the second mode TE20 (100 GHz) (first second mode to appear).

2.2.2. First device design

To devise a way to excite the structure, it was chosen to short a CPW line on the bottom plane to the top cover using a VACNT stub (Figure 52). This solution was considered among others for various reasons we will detail later in II.4.

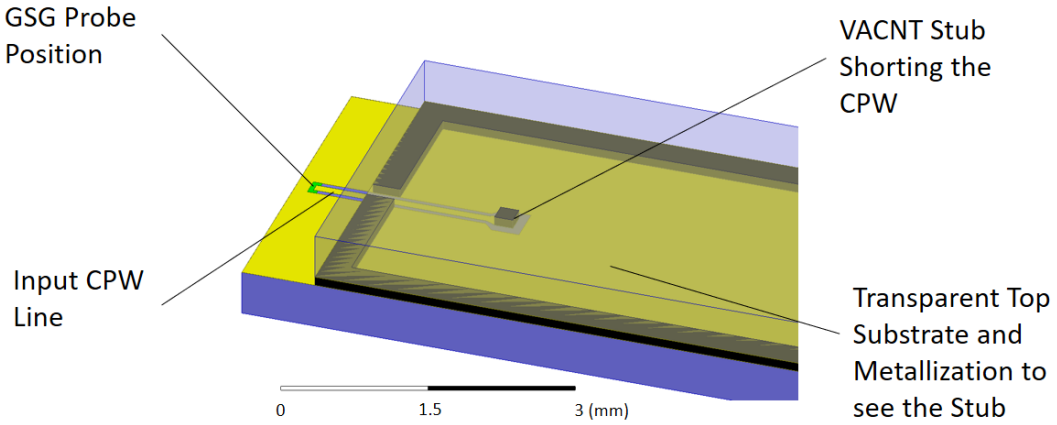

Figure 52 : Design of the Input/Output Accesses

The principle of this excitation is as follows. The CPW lines penetrates in the VACNT waveguide structure where after a certain length its signal is shorted to the metallization of the top of the waveguide. In order to have a good matching between the CPW line and the WG two things can be tuned, the taper before the stub and the penetrating length. By shorting the signal, a magnetic field is created around the short-circuited pillar and it couples with the magnetic field of the TE10 WG mode. One can note that if the pillar is at a short distance from the top layer (less than 10 um in our case) the excitation still works by coupling the resulting E field between the top of the stub and the cover, and the E field of the TE10 mode, Figure 53.

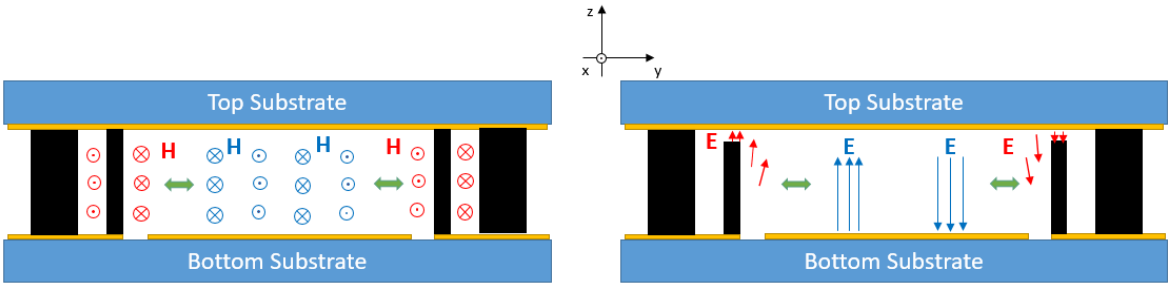

Figure 53 : Different Excitation Couplings

The 3D EM simulations for such a structure (ideal contact with the stub) yield the following S-parameters, Figure 54. The whole structure was simulated, meaning both transitions and the waveguide. The adaptation is not -10 dB on quite the whole E band. Yet, by shifting the cutoff frequency to lower ones we could get such a result. Our targeted band for the TRiCOT project is 71-76 GHz or 81-86 GHz.

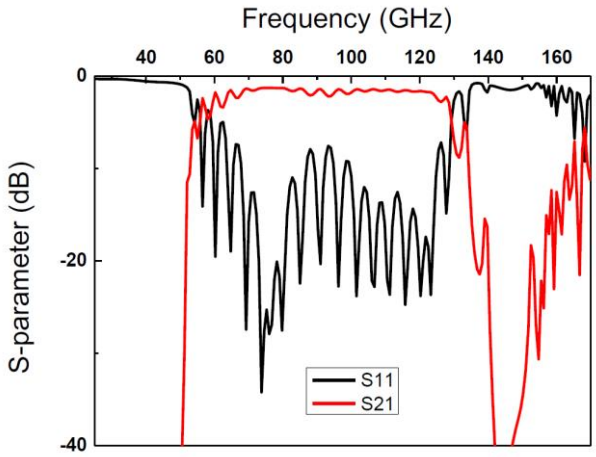

Figure 54 : 3D EM Simulated S-parameters for the whole Waveguide with Back to Back transition [86]

2.2.3. First Designs Fabrication

All the fabrication steps for these devices were done in CINTRA.

The first design was fabricated using direct growth of the CNTs on the substrate [86]. However, due to the high growth temperature (around 700 °C), the gold layer flaked (Figure 55) and the measured waveguides showed no transmission. Indeed, the difference of Thermal Expansion Coefficient (TEC) between silicon and gold is important, 2.6e-6 K^{-1} and 14 K^{-1} reciprocally, and consequently when the temperature rises the gold layer expands more than the silicon substrate thus creating flakes when the temperatures decreases back to room temperature

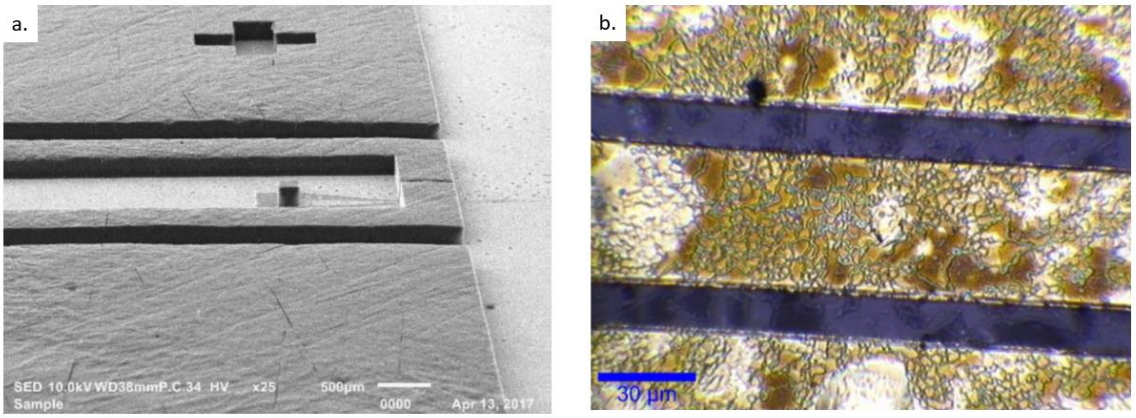

Figure 55 : a. SEM picture of the Waveguide and b. Optical Microscope Picture of the Access Line (gold flakes)

In accordance with the conclusions that we have deduced from this first run, it was decided to use a transfer process, with lower process temperatures. The design was also changed to showcase the different shapes that could be transferred. The triangles on the side of the walls are used as mechanical support for the top cover (Figure 47).

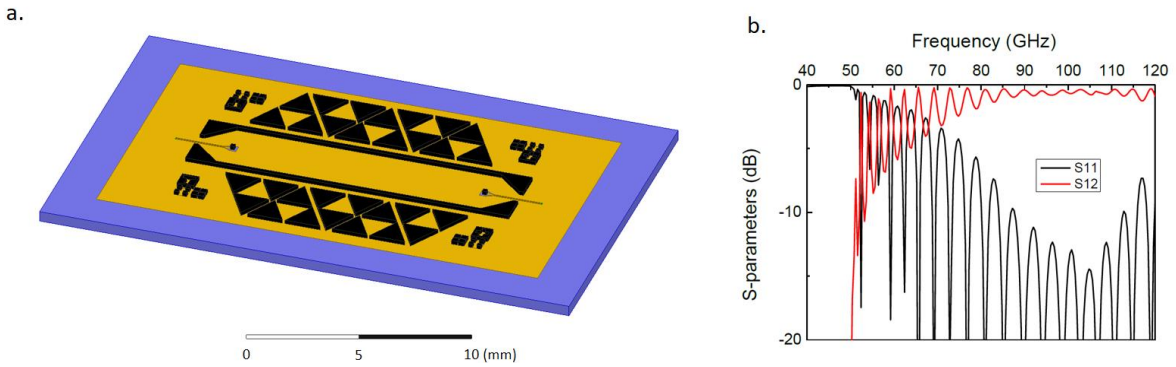

Figure 56 : a. Design of the waveguide, b. Preliminary simulated S-parameters [86]

The transfer process, developed and optimized by CINTRA in collaboration with XLIM, is described in Figure 57. Let us go through it step by step:

- Step 1: The CNTs are grown on separate substrate using TCVD
- Step 2: The patterns of the waveguide (pillars, walls, support and markers) are deposited on top of the CNT forest in gold. This is done by using evaporation (E beam) through a shadow mask[8].
- Step 3: The patterns of the waveguide (pillars, walls, support and markers) are deposited on top of the bottom substrate in SAC 305[9]. This is done by using evaporation (E beam) through a shadow mask.
- Step 4: The separately grown VACNTs and the bottom substrate are aligned with one another and contact is made. Pressure and temperature profiles are applied so as to have good gold-SAC-gold bonding. Temperatures do not go above 200°C.
- Step 5: The two substrates are separated, CNTs remain only where there was bonding.

[8] Metallic plate with holes used as a mask for certain applications.
[9] Alloy used for soldering purposes, Tin, Silver (3%) and Copper (0.5%), hence the name.

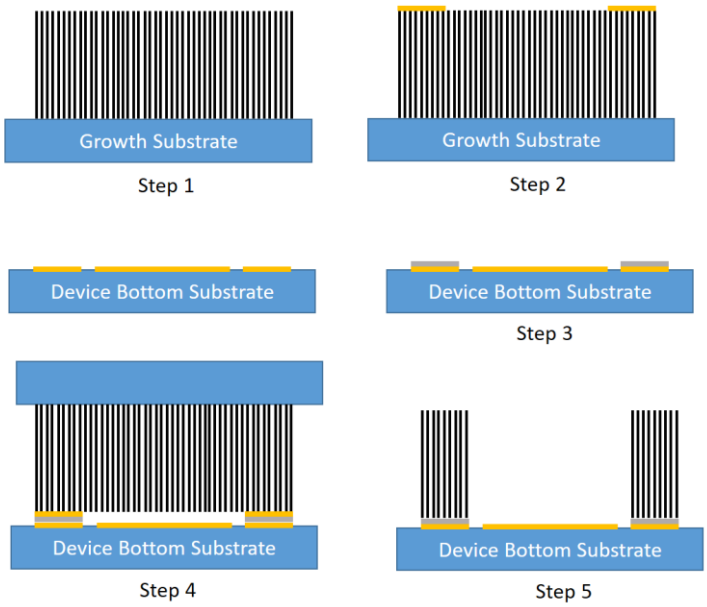

Figure 57 : Steps of the Transfer Process (Patented by CINTRA)

Only remains the cover for the device to be fully assembled, at this step of the project it was simply manually deposited. Later in this work, different assembly processes were investigated.

2.2.4. First Design Measurements

These measurements, as well as all the RF measurements of this PhD,were made in XLIM, in the PLATINOM platform, with the precious help of Damien Passerieux. The measurements were divided in two bands: 10 MHz to 65 GHz and 65 GHz to 105 GHz. The equipment can be pushed to have 10 MHz to 110 GHz but the results are not yet coherent.

For the 10 MHz-65 GHz band, the measurements were made using 125 um pitch infinity probes, a probe station made in XLIM and a PNA-X. The 65 GHz-105 GHz S-parameters were measured using the following bench: a Vectorial Network Analyzer (VNA), PNAX N5247A from Keysight, coupled to two millimeter-frequencies converters from VDI. The probe station is the PM8 from Cascade Microtech and the probes are the Infinity|110-S-GSG-100-BT from Cascade Microtech. Pictures of the benches are shown in Figure 58.

Figure 58 : Measurement Bench in XLIM, Left 10 MHz to 67 GHz, Right 75 GHz to 105 GHz

Quite a few devices were measured, one of the measurements is presented in Figure 59. As we can see, the transmission between around 70 GHz is noisy but gives an idea of the S-parameters. More importantly, we can estimate a -3 dB cutoff frequency around 50 GHz, from the S21 behavior. We witness the same cutoff frequency as simulated, which partly validates the EM modeling of our devices. Unfortunately, the transmission level after 50 GHz hovers around -15 dB, much less than in the simulations (around -1 dB).

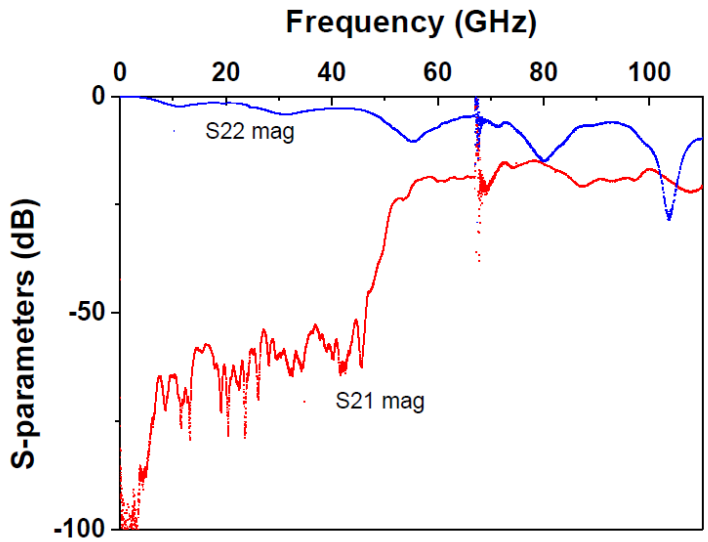

Figure 59 : Measurement S-parameters of a waveguide fabricated using the transfer process (design Figure 56) in the 10 MHz-110 GHz band, in red, transmission, in blue, adaptation [86]

Because the cover is manually attached, measurements applying different pressures on the cover of a same device were also made (Figure 60).

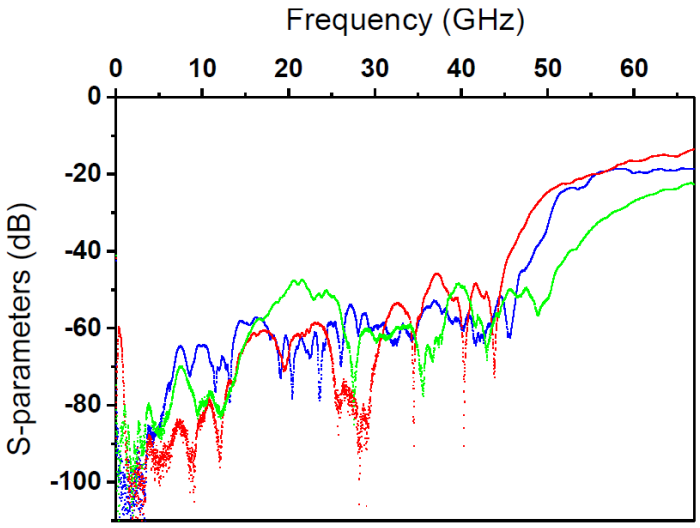

Figure 60 : Transmission for three different cover assembling processes, red, blue and green (explained below) [86]

The red curve represents the transmission of the device, when pressure was applied on the cover during the measurement, the blue one, is the measurement after releasing pressure and the green one is for a cover gently set on top of the CNTs without other pressure than the one from its weight. As we can see, changing the pressure on the cover impacts the transmission. The explanation is that it is probably due to the nature of the contact between the cover and the top of the CNT walls. Because there is no solder, by applying pressure, the leakage decreases.

The poor contact between the cover and the top of the CNTs was confirmed in [86] by SEM observation and EM backsimulations showed that a gap as little as 1 um could explain such losses (Figure 61).

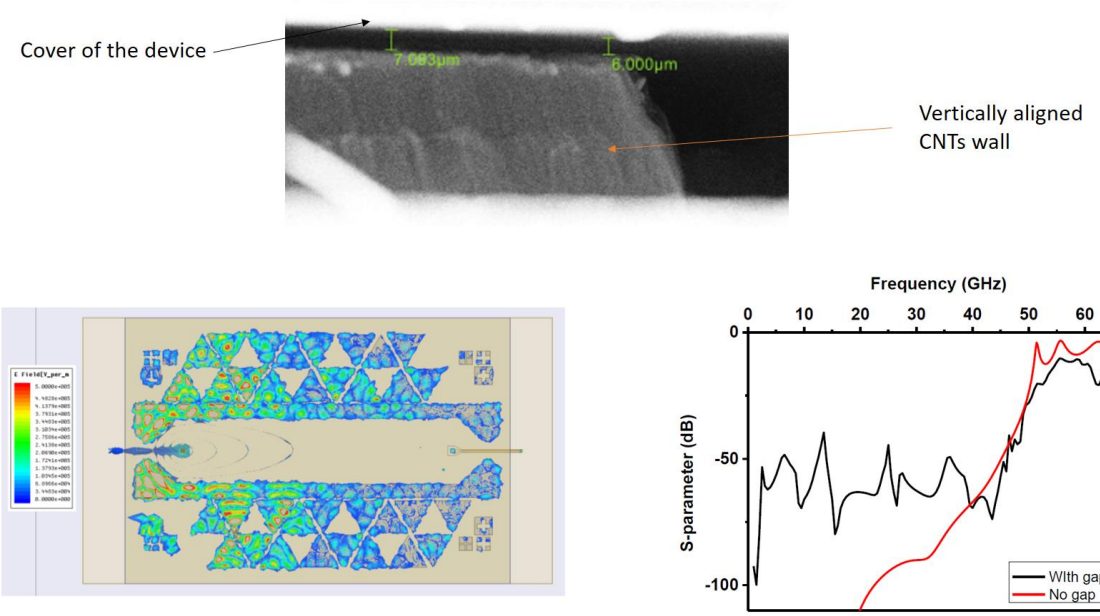

Figure 61 : Top, SEM picture of the gap between the top of the walls and the cover, Bottom left, simulated density of electric field for a waveguide with a gap (leakage through the gap), Bottom right, simulated transmission with and without gap [86]

It was also shown in [81] that by applying too much pressure the CNTs were crushed which led to a height reduction down to 20 um (the simulated optimal height is of 200 um). For a CNT height of 20 um, the simulations show a transmission level around -15 dB [81].

Though the transmission levels are very low, the fact that we estimate a cutoff frequency at 50 GHz is encouraging. It shows that the CNTs are at least conductive to a certain amount and it shows the equivalent bulk model used for VACNTs gives a good estimation of the EM behavior.

To conclude, the poor performances of the waveguide can come from different things:

- The poor contact between the CNT walls and the bottom and top metallic covers
- The crushed CNTs leading to a height too small (20um instead of 200um)
- The excitation pillar having poor contact with the top and bottom metallization

- The intrinsic conductivity of the CNTs being too low

This led to three different actions:

- try different fabrication processes for better contacts
- change the excitation method to limit the unknowns (pillar contact)
- characterize the CNTs and the assembly process.

In what follows we will go more in details about these three actions, in order.

2.3. Changes in the Fabrication Process

The way the devices are assembled and the mode propagating (TE10) make them particularly prone to leakage currents and sensible to this type of assembly. That is why the fabrication process was particularly studied.

In this section we will present the different changes that were introduced in the fabrication process, during this PhD work, and the different observations that were made. These technical evolutions have been elaborated in close collaboration between CINTRA and XLIM. The work presented in this section relied heavily on Chun Fei Siah and Simon Goh fabrications in Singapore. The different structures were fabricated in CINTRA and measured in XLIM.

2.3.1. Assembly of the cover

Because it is the one major unknown of the fabrication process. The first thing that was studied is the attachment of the cover.

2.3.1.1. Design Changes

The first thing to do in order to improve the fabrication process was to make the design compatible with the fabrication process. The effect of wall thickness is shown in Figure 62.

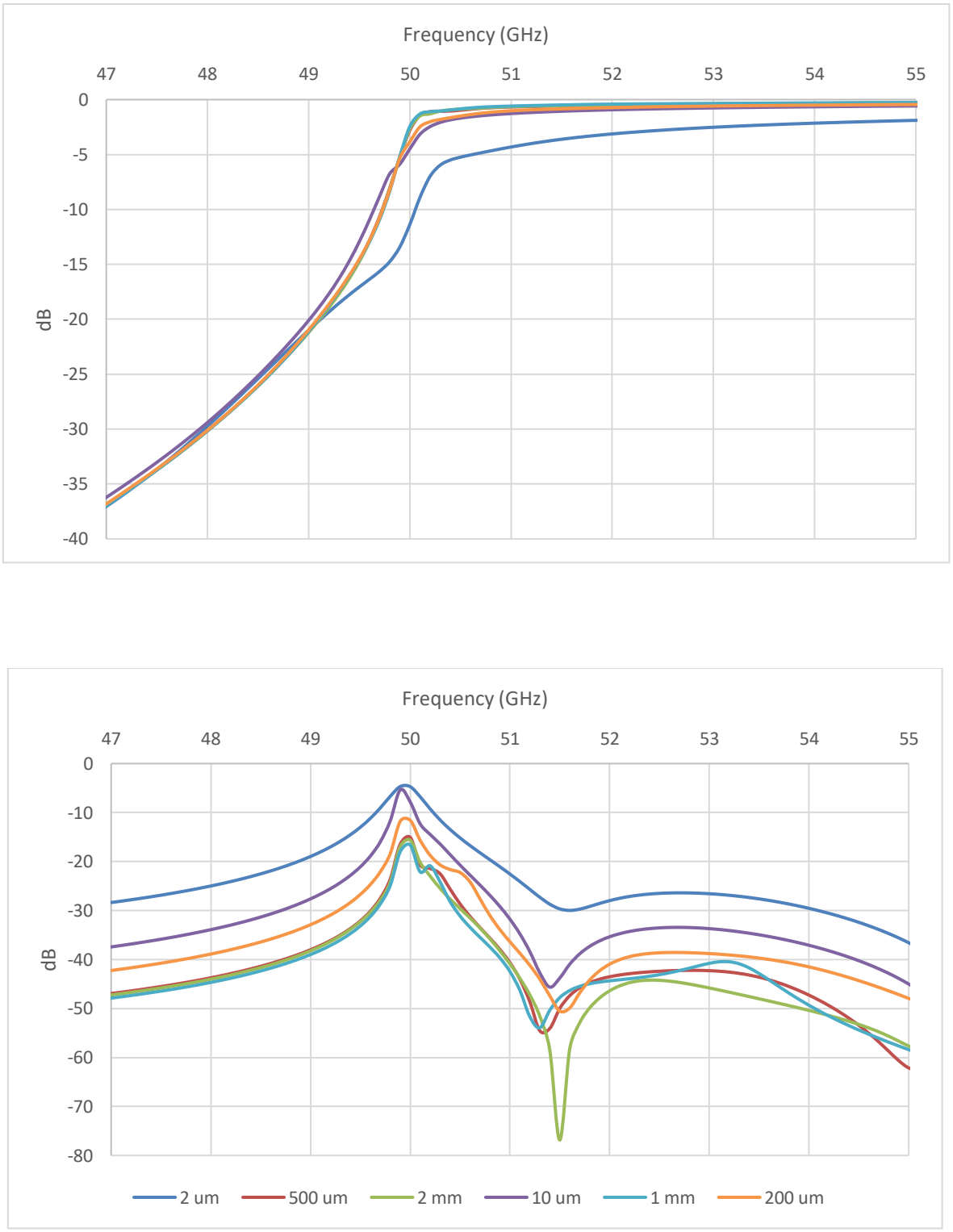

Figure 62 : Top, S21, transmission for different wall thicknesses, Bottom, S11, adaptation for different wall thicknesses

As we can see, changing the wall thickness does not impact transmission and adaptation, as long as the wall is thicker than 200 um. For an isotropic metal, the skin depth δ is given by:

$$\delta = \frac{1}{\sqrt{\pi \mu_0 \mu_r \sigma f}}$$

With, $\mu_0 = 4\pi * 10^{-7} * 1\ F/m$, the permeability of free space, $\mu_r = 1$, the relative permeability of our metal, $\sigma = 1.62 * 10^5\ S/m$, the conductivity of our metal (according to chosen density), and $f = 50\ GHz$. We obtain a skin depth of 5 um, which is coherent with our simulations. Though skin depth evaluation might not be directly applicable to an anisotropic material, which is our case, it can give insight.

Thus, it was decided to keep the exact same dimensions as the waveguide in Figure 52 but to have bigger lateral CNT walls[10], and to add some space on the sides in case we might need spacers[11], as shown in Figure 63.

Devices in 2.3.1.2 and in 2.3.1.3 have the same design as in Figure 52 but it does not change the conclusions that were drawn.

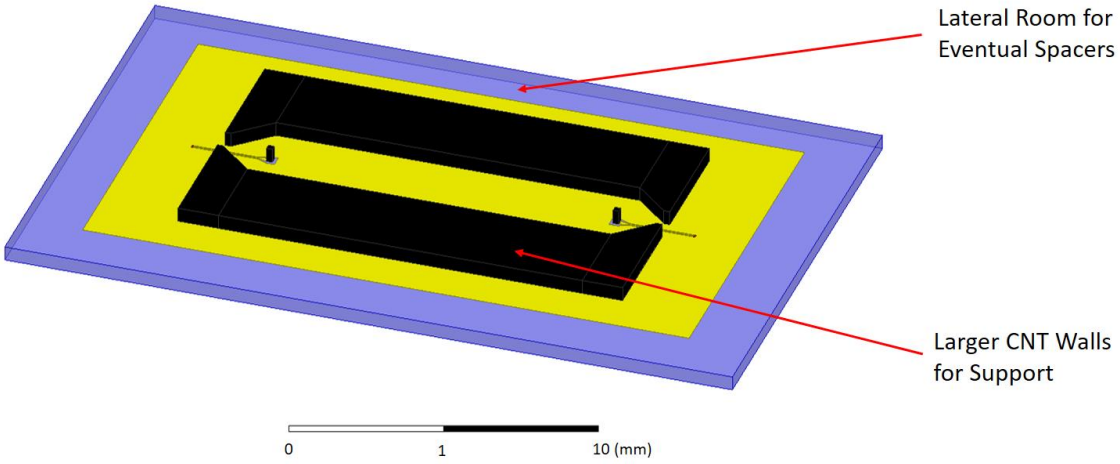

Figure 63 : New Design with Bigger Walls and Room for Spacers

The use of groove gap technology was also investigated . The idea was to replace our lateral walls, by periodic structures made of CNTs. Each wall would consist in a bed of VACNT bumps. In a similar way that bed of nails is used in classical waveguides, the bundles of VACNTs would replace the “nails”. The interest behind the groove gap technology is that waves cannot propagate between the top cover and the lateral walls (bed of nails), thus, pushing aside the contact issue. Unfortunately, the anisotropy of the VACNTs does not allow for the forbidden band to appear.

The changes in the air-filled waveguide design that fundamentally change the behavior of the structure are explained in 2.4 to 2.6. This small change in the design presented here was done for simpler fabrication processes, but does not change the response of the structure in itself.

[10] It was observed in CINTRA that growth of VACNTs bundles of different areas have different speeds, which leads to different heights. In the previous design, the support could be taller than the walls, which we want to avoid.

[11] Physical pieces of a given height to intersperse between bottom and top substrate to avoid crushing of the device.

2.3.1.2. Gold-SAC-Gold cover attachment

To make sure there is no gap, the first proposition is to solder it using the process described in Figure 64.

The attachment process is as follows:

Step 1: Fabricate the bottom part of the device and transfer the CNTs as in Figure 57.

Step 2: Fabricate the cover of the waveguide using classical photolithography processes.

Step 3: Using a Shadow Mask, deposit gold on top of the transferred CNTs

Step 4: Deposit SAC305 on the cover of the device where we want soldering to happen with the CNTs

Step 5: Assemble the two parts, and solder with proper pressure and temperature profile.

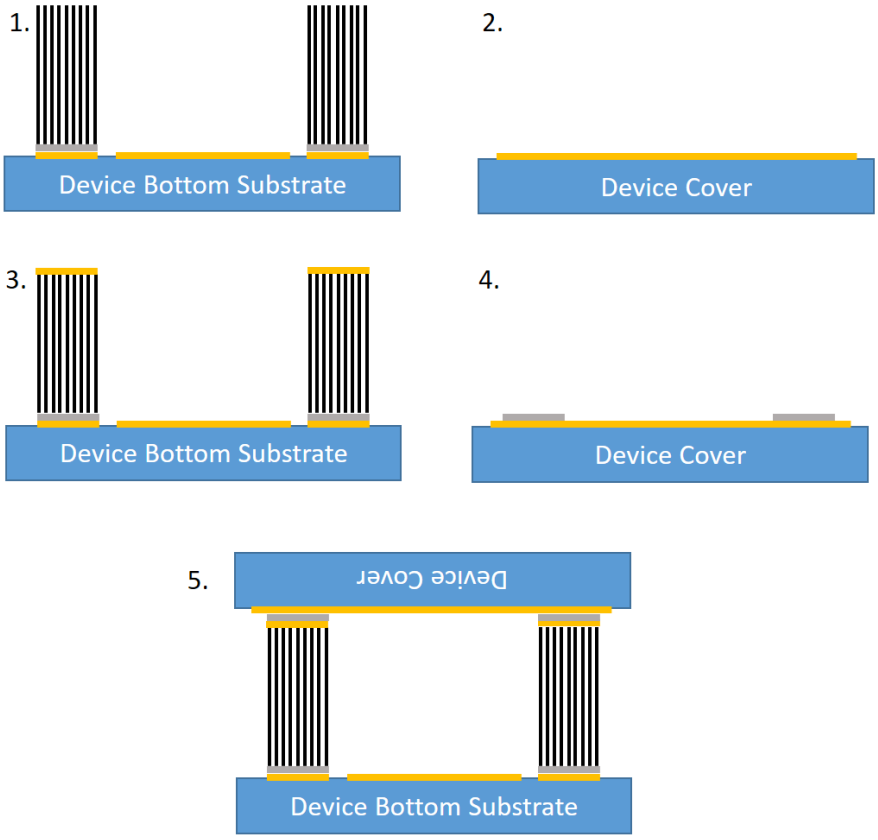

Figure 64 : Solder Process for the cover, in chronological order from left to right, and top to bottom

Devices were fabricated and measured. The S-parameters are shown in Figure 65.

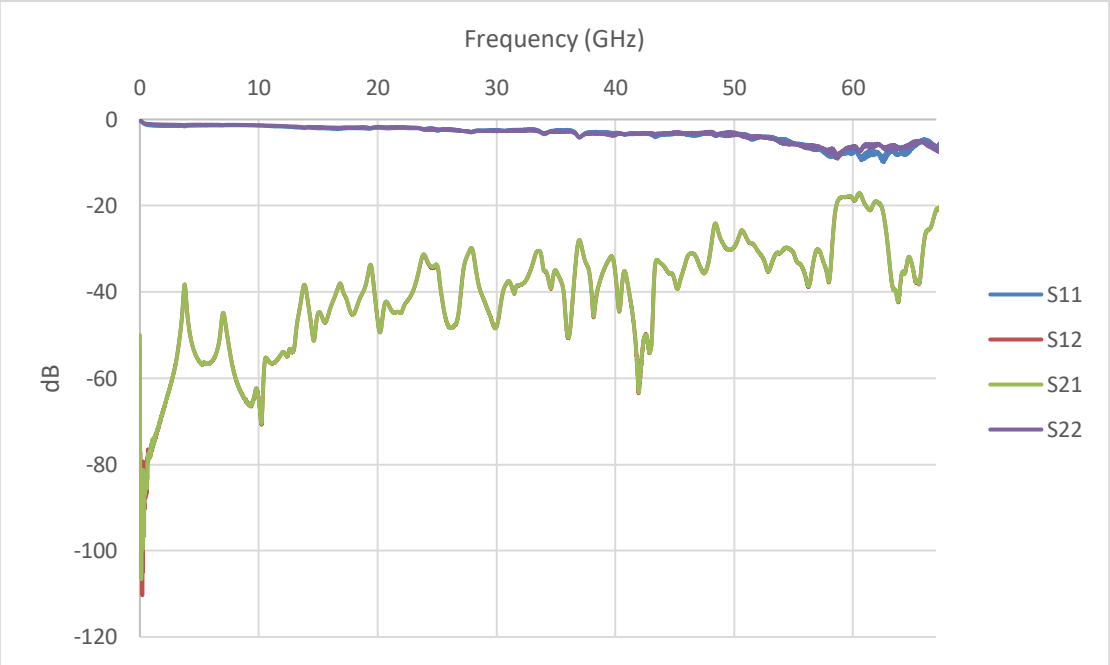

Figure 65 : Measurements of the Gold-SAC-Gold waveguide

As we can see, the measurements show no cutoff frequency at 50 GHz. The problem with this process lies in the use of the shadow mask. Indeed, the shadow mask is difficult to align with the bottom device without crushing our CNT walls and pillars[12]. The height of the device was measured at 20um using SEM. The shadow mask probably has ripped some part of the VACNTs walls off, because we do not see a cutoff, in the transmission.

[12] This is not a problem during the transfer process, because the crushed CNTs are not transferred.

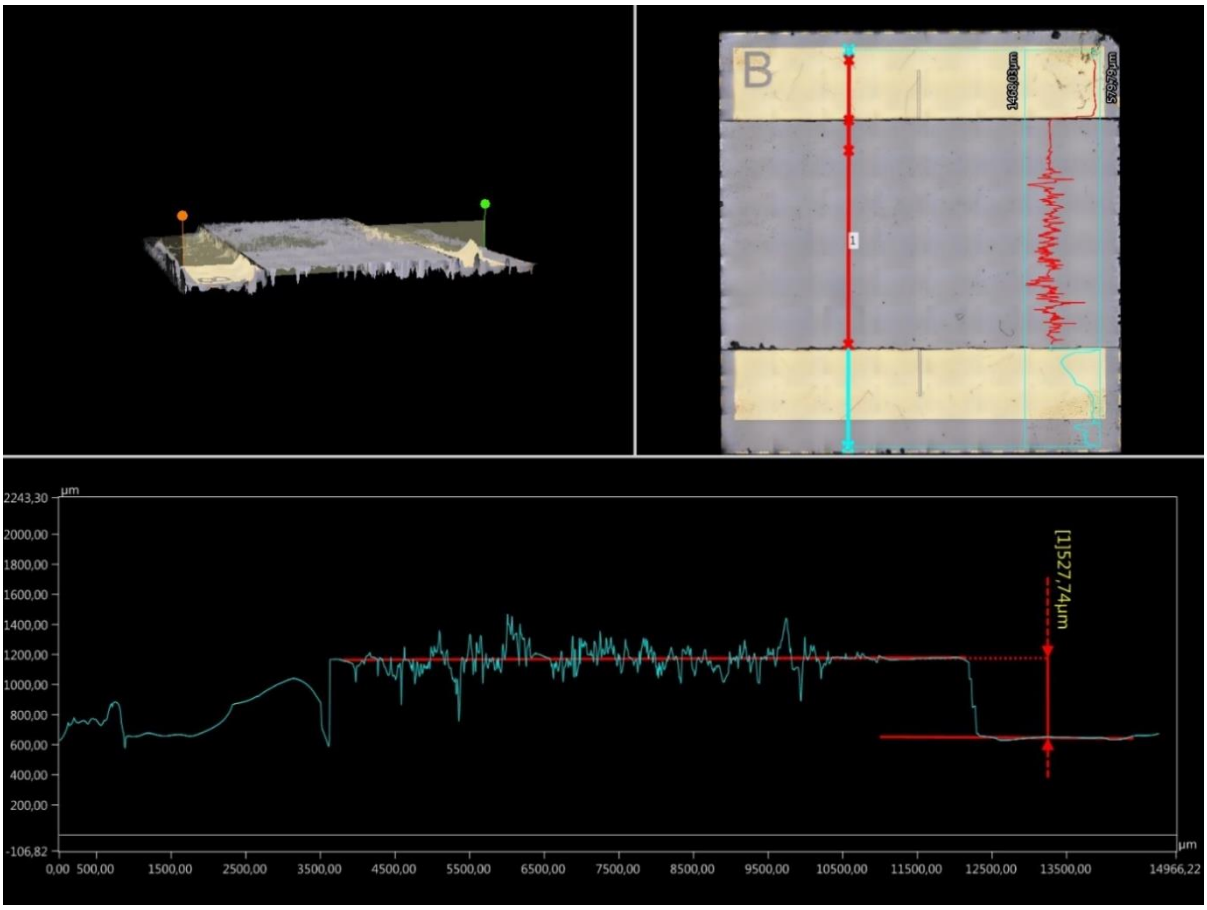

Figure 66 : Measured height using Keyence 3D numerical microscope, the thickness of the substrate is 500 um, meaning the height of the CNT is 30 um approximately

2.3.1.3. H20E glue on the cover

The second method to solder the cover to the top of the CNTs, that was investigated was a simpler one. The idea originated from our partners in Palaiseau, the III-V lab. It consisted in covering the cover with H20E glue and then gluing the cover directly on the top of the CNTs. There are pros and cons to this method.

The main advantage is that it is easy to implement, one simply needs to find a way to spread a uniform layer of H20E on the cover. The method used to do it was artisanal serigraphy, two pieces of 50 um-thick tape were placed on the sides of the cover, and an initial dot of glue was spread using a doctor's blade so as to fill uniformly the area. After removing the pieces of tape the resulting layer of H20E is about 50 um. The cover was then gently deposited on top of the waveguide walls, with a weight of 10g, and cured for a night at 80°C (Figure 67).

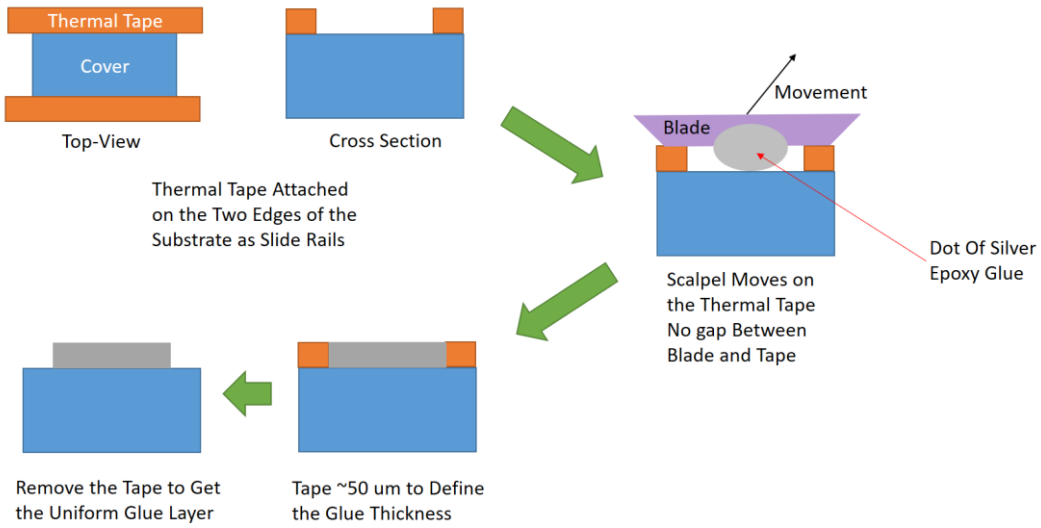

Figure 67 : Fabrication Process of the Silver Coated Cover

The main inconvenient of this process is that it could potentially degrade the transmission parameters. Indeed, adding a layer of H20E glue will greatly decrease the conductivity of the cover. Initially, the considered cover is in gold (with a conductivity of $4.1e^{-7}$ S/m), but by adding a layer of H20E glue, the transmitted wave will be degraded by the poor conductivity of the glue.

The H20E glue was characterized in XLIM using the resonant cavity method at 10 GHz (Appendix 1), an average conductivity of $3e^{5}$ S/m was found .

Devices were fabricated in CINTRA and III-V lab, and the measurements done in XLIM, are shown in Figure 68.

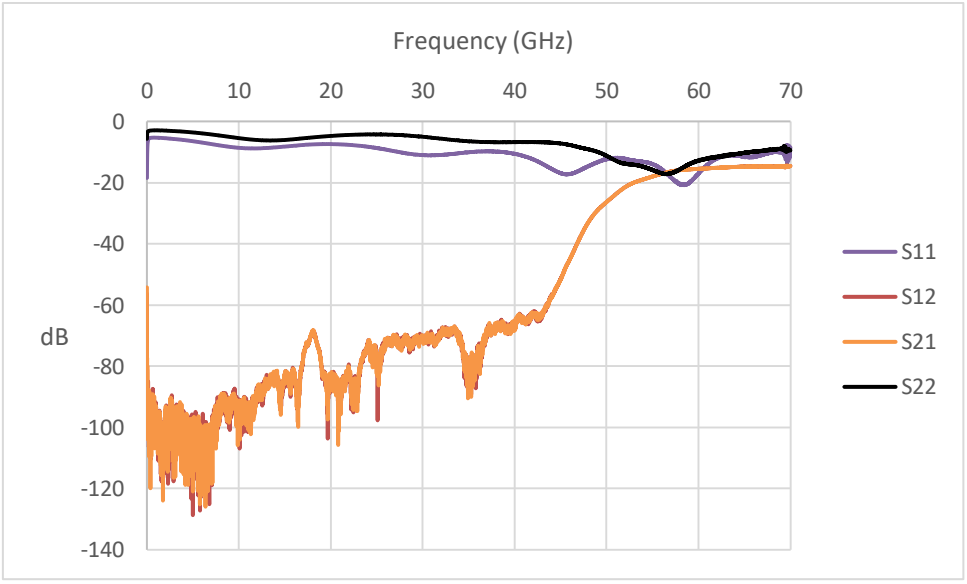

Figure 68 : S-parameters of the waveguide with a H20E cover

We still have a transmission level at -15dB.

We determined the height of the WG using SEM. The picture is shown in Figure 69.

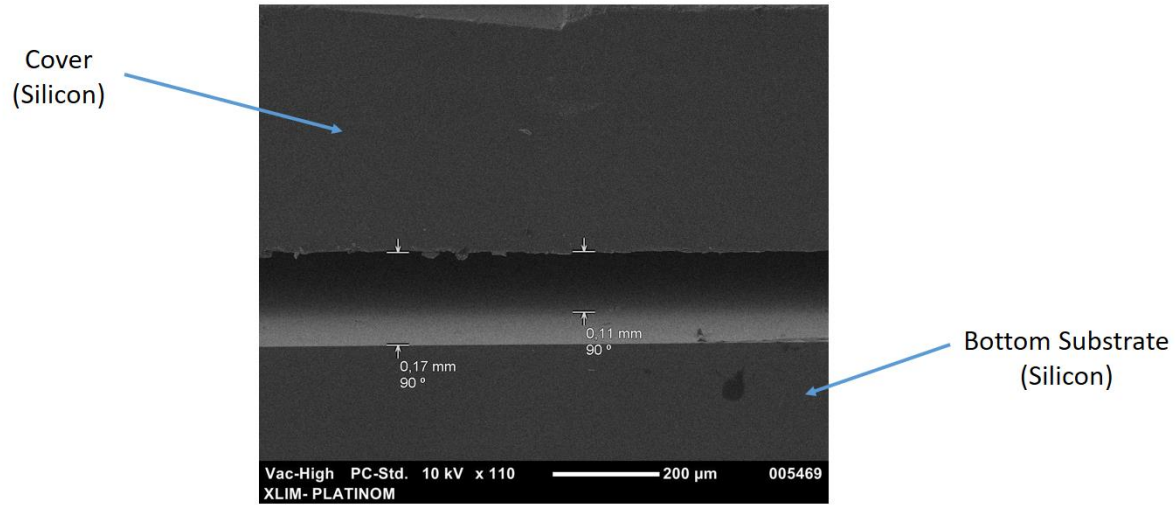

Figure 69 : SEM image of the distance between the top and bottom substrates, approximately 110 um

As we can see, the distance between the top and bottom covers is 110 um maximum. Yet, the thickness of the silver glue layer is 50 um. That implies a WG height of 60 um, which is not optimum according to the 3D EM simulations (we remind that the optimal value between the top and bottom covers should be 200 um).

In order to see if the layer of silver decreased greatly the performances, we decided to try a similar process. Instead of spreading glue all over the cover, it was decided to put it only on top of the CNTs.

2.3.1.4. H20E glue by stamping

In parallel, of the other changes in the fabrication process, the use of spacers was introduced at this point. In order to avoid the crushing of the CNTs witnessed precedingly, the use of spacers was introduced in the fabrication process. Basically, they are pieces of silicon wafer (384um) that we intersperse between the bottom and top substrate, more on that in 2.4.

The fabrication process used in order to deposit glue only on top of the CNTs, thus theoretically diminishing the losses is described in Figure 70.

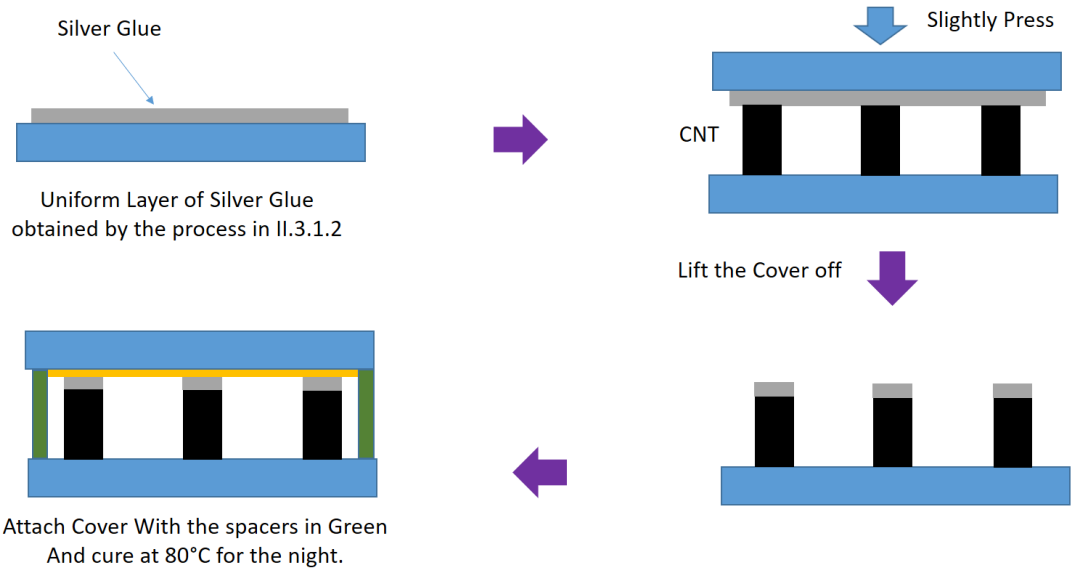

Figure 70 : Fabrication Process of the new type of Waveguide

Two of these waveguides were fabricated and observed using SEM, before measurements. As we can see on the images of Figure 71, the contact seems to be good, and this time, we have the correct height of 384 um, that is the height of the spacers used. However, transport from Singapore to Limoges might have damaged the structure.

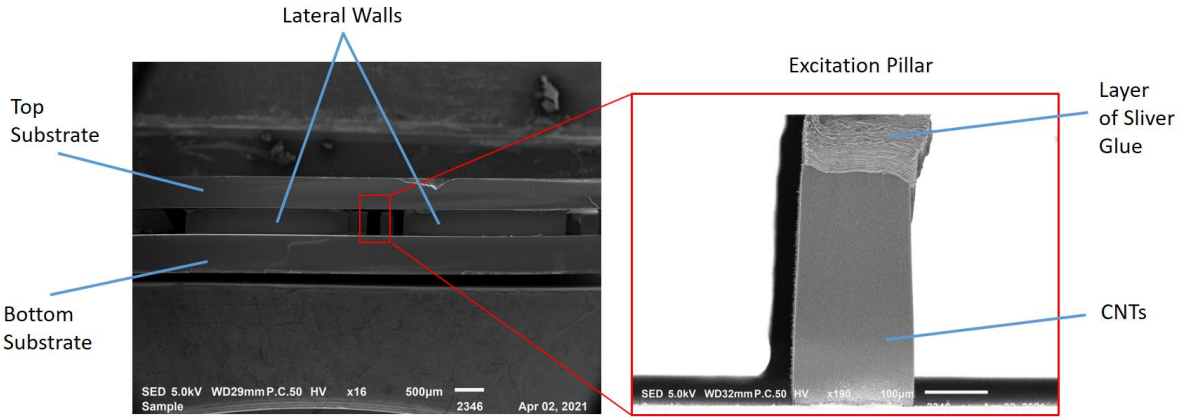

Figure 71 : SEM pictures of one of the waveguide curtesy of Chun Fei Siah and Simon Chun Kiat Goh in CINTRA

The measurements still show a transmission level around -15 dB, in Figure 72. The measurements are compared to the 3D EM simulation of the waveguide for a height of 384 um (Figure 72)

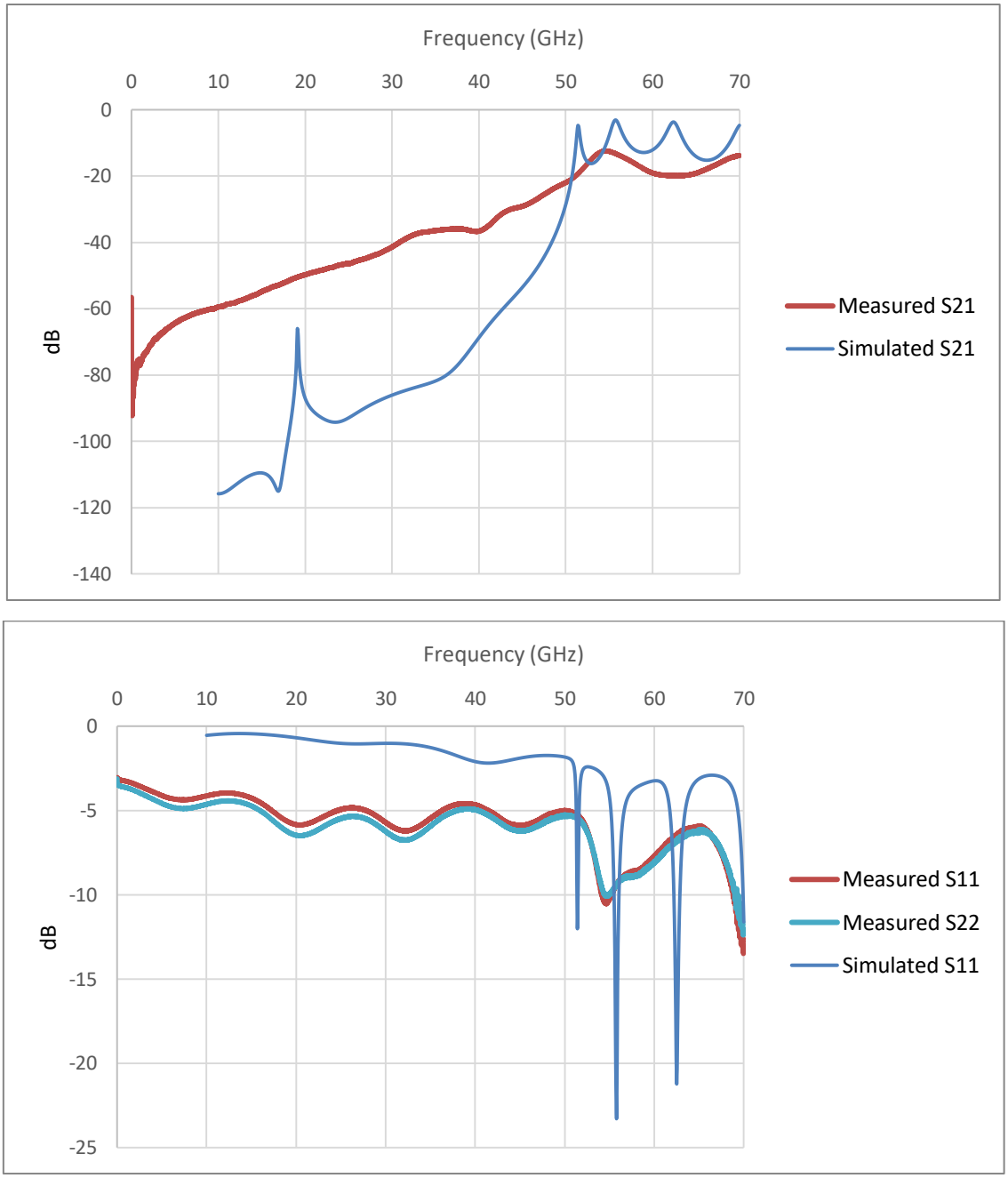

Figure 72 : Measurements and 2D EM back-simulation of the structure, Top, transmission, Bottom, Adaptation

The transmission level is still around -15 dB, however, the simulated S-parameters show that for a height of 384 um, the transmission parameter has greater amplitude variations, because the waveguide is not well adapted. Still, we have losses in the structure.

This time the attachment of the cover is good, as shown by a measurement of a waveguide with a cover that was only deposited and not soldered using H20E glue. The fabrication process was the same but the cover was not attached, meaning we have glue on top of the CNTs, but the cover was not bonded. The measurements are shown in Figure 73.

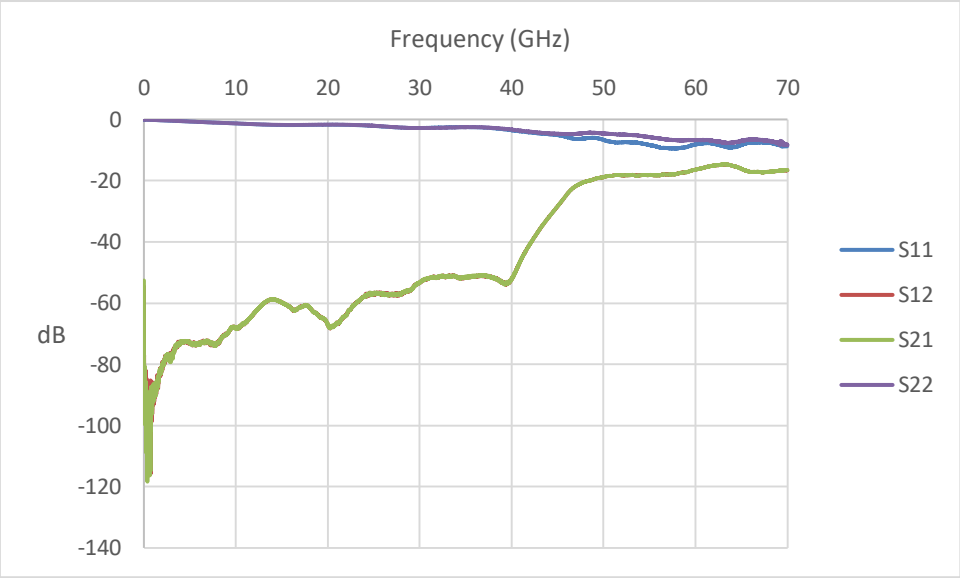

Figure 73 : Measurement of a waveguide with cover not soldered

As we can see, the transmission for the device which cover was only deposited (not bonded) (Figure 72) is lower than when the cover is bonded (Figure 73). This suggests that the contact between the cover and the top of the excitation pillar and bumps is happening. However, there might be an important contact resistance.

The losses of the structures can come from many variables, misalignment of the pillars, high contact resistance between CNTs and cover, low VACNT conductivity, bad electrical contact from transfer, etc. There is a need to simplify the structure in order to be able to extract data. Which is what will be done in sections 4, 5 and 6 of this chapter.

2.3.2. Other Fabrication Process Changes

Our partners in CINTRA made many other fabrication changes and observations, as part of Chun Fei's PhD work in CINTRA for the TRiCOT project.. We will mention a few of them in this paragraph.

The use of Teflon spacers proved to be ineffective due to its high deformability. Indeed, height of devices were measured to be 50um while, 200 um spacers were used. The pressure applied for attachment of the cover was too great.

The growth of CNTs migrated from the Black Magic to the FirstNano CVD. This allowed for CNTs of better quality using H2O etching, but also potentially longer.

Because the CNTs are crushed during the transfer process, the height before and after transfer is not the same. An extensive study has been made to determine the height ratio in function of initial height. This allowed for a better control of our devices height.

To conclude, many different fabrication processes were tested but all show high losses. The losses can still come from too many parameters to allow us to conclude on poor conductivity of the CNTs. That is why it was decided to explore several changes in the design of the test structure, in order to have less unknowns.

2.4. Different excitation methods

As the simulations show in Figure 74, if there is a gap too important between the top of the input/output pillar and the cover, while good contact is present with the top of the CNT walls, the transmission decreases greatly. The adaptation is also very sensitive to such a gap. As we said earlier, different areas grow at different speeds and behave differently during transfer. Furthermore, any misalignment or bending will reduce transmission levels.

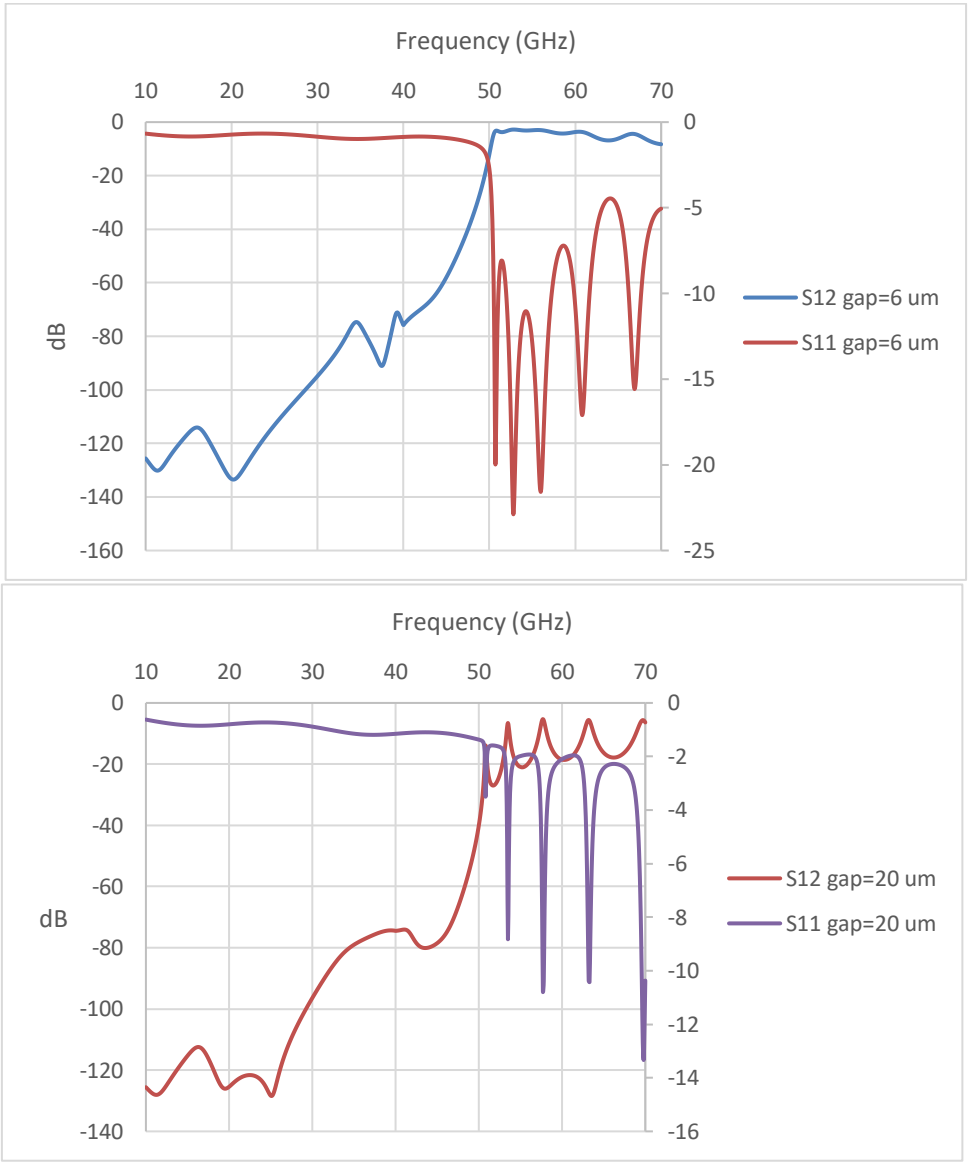

Figure 74 : 3D EM Simulated S-parameters for different gaps between the pillar and the cover primary axis on the right for S21, secondary axis on the right for S11, Top, gap of 6 um, Bottom, gap of 20 um (density of 10^{15} CNTs/m^2) (Scales on the right are for the adaptation, on the left for transmission)

To remove this major experimental unknown, different ways of excitation were investigated. Both of them will be presented in what follows. Due to the fragility of our devices no volumic excitation was studied [222], [223], only planar to rectangular waveguide transitions.

2.4.1. Short-Circuited CPW Line

The excitation method investigated by our TRICOT partners from Grenoble is presented in Figure 75. It is a well-studied method for the excitation of SIW structures [160], [224]. In this design, the transition is modified a bit. The access line is a CPW which transition to a grounded CPW (GCPW) in the aperture, to finish short circuited in a triangular shape inside the cavity. The different parameters :

- Wcpw, Ws1, d, Wgcpw, Ws2, allow to tune the impedances of the lines,
- $l_{t1,}$ θ_{t1} and θ_{t2} will determine the bandwidth and coupling of the excitation,
- and W_{wg} the cutoff frequency of the waveguide.

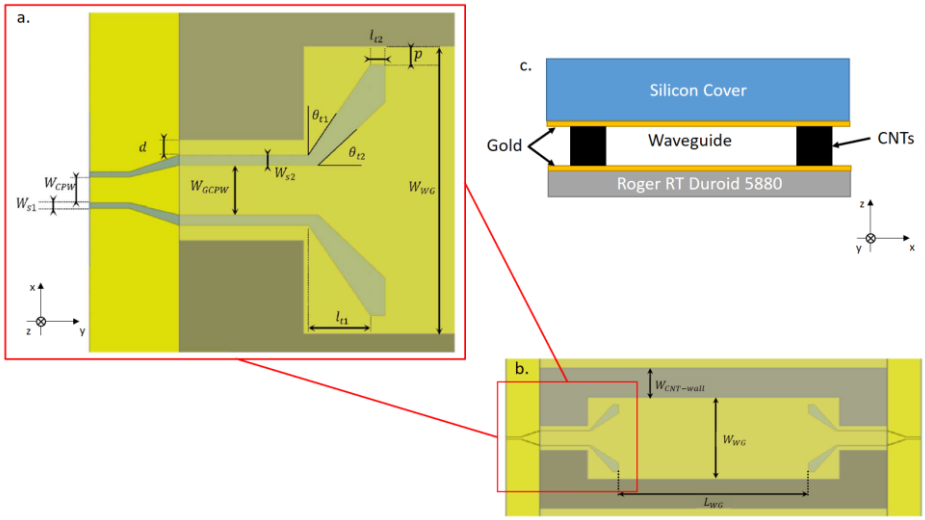

Figure 75 : Transition design from RFIC lab [160], a, zoom-in on the shorted CPW, b, design of the waveguide with input/output, c, cross-section of the device with different layers

The 3D EM simulated results show very good adaptation and insertion losses on the whole E band, Figure 76.

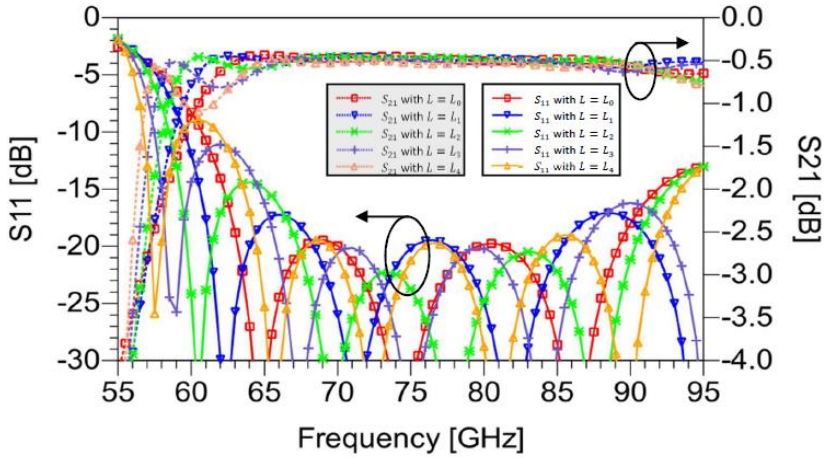

Figure 76 : 3D EM Simulated S-parameters for waveguides of different lengths

The different lengths simulated WG obey the following equation:

$$\mathrm{L}_i = L_0 + \mathrm{i}\Delta\mathrm{L}\,,\ \ 0 < i < 4$$

With $\Delta\mathrm{L} = 0.9\ \mathrm{mm}$ close to a quarter wavelength. These different lengths were chosen in order to extract the intrinsic parameters [160] of the waveguide without the transition (Explanation of the Thru-Line calibration in Appendix 2) [225], shown in Figure 77.

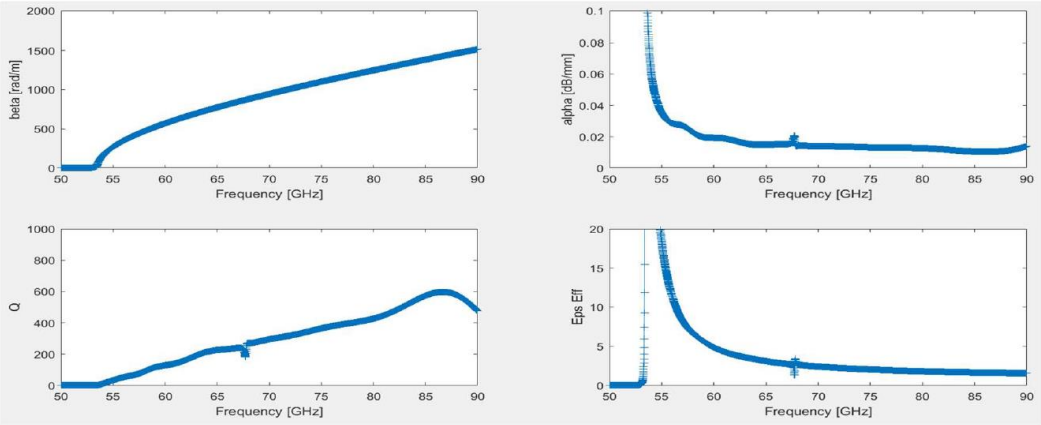

Figure 77 : Intrinsic parameters of the Waveguide (Simulations) [160]

The quality factor ($\frac{\beta}{2\alpha}$) at 80 GHz is about 400, and the attenuation is 0.015 dB/mm, for simulations with a density of 10^{15} CNTs/m^2 (close to results in Figure 51). Unfortunately, to design such an excitation at these frequencies, there was a need for a low permittivity substrate, in order to allow transfer of energy to the propagating medium, i.e. air (permittivity equal to 1). And, to avoid propagation of substrate modes the substrate needed to be 254um thick maximum. This led to the use of ROGERS RT Duroid 5880 (with a thickness of 0.127 mm and a relative dielectric permittivity of 2.2), a flexible substrate[13].

The assembly was too difficult (because of the flexible substrate), and colleagues at CINTRA observed delamination of the CNT forest on the substrate, Figure 78.

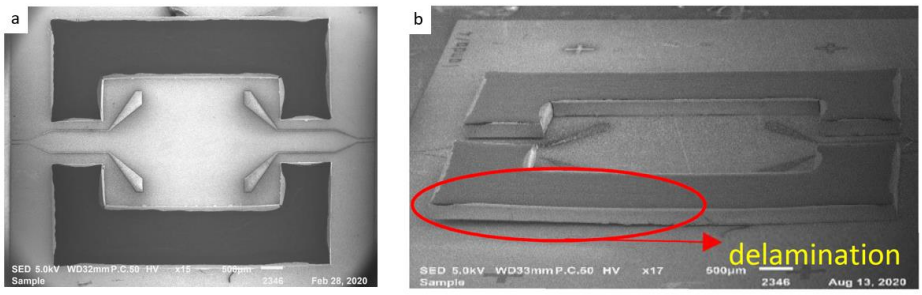

Figure 78 : a, Top View of the Fabricated Waveguide and b, Side View, with Delamination Highlighted

[13] Hard and thin substrates with low permittivity are hard to find, because they are either porous (air inside of permittivity 1) or use more Teflon as constitutive.

Still, we made measurements in RFIC Lab and in XLIM. The same experimental behaviors were measured in both cases. The results are shown in Figure 79.

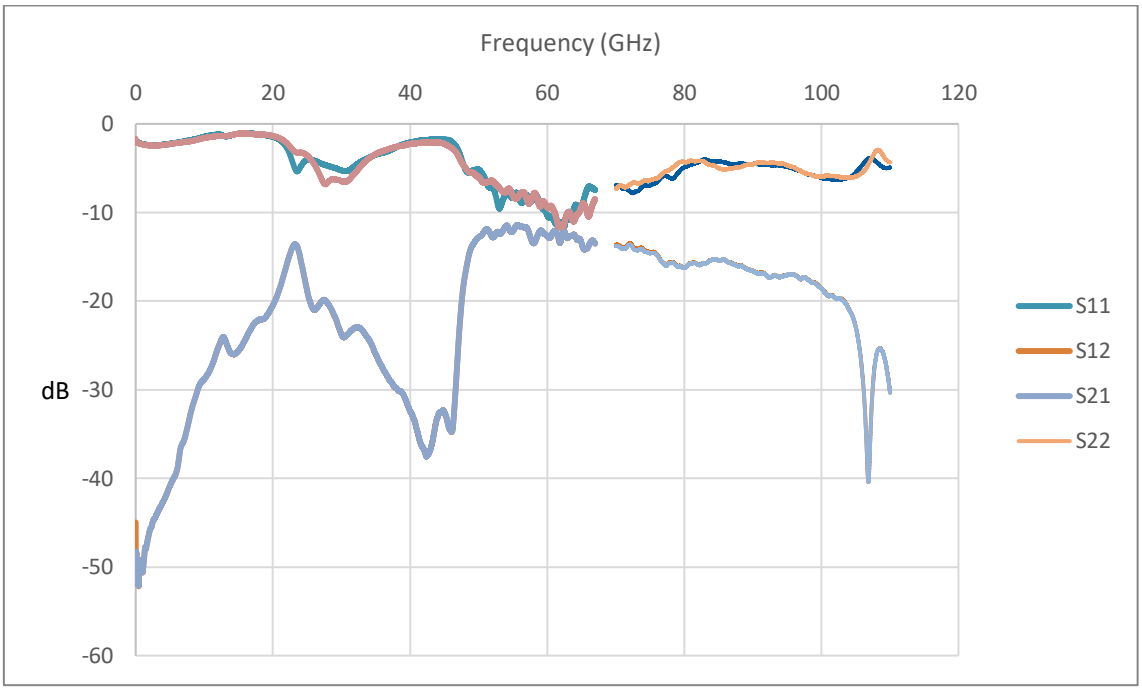

Figure 79 : Measurements of Grenoble's Waveguide in XLIM

We can observe the cutoff frequency around 50 GHz and a behavior in transmission globally similar to the theoretical one , except for the transmission level. This later is around -10 dB at 55 GHz and then slowly decreases with higher frequencies down to -20 dB at 110 GHz. The higher the frequency the more sensitive the mode is to poor contact with the lateral walls. In [160], more measurements are made and analyzed.

To conclude, this type of excitation can be a solution but it remains difficult to fabricate as the measurements show. The losses in transmission are quite high due to delamination of the CNTs on the flexible substrate which induces leakage.

2.4.2. Slot excitation

In this PhD work, we investigated the slot excitation approach to generate the TE10 mode in the WG. It was investigated because it was in adequacy with our final objective, the Butler Matrix. Indeed, we want to excite the array of antennas using slots, in order to gain space. This method is usually used to excite antennas [226]–[228]. The principle is to have a microstrip on one side of a substrate and a slot in the ground plane on the other. We then assemble another substrate on the side of the ground plane with a patch antenna, the new substrate is between the slot and the antenna. The radiating fields through the slot will excite the antenna. The schematic oh this structure is shown in Figure 80, from the original article of D. M. Pozar [226].

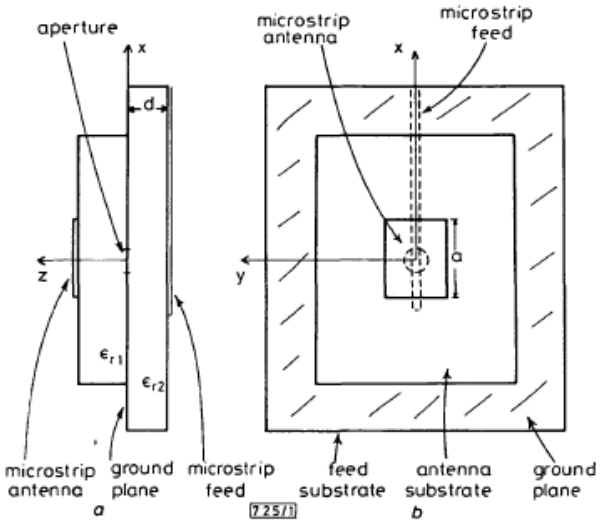

Fig. 1 *Side view (a) and top view (b) of a rectangular microstrip antenna aperture coupled to a microstripline*

Figure 80 : Schematic of the slot excitation [226]

In our case we will consider this approach to excite the TE10 mode in the waveguide, the same way as in [229]. The H-field of the microstrip will leak through the slot and couple with the H-field of the TE10 propagating mode. The principle and design are shown in Figure 81.

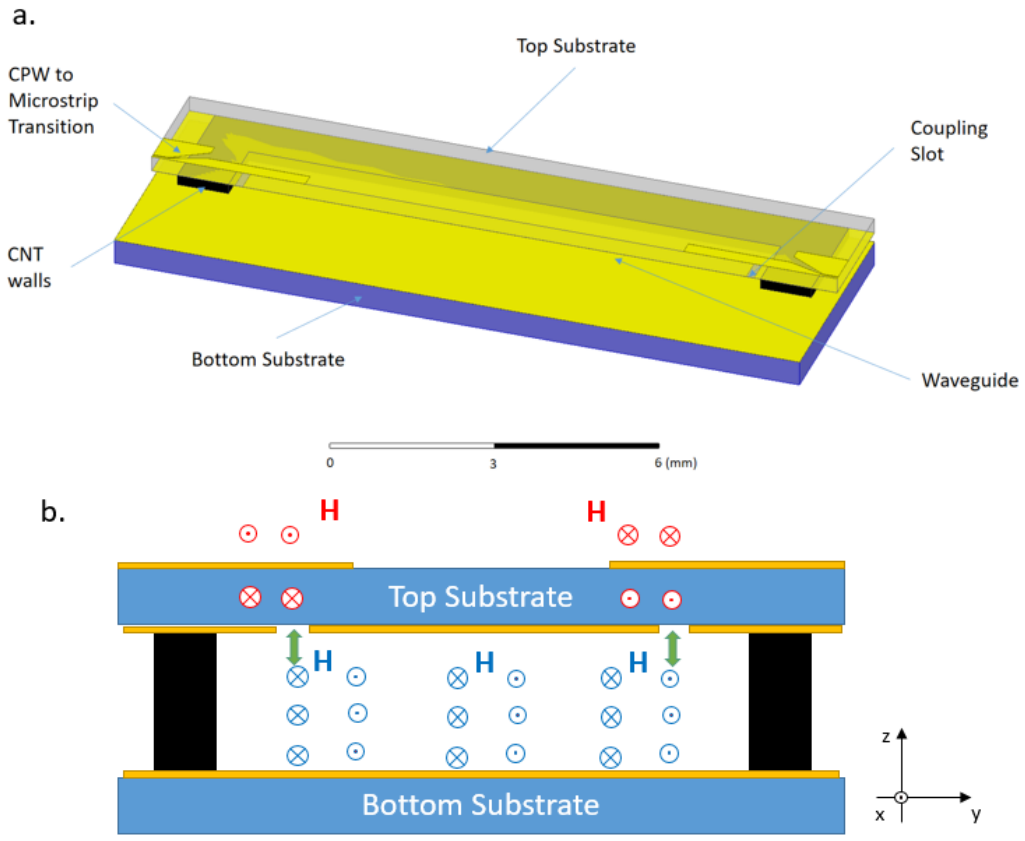

Figure 81 : a. HFSS design of the device (cut in the yz plane), b. Coupling Schematic of the Slot

As we can see on Figure 81.a, a transition from CPW to microstrip is needed in our case. That is due to the fact that we do measurements using GSG probes. To optimize that transition different designs found in the literature were studied [229]–[233], but the best performances were from the design in Figure 82.a.

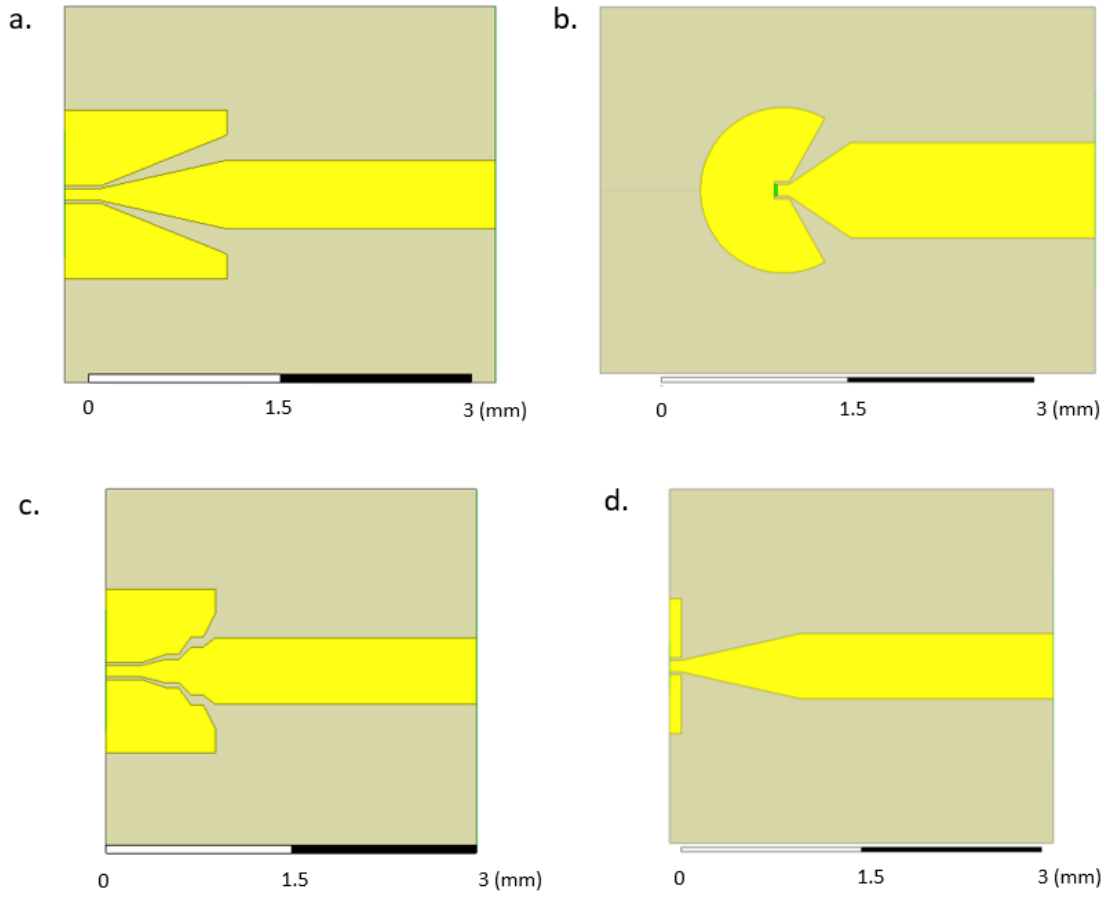

Figure 82 : Different designs for transitions between 50 Ω CPW and Microstrip: a. Linear taper, b. Circular ground [229], c. Steps of 50 Ω intermediary CPW, d. Linear Taper without Lateral Ground Planes

This method was previously investigated by Cometto in [86] but had transmission levels around -5 dB for only one transition (simulation between the CPW input and the middle of the CNT waveguide). We suppose it was due to the use of a silicon substrate for the CPW. Due to its high permittivity compared to the one of air, the propagating medium in the waveguide, the coupling was too low.

We propose to use ROGER 4003 of 254 um thickness, which permittivity is 3.3, as in [229].

The main design rule to follow as a starting point is to place the slot at a distance of $\frac{\lambda_g}{4}$, with λ_g the guided wavelength in the microstrip, of the end of the microstrip line. Since the line is open ended we will have a maximum H-field there. The other parameters, such as the width of the waveguide, its height, the shape and orientation of the of the slot [86], [234]–[236], etc. will play on the adaptation. The best simulated results are shown in Figure 83.

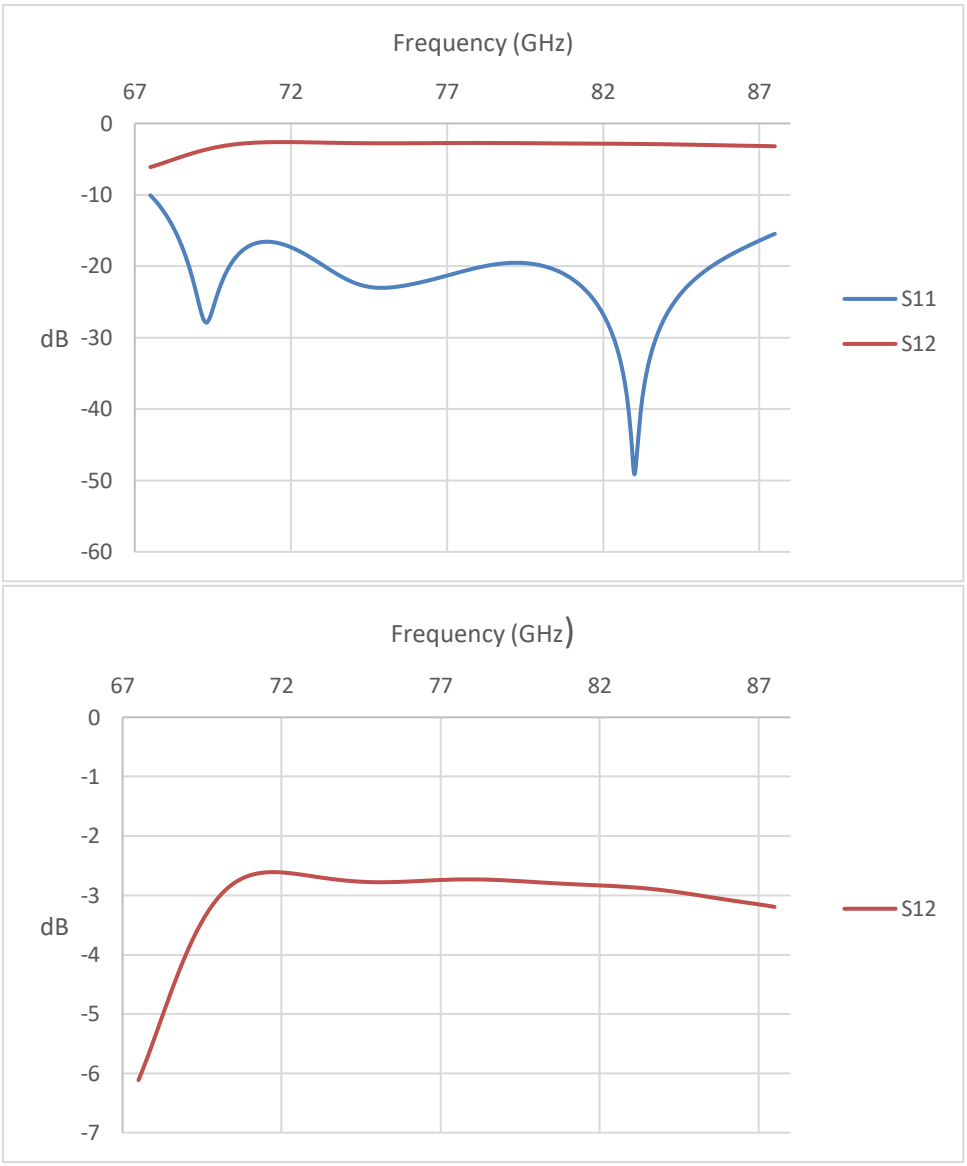

Figure 83 : Above, Transmission and Adaptation, Below, Insertion Losses

As we can see the insertion losses are quite high (around -3 dB) in the 71-86 GHz band (TRiCOT application). Yet the simulations were made without dielectric and metallic losses, which means the losses are due to radiation. Using different shapes of slots one might obtain better results, or as it was shown in [86], by introducing VACNT in the waveguide for slow-wave effect.

To conclude: The simulated performances of this type of excitation are far from as good as the performances (for the different types of slots tested so far) of the shorted CPW line excitation from the previous section. Furthermore, the fabrication process is quite complicated because the substrate has to be etched both on top (for the microstrip and CPW to microstrip transition) and on bottom (for the slot) and alignment is difficult to achieve perfectly. Also, due to the CNTs flexibility, our devices might not be so robust and having to put the probes on top of our devices is another challenge. Finally, the high losses we already witnessed in previous measurements, and the poor performances compared to the simulations of the waveguide with the shorted CPW excitation, did not encourage us to further invest ourselves with this excitation.

Note regarding the Butler Matrix : However, the excitation of the antenna array, should be less difficult (from waveguide to patch antenna). The substrate used for antennas usually have a permittivity of 2.2 for better efficiency[14].

To conclude the study of the different excitation methods described in this section 2.4, the best design is Grenoble's in terms of adaptation and transmission. But unfortunately it is too difficult to fabricate. The flexible substrate cannot be glued to another hard substrate below for reasons we will see in the next section (2.5). The slot excitation was deemed to have too low transmission to be fabricated, but by changing the substrate and the shape of the slot, one might get better results.

2.5. Characterization of the CNTs

Because we had troubles to explain the waveguide experimental S-parameter behavior, it was decided to study a simpler test structure : a rectangular cavity, excited by shorted CPWs. This allows two things: to have simpler designs with simpler backsimulations and analysis of the results; and to have a characterization method for the fabrication process.

From this point on, we will call "equivalent conductivity", the conductivity extracted from the cavity measurements. This conductivity comprises the conductivity of the VACNTs and the contact resistance due to transfer and assembly of the cover. This "equivalent conductivity" depends on the fabrication process, but it can be directly implemented in all the air-filled designs of the BM (waveguide, coupler, crossover) simulations. For cavities fabricated differently but with the same CNTs, we can obtain different values. These cavities allow to characterize in their whole (CNT quality, transfer quality, assembly quality) the fabrication processes, the higher the "equivalent conductivity", the better the fabrication process

The structure is presented below, in Figure 84. It is a rectangular cavity in all points similar to the previously shown waveguides, except for the excitation. As we want to extract from measurement the unloaded Q factor of the cavity, we don't need strong input/output coupling to generate resonance modes. Then, the cavity is excited using shorted CPW lines.

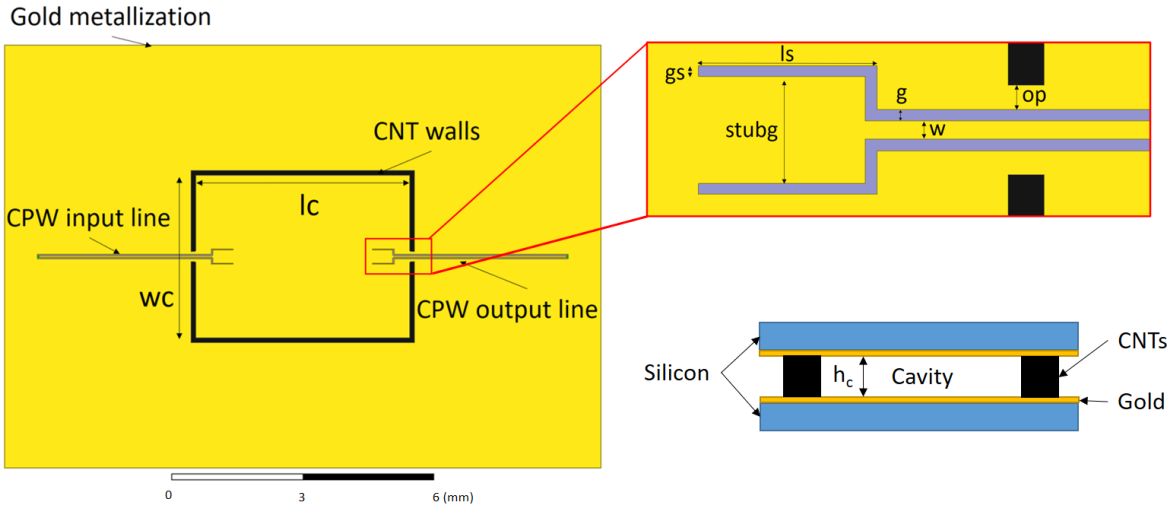

[14] The energy stored in the substrate is equal to $\frac{1}{2}\iiint \varepsilon \boldsymbol{E}\boldsymbol{E}^{*} dV$ [237]

Figure 84 : Design of the cavities

A table with all the dimensions of the cavity is given below.

Table 4: List of dimensions of the cavity

Parameters	wc	lc	op	w	g	gs	ls	stubg	hc
Dimensions (um)	3730	4970	67	50	33	30	50	300	500

With such dimensions (and a density of CNTs equal to 10^{15} CNTs/m^2) the resonant frequency is around 50 GHz, and the S21 around -10 dB at the peak, in order to determine the unloaded Q factor (by neglecting the external Q factor) . The excited mode is the TE101, we chose this mode because the electric field is aligned with the CNTs just as in the waveguide. The conductivity we determine is thus the one in the direction of the CNTs axis. If we wanted to determine the lateral conductivity we would have excited a TM mode, for which the currents are perpendicular to the CNTs.

The simulations for different CNT densities while keeping the same dimensions for the CPW input /output accesses show that the S-parameter are modified. That implies that the Q factor of the cavity varies. This is what was expected as the density determines the conductivity of the CNT wall. The S-parameters are shown in Figure 85.

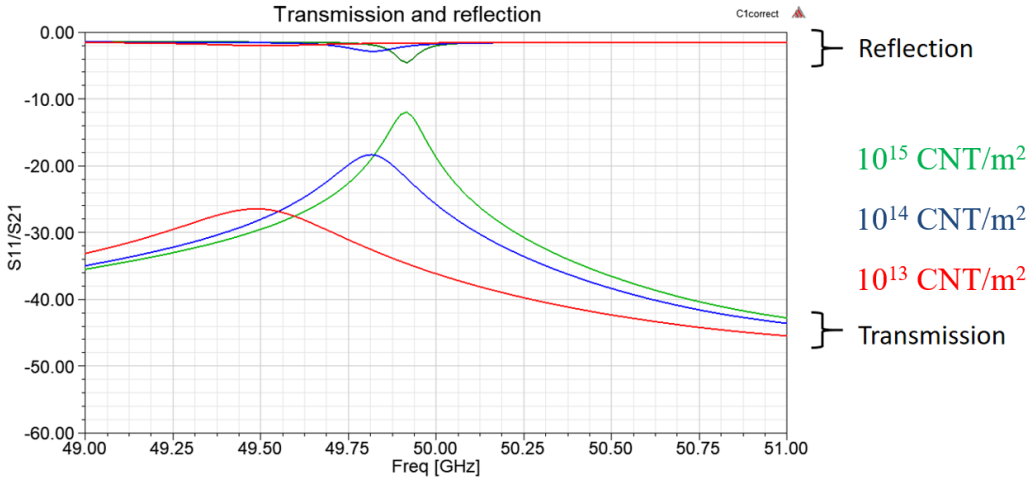

Figure 85 : Simulated S-parameters for different densities of CNTs in the lateral walls

The different unloaded quality factors are listed in the Table below.

Table 5: Quality Factors of the cavity for different CNT densities (Height of cavity is 500um)

CNT Density (CNTs/ m^2)	1e13	1e14	1e15

Unloaded Quality Factor	113	400	675

We now have a way to characterize the CNTs. Yet, one can argue that when we fabricate the cavities, depending on the contact resistance created by the transfer process or the closing of the cavity, we will have different quality factors, as explained earlier. That much is true. However, if we bear in mind that our objective is the interposer, or at least the waveguide, such a characterization is what we want. We characterize as a whole, the fabrication process and the CNTs.

Cavities were fabricated but we failed to see any obvious resonance at 50 GHz, as shown in Figure 86.

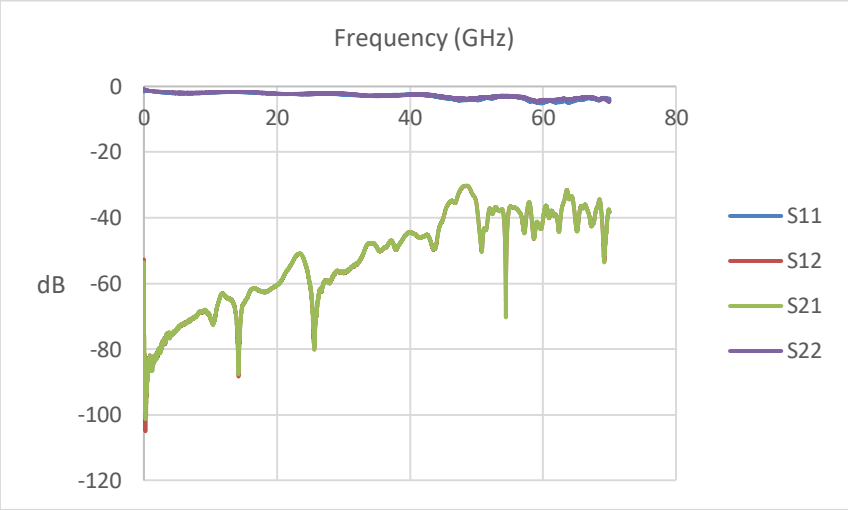

Figure 86 : Measured S-parameters of the cavity

We now need to come back a bit on an important point that was not mentioned until now. While we were measuring the devices, instead of placing them directly on the metallic chuck of the probe station, we would usually place an absorbent between the device and the chuck (in orange), as shown in Figure 87. This was done because it was observed, experimentally, that the measured S-parameters were less noisy., It was strange because the substrate we used was 500 um thick and the fields of a CPW are concentrated near the surface. The substrate was supposed to be big enough to isolate from the chuck. We thought it was due to the silicon being slightly conductive and interacting with the chuck.

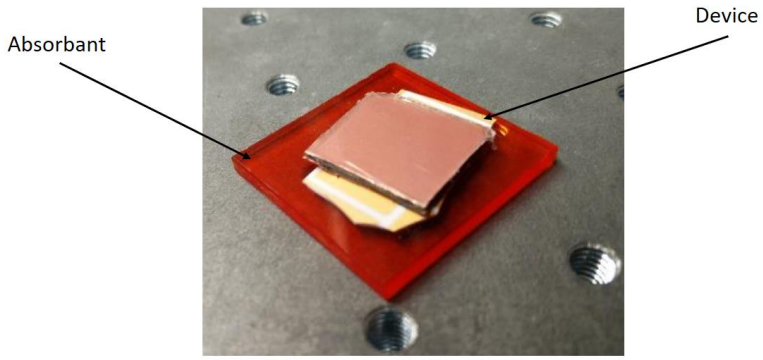

Figure 87 : Photo of a device with the absorbent below [86]

Meanwhile a cavity was being fabricated by the III-V lab. The cavity was fabricated using the process from 2.3.2, with silver glue all over the cover. An X-ray image of the cavity was taken to check the quality of the walls between the two silicon substrates in Figure 88.

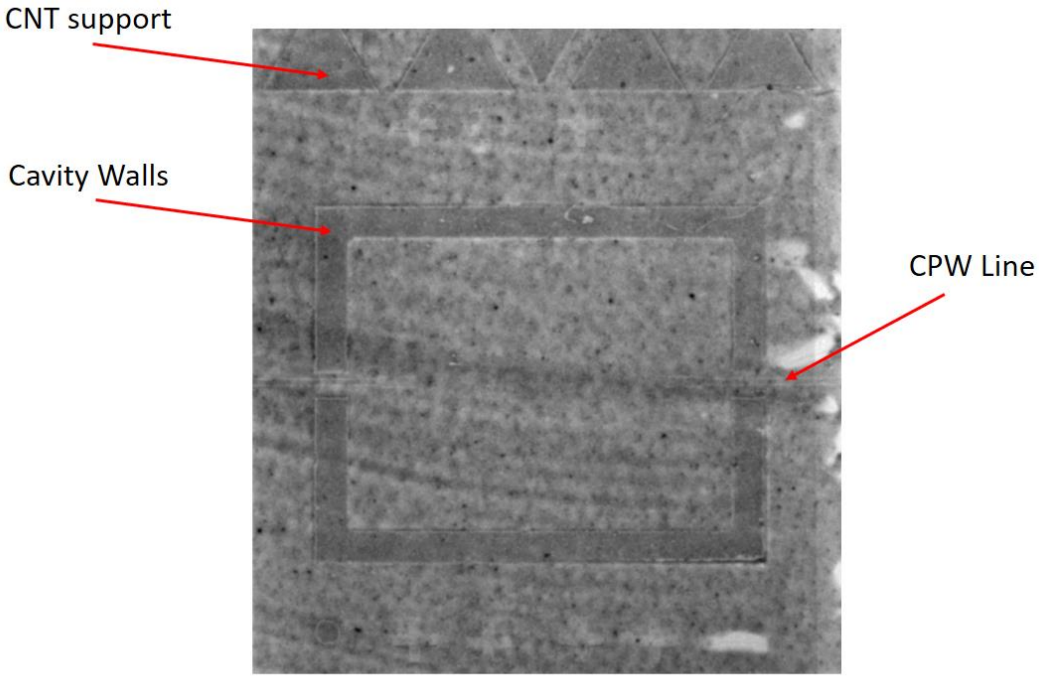

Figure 88 : X-ray image of the assembled cavity

Our partners measured it and were not able to measure any resonance, without absorbent (Figure 87). Then new measurements were done with several absorbents and, finally, they obtained the results from Figure 89.

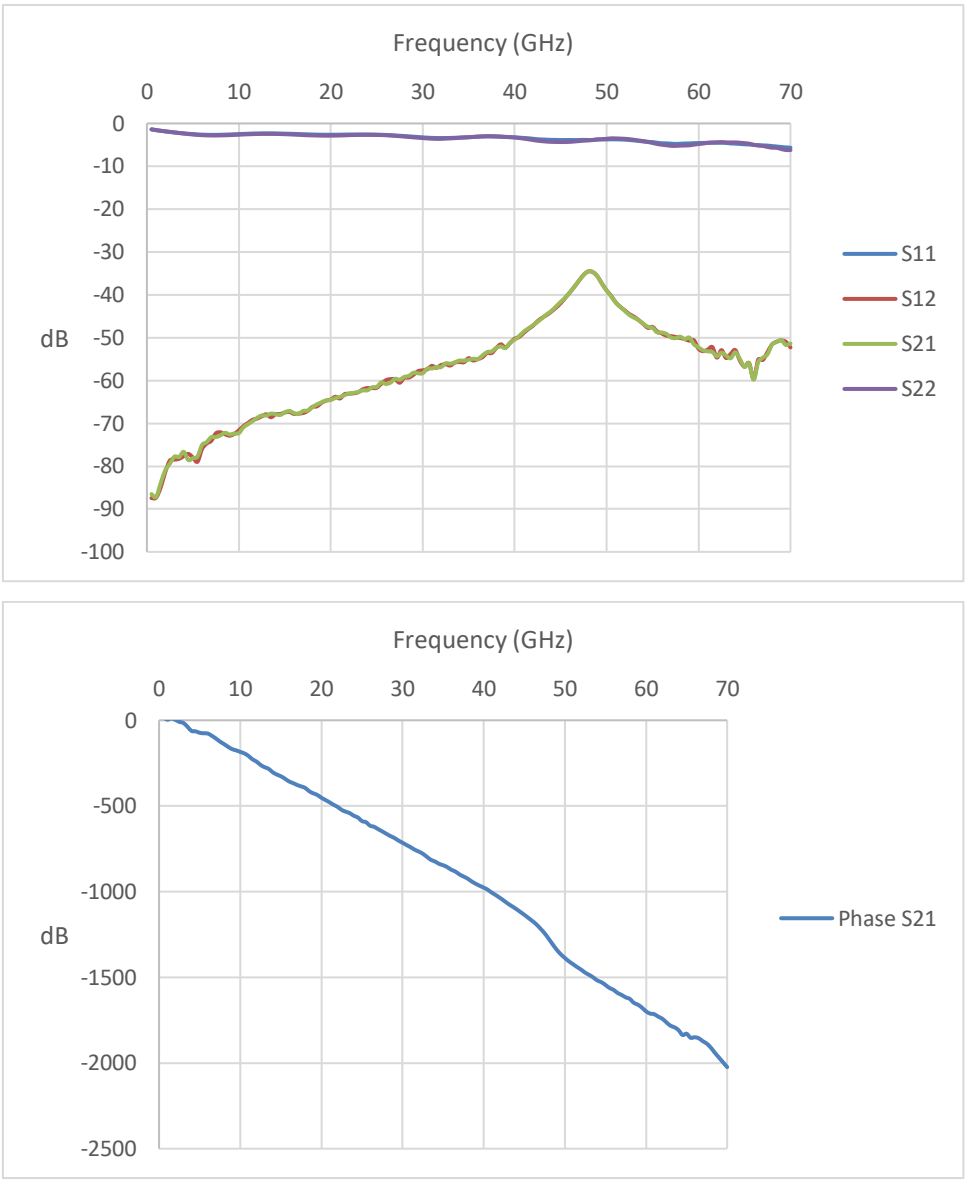

Figure 89 : Above, S-parameters of the cavity measured in III-V lab, Below, Phase of S21 with the inflexion point at the resonant frequency

The different “absorbents” tried are shown in Figure 90, they consist of anti-electrostatic discharge plastic boxes for active devices.

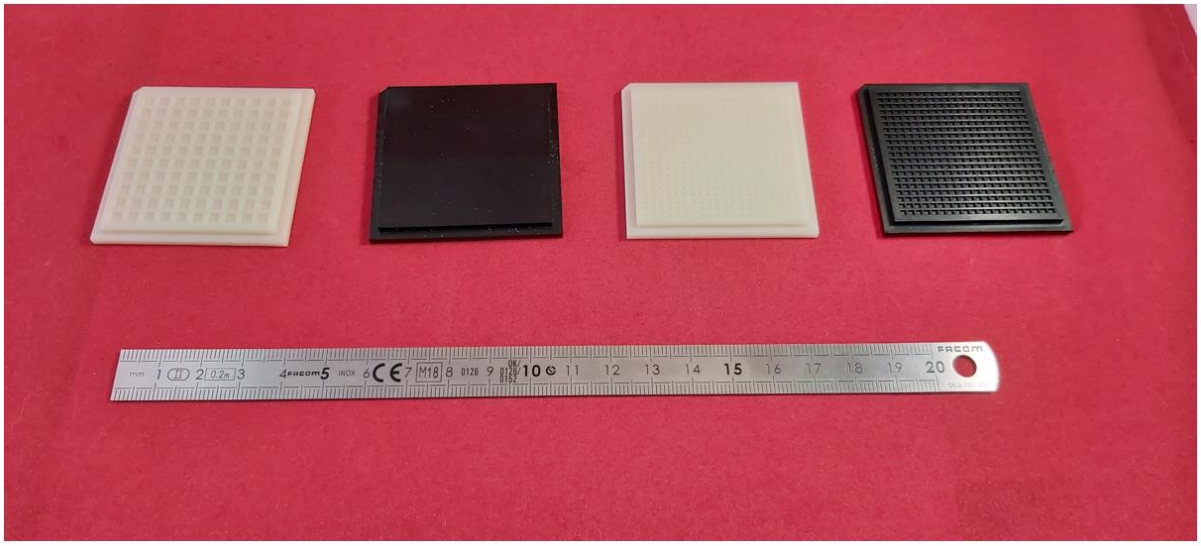

Figure 90 : Anti-Electrostatic Discharge boxes used as absorbents

These measurements were also confirmed in XLIM for the same cavity with the same absorbent, and with another RF high frequency absorbent (datasheet in Appendix 3), though the response is not as clean, probably due to transportation, Figure 91.

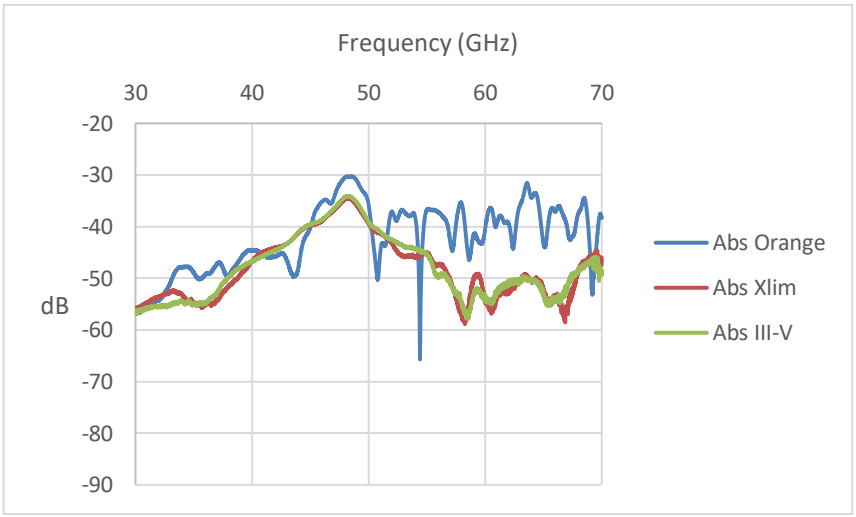

Figure 91 : Measured Transmissions (S21) of the cavity with different absorbents, the orange one from figure 76, III-V lab absorbent (plastic box) and MF-117 from XLIM

The measured quality factor of the cavity is 17. However, the cavity height was measured to be 110 um, the thickness of the glue layer was taken at 30 um and the data sheet of the MF-117 absorbent was used (Appendix 3). This back-simulation gave us a density of $7e^{12}$ CNTs/m^2, Figure 86. Let us note we characterize the fabrication process too (with the defects due to the contact resistance and others) and that the density of the VACNTs is probably higher.

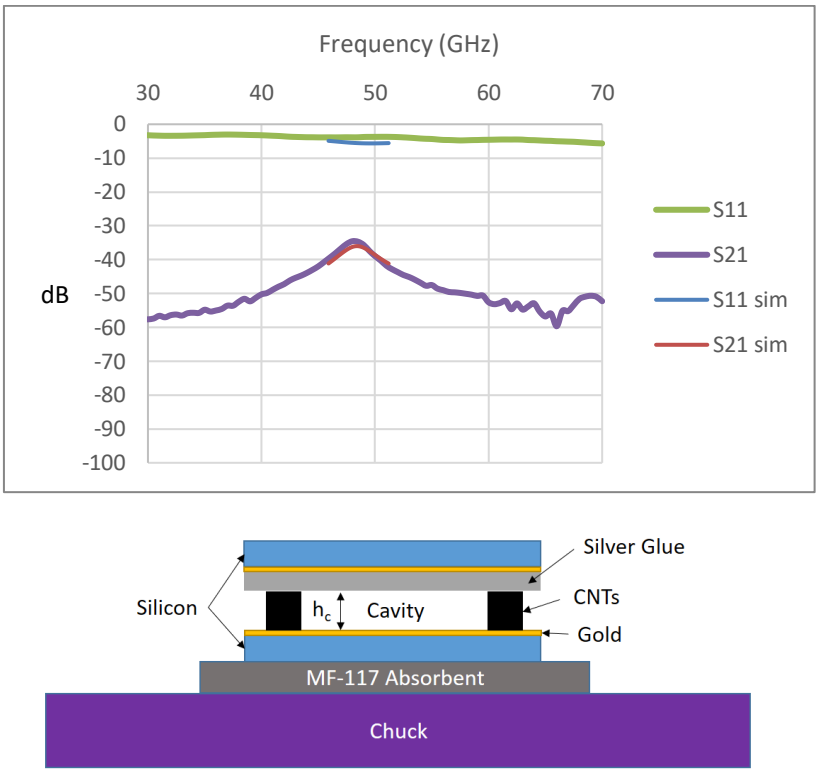

Figure 92 : Top, 3D EM Backsimulation of the Cavity, Bottom, Schematic cross-section of the cavity

That study on a resonant cavity permits to

- Validate the theoretical approach according to the agreement between EM simulations and measurements
- Estimate the properties of the transferred CNTs and CNTs bundle , we are considering
- Validate the transfer process, even if it has to be improved

We also noticed that the absorbent decreased transmission (during back-simulations), which prompted us to analyze the effect of the absorbent on the waveguide simulations.

We decided to redo all the 3D EM simulations of the WG with the different boundary conditions below the substrate. Until now, all the simulations by HFSS were made within an air box, which faces, distant of lambda/4 from every edge of the device, acted as a radiation boundary. It meant the device was surrounded by air in all directions.

The waveguide we simulated is shown in Figure 93, its cutoff frequency is at 25 GHz. We lowered the working frequency for faster simulations.

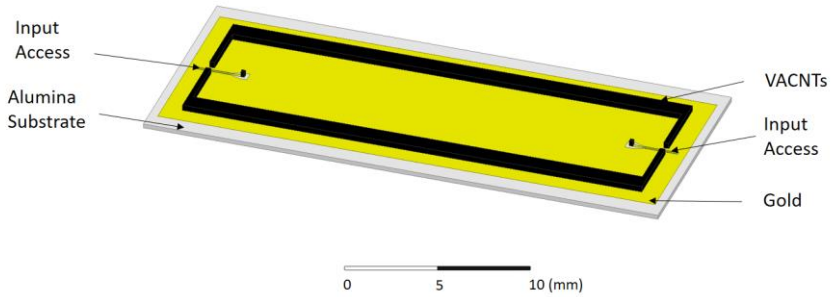

Figure 93 : Waveguide with a 25 GHz cutoff, cover made of gold on silicon is transparent

We consider three boundary conditions (Figure 94):

- In the first case, we place a Perfect Electric Conductor (PEC) boundary condition on the airbox face in contact with the bottom face of the substrate, equivalent to the chuck
- The second case is the one where air is surrounding the device (paragraph above),
- and the last one is the simulation of the measurement setup with the absorbent between the device and the chuck (PEC boundary condition on the bottom face of the absorbent).

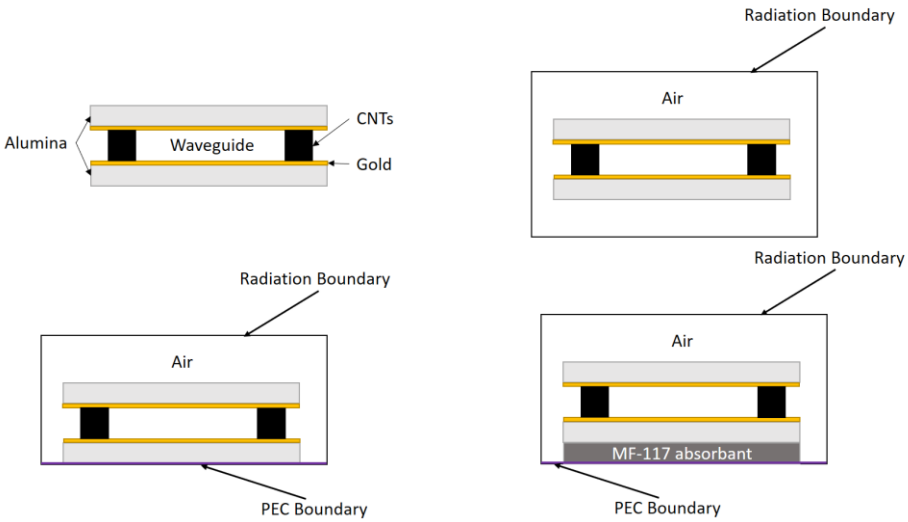

Figure 94 : Different simulation setups

The results of the simulations are plotted in Figure 95.

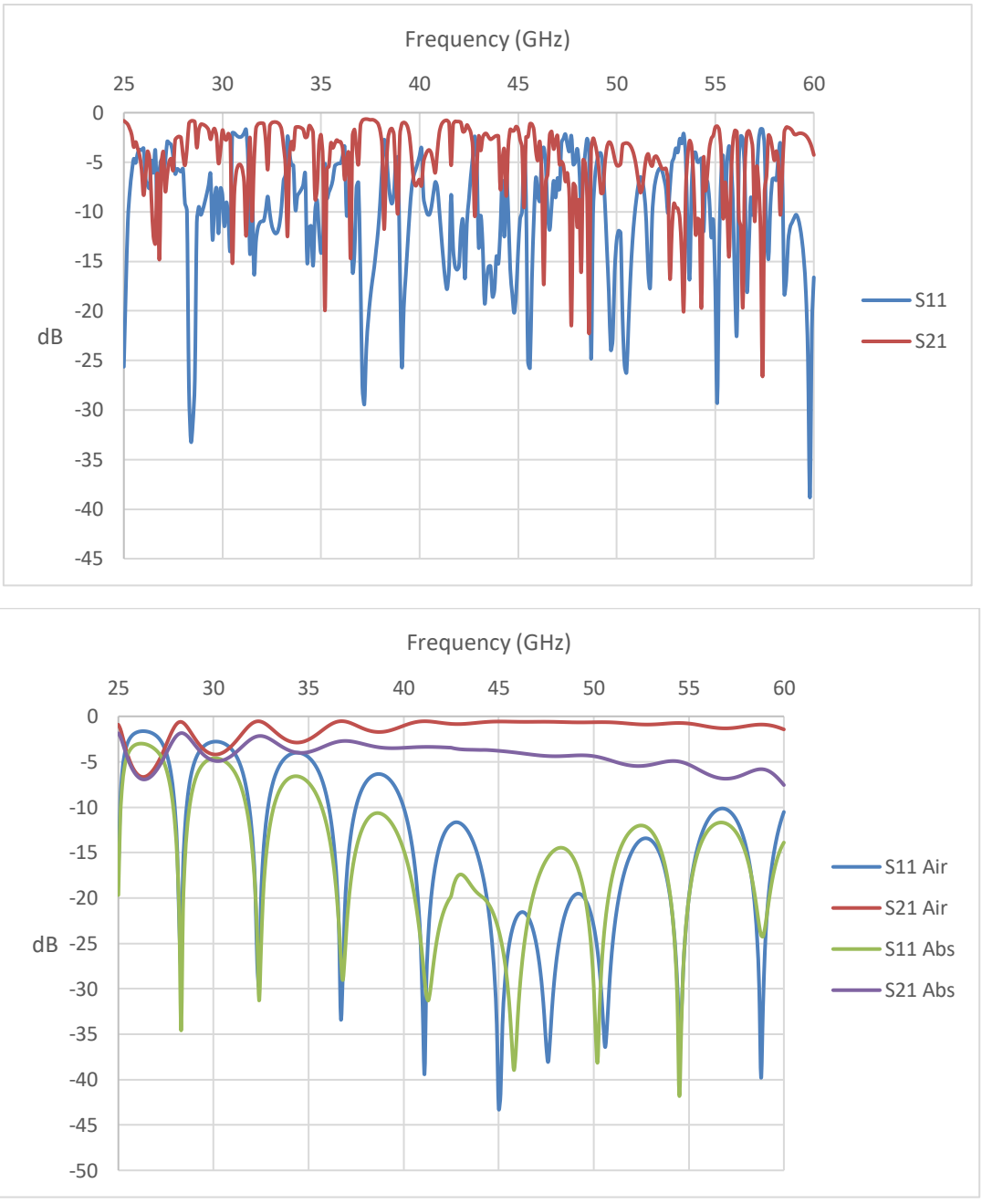

Figure 95 : Above, Simulated S parameters with a ground Plane, Below, Simulated S-parameters with the MF-117 absorbent and air underneath

We notice two things:

- it is not possible to place our device directly on a ground plane without degrading greatly the performances because of parasitic modes in the substrate,
- and, the use of an absorbent, while eliminating the parasitic modes, decreases the transmission levels from 1dB to 5 dB.

Furthermore, the simulations for the waveguide which cutoff is at 50 GHz, were done again, with stronger convergence conditions in terms of EM simulation and it appears that substrate parasitic modes start propagating after 80 GHz, as shown in Figure 96.

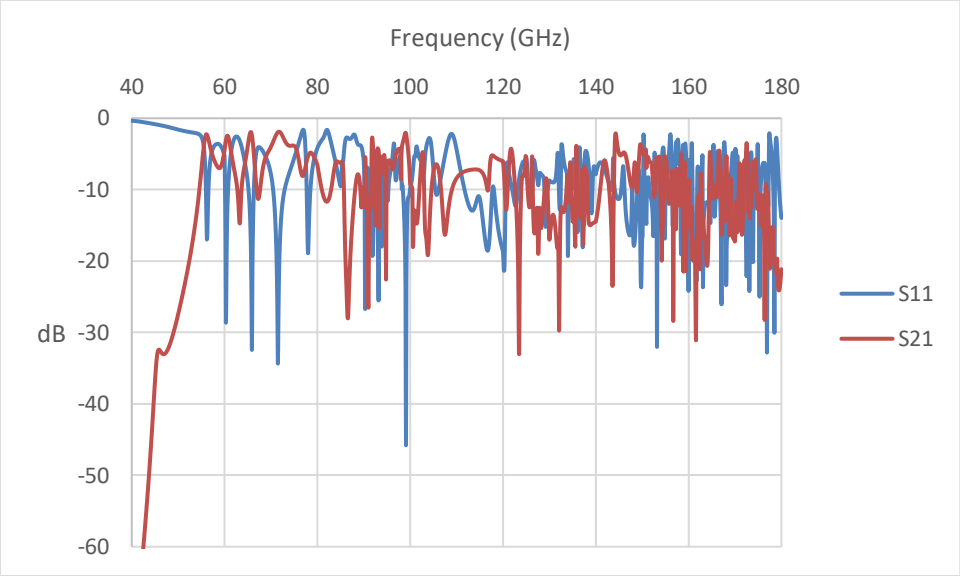

Figure 96 : Waveguide Simulations with Substrate Modes appearing after 80 GHz (Air Below)

At this point, it is important to note that all the measurements presented in section 2.3 were done using the RF absorbent from XLIM for cleaner results, though it has not been said earlier. The measurements made on the orange absorbent were not as clean. It does not change the conclusions about the fabrication processes because the transmission levels remained at the same levels.

Still, as we have seen in simulations, the use of an absorbent greatly decreases the transmission levels measured (Figure 95). In order to check that the transmission levels around -15 dB that we measured in section 2.3 are not due to the absorbent, we decided to do the following experiment. We hoped to gain a few dBs, but at -15 dB the difference is les flagrant as we will see. Measurements of a new waveguide (H20E all over the cover) with Rohacell between the bottom substrate and chuck were made Figure 97. Rohacell having a permittivity similar to air, the idea was to have a measurement setup close to the simulation design with air all around (Figure 94). However, the transmission levels do not increase, since we are already as low as -15 dB. The measurements are a bit more noisy using Rohacell, probably due to the fact that at these frequencies its permittivity is not quite exactly of one.

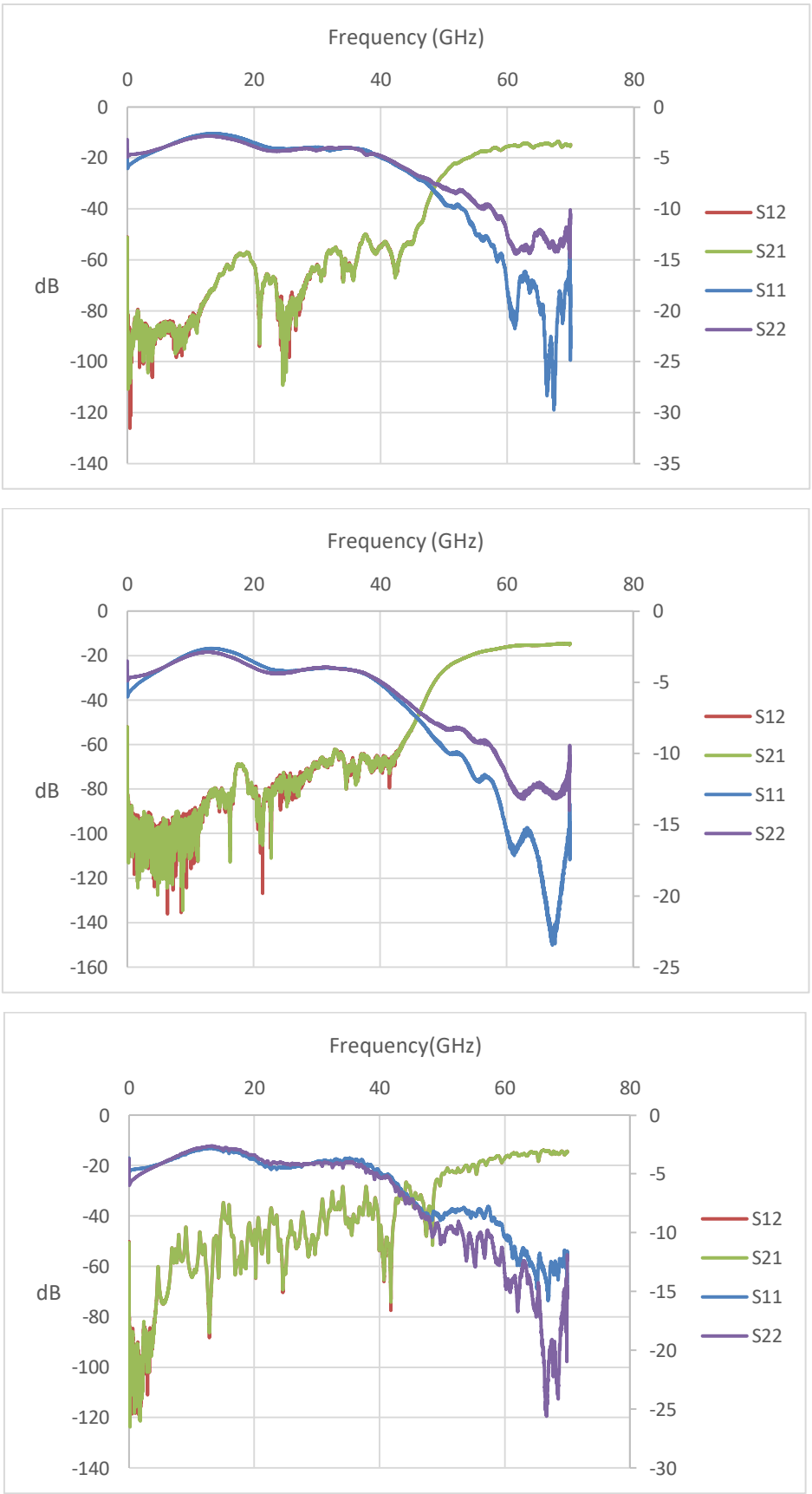

Figure 97 : Above, Measurements of the waveguide on Rohacell, Below, Measurements of the waveguide on the absorbent, Below, Measurements of the waveguide on the chuck

To conclude and summarize:

- Our initial guess that with a substrate thick enough, we would not have parasitic modes in the substrate because the fields of a CPW are concentrated on the surface was proven to be wrong. Because there are discontinuities in the input/output lines (excitation) we have to compare the thickness of the substrate to the wavelength in silicon $\lambda_{\mathrm{silicon}}=\frac{\mathrm{c}}{\sqrt{\varepsilon_{\mathrm{r}}}\mathrm{f}}\simeq 1\ \mathrm{mm}$, at 90 GHz. If we do not want substrate modes to appear the thickness should be below $\frac{\lambda_{silicon}}{8}\simeq 125\ um$.
- The use of an absorbent below the substrate decreases the transmission levels greatly, and is not a viable solution, as it adds a layer to the mm-wave package.
- Elevating the bottom substrate on the sides so that it is above air is a complicated process (layer of air between motherboard and package), and works only for frequencies up to 70 GHz.
- The CNTs along with the transfer process using H20E glue were characterized and we found an equivalent density of $7e^{12}$ CNTs/m^2 or a conductivity of $5.6*10^3$ at 50 GHz.

On Grenoble side, simulations were made using air below the substrate as a boundary condition. This was probably due to the fact that they planned to measure their devices on a special foam [160] due to its fragility. However, when doing the simulations with a ground plane substrate modes appeared meaning this design is difficult to implement for the interposer application (Figure 46).

That is why we decided to change the design of the waveguide, so as to avoid substrate modes. Because the “equivalent conductivity” of the “CNTs and H20E glue assembly” was found to be $5.6*10^3$ S/m, the fabrication process will also be changed.

2.6. New waveguide design without substrate modes

2.6.1. Design of the devices

To avoid substrate modes and dependence on the bottom substrate boundary condition, it was decided to use grounded CPW. Four designs were simulated:

- two pillar excited waveguides (Air-Filled SIW) of different lengths to extract their intrinsic properties with VACNT lateral walls in the band 81-86 GHz
- a cavity resonating at 50 GHz to characterize the fabrication process
- a cavity resonating at 80 GHz to characterize the fabrication process closer to our target band (81 to 86 GHz)

We decided to use pillar excited waveguides for different reasons: it will allow to see if such an excitation is possible; it will show the minimal size limit is now smaller with the new fabrication process (II.6.2); it was a design we were more familiar with in XLIM.

Should one want to try to do RFIC lab excitation method with vias, it should be possible, and a wider bandwidth would be achieved.

In the event the waveguides do not work, the process will still be characterized using the cavities (no pillars).

In order not to have substrate modes, vias were used around the CPW accesses and pillar. The design rule is to have no resonating structures with length lower than $\frac{\lambda_{substrate}}{8}$, it is usually approximated by a distance between the vias below $\frac{\lambda_{substrate}}{8}$. The waveguide structure is shown in Figure 98.

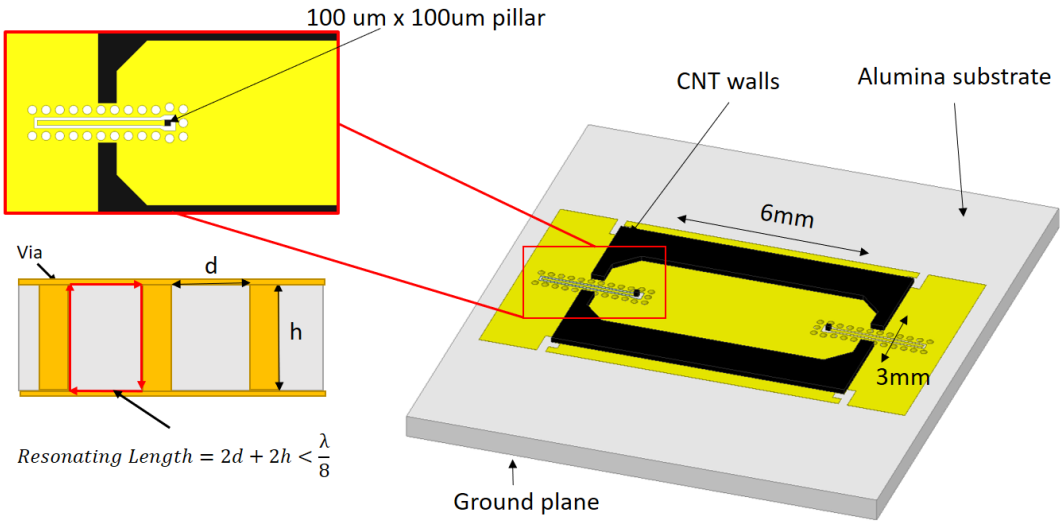

Figure 98 : Design of the waveguide

The design was made with a bottom substrate of alumina with a thickness of 254 um, the vias have a diameter of 150 um. We are at the lower limit of the fabricant's capabilities (Thin Film Products). The vias will be conic and might touch each other on the ground plane, but that is not a problem in our case. The height of the waveguide is 110 um for optimal performances. The input/output pillars' base are squares with 100um side. The simulated S-parameters for two lengths, 6 mm and 6.9 mm, are shown in Figure 99.

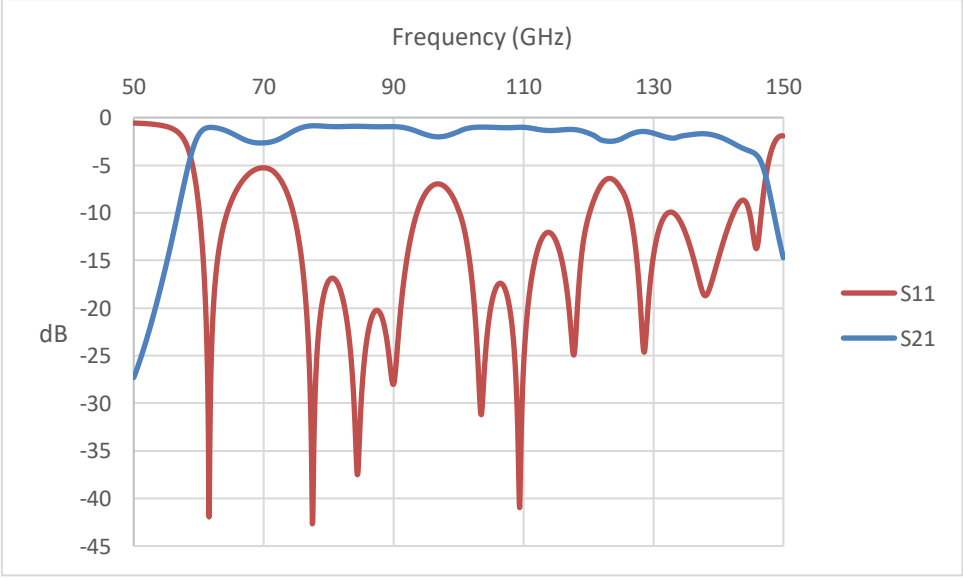

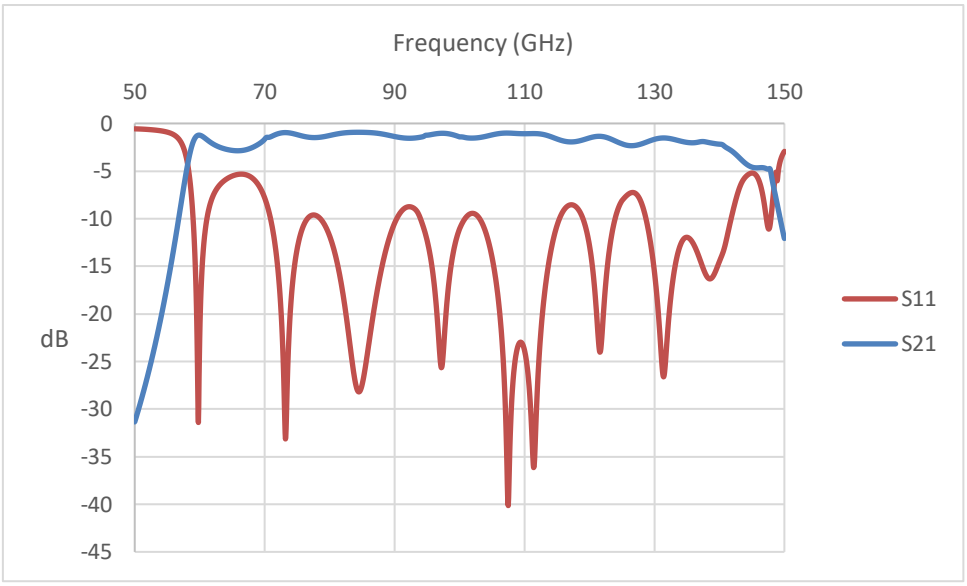

Figure 99 : Above, Simulated S-parameters for the 6 mm waveguide, Below, for the 6.9 mm

The adaptation for both lengths is below 15 dB in the target band: 81-86 GHz, the insertion losses are around -1 dB. The two lengths allow to extract the intrinsic properties of the waveguide using a simple Thru-Line calibration (Appendix 2).

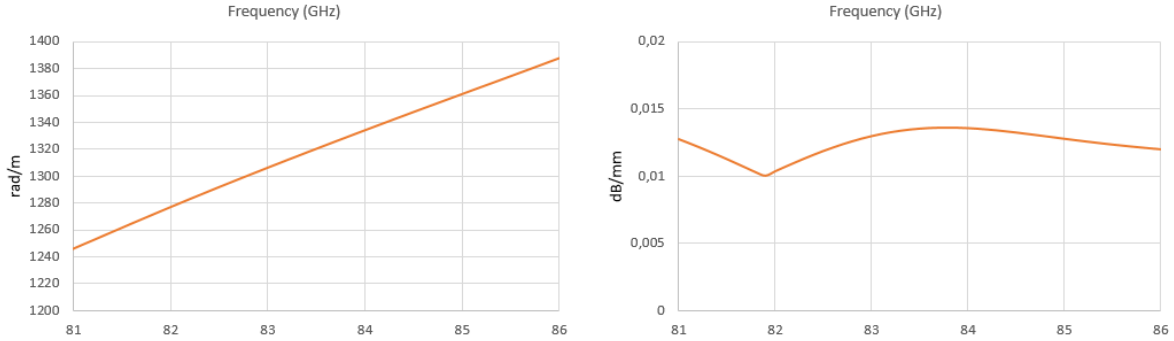

Figure 100 : Extracted Beta (Left) and Alpha (Right) in the 81-86 GHz band

We find a propagation constant of approximately 1320 rad/m at 83.5 GHz, and an attenuation constant of 0.012 dB/mm. We can note that we find very similar values than the ones extracted from the shorted-CPW design in Figure 77. This is logic because; we simulated our waveguides with the same parameters, in the end, the “intrinsic waveguide” (without the transmission) is the same.

However, we can say their transition has better performances, wider bandwidth, lower insertion losses (0.5 dB instead of 1 dB for us), and better adaptation. This is partly explained by the CNT pillar (only 10^5 S/m).

Two cavities were also designed at 50 GHz (3.7 mm width, 5 mm length and 0.5 mm height) and 80 GHz (2.4 mm width, 2.86 mm length and 0.5 mm height). The designs and simulated S-parameters are shown in Figure 101.

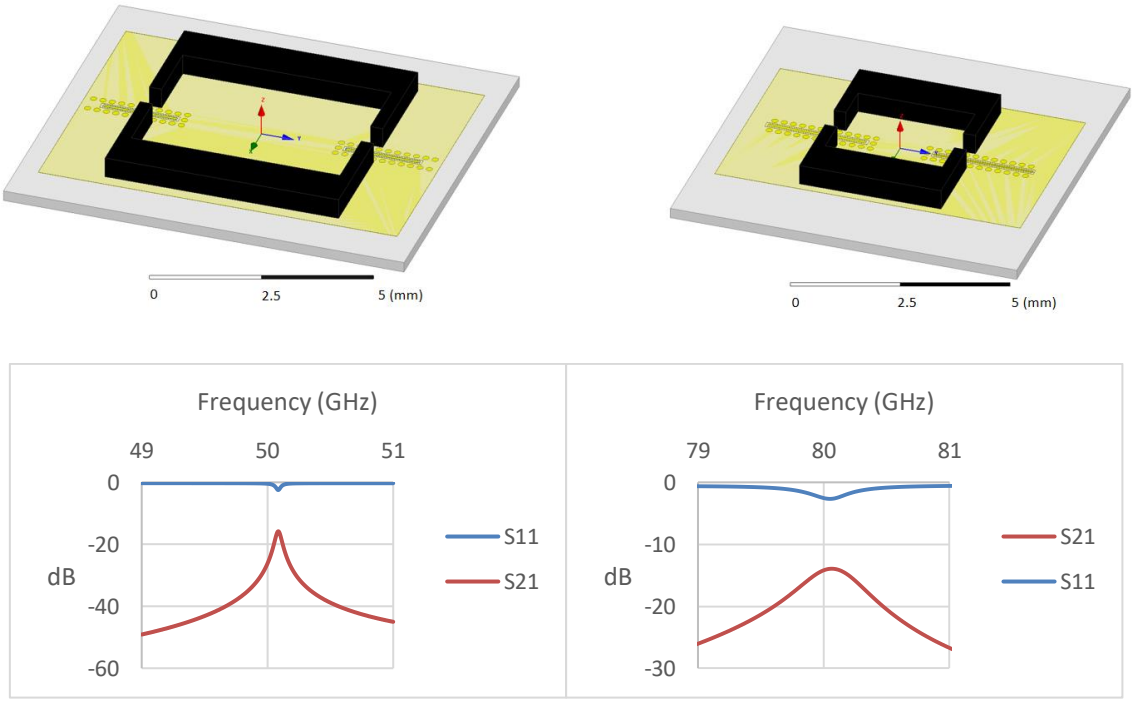

Figure 101 : Design of the 50 GHz and 80 GHz associated with their simulated S-parameters

The same process of measurements and backsimulations explained in section 2.5, can be used with these new cavities. The cavities have been simulated with a height of 500 um. During fabrication 500 um thick spacers will be used.

2.6.2. Fabrication process

The fabrication process (CNTs, transfer and assembly) was characterized and we found that the equivalent conductivity was not high enough for acceptable performances. After several discussions with CINTRA, we decided to change the fabrication process. The fabrication process is described in Figure 102.

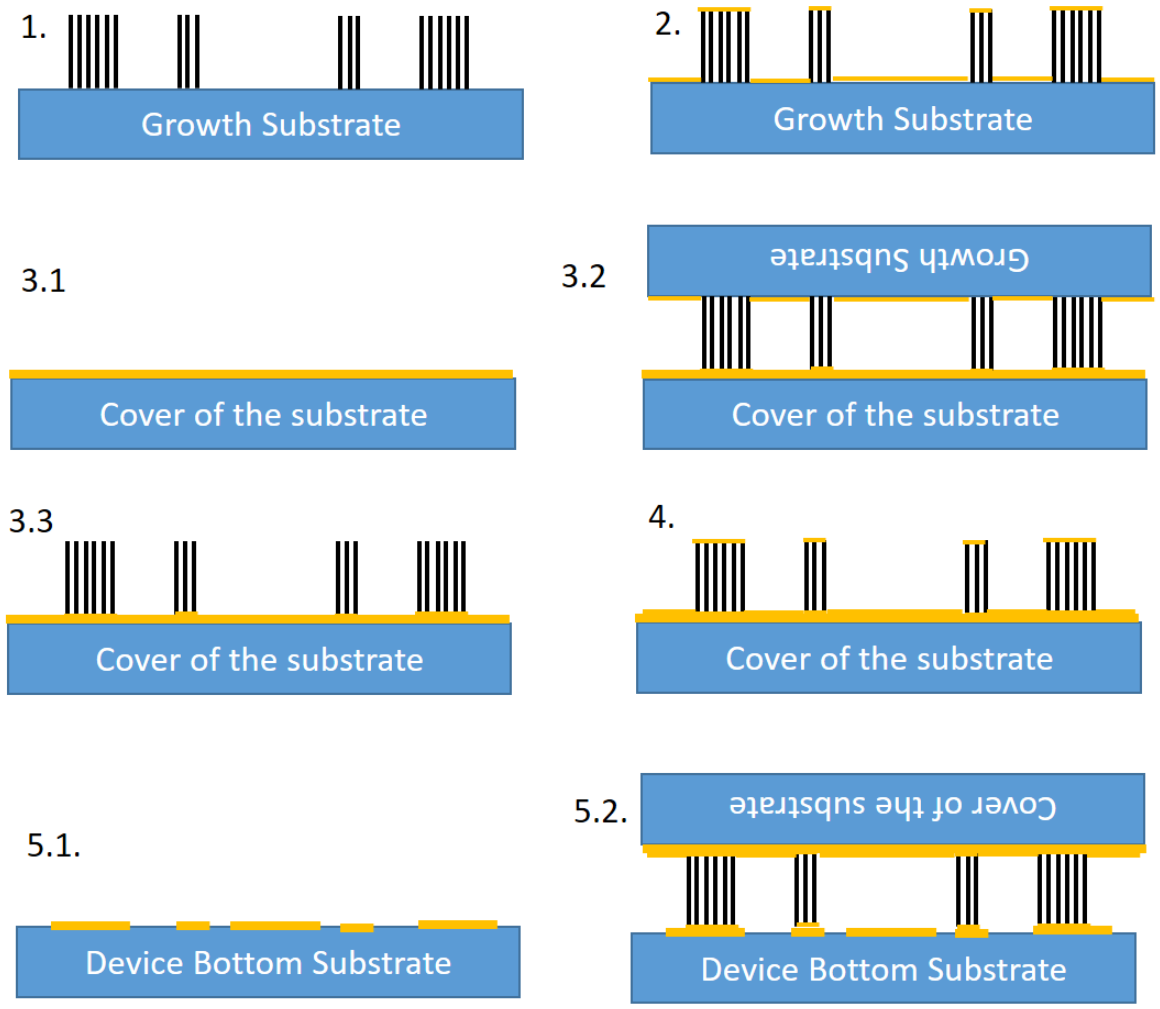

Figure 102 : Fabrication Process for the new devices, Left to Right top to bottom in order

Step by step, the process is as follows:

Step 1: The CNTs are grown on a separate substrate using pre-patterning of the catalyst so as to have the shapes of the pillar and walls. The resolution of the grown patterns is as low as the classical photolithography processes allow it. Thus allowing for pillars 100x100 um where we were limited to 200x200 um with a shadow mask.

Step 2: The substrate with the patterned CNTs is totally covered with a layer of gold using E-beam.

Step 3: The patterned CNTs are transferred on the cover using gold to gold bonding.

Step 4: The transferred CNTs on the cover and the cover are totally covered with a layer of gold using E-beam. There are no particular shapes with gaps on the cover that we could short circuit.

Step 5: The cover with the transferred CNTs covered in gold is flipped onto the bottom part of our device and gold to gold bonded. (110 um spacers are used)

This process allows for theoretical overall better conductivity of our devices since only gold is used and no H20E glue. The fabrication process for the cavities is the same.

2.6.3. Measurements

Two long and two short waveguides have been manufactured in CINTRA, and were measured in XLIM (10 MHz-67 GHz and 75 GHz-110GHz bands). The measurements are shown in Figure 103.

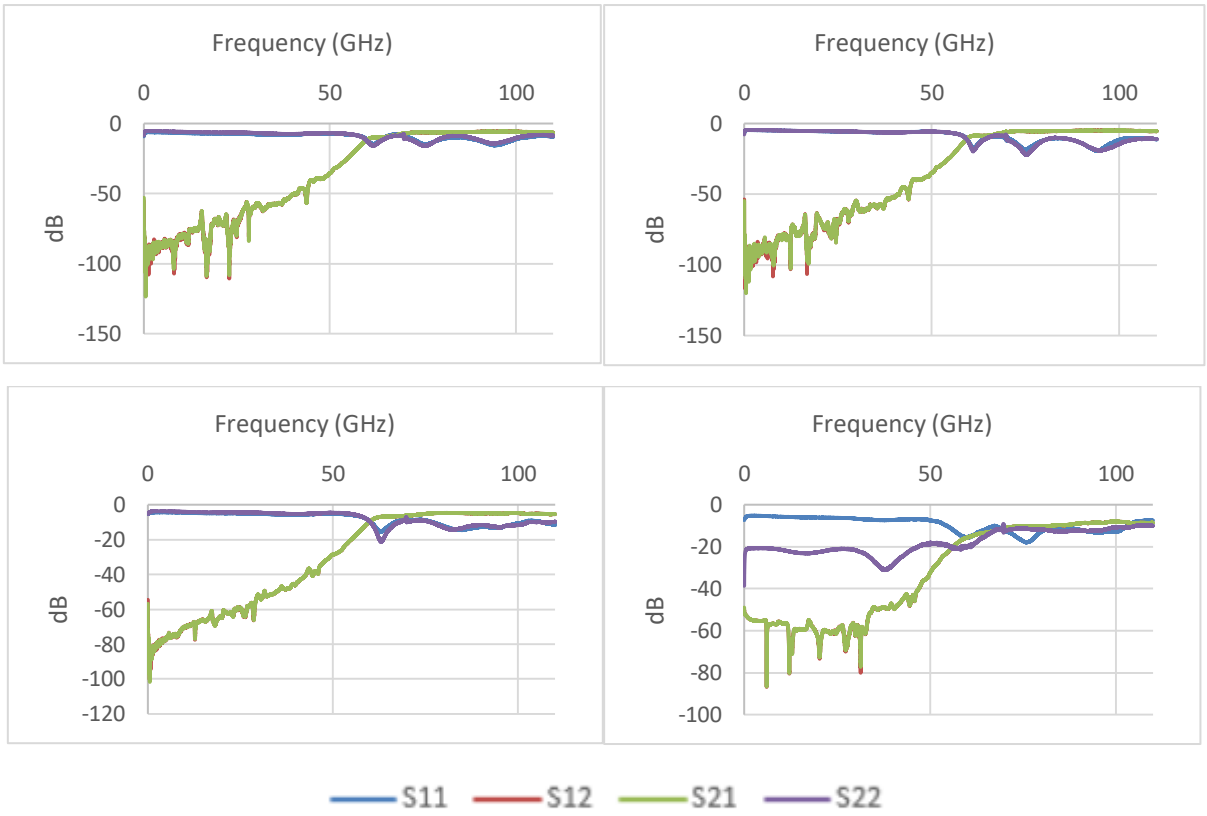

Figure 103 : On the top, Measurements for the long waveguides, On the bottom, Measurements for the short waveguides

As we can see, the transmission levels are much higher than with the previous designs. Of the four devices, only the second short waveguide (bottom right) has insertion losses similar to previous designs (around -10 dB). It is probably due to bending of the pillar on access 2, that was reported by CINTRA during the fabrication process.

In the targeted band 81-86 GHz band, S21 are now close to -5 dB in average. The return loss, is around -10 dB. The transmission and adaptation, in the 40-110 GHz band, are plotted on separate graphs in Figure 104, for the “top right” and “bottom left” measurements (second long waveguide and first short waveguide).

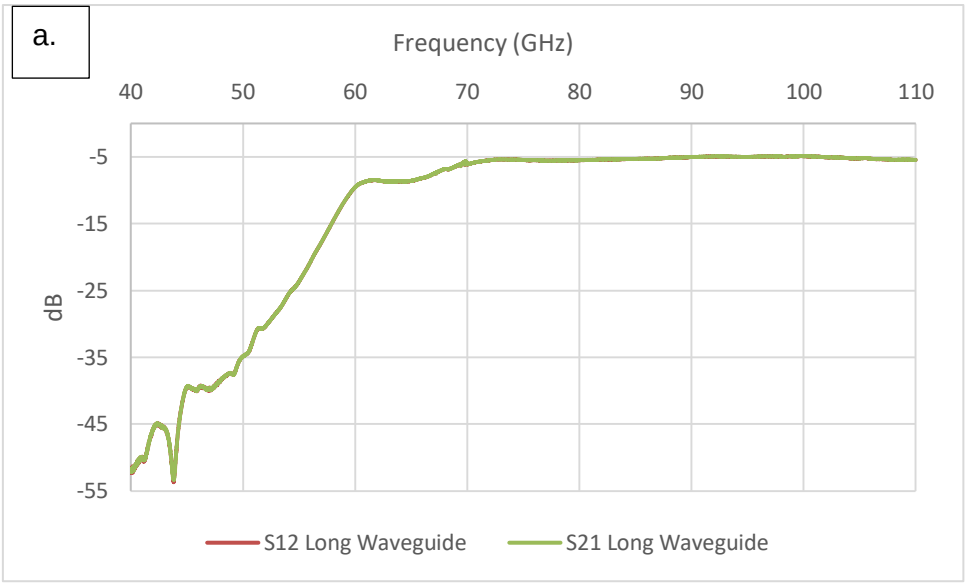

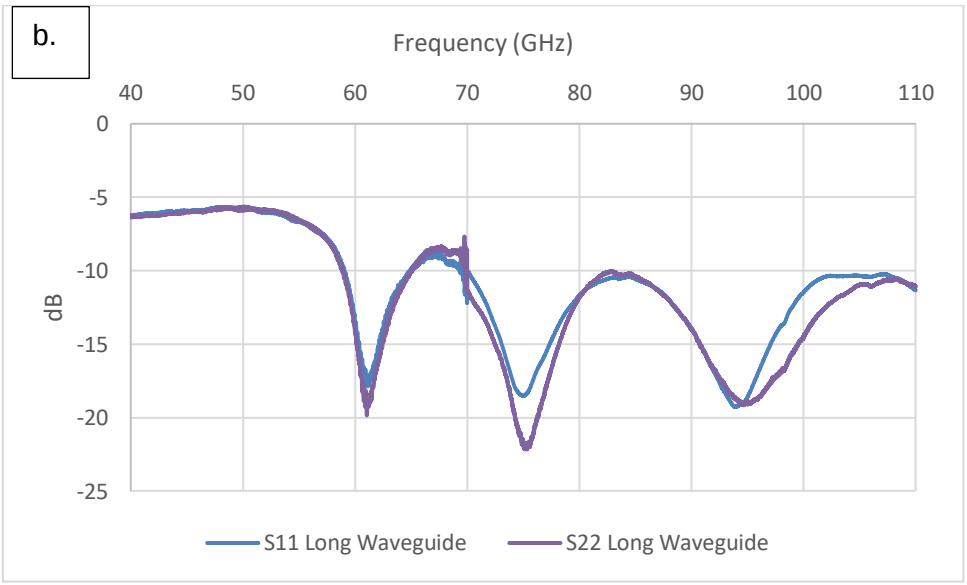

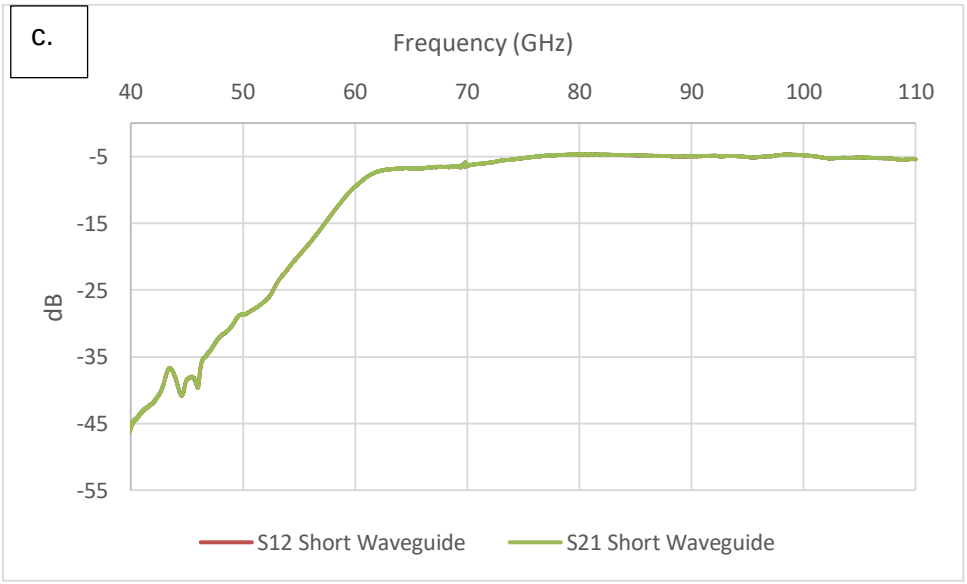

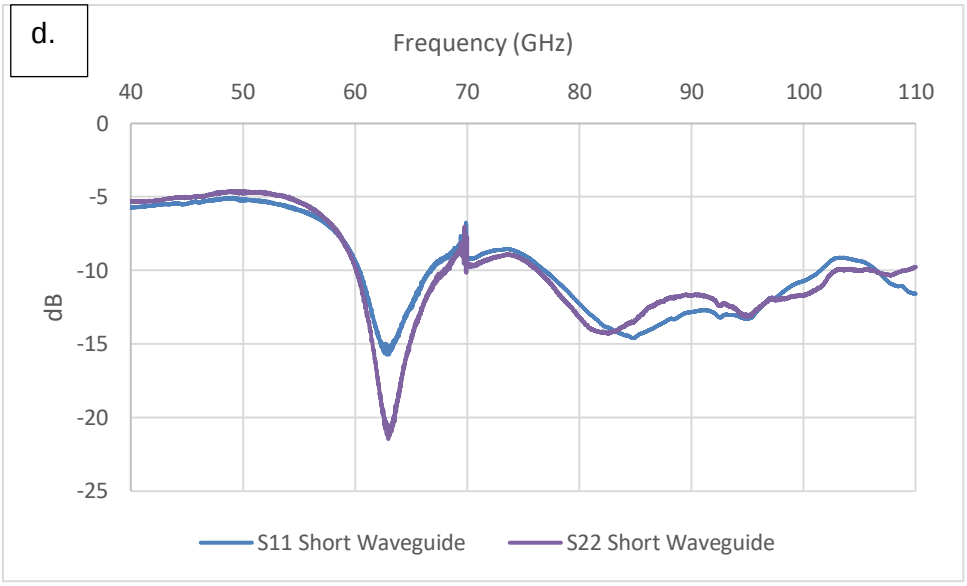

Figure 104 : S-parameters of a long waveguide (a. and b.) and a short waveguide (c. and d.)

The insertion losses are around -5 dB and the adaptation is below -10 dB for both waveguides in the frequency band (81-86 GHz).

The insertion losses are still quite important. They are probably due to two different factors:

- The “equivalent conductivity” of the CNTs
- Miss-alignment or poor contact of the input/output pillars

Indeed, we can note that the adaptation outside the band is around -5 dB, when in simulations (Figure 99) it is around -0.8 dB. This is typical of resistive dissipation of energy. This energy loss is due to the pillars. If the excitation pillars have a high resistivity, energy is dissipated. This phenomenon occurs before and after cutoff because the resistivity of the pillars do not vary much within this range of frequencies. The high resistivity of the pillars can be due to two things, a low “equivalent conductivity”, and a gap between the top of the CNT pillars and the cover. Simulations of these phenomenons are shown in Figure 105 and 106.

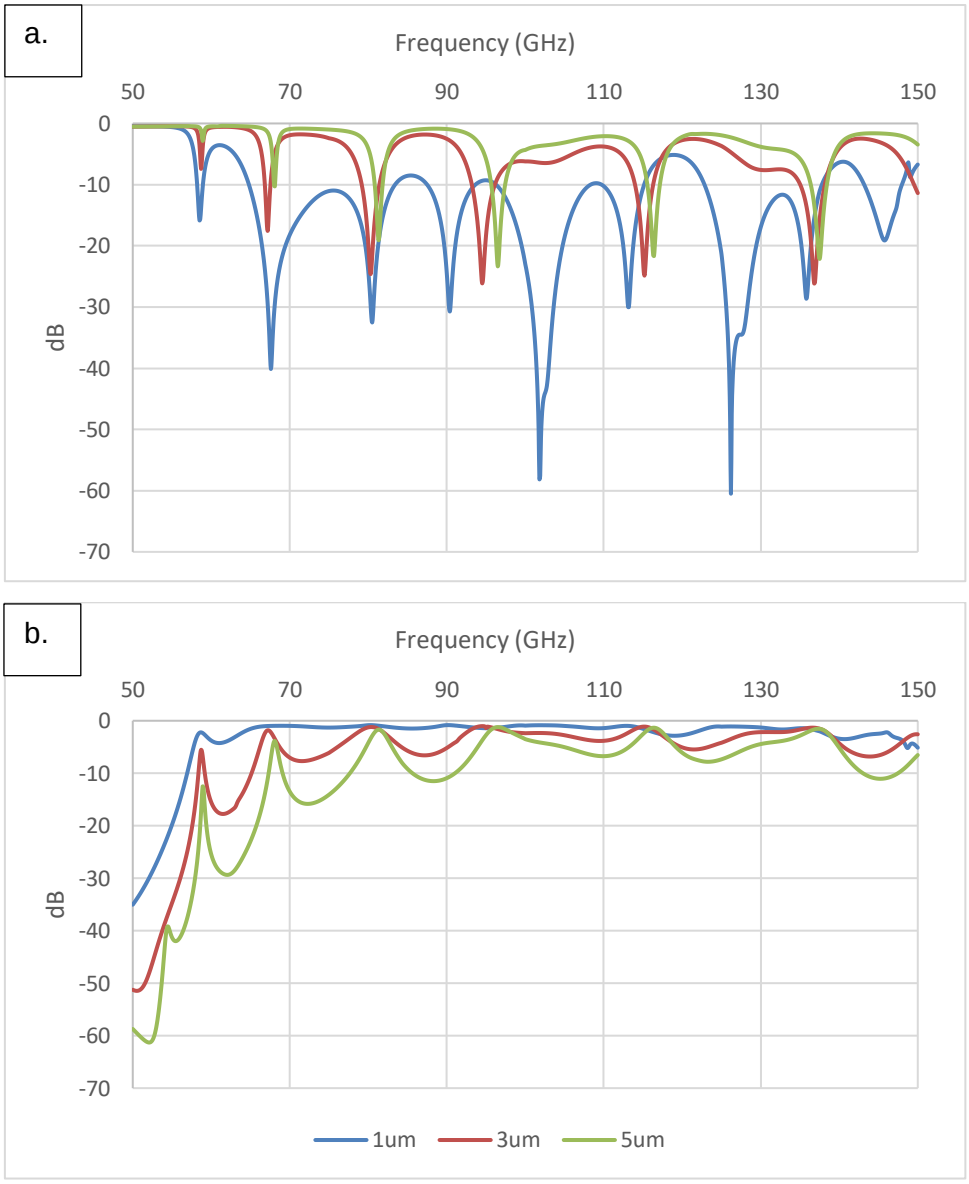

Figure 105 : Simulated S-parameters for different gaps between the pillar and the cover a. Adaptation, b. Transmission

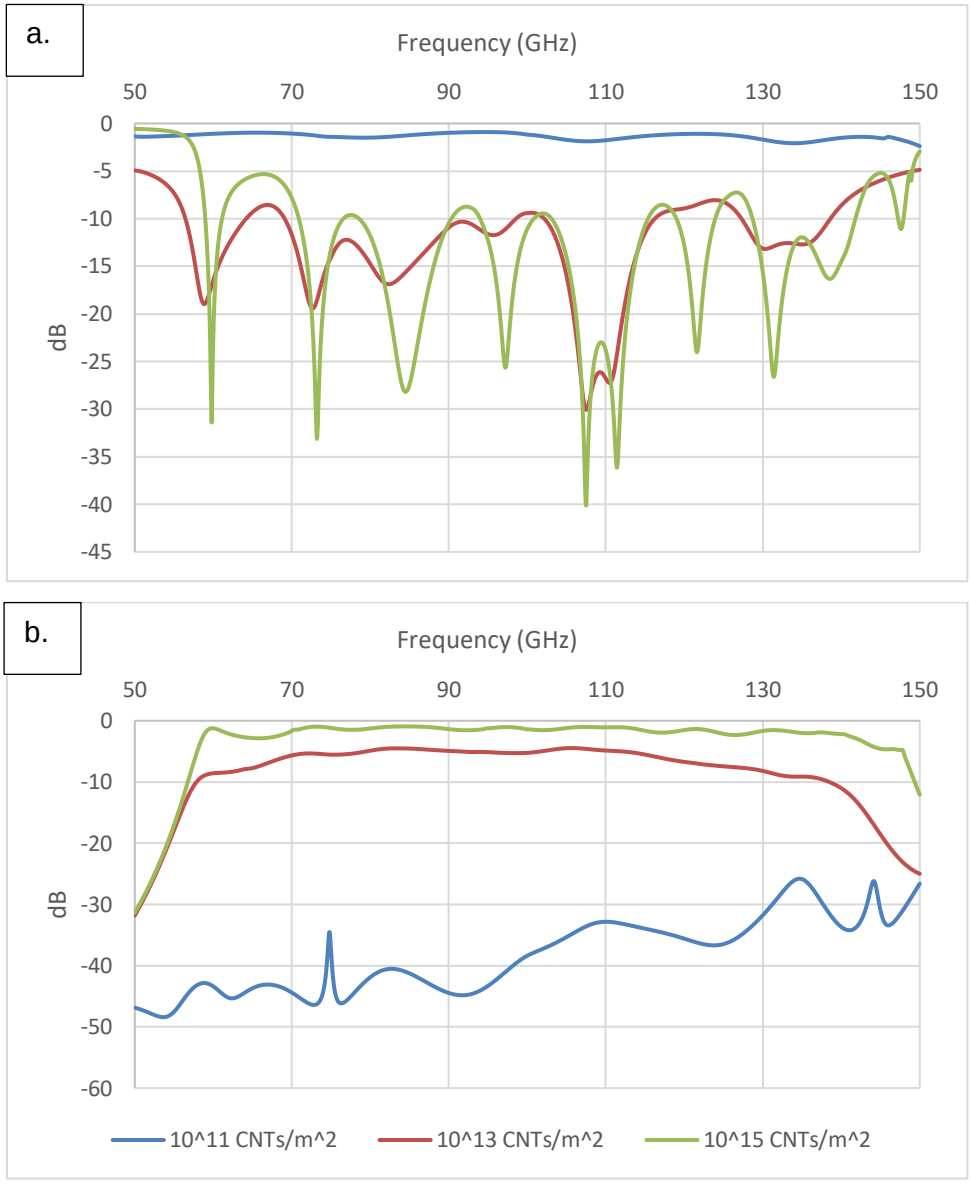

Figure 106 : Simulated S-parameters for different densities a. Adaptation, b. Transmission

As we can see, the losses are mainly explained by the low “equivalent conductivity” of the CNTs. A gap between the top of the pillar and the cover creates poor adaptation that we do not see to this extent in our measurements. In order to do complete back-simulations, we would also need to know the exact positions of the excitation pillars, a misalignment changes the adaptation.

The measured propagation constants Alpha and Beta are given below, and superimposed with the simulated ones (Figure 107).

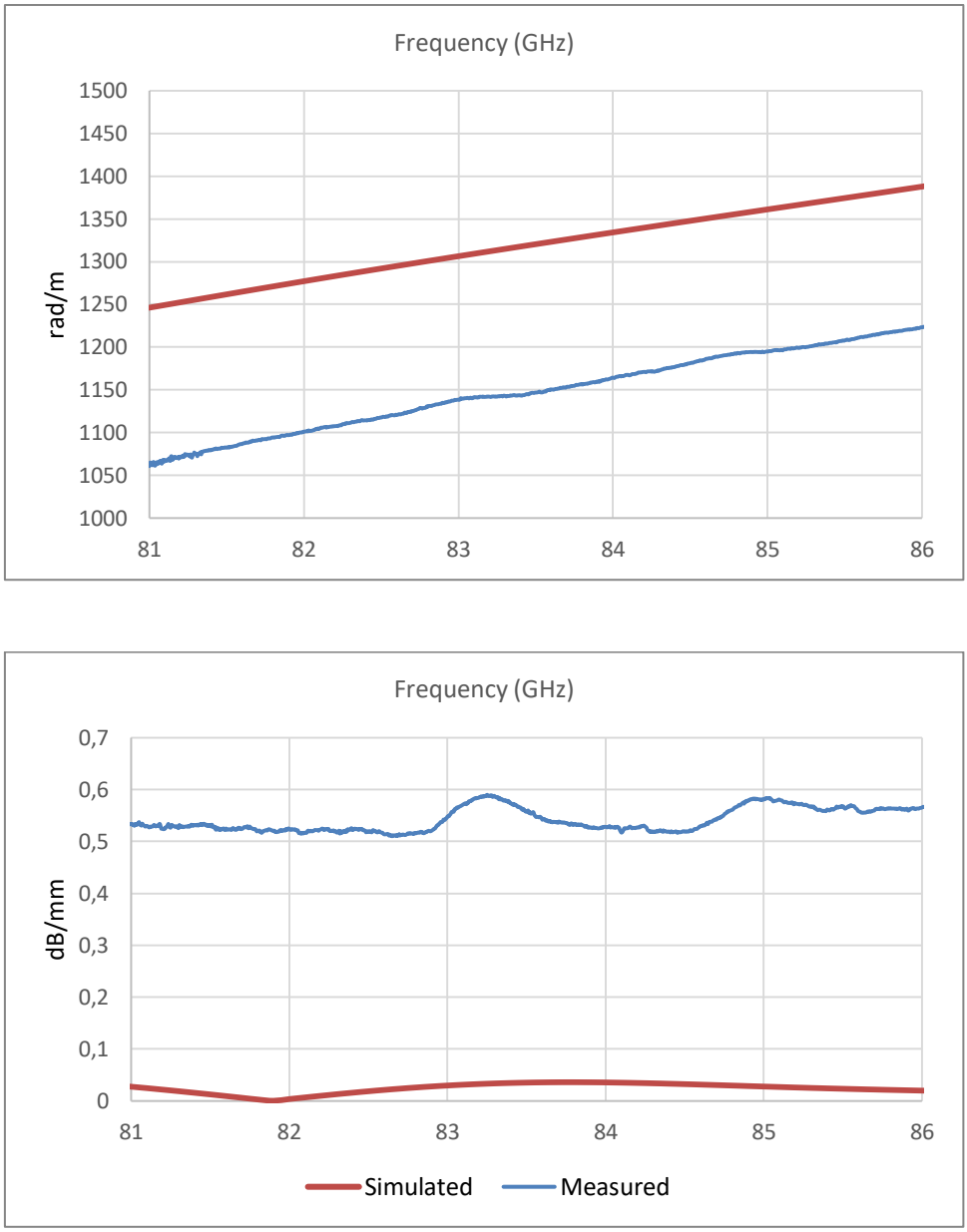

Figure 107 : Above, Simulated and measured Beta, Below, Simulated and measured Alpha

As we can see, the measured losses are higher than the simulated ones. This is due to the lower conductivity of the walls in reality than in the simulations. Furthermore, Beta is higher in simulations than in measurements, probably due to different lateral dimensions between experimental and simulated waveguides.

A this point it is interesting to compare our results to the ones obtained in [157], by the RFIC Lab team, for the same type of structure using nanoporous membrane filled with vertically aligned metallic nanowires. The structure and measurements are shown in Figure 108.

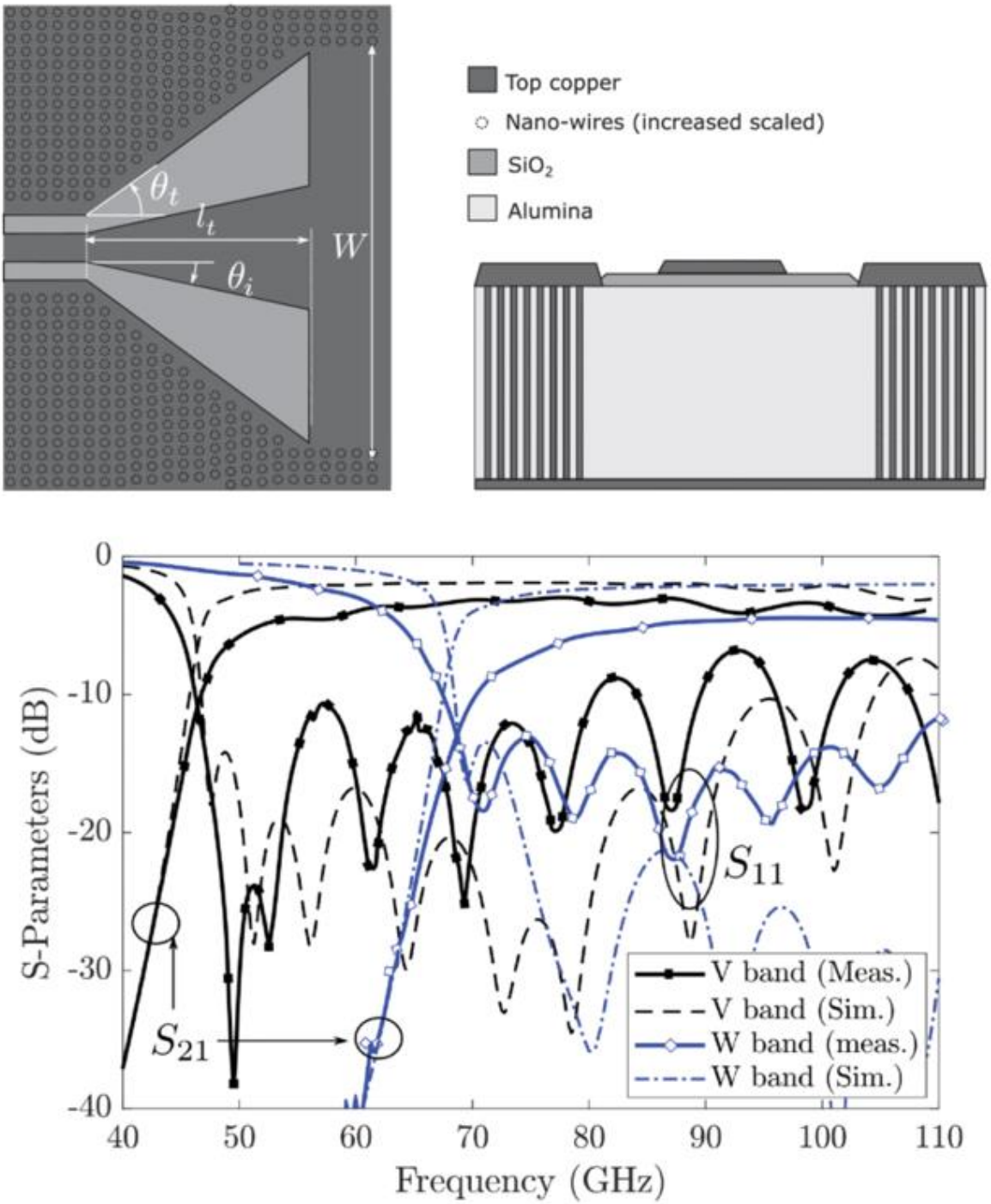

Figure 108 : Top, schematic of the integrated waveguide in nanoporous alumina filled with metallic nanowires, Bottom, measurements and simulations for waveguides designed for the V and W bands [157]

As we can see, the results are quite similar. The insertion losses are quite high for these structures also. However, the adaptation is several dB better. The transition from CPW to the integrated waveguide, used for these structures, is the one described in 2.4.1. Compared to the pillar excitation, it has better simulated performances, and it is less sensitive to the fabrication processes. If we can find a way to implement this excitation in our structures, we can expect much better results.

In parallel, several cavities (50 GHz and 80 GHz) were fabricated and measured. The cavities were designed with weak coupling, for more accurate conductivity extraction. Due to high losses, the measurements are more difficult to interpret; the resonances are not clearly visible. Measurements of a 50 GHz cavity and of a 80 GHz cavity are shown in Figure 109.

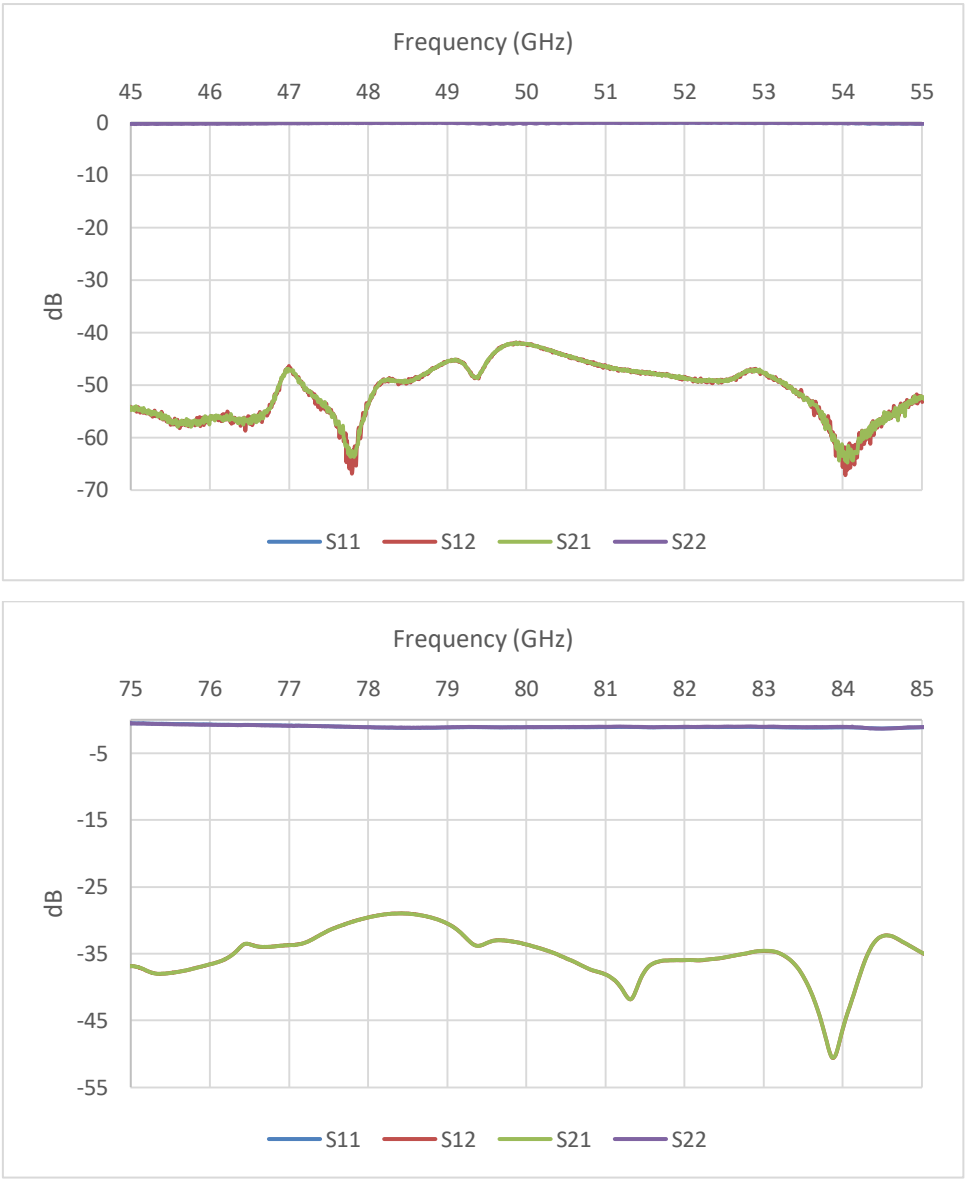

Figure 109 : Measured S-parameters of a 50 GHz cavity (top) and 80 GHz cavity (bottom)

As we can see, the transmission levels are quite low, below -40 dB for the 50 GHz cavity, and below -30 dB for the 80 GHz cavity. It is difficult to extract the resonances of the cavities from the parasitics.

In order to improve the cavity measurements, and be able to extract conductivity measurements, two steps need to be taken. First, during the design, one should not aim for a resonance at -15 dB for a density of 10^{15} CNTs/m^2. Indeed, for lower densities the resonance peak might not be detectable in the noise of the measurements. Second, during the fabrication

process, the spacers used should be bonded more strongly. Indeed, during transportation of the devices from CINTRA to XLIM, some spacers broke away from the cavities and might have damaged the CNT walls. In general, the height of the cavities is 500 um, much more than the 110 um of the waveguides, which make them much more prone to deterioration after transport.

2.7. Conclusion

In this chapter, we have studied the different possibilities and problems raised when it comes to the fabrication of air-filled waveguides based on VACNT bundles. Different fabrication processes were studied, and a characterization process was used to determine the “equivalent conductivity” of our process (from growth of the VACNTs to assembly). The characterization of one of the processes was made, showing a low “equivalent conductivity” around $5.6*10^3$ S/m. This low value is due to the contact resistance from the transfer process and assembly of the cover and/or the quality of the CNTs. The characterization structure revealed the problems caused by substrate modes in our designs. This prompted the creation of other designs without this flaw. These devices were fabricated and measured. While the performances are better, they are not at the state of the art. The pillar excitation causes some problems in practice.

Chapter 3: VACNTs for slow wave effect

We showed in the previous chapter how it is possible to use VACNTs to guide electromagnetic waves. However, the propagating medium being air, which permittivity is one, it implies a bigger footprint. Furthermore, the chips on top of the interposer are getting smaller and smaller which make them unlikely to become the limiting factor in terms of footprint. Since we aim at using the CNTs as an interposer, the room on the RF substrate (usually materials with high permittivities such as alumina (9.8) or silicon (11.2)) might not be sufficient to host a whole Butler Matrix on top. That is why it is crucial to find a way to reduce the size of the interposer. While until now we have not exploited the anisotropic conductivity of our VACNT bundles, per say, but rather used them as we would have isotropic metallic walls, interestingly, we can make use of the anisotropy of the nanomaterial for size reduction. This property of VACNT bundles is immensely profitable in that it allows for an important size reduction while avoiding the dielectric losses that come with high permittivity materials that are often used for this purpose. In addition, the use of VACNTs for size reduction is perfectly compatible with the fabrication processes we have presented before.

In this chapter, we will start with a brief state of the art of the different technologies that allow the miniaturization of propagating RF devices. Next, we will explain more in details the slow wave effect. Then we will modelize the possible improvement of the devices using this technology. Finally, we will present an experimental proof of concept at 20 GHz in order to free ourselves from the fabrication uncertainties that were raised in chapter 2.

3.1. State of the art

With the increasing number of telecommunication channels in mobile phone, or for multimedia broad band applications, the number of devices needed has increased inside our connected appliances. Thus, the need for miniaturization is increasing [238]. There are two main ways to miniaturize devices. The first one is to aim for higher integration and functionalization through new topologies and design methods, such as filter antenna co-design [239], [240] or new ways of packaging [238], [241]. The second one aims for miniaturization of the devices themselves using high permittivity materials [242], or particular micro/nano engineered propagating mediums [243]. The two approaches are not separate from each other and are often combined in the literature, such as 3D printed high permittivity ceramics [244] or highly integrated SAW packages [238].

Since their development in the early 2000s by Ke Wu [245], [246], SIW have drawn a lot of attention for their interesting properties. They consist of a thin dielectric substrate with metallic plates on top and bottom, pierced with rows of vias. The rectangular section made by the vias and the two metallic planes confine the fields, provided that the vias are close enough to each other compared to the wavelength. Compared to classical metallic waveguides, they have the advantage of being low weight, of having high integration capabilities while maintaining a rather low cost of fabrication. Compared to classical planar technologies such as CPW or Microstrip lines, SIW have lower radiation losses, due to the fields being confined in a rectangular section, and therefore higher quality factors. However, they do suffer from high footprints, the ratio between the height of the SIW and its width is usually quite large. In order to reduce this footprint, many research teams have studied ways to reduce the lateral dimensions [247]–[249]. In this section, we will have an overview of the different miniaturization methods described in the literature.

3.1.1. Ridged SIW

This first method is directly derived from the ridged technology in classical metallic rectangular waveguide [250]. The idea is to change the section of the waveguide by introducing a ridge in the waveguide, Figure 110. This ridge will decrease the cutoff frequency of the fundamental mode TE10. Indeed, the ridge being in the center of the waveguide, where the electrical field is maximum, will induce a capacitive load. For the same dimensions a and b, the waveguide will work at a lower frequency, which means miniaturization. We can note that for the first mode of superior order, TE20, the electric field is equal to zero in the center of the waveguide; the cutoff frequency of this mode remains almost the same. This implies a greater bandwidth.

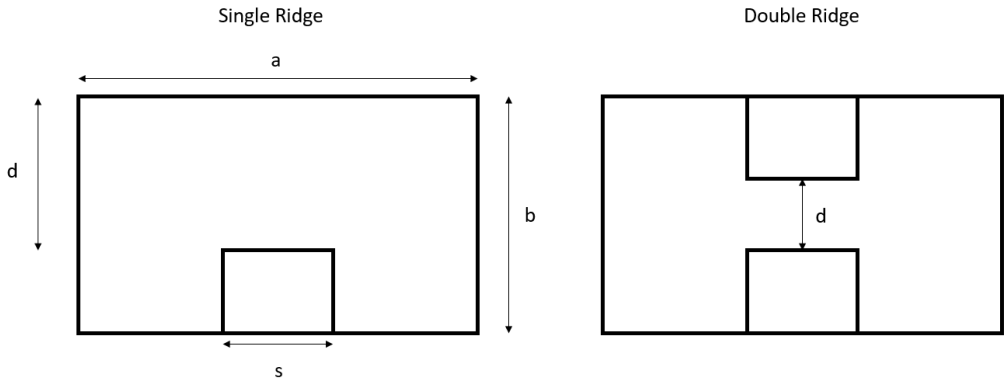

Figure 110 : Cross-sections of Single Ridge and Double Ridge rectangular waveguides

This method was used for SIW structures by simply replacing the ridge, by a row of blind vias [251] or a row of blind vias connected by a thin plate [252] as shown in Figure 111. The fabrication process is similar to the LTCC one with multiple layers soldered together.

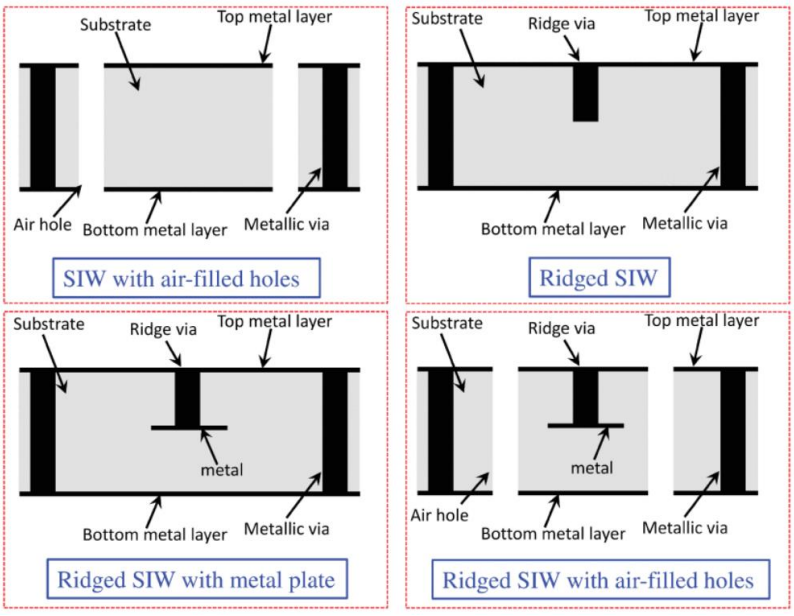

Figure 111 : Different topologies of SIW to improve bandwidth, ridges and air holes [247]

This method is particularly used for increasing the bandwidth of the waveguides. It has been combined with the drilling of non-metallized holes near the metallic posts on the sides, to achieve a bandwidth improvement of 232% [253]. The idea is that by reducing the effective permittivity on the sides of the section, where the second mode maximum electronic fields are located, this mode is pushed even further into higher frequencies.

3.1.2. Folded SIW

This method is also directly derived from classical rectangular waveguides technology, it was first presented in [254]. The idea is that by bending a rectangular waveguide in its lateral dimensions, the fundamental mode will remain the same since the boundary conditions do not change. If the guide is bended enough it is equivalent to it being folded. Different folding topologies are presented in Figure 112.

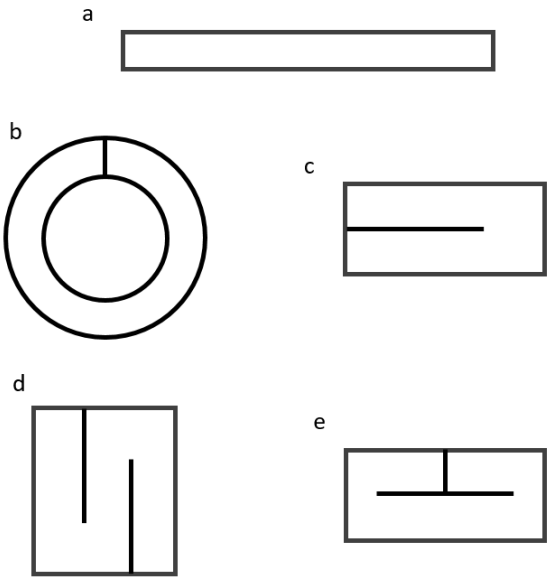

Figure 112 : Different cross-section topologies for folded waveguides a. Rectangular waveguide, b. Septate coaxial, c. C-shape folded, d. Thrice folded and e. T-shape folded

To the knowledge of the author, the first use of folded SIW is reported in [255], for a T-shape topology. Since then, the C-shape has also been studied [256]–[258] even though it is more difficult to excite due the disappearance of the vertical symmetry of the electric field. Folded SIW devices in the literature include: a Quadri-Folded SIW bandpass filter in [259], a 180 GHz to 220 GHz bandwidth folded SIW [260], a ring coupler [261], etc.

However, the fabrication processes require multi-layer technologies, such as LTCC, implying higher cost fabrication and the losses are usually slightly higher than in ordinary SIWs [247].

3.1.3. Half mode SIW

The first article which reports the use of half-mode SIW is published in 2006 [262]. The idea is as follows. In a classical rectangular waveguide, and by extension for SIW, the fundamental mode is the TE10 (provided the width is bigger than the height). This mode has a symmetric

plane along the transmission's direction, which is equivalent to a magnetic wall. In the case of SIWs, the ratio of width to height is usually very high. This leads to the fact that simply "opening" the SIW in the middle, by removing any metallization will be equivalent to a magnetic wall. The resulting structure is called a half-mode SIW. It is shown in Figure 113.

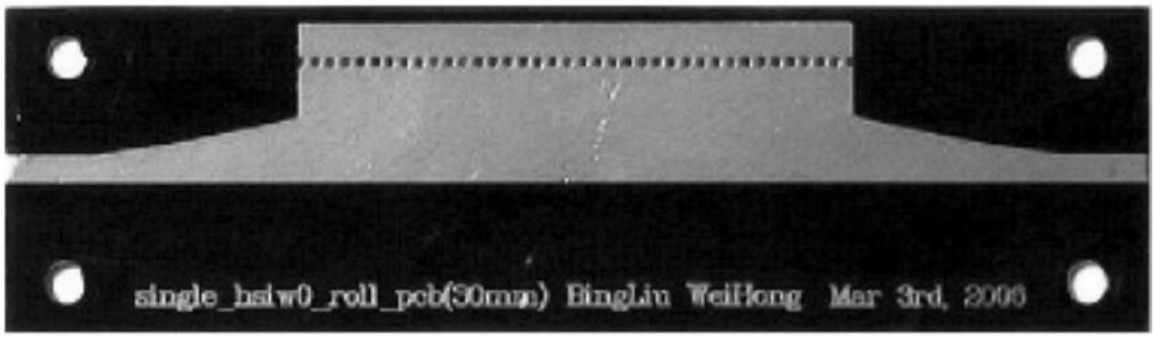

Figure 113 : Picture of a manufactured Half-mode SIW on PCB [262]

Half-mode and regular SIW structures present approximately the same insertion losses [262]. However, in a complete integrated system, there are still some radiation losses that can affect the neighboring elements.

The use of this topology has been reported for couplers [263], power dividers [264] and antennas [265], but the main use is for filter applications [266]–[269]. Indeed, the number of symmetric planes in the case of a circular cavity for the TE101 mode is infinite. This allows for consequential size reduction of the resonators. In [247] a list of different filters made with this technology, called partial mode SIW (PMSIW) devices, is given. With resonators as little as 1/32nd of a cylinder [270], the authors obtain a 96.87% size reduction when compared a filter with full resonators. However, we can note that the size of the devices decreases logarithmically with the angle of the resonator.

3.1.4. Slot loaded SIW

The idea, for slot loaded SIW, is to shift resonance frequencies of cavities by inductive or capacitive loading. In order to load the resonators, the metallic surface is patterned and the generated reactive effects will shift the frequency [271]. Depending on the shape of the pattern and the mode of the cavity, one can shift differently the resonance frequency.

In [272], the use of C-shaped slots on top of the resonators, such that they couple with the magnetic field, allow for a size reduction. In [273], the shifted mode is the TE102 using an H-shape slot in the middle of the cavity. In [274], the authors use a T-shaped open ended stub in the center of the cavity. In [275], a size reduction of 70% is achieved using open ended semicircular slots. The structures are presented in Figure 114.

We can note that this method, is only applicable for the size reduction of filters or resonant cavities, which we do not have in a Butler Matrix. But such devices are always used to filter the signal coming from the antennas.

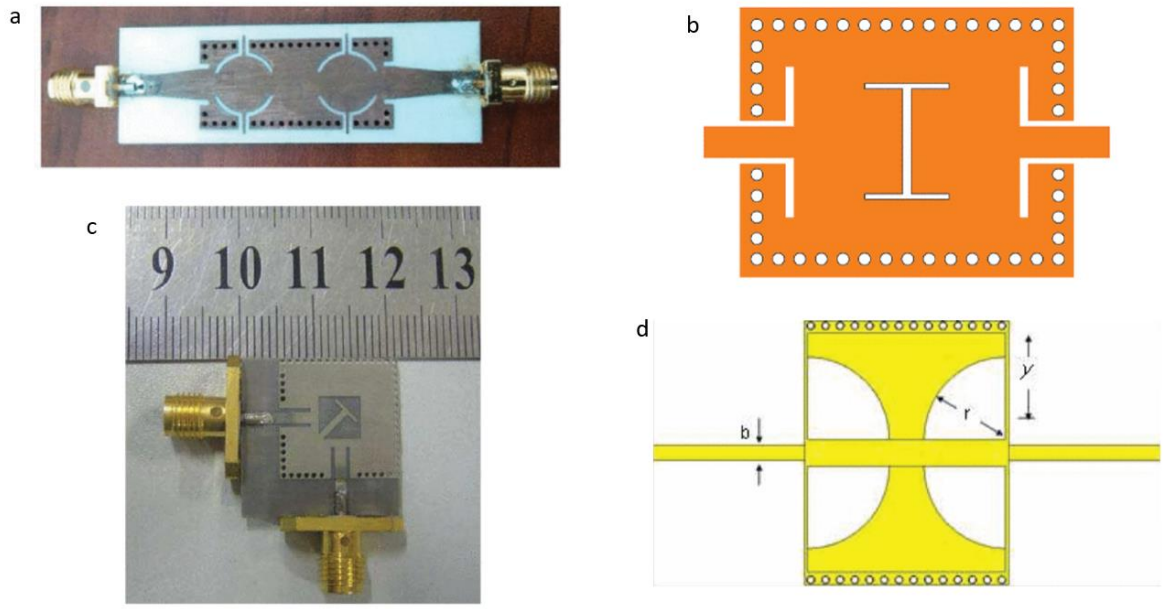

Figure 114 : a. C-shaped patterns [272], b. H-shaped pattern [273], c. Open ended T-stub [274], d. Semicircular patterns [275]

Interestingly, it is perfectly possible to extrapolate this technique and to load the top metallic plate with smaller patterns (compared to the wavelength), that will have a distributed capacitive or inductive effect. In the circuit equivalent model of the waveguide, the values of the inductance and capacitance will vary and thus change the propagation constant. The designers can tune the design in order to increase/decrease one or the other and change the cutoff frequency. This has been done by Ke Wu's team in [276] and [277]. By loading the top metallic plane with small Microstrip patterns acting as inductors in [276] or by soldering active inductors [277], the authors manage a size reduction of 40% and 35% respectively. The designs are shown in Figure 115.

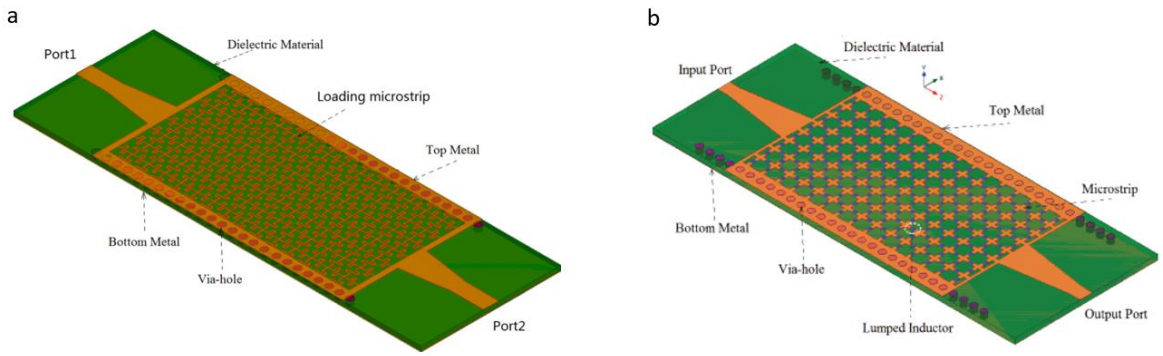

Figure 115 : Designs of the miniaturized surface loaded SIW with distributed elements a. Inductance from Microstrip pattern, b. Soldered Inductances

3.1.5. Metamaterials Structures

Since the late sixties and the introduction of the notion of metamaterials by Veselago [278], numerous applications have been found in the different fields of wave propagation. This field consists of engineering materials (by adding resonant structures small enough compared to the wavelength of the propagating wave) so as to obtain uncommon properties, such as negative permeability and/or permittivity.

3.1.5.1. Split Ring Resonator

Of all the possible metamaterials technologies the most studied is probably the split ring resonator (SRR). The magnetic susceptibility that ensues (coupling between the rings) allows for negative permeability, a property not found in conventional materials. In the field of RF devices, the most used is the complementary split ring resonator (CSRR), which is the dual of the SRR, because it allows for negative permittivities [279].

In the case of SIW devices, the idea is to pattern the metallic plates with such structures. In order to improve the frequency shifts, research has shown that adding stepped impedance to complementary split ring resonators structures was more efficient. In Figure 116, different structures are listed, that were implemented for SIW structures. In [280], the authors manage to reduce the footprint by 60% approximately compared to classical SIW structure.

This technology can be applied to waveguides as opposite to the one presented before. However, it has the inconvenient of being narrow band [281]. The behavior of the CSRR is not broadband because it is based on a resonating behavior. However, with different sizes of SRR broadband negative permittivity materials have been reported for higher frequencies (optics) [282].

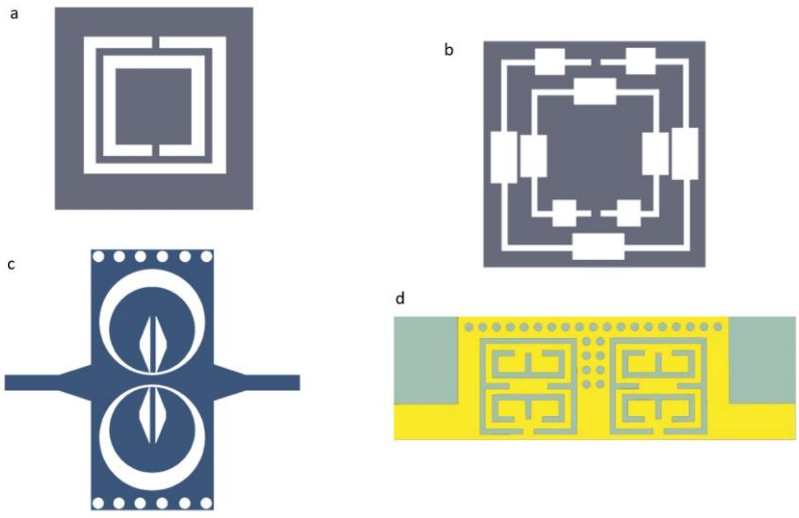

Figure 116 : a. Conventional CSRR [280], b. Stepped impedance CSRR [280], c. G-shaped Stepped Impedance CSRR [283], d. E-shaped Stepped Impedance CSRR [284]

3.1.5.2. Other Structures

The use of other structures to obtain RF materials with unconventional properties is usually referred to as the use of Composite Right/Left Handed Materials (CRLHM) in the literature. Left handed materials (as opposed to right handed materials) are materials with negative

permeability and permittivity. The term CRLHM is more complete term than Left Handed Materials, which includes the possible right handed propagation in these materials.

In [285], the folded SIW topology is used to incorporate the left handed material properties in the device. The plate used for folding is patterned to add distributed elements to the transmission line model, and decrease the cutoff frequency, as shown in Figure 117.

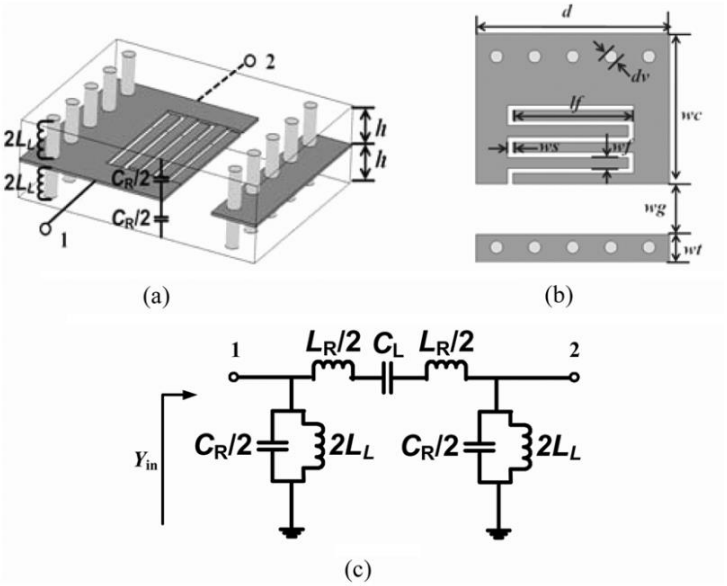

Figure 117 : (a) 3-D view of the unit cell for the proposed CRLH transmission line based on the FSIW. (b) Top view of the middle metal layer in the unit cell. (c) Equivalent circuit model for the unit cell [285]

The motifs can also be engraved on the top metallic plates as shown in the following articles [286], [287], [288, p. 3]. A size reduction of approximately 50% compared to classical SIW is obtained. Another drawback of these metamaterials is the decreasing size of the patterns at higher frequencies, which make it difficult to implement in classical fabrication processes for SIWs.

All the technologies mentioned above are often mixed in order to achieve even greater size reduction as shown in [282], [289], [290].

3.2. The Slow Wave Technology or decoupling Electrical and Magnetic fields

In the literature, the term slow-wave is generally used for any method that decreases phase velocity in propagating structure. Hence, all of the methods aforementioned can be considered as slow-wave technology and using high permittivity substrates can also be considered as slow-wave technology (phase velocity being directly linked to permittivity of the propagating medium). In previous articles the physical phenomenon that will be detailed in this section has been referred to as the slow-wave effect. That is why, in the ANR TRICOT project this is the term that was used. However, this term does not reflect the particularities of the phenomenon at stake and can lead to confusion with other technologies. In the following section it will rather be referred to as the decoupling of the electrical and magnetic fields.

3.2.1. Planar slow wave

In the 70s, the democratization of planar transmission lines in the microwave ranges, and the performances of transistors such as the MESFET relied on the quality of the semiconductors used. Semiconductors, such as silicon or GaAs of the III-V family, with high resistivity allowed for transmission lines with good performances. Consequently, monolithic integration seemed liked a promising prospect. Yet, the wavelengths of the propagating waves at these frequencies were simply too big. The price of the semiconductors at that time was too high to make matching networks, filters or couplers integrated to the single crystal substrate [291]. It is for this reason that the slow-wave effect arising from decoupling the electric and magnetic fields was studied by Hasegawa in [292]–[294], in order to reduce the dimensions.

The first article to theorize the existence of the slow-wave propagation mode is [295], in which the authors study the behavior of interconnects on bi-layered substrates (Si-SiO_2). However, the first article to experimentally observe the slow-wave propagation is [294]. In this article, the microstrip on Si-SiO_2 bi layered substrate is analyzed numerically using the model of the parallel plate waveguide (Figure 118).

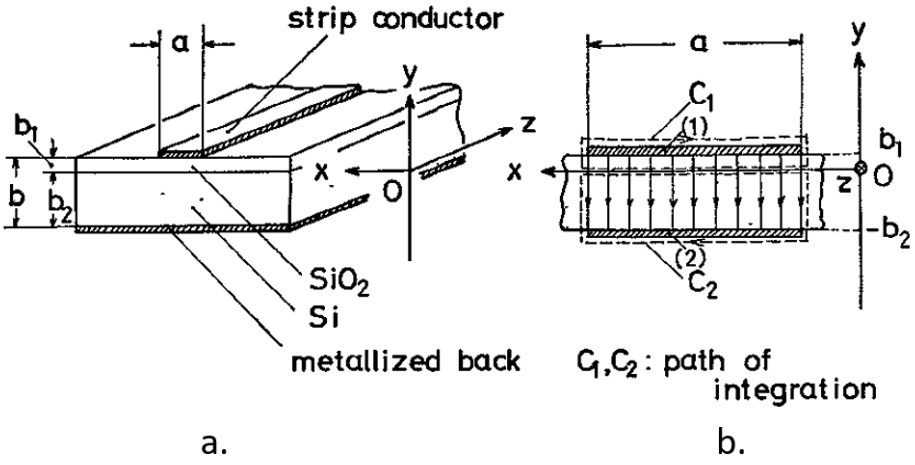

Figure 118 : Line structure and coordinate system for analysis, a. Microstrip line on Si-SiO_2 substrate, b. Its parallel plate waveguide model [294]

The introduced effective permittivity and permeability of the bi layer substrate allow for the characterization of the fundamental modes. The SiO_2 layer is considered to be a lossless dielectric. Three different modes are characterized depending on the frequency and the conductivity/resistivity of the Si layer:

- The product of the frequency and the resistivity of the Si layer is high enough that the dielectric loss angle of this layer is small. In this case, the Si layer behaves as a dielectric substrate, and we have the conventional TEM propagation.
- The product of the frequency and the conductivity of the Si layer is high enough to yield a small depth of penetration. In this case, the Si layer behaves as a ground plane, and we have TEM propagation in the SiO_2 layer. If the skin depth is too big, the system becomes highly dispersive.

- The frequency is not so high and the resistivity is moderate. In this case, the Si layer behaves differently than in the two previous cases, and we have slow-wave propagation.

Figure 119 shows the different fundamental modes propagating in function of frequency and resistivity of the Si layer.

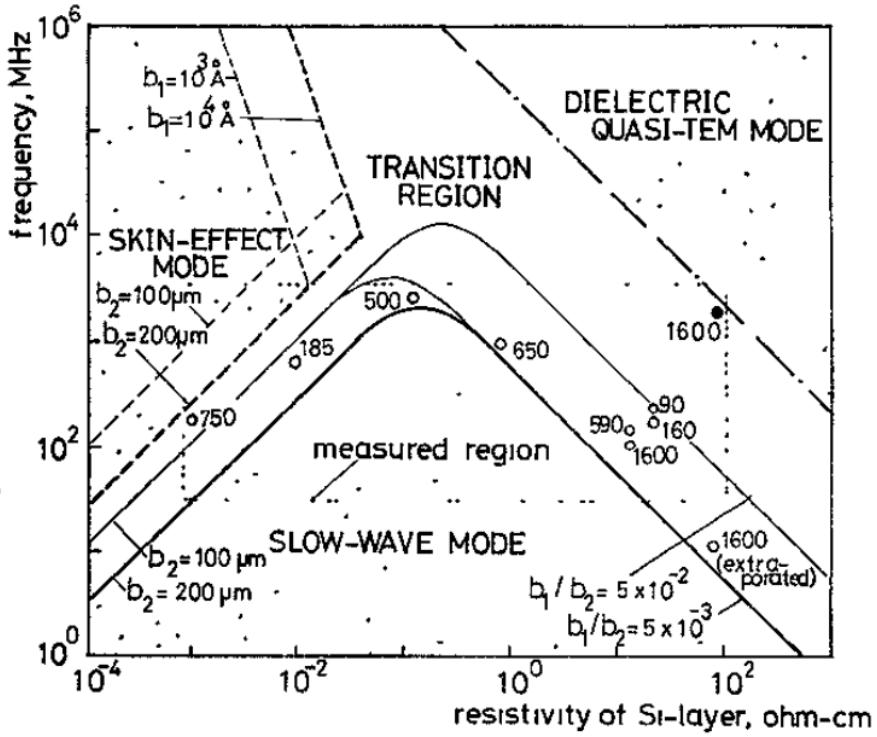

Figure 119 : Resistivity-Frequency domain chart. Permittivity of SiO_2 and Si, 4 and 12 respectively. The hollow points and full points are measured Slow-wave and TEM modes respectively. Numbers next to them give the width of the microstrip.[294]

The field distribution analytically determined in the article shows an interesting phenomenon that explains the low phase velocity. The electric field is concentrated in the SiO_2 layer while the magnetic field is present in both layers. Meaning all the active power is transmitted through the SiO_2 layer while the magnetic energy stored in the waveguide is mainly in the Si layer in that it is thicker ($b_2 >> b_1$). The sum of these energies is transmitted in the propagation direction through the thin SiO_2 layer. The propagation velocity slows down owing to the energy transfer at the interface.

This decoupling of the electric and magnetic fields was further exploited the authors in [292], [293] on GaAs substrates. Unfortunately, these structures had high losses because conduction takes places in a semi-conductor during the exchange of magnetic and electric energy.

Fortunately, more recently, the slow wave CPW structure in [293], that decoupled the electric and magnetic field using patterned floating ground strips perpendicular to the direction of propagation was later improved in order to have high quality factors by other teams in [296]–[298], due to new topologies attainable with the new fabrication processes. The structure is shown in Figure 120, as well as the measured quality factors that are the state of the art.

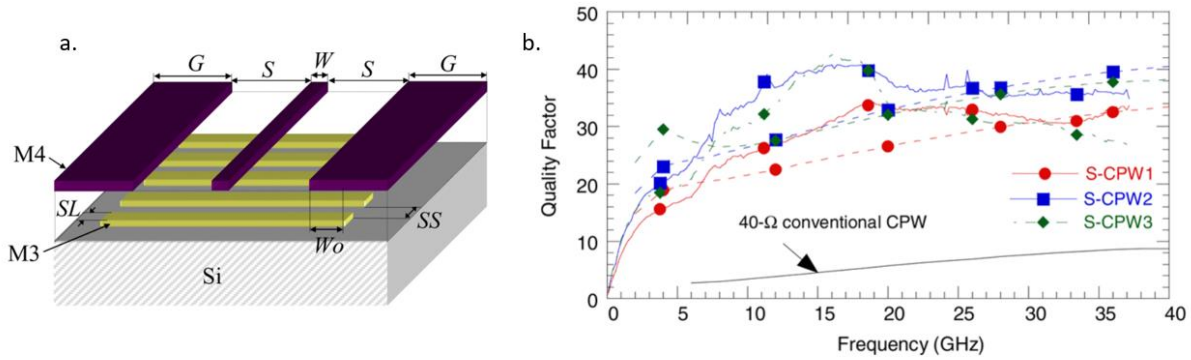

Figure 120 : a. Schematic of the cross-tie structure, b. Measured quality factors of the lines with different W, S and G dimensions

Finally, in 2014, a slow-wave microstrip line using vertically aligned nanowires in a porous alumina substrate was showcased by our partners RFIC Lab [299]. The structure is shown in Figure 121. Since then different passive devices were thought of using this technology, inverted microstrip [300] and Butler Matrix [301].

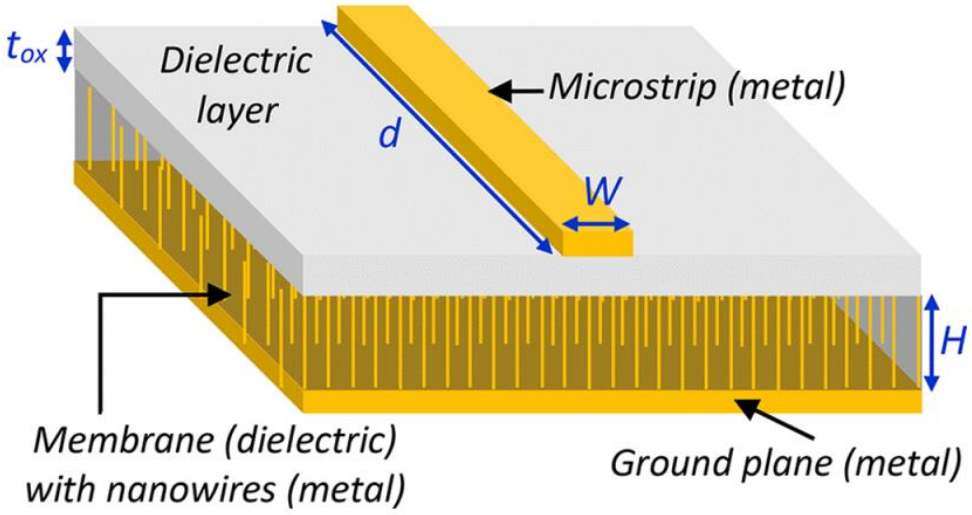

Figure 121 : Schematic of the microstrip on porous alumina with nanowires

The idea is that the electric field cannot penetrate in the membrane while the magnetic field lines are left untouched. Indeed, on the one hand, the vertically aligned wires, do not allow a vertical electric field to exist (the electric field is vertical in the case of TEM mode). And, on the other hand, the magnetic field is not impacted because it is perpendicular to the direction of the metallic nanowires. The difference in the distribution of the field lines between a classical microstrip and a microstrip on a porous membrane with metallic nanowires is schematized in Figure 122.

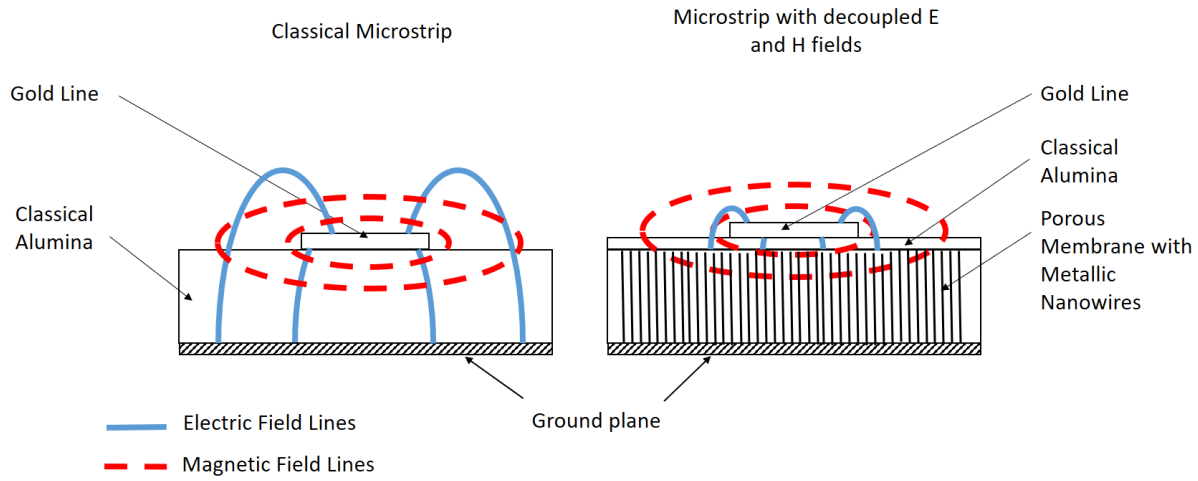

Figure 122 : Classical Microstrip vs Decoupled Fields Microstrip, with field lines

To conclude, the separation of the fields is the same in all the designs presented above. In terms of equivalent transmission line model : the capacitance (C) increases due to the smaller area occupied by the electric field, the inductance (L) remains the same because the magnetic field is not disturbed. For a transmission line the phase velocity (v_φ) is given by:

$$v_\varphi = \frac{1}{\sqrt{LC}}$$

Thus, the phase velocity decreases, and we have the slow-wave effect. In order to augment the slow-wave effect one might aim to increase the inductance as well [296].

3.2.2. Volumic slow wave with vias

The first article transposing the slow-wave technology (decoupling of the electric and magnetic fields) to SIW structures was published in 2014, by our partners in Grenoble [302]. A schematic of the structure's topology is shown below, in Figure 123.

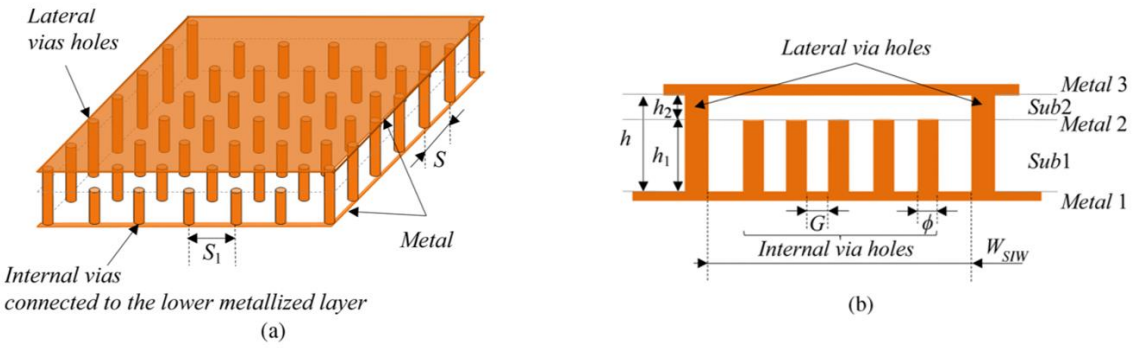

Figure 123 : Schematic view of the proposed SW-SIW (a) 3D view. (b) Transversal cross section of the SW-SIW (example with five internal via-holes)

Two PCB layers compose the structure. The bottom layer consists of the lateral vias that make up the lateral walls, the bottom metallization and vias in the propagation zone. The top layer consists of the lateral vias that make up the lateral walls and the top metallic layer. The two layers are assembled together to form a SIW, which has a bed of blind vias in its propagation zone. The space between the blind vias has to be smaller than an eighth of a wavelength. The idea is the same as the one used for planar structures. The electric field for the TE10 mode cannot penetrate in the bed of vias because it is collinear to the vias. The magnetic field is perpendicular to the direction of the vias and is not obviously disturbed. The structure is simulated using the finite element method and the density of both electric and magnetic fields are plotted in Figure 124.

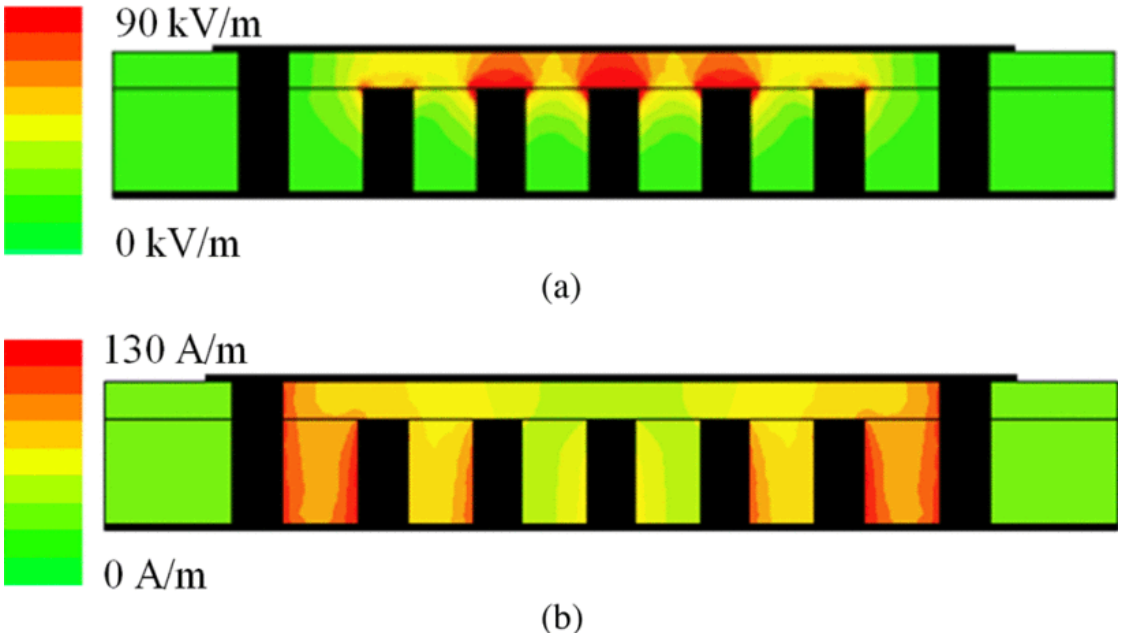

Figure 124 : Cross-section view of the sw-siw in the middle of a transversal via-holes section for a via-diameter ϕ=400 µm. (a) electric field magnitude. (b) magnetic field magnitude. (h1=0.813 mm, h2=0.3 mm).

The simulation results confirm the intuitive reasoning. The electric field is confined above the bed of blind vias, thus increasing the shunt capacitance, capacitance being inversely proportional to the distance between two metallic plates. The magnetic field is more or less left undisturbed and occupies the whole section of the guiding structure, meaning the inductance remains the same as in a classical SIW. As a result, the phase velocity decreases i.e. the equivalent permittivity increases.

The measurements of the S-parameters were in accordance with the simulated ones, and showed reduction of size of 40%. We can note that an excitation method (Microstrip to SIW) was proposed as well as a comprehensive study showing dependence of the blind vias' diameter and height for size reduction.

This idea was prolongated in [249], by instead of using two layers, with only one containing blind vias, the authors used three to have better ratio between the space occupied by the electric field compared to the space occupied by the magnetic field. The topology of the structure is shown in Figure 125.

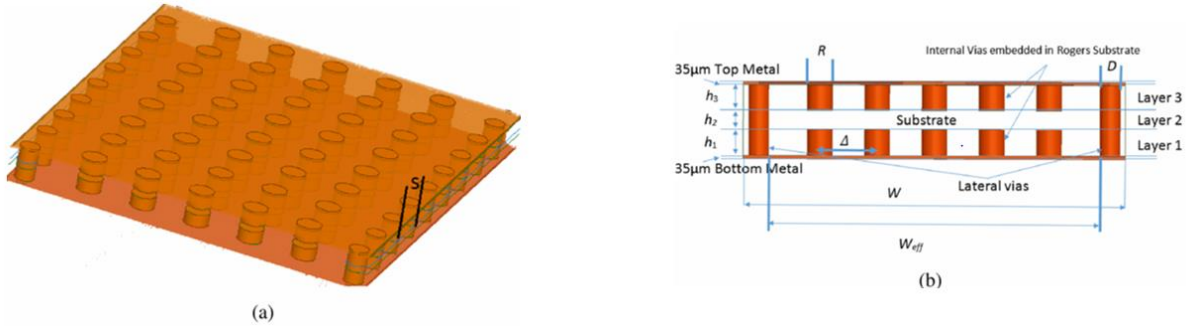

Figure 125 : Cross-sectional and 3D view of the new SW-SIW design. (a) 3D view (b) cross-sectional view.

No experimental results were shown, probably due manufacturing difficulty. The three layers stacked vertically, can induce a lot of losses due to the localization of current maximums for the TE10 mode. However, the simulations show better bandwidth. The slow-wave factor (ratio of phase velocity between the slow wave structure and the SIW) is roughly the same.

To overcome the losses that come from multilayer fabrication (also present in the bilayer original structure), the authors in [303] come with the following idea. They virtually reduce to zero the distance between the top of the vias and the metallic top plane. The vias are simply not blind but connected to the top layer. In order to allow propagation, the top surface is patterned. The geometry of the structure and the spatial distribution of fields are shown in Figure 126.

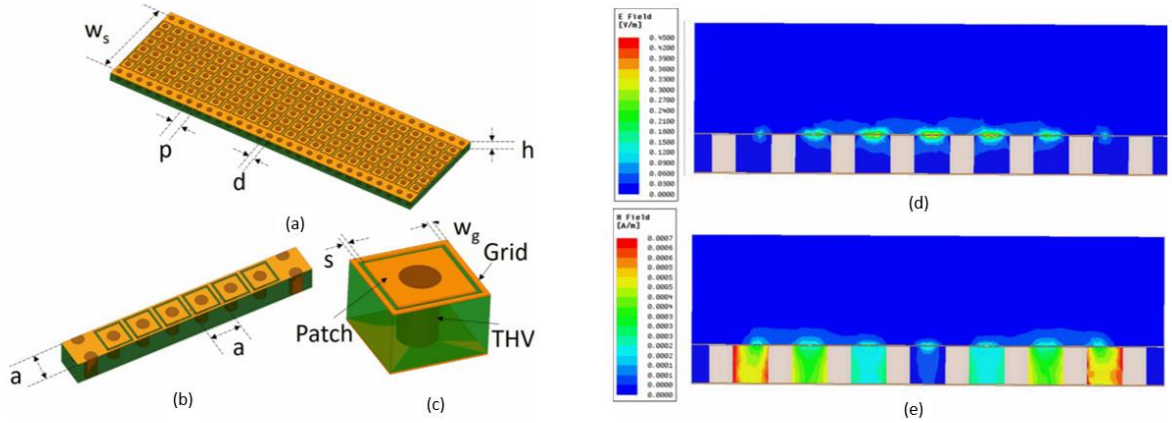

Figure 126 : Left, Schematic view of proposed SW-SIW: (a) 3-D view. (b) Super-cell of the proposed SW-SIW. (c) Unit cell of the SW-SIW, Right, Cross section of the proposed SW-SIW: (d) E-field. (e) H-field.

As we can see, the gaps between the top metallization and the top part of the “mushroom” vias allow the electric field to propagate on the surface. Meanwhile, the magnetic field occupies the whole substrate. The authors realize a band pas filter (BPF) using this technology and manage a size reduction of 58.8% compared to classical SIW structure.

Finally, in [304], a 73% reduction of the longitudinal length is achieved. A schematic of the device is shown in Figure 127.

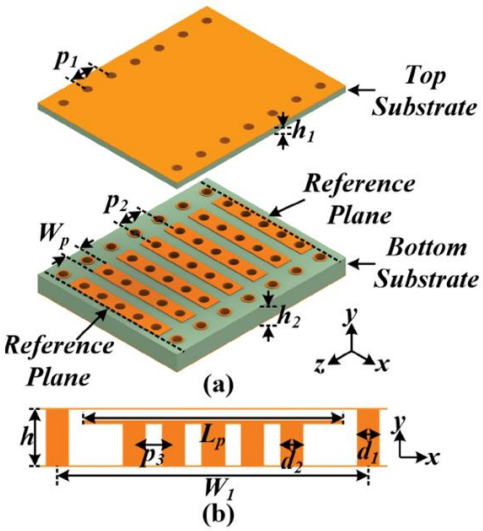

Figure 127 : Geometrical configuration of the proposed SW-SIW with dimensional parameters. (a) Exploded 3-D view. (b) Transversal cross section of the SW-SIW.

This improvement of size reduction compared to [302] is explained by two things. First, the capacitance has increased because the surface of the capacitance has increased (the top of the vias is replaced by a full metallic plate). Second, the inductance increases. Indeed, by adding the patches on top of the vias, the current path is lengthened i.e. permeability is increased, as shown in Figure 128.

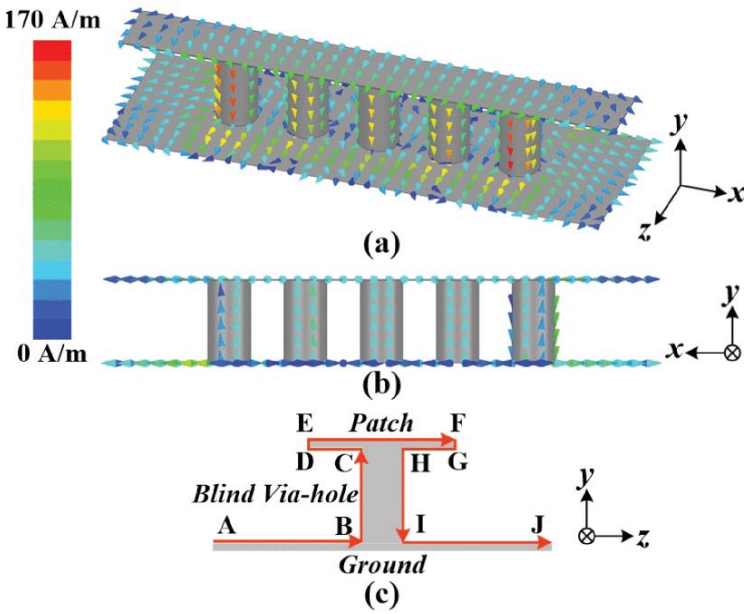

Figure 128 : Current vector distribution on the SWS in a unit element of the SW-SIW. (a) 3-D view. (b) Back view. (c) Heuristic diagram

3.2.3. Anisotropic metallic materials for slow-wave applications

At higher frequencies, the vias' diameter and interspace need to be smaller, the dimensions being directly linked to the wavelength. Unfortunately, current fabrication processes do not translate well to lower dimensions. This is what limits the technology presented before to frequencies below 30 GHz.

However, nanomaterials such as VACNTs or nanowires (NWs) might be an answer to such a technological bottleneck. The solution that was thought of in the project TRiCOT, was to replace the bed of blind vias by VACNTs or vertically aligned nanowires. Provided the density of the CNTs or NWs is sufficient, the behavior of the vertically aligned nanomaterials can be assimilated to a bulk anisotropic material. During the course of this PhD, our partners in Grenoble, RFIC Lab, published measurements of a waveguide (E band) partially filled with nanoporous alumina filled with vertically aligned nanowires as proof of concept [218].

The electric field cannot penetrate in the aligned nanowires, but the magnetic field is undisturbed because perpendicular to the uniaxial conductivity. The propagation of the TE10 mode should be modified in the same way as with blind vias.

3.3. Application to the Butler Matrix

It is particularly interesting in our case to add VACNTs in the propagation zone of the air-filled SIW with VACNT walls. Indeed, the material used for the slow wave effect is the same than the one for guiding the electromagnetic waves. Thus, the fabrication process is easily modified to incorporate the slow wave effect in our functionalized interposer.

Simulations were made using the finite element method and the bulk equivalent model of our VACNTs, to verify the behavior of a partially filled waveguide with VACNTs. The simulation design is shown in Figure 129. The simulated structure consists only of the rectangular waveguide without the transition from CPW to rectangular TE10 mode. The excitations consist of waveports, which allows us to directly extract the propagation constants from HFSS. The height of the waveguide is taken to be 110 um and the width 2.7mm, the same dimensions as the last designed waveguide of Chapter 2.

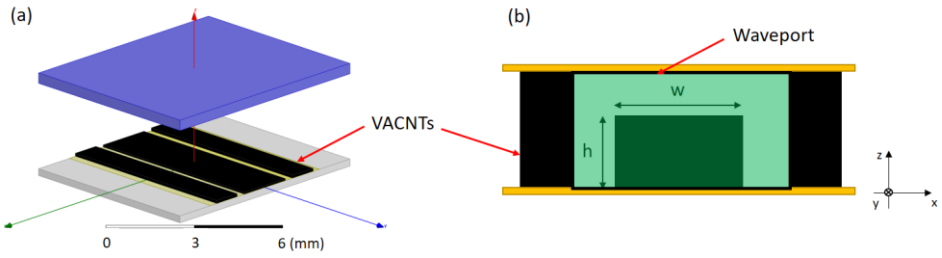

Figure 129 : (a) Exploded 3D view, (b) Schematic of the section

Height plays an important role in the slow-wave effect. The ratio between the height of the waveguide and the height of the slow-wave CNT pattern (h) is called the filling factor. The bigger the filling factor the bigger the propagation constant. The effect of height (h) of the VACNT pattern used for slow wave is plotted in Figure 130. With increasing aspect ratio, the field is more confined, leading to an increased capacitance and higher propagation constant.

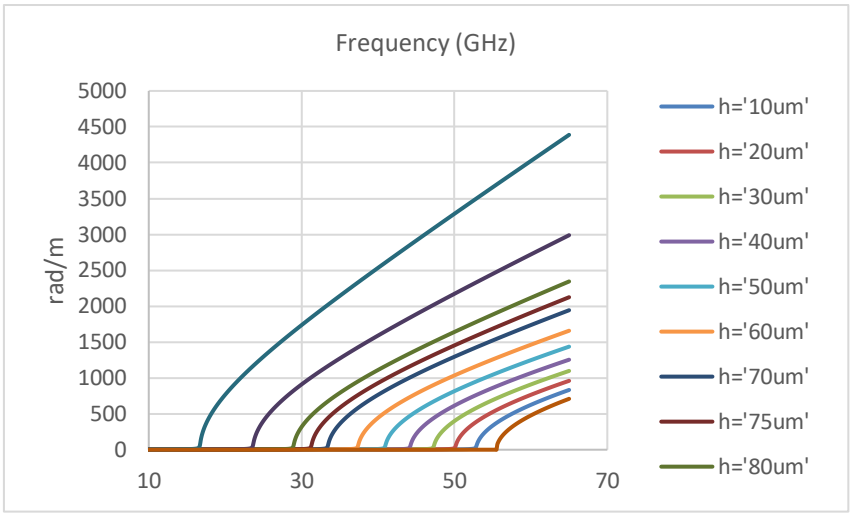

Figure 130 : Beta for different heights of VACNT patterns in the center of the waveguide (for a fixed pattern width of 2.7 mm)

However, for a filling factor too high, the losses will be too important to have interesting performances as a waveguide. Indeed, the dielectric losses (L_d) will increase with the square of the electric field (equation below), and the metallic losses will increase with the current in the nanotubes.

$$L_d = \iiint \varepsilon_d \, |E|^2 dV$$

The frequency shift does not depend much on the width of the pattern as long as the width of the pattern is close to the width of the waveguide as shown in Figure 131. The width of the waveguide is of 2.7 mm. The cutoff frequency for pattern widths of 2 and 2.5mm is almost the same. It then decreases, for 1.5mm and 1mm.

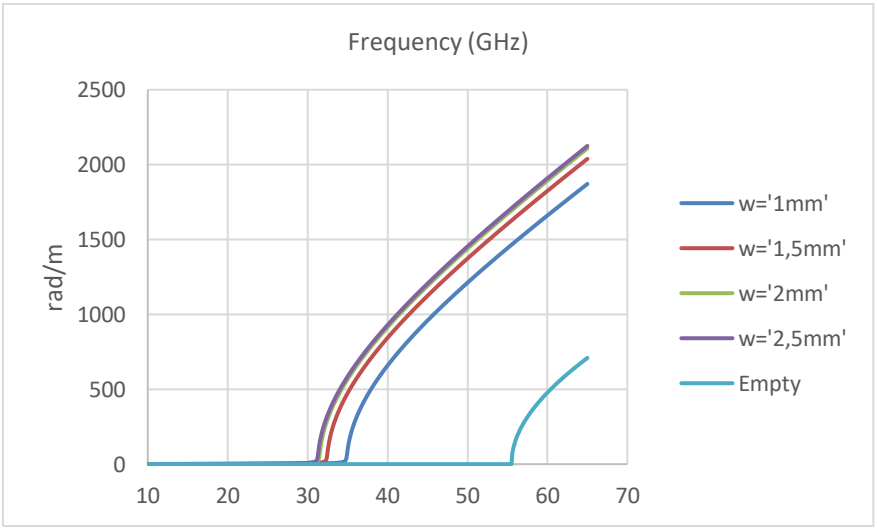

Figure 131 : Beta for different width of VACNT pattern (for a fixed height of 75 um)

The effect of density is an important case to study. If the density of CNTs is not important enough, the conductivity will not be very high and the current going through the nanotubes will not be sufficient to create the magnetic field necessary for separate energy storage. In Figure 132, beta was plotted for different conductivities in the direction of the CNTs. As we can see, as long as the density is above 10^{13} CNTs/m^2 ($1.6*10^3$ S/m at 50 GHz) it does not change the propagation constant much.

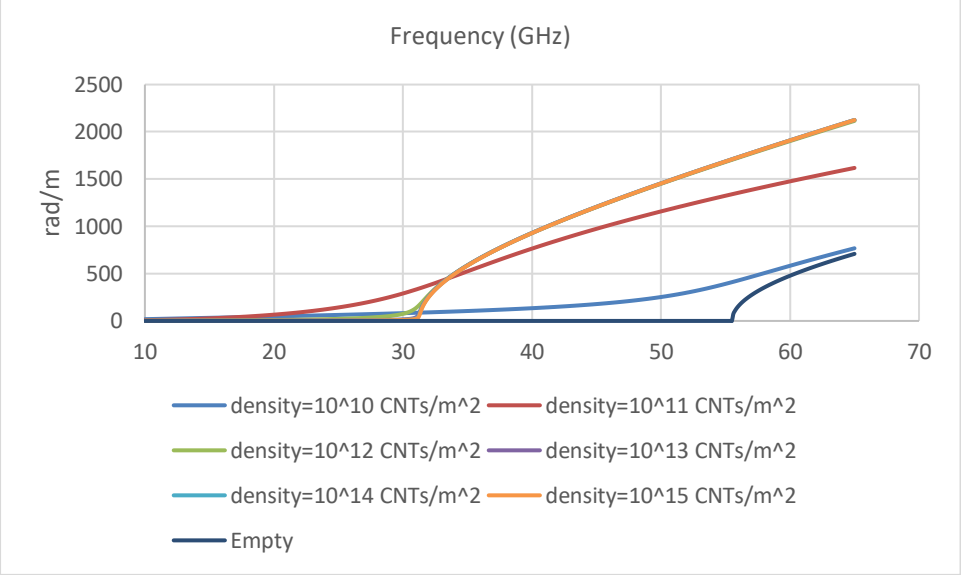

Figure 132 : Beta for different densities (conductivities), fixed height of 75 um and width of 2.7 mm)

For low densities, the behavior of the waveguide is different, there is a slow-wave effect since beta is higher, but it is probably more due to the VACNTs pattern behaving as a lossy metallic wall (c.f. 3.2.1). No cutoff frequency can be determined.

Finally, in all the simulations made before, the lateral conductivity[15] was taken to be zero. However, if there is too much lateral conductivity in the VACNTs, the slow-wave effect will not be happening at the same scale (smaller increase of beta). Indeed, the magnetic field cannot propagate unless its direction is perpendicular to the conductivity. In case of high lateral conductivity, the VACNTs will behave similarly to an isotropic metal, which does not allow for the slow-wave effect. The simulations were made for different lateral conductivities, and the results are plotted in Figure 133.

The simulations show an increase in Beta even for a lateral conductivity of 10^4 S/m. However, the slow-wave effect is much less visible, and a cutoff frequency cannot be extracted. That is because of the way the waveport is defined (Figure 127). In fact, in order to see the real behavior (TE10 mode propagating in a waveguide with a smaller section) there is a need for a Thru-Line calibration (see 3.4.6).

[15] The “lateral conductivity” is the conductivity in the directions perpendicular to propagation. In the conductivity tensor (section 1.4.3) it corresponds to the first two diagonal terms of the matrix (x and y directions).

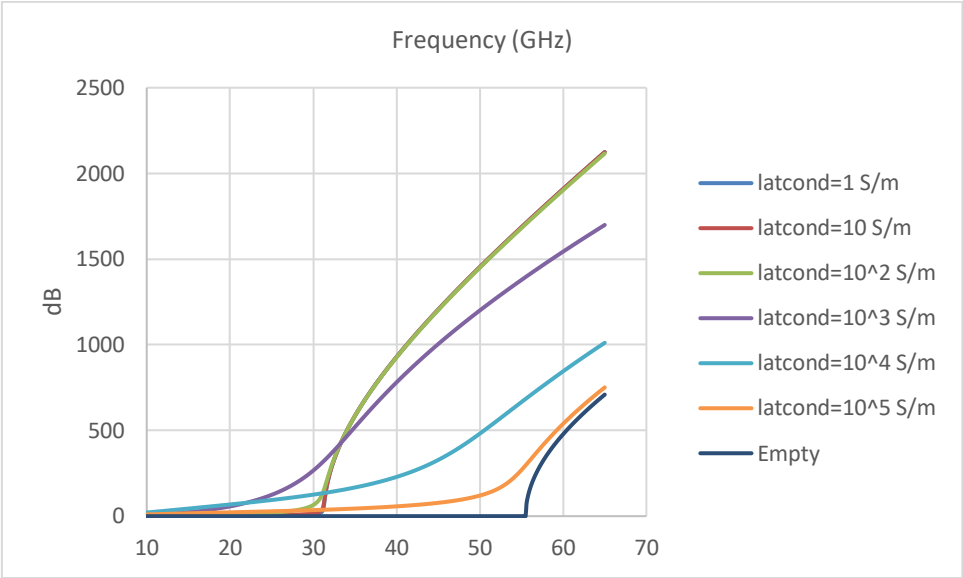

Figure 133 : Beta for different values of lateral conductivities

Though we do not see it on the propagation constant Beta, the lateral conductivity can induce high losses in the waveguides, as it is shown in Figure 134. For a slow-wave pattern of respective height and width, 75 um and 2.7 mm, an axial conductivity of $1.6*10^5$ S/m (10^{15} CNTs/m^2)and a lateral conductivity of only 10^2 S/m, the insertion losses amount to 3 dB.

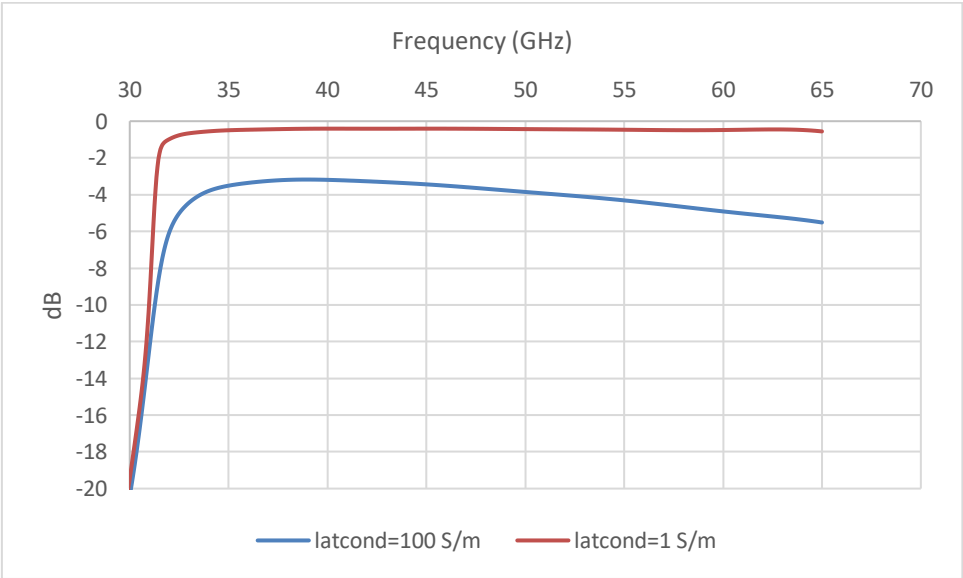

Figure 134 : Losses if 100 S/m lateral conductivity

After the description of the main properties of the slow-wave effect for the intrinsic waveguide (without the transitions from CPW to TE10 rectangular mode) we now come back to the whole structure with transitions (pillar excitation).

Adding a slow-wave pattern to our final waveguide structure is quite simple (in simulation). If the properties of the VACNTs are supposed well known, the adaptation (71-76 GHz band) is even simpler to achieve because of a larger number of variables that can be changed. The design of the structure is shown in Figure 135 as well as the S-parameters. For a slow-wave pattern height of 75 um, in order to have the same cutoff frequency as the waveguide without slow-wave pattern (Figure 99) we need a waveguide width of 1.6 mm. This is equivalent to a lateral size reduction of 59%. Longitudinally, the size reduction can be obtained from the previous curves for the propagation constant.

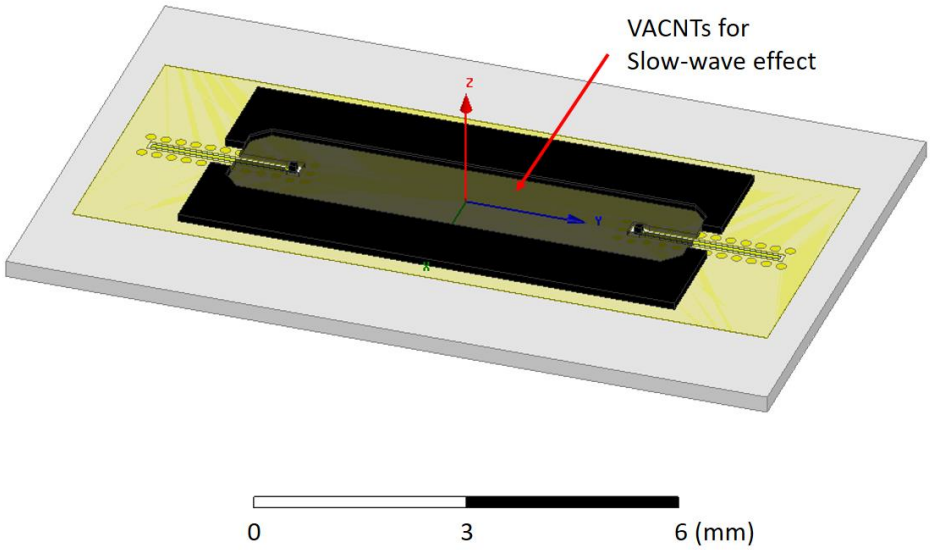

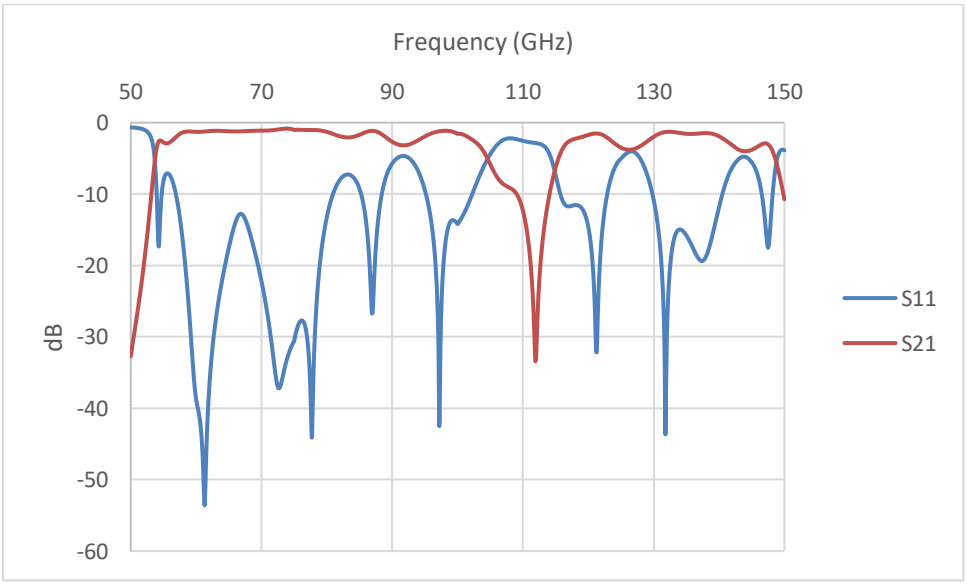

Figure 135 : Slow waves for the total waveguide, Design and Simulated S parameters

For further and more complete simulations regarding size reduction for the other passive elements of the Butler Matrix (couplers and crossovers) the reader can refer to [160] from our partners from the RFIC Lab in Grenoble.

3.4. Proof of concept at 20 GHz

Due to the fabrication difficulties, we had encountered for the simpler devices without the slow-wave effect (Chapter 2), we decided to simplify the structure used for the proof of concept of the slow-wave effect based on VACNTs. Once the fabrication process of the air-filled structures is finalized, the insight gained because of this simpler experimentation will allow for an easier design.

The design we use in this section allows us to get rid of a certain number of unknowns (such as current leakage) and makes back-simulations easier. Furthermore, the lower operating frequency makes measurements easier, without the need of a transition design for the use of CPW probes. Yet, it allows us to have better insight on properties of the CNTs we used, as well as a proof of concept of slow wave effect.

3.4.1. Simulations

The chosen structure in order to highlight the slow-wave effect is presented in Figure 136.

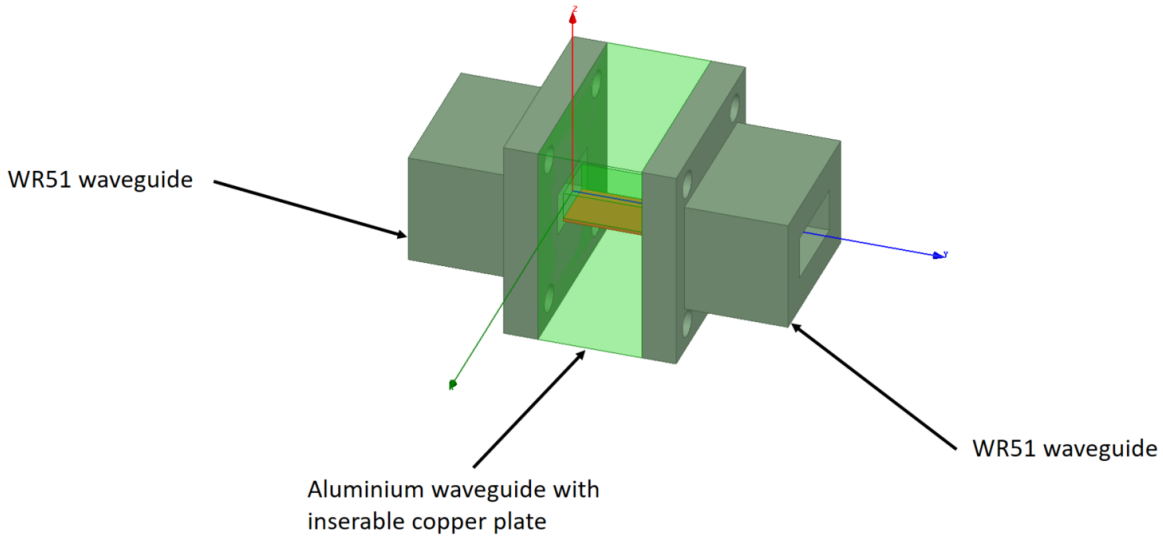

Figure 136 : Proof of concept structure

The structure consists mainly of an aluminum rectangular waveguide with a section of 8 mm width by 4.5 mm height (length of 10 mm or 15 mm). This waveguide has a cutoff frequency for the fundamental TE10 mode of 18.8 GHz. When connected to two WR51 waveguides, whose recommended bandwidth is 14.5 GHz to 22 GHz, the simulated S-parameters are plotted below (Figure 137).

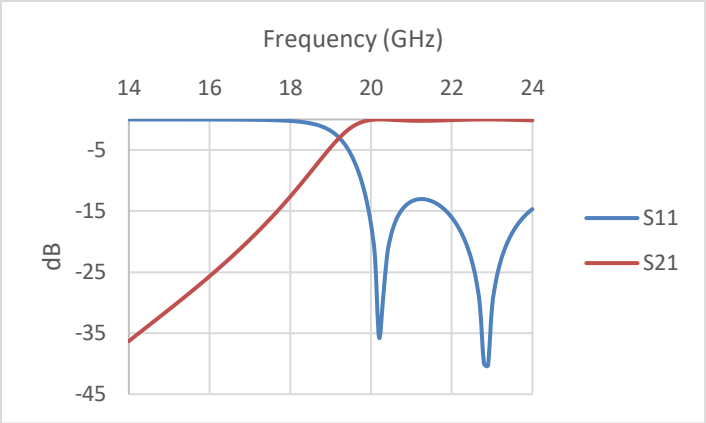

Figure 137 : Simulated S-parameters of the structure

As expected, we can observe the cutoff frequency of the aluminum waveguide between the two WR51 waveguides whose cutoff frequencies are outside of the 14-24 GHz band. We can note the adaptation stays below 10 dB in the 20 GHz to 24 GHz band.

By adding CNTs inside of the aluminum waveguide, we should see a shift in the cutoff frequency. By comparing measurements for two different length of waveguides, we can extract the propagation constant using the TL calibration (Appendix 2). However, it is difficult to grow CNTs directly inside of the waveguide, given the fabrication process (Chapter I). The idea is to insert a metallic plate (copper in our case) which would itself support the CNTs, for an easier fabrication process.

The three cases we can compare are the following ones: an empty waveguide, the waveguide with a copper plate but without CNTs and the waveguide with the copper plate supporting CNTs (Figure 138). The fabricated copper plates have a width of 8 mm (same width as the waveguide). In reality, during fabrication, 100 um were removed, in order to make sure the insertion in the waveguide was possible. The thickness of the copper plates is approximately 500 um. Two length of copper plates were fabricated, 10 mm and 15 mm, for each length of aluminum waveguide.

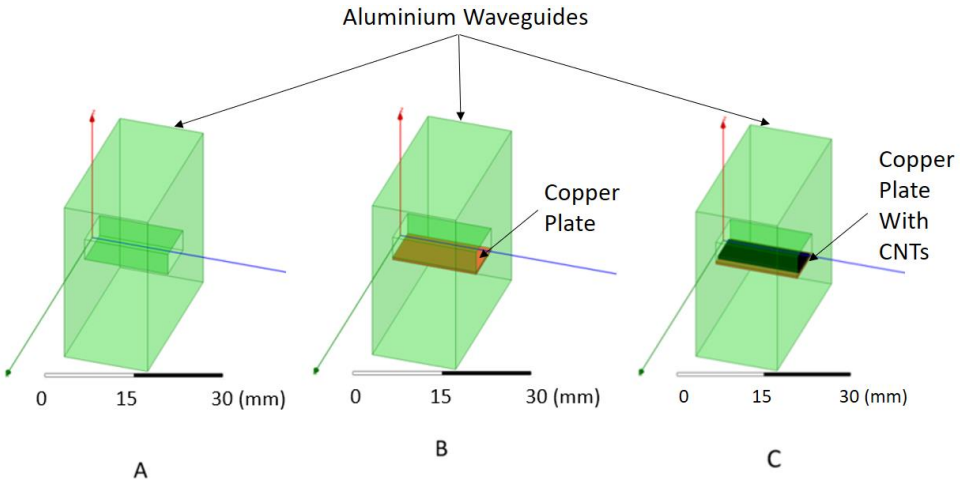

Figure 138 : The three scenarios, A. Empty waveguide, B. Copper Plate without CNTs and C. Copper plate with CNTs

We can simulate the S-parameters of the three scenarios and superimpose the data on the same graph in order to see the frequency shift (Figure 139).

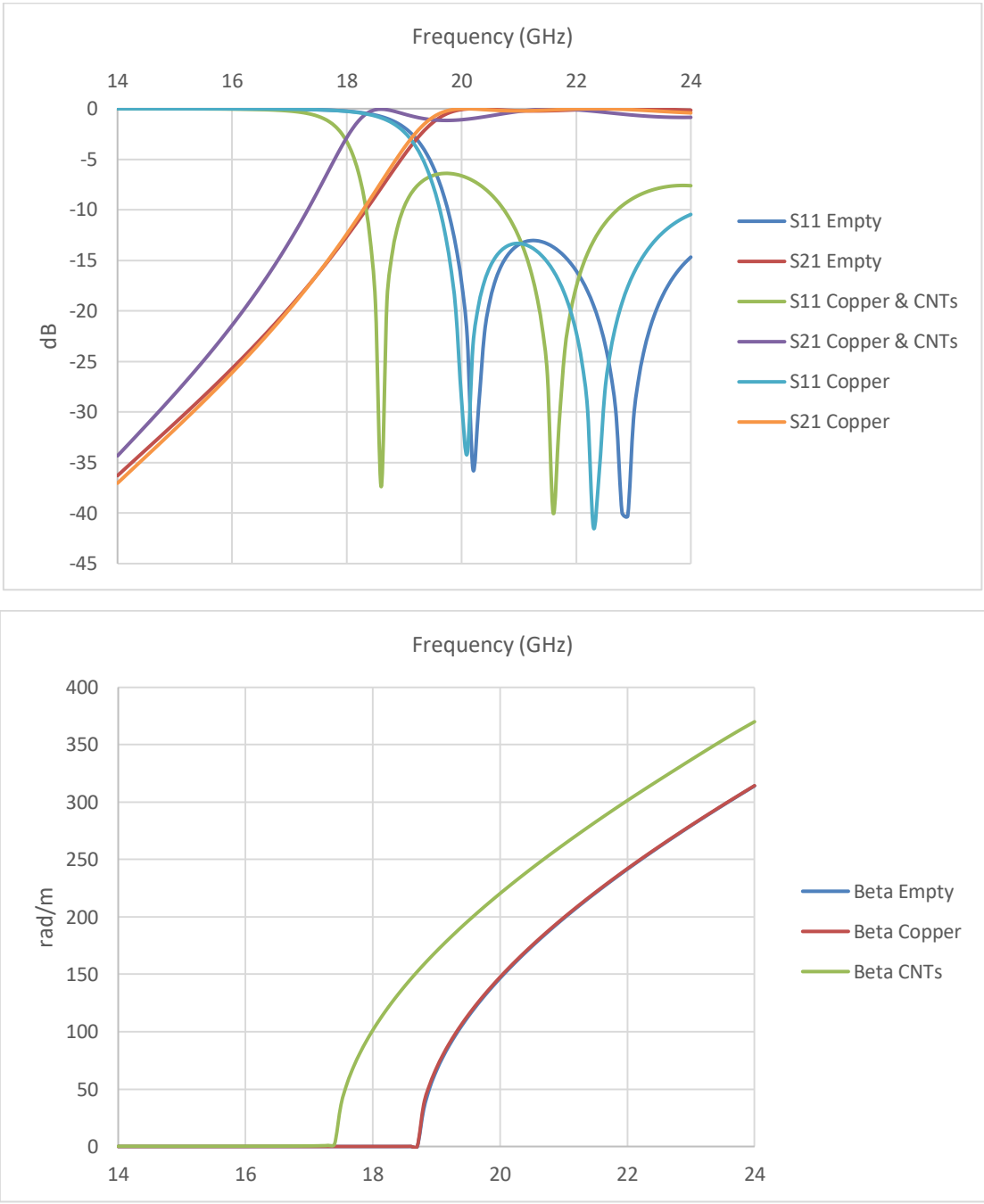

Figure 139 : Cutoff frequencies in the three scenarios, Above, S-parameters, Below, Propagation constant

In scenario B, when only the copper plate is inserted in the waveguide, the cutoff frequency does not shift compared to scenario A. This is expected because the cutoff frequency is determined by the width of the waveguide for the TE10 mode, and adding the copper plate only changes the height of the waveguide.

In scenario C, the VACNTs pattern on the copper plate has the following dimensions: 500 um height, 8 mm width and 5 mm/10mm lengths for the 10 mm long and 15 mm long plates respectively. The filling factor, ratio of CNT height to waveguide height, is 12.5%. The cutoff is shifted to lower frequencies (approximately 1 GHz).of CNTs induce the slow wave effect and the cutoff is shifted to lower frequencies (approximately 1 GHz).

3.4.2. Fabrication of the devices

The two aluminum waveguides were fabricated in XLIM, using an electroerosion fabrication process . The two waveguides have different lengths (15 mm and 10 mm), in order to be able to extract the propagation constants by a simple Thru-Line calibration. Multiple copper plates were fabricated and sent to CINTRA in order to transfer CNTs on them.

In order to be able to transfer the CNT patterns on the copper plates, those were previously polished . Indeed, if the roughness of the receiving substrate during transfer is too high, (above several hundreds of nm) the CNTs do not adhere uniformly and transfer is not possible. Furthermore, given the high temperatures of the transfer process (200 °C) and the ambient humidity levels in Singapore (80% humidity in average in the year), we decided to electrolyze the copper plates with gold to avoid oxidation.

The CNTs were transferred using 500 um spacers, in order to obtain the wished height. A picture of the devices is shown in Figure 140.

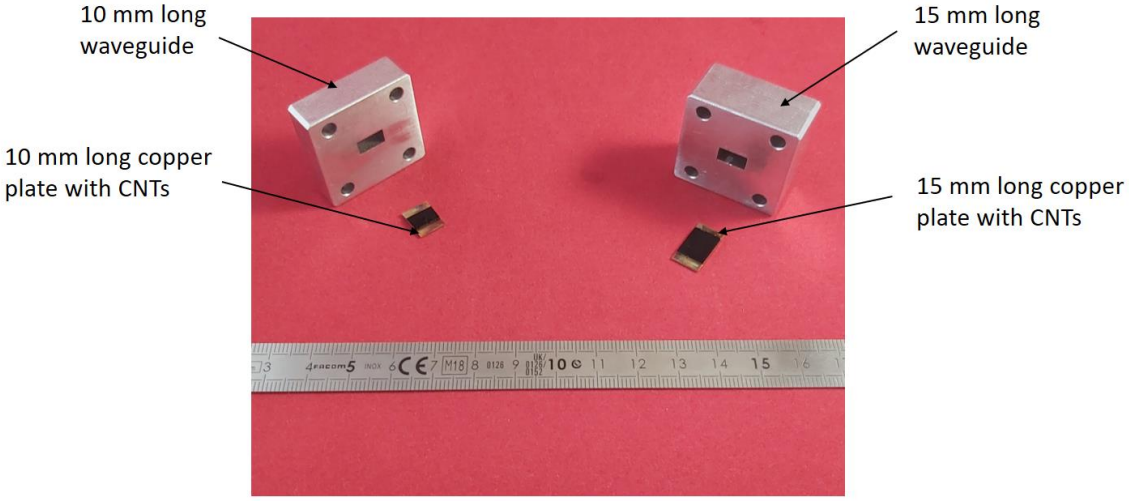

Figure 140 : Aluminum waveguides and Copper plates with transferred CNTs

3.4.3. Measurements for classic CNTs

The two waveguides (15 mm and 10 mm long), in the different scenarios A, B and C (Figure 141), were measured using a ZVA 40 VNA from Rhodes&Schwartz, transitions from coaxial to rectangular WR51 (Inoveos) and Maury Stability Plus coaxial cables. The setup is shown in figure 139.

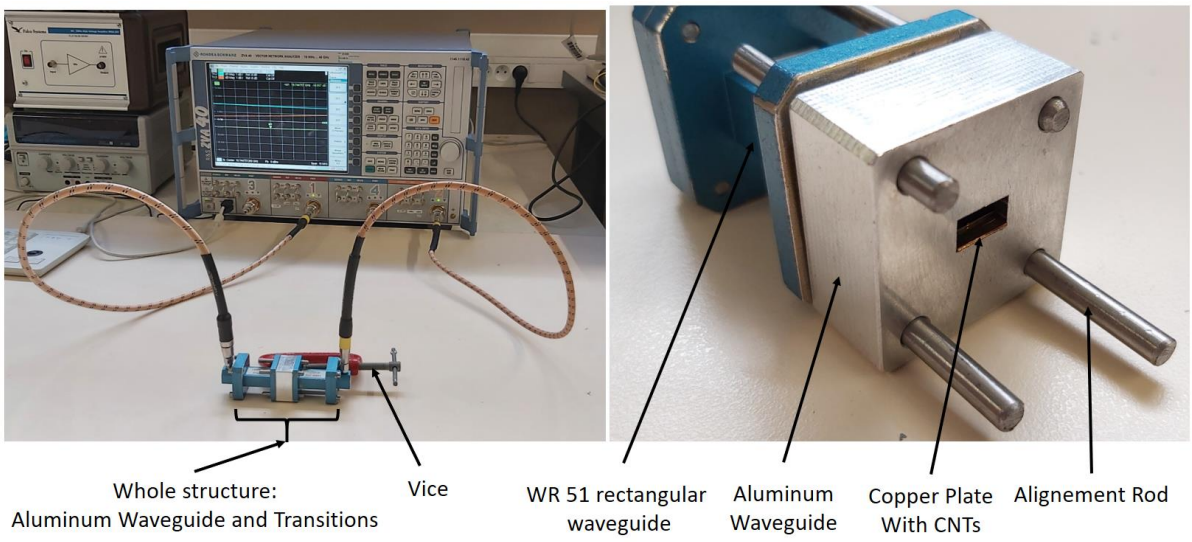

Figure 141 : Setup for the slow-wave measurements

The measurements are plotted in Figure 142 and 143.

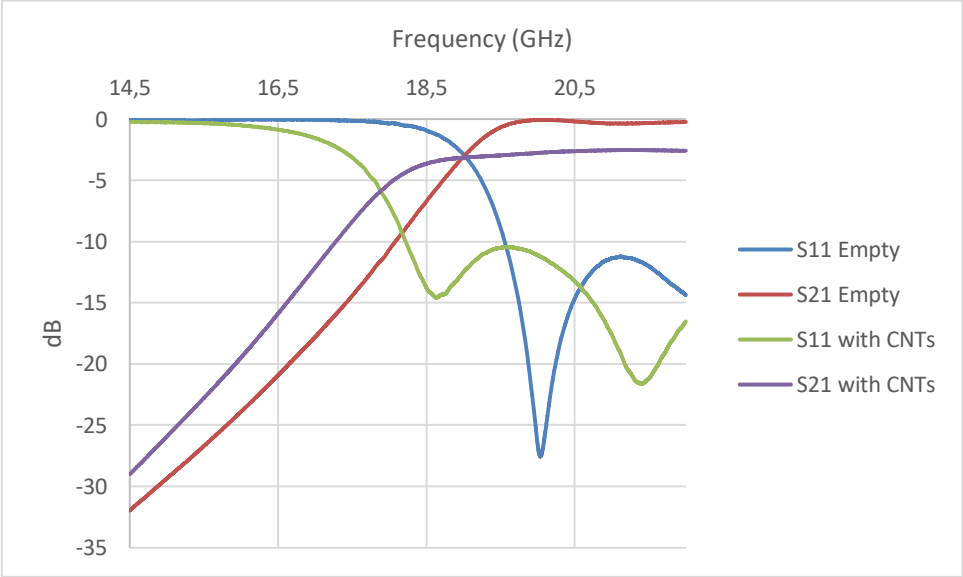

Figure 142 : Measurements for the 15 mm long waveguides

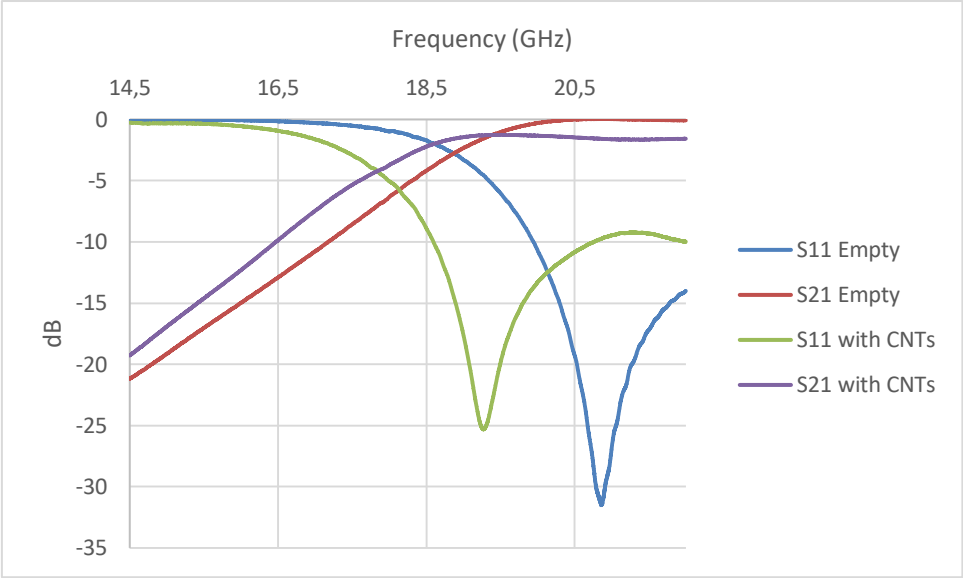

Figure 143 : Measurements for the 10 mm long waveguide

We can clearly observe a shift to lower frequencies of the cutoff frequency. Furthermore, the shift is roughly around 1 GHz, which is coherent with the measured heights of the CNTs placed on the copper plates (500 um).

Using the Thru-Line calibration (Appendix 2) we can extract the propagation constant of the waveguide in the three scenarios, the results are plotted in Figure 144 and superimposed with the simulations.

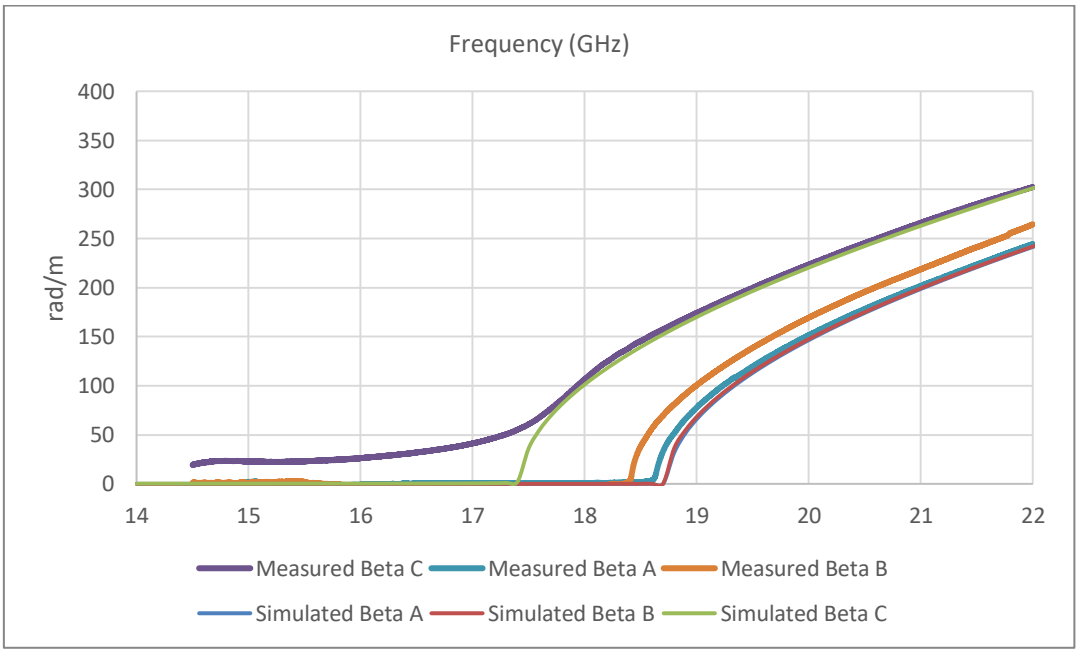

Figure 144 : Simulated and measured Propagation constants for the three scenarios, A, Empty waveguide, B, Copper Plate Only, C, Copper Plate with CNTs

First, we can note that the cutoff frequency of the simulated waveguide is a bit below the simulated one. This is due to the fabricated waveguides having a slightly larger width. Second, we can clearly see a shift for the measurements in scenario B. This is due to the copper plate being narrower (smaller width) than simulated. In that case, we have space between the sides of the copper plate and the lateral walls of the aluminum waveguide leading to capacitive effects and a frequency shift (ridged waveguide 3.1.1). Finally, because these effects should accumulate with the slow wave effect, we should have a bigger shift measured than in the simulations for a height of 500 um. But, as shown in Figure 145, during transfer, the CNTs can bend partially due to the force applied. This phenomenon has been observed before for other devices and close-up SEM images of the slow wave samples should give useful insight. In the bottom part of the slow-wave pattern the conductivity is anisotropic, and no slow-wave can propagate, reducing the equivalent filling factor and the slow-wave effect.

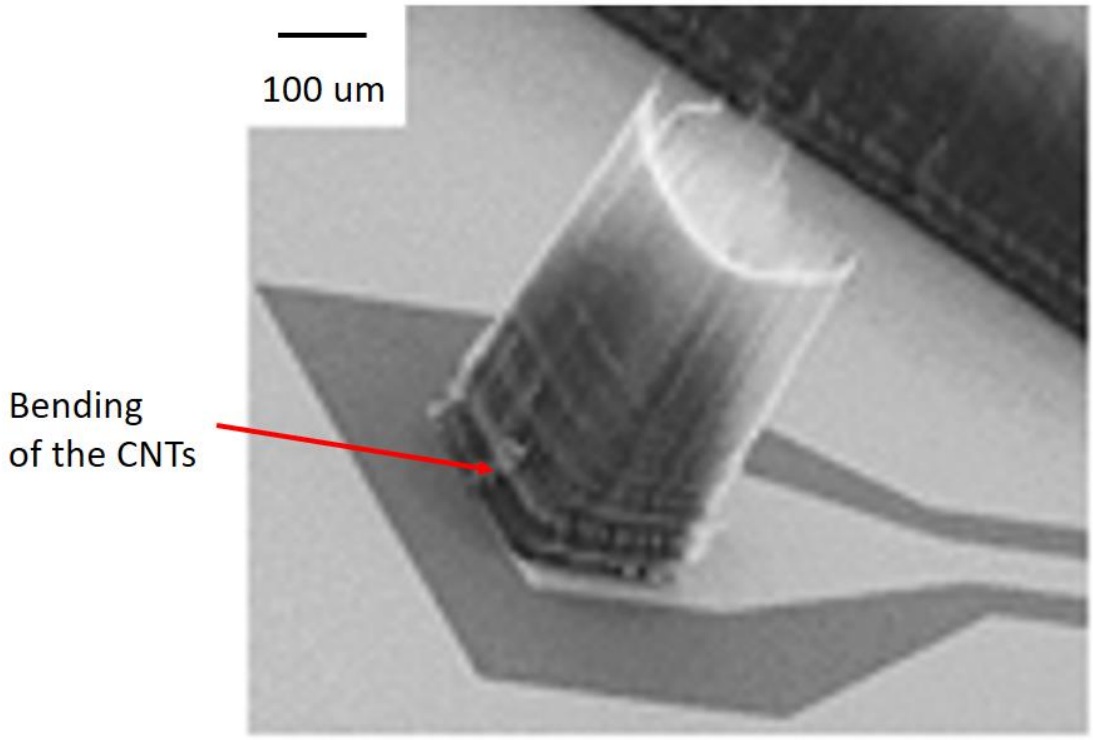

Figure 145 : SEM picture of the bending of the CNTs during transfer process on a previous device

However, we do have high losses that we do not explain. These losses most likely come from lateral conductivity. That hypothesis will be tested later in section 3.5. .

3.4.4. Measurements for the sparse CNTs

Of the CNT samples that were made in CINTRA, it was decided to verify the impact of density on the slow-wave effect. On one of the copper plates that was sent, low density CNTs were transferred. The low density CNTs were obtained because of diffraction effect through the chromium mask while catalyst deposition for CNT growth. The difference of density is visible, in the SEM picture of Figure 146.

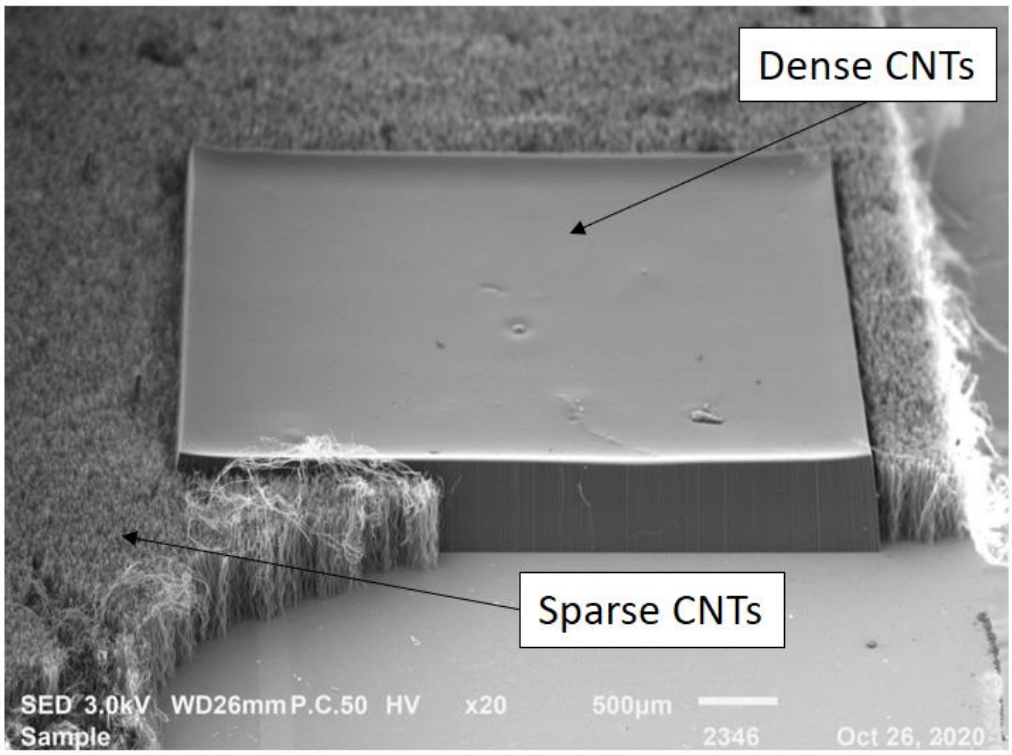

Figure 146 : SEM image of the lesser dense CNTs

Still, even with a lower density, the cutoff frequency shift was still approximately the same, as shown in Figure 147. The propagation constant cannot be extracted because this type of CNTs was only transferred on a 10 mm plate.

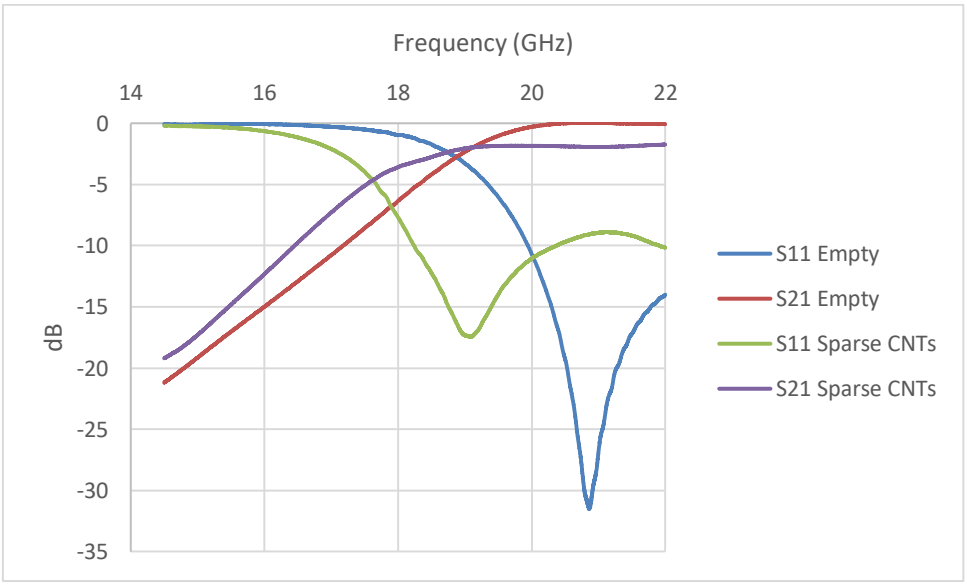

Figure 147 : Frequency Shift for CNTs with lower density

These measurements show that the slow-wave effect we are measuring is due to the conductivity of the CNTs. Indeed, in order to increase phase velocity, one can simply increases the effective permittivity. This can be done by inserting a high permittivity medium in the waveguide. In our case, for the shift we have and for a height of 500 um, we would need a material of permittivity 10. Though the conductivity of VACNTs has been proven before, the fabrication process could be flawed and the material a dielectric. However, from these measurements, we can infer we are witnessing field separation and slow-wave propagation. Indeed, for two different densities of the same material, the shift is almost the same. If the material was a dielectric, the permittivity would not be the same (effective medium approximation, Bruggeman's models) and the shift would vary.

However, we still have to determine the source of the losses witnessed. Back-simulations will be done in section 3.4.6.

3.4.5. DC measurements

To check if there was lateral conductivity, it was decided to do DC measurements. A schematic of the setup is presented in Figure 148.

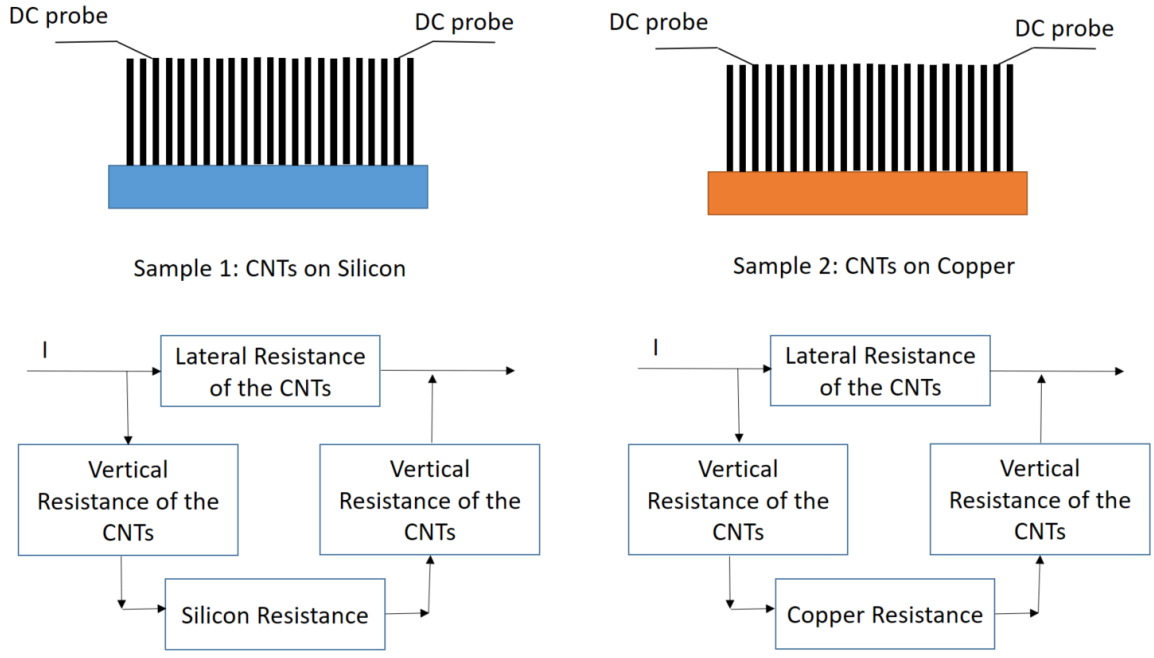

Figure 148 : DC measurements for CNTs on two types of substrates, with the "equivalent" circuit

The DC measurement for sample 1 gives a resistance of 300 Ω. The measurement for sample 2 gives 30 Ω. The distance between the DC probes remained the same for the two measurements.

Silicon resistivity is above 10^4 Ω.m as given by the manufacturer datasheet. Furthermore, the resistance of the silicon wafer was measured (still for the same distance between the two DC probes) and was found to be $30*10^6$ Ω. This means silicon resistance is very high compared to the measured value (300 Ω).

We can approximate the measured value for sample 1 ($R_{sample1}$) with the following formula (c.f. equivalent circuit Figure 146):

$$\frac{1}{R_{sample1}} = \frac{1}{R_{lat}} + \frac{1}{R_{vert} + R_{silicon} + R_{vert}}$$

With, R_{lat} the lateral resistance of the CNTs, R_{vert} the vertical resistance of the CNTs and $R_{silicon}$ the resistance of the silicon wafer.

Because, we have:

$$R_{silicon} \gg R_{sample1}$$

We can make the approximation:

$$R_{lat} \approx R_{sample1}$$

We can approximate the measured value for sample 2 ($R_{sample2}$) with the following formula (c.f. equivalent circuit Figure 146):

$$\frac{1}{R_{sample2}} = \frac{1}{R_{lat}} + \frac{1}{R_{vert} + R_{copper} + R_{vert}}$$

With, R_{copper}, the resistance of the copper substrate. This resistance was measured and is negligible in front of the measured value.

Furthermore,

$$R_{lat} \gg R_{sample2}$$

Meaning that we can make the approximation:

$$R_{vert} \approx \frac{R_{sample1}}{2}$$

Let us note here that R_{vert} includes the contact resistance due to transfer and the contact resistance with the DC probe.

From these measurements, we can suppose the lateral conductivity of the forest is at least ten times higher than its axial conductivity.

Finally, the measured silicon resistance is $30*10^6$ Ω i.e 10^5 times more than the evaluated lateral conductivity of the CNTs (300 Ω). If we consider an equivalent isotropic material similar to silicon with a resistance of 300 Ω, its resistivity would be 10^5 times lower. If we suppose our silicon resistivity is equal to 10^{-4} S/m (datasheet $\rho_{silicon} > 10^4\ \Omega.m$), this gives a lateral conductivity for the equivalent material of 10 S/m. The lateral conductivity of the VACNTs is probably close to this value.

Note: In all the above, we considered resistance to be directly proportional to the conductivity. However, this is not necessarily true, the field lines do not have the same shapes for different conductivities, the current path might differ leading to different coefficients between conductivity and resistance.

3.4.6. Back Simulations

In this section, we will try to explain the losses observed, through back-simulations, of the fabricated devices.

The first reason that was considered to explain the losses was the contact resistance due to transfer. Thus, we simulated our structures with a low conductivity layer between the copper plate and the bottom of the VACNTs pattern. The simulated propagation constants are plotted in Figure 149 for three different cases: (1) Ideal case: the contact resistance between the VACNTs and the copper is supposed to be zero, (2) Lossy transfer: a layer of 1 um is added between the CNTs and the copper plate with conductivity 10 S/m, (3) Levitating CNTs: the layer of 1 um is considered to be air (infinite resistivity).

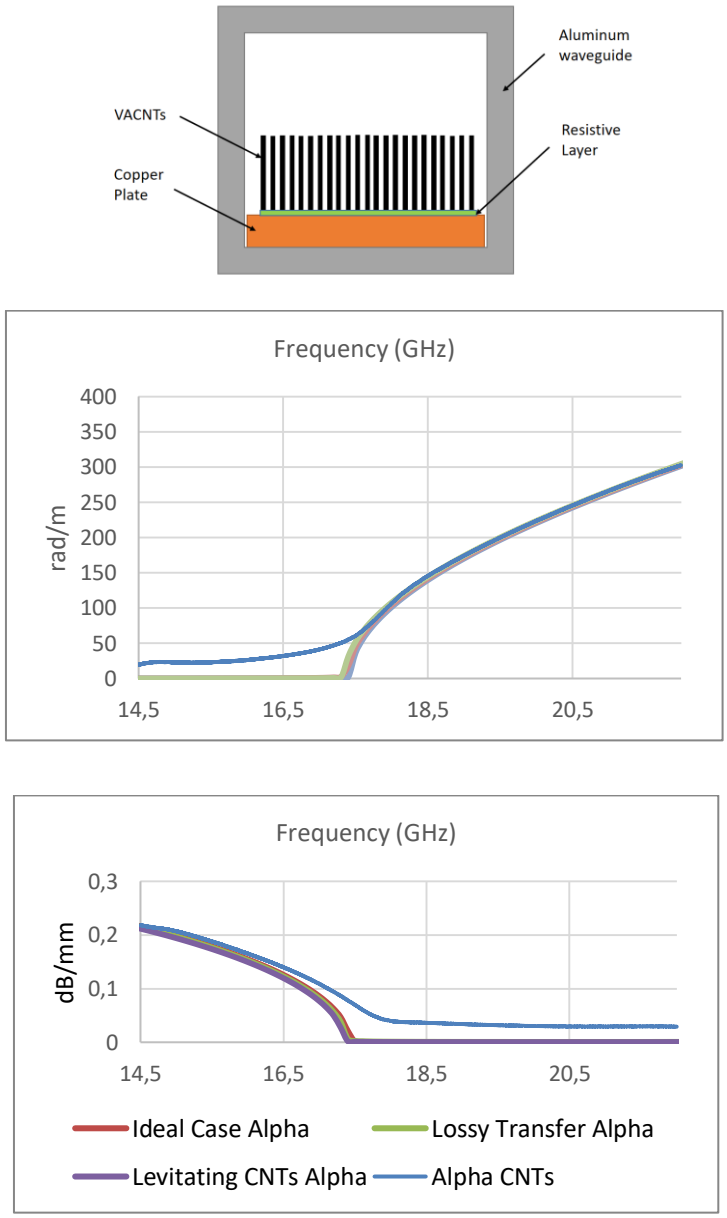

Figure 149 : Top, simulation Setup, Middle, Simulated Beta, in the three simulation setups (superimposed with measured Beta), Bottom, Simulated Alpha in the three simulation setups (Superimposed with measured Alpha)

It seems like the quality of the transfer process does not impact the results. This is simply explained by the fact that as long as there is a region of space inside the waveguide where the conductivity is “anisotropic vertical” and the electric field cannot penetrate. The electric field is confined to a smaller area while the magnetic is not, giving birth to the slow-wave effect.

Note: Poor contact between the copper plate and the waveguide was also simulated, the slow-wave effect is not impacted. It was verified in measurements by gluing the copper plate with silver glue, to no avail. This is coherent with the explanation given above.

The second hypothesis was poor axial conductivity inducing metallic losses due to the current inside the VACNTs pattern. The simulation results are plotted below (Figure 150).

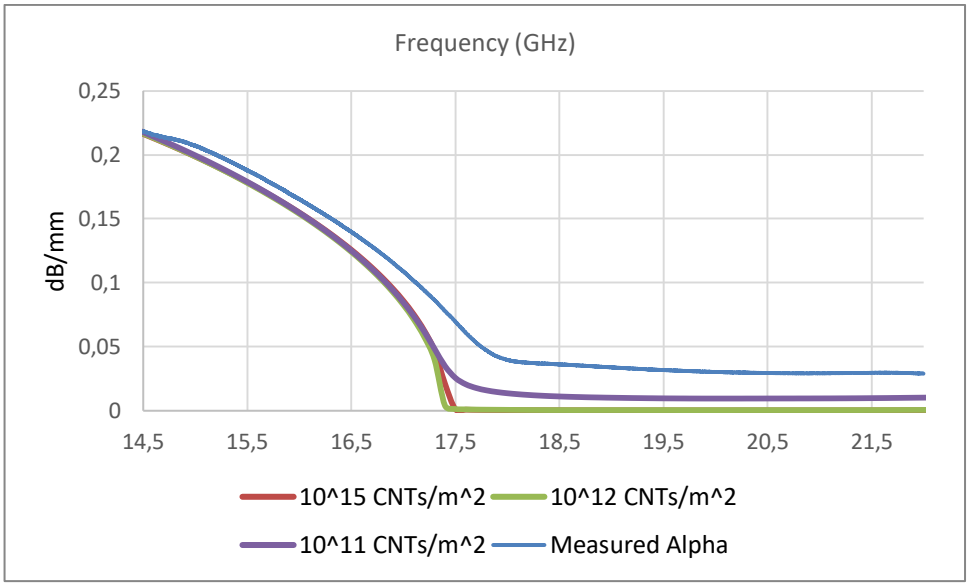

Figure 150 : Attenuation Constants For different CNT densities (measured attenuation superimposed)

As we can see, the low density cannot explain the high losses. Also, we can note that we have different results from section 3.3 simulations. This is due to the definition of the waveports and the way the propagation constants are calculated in HFSS. It is unclear how HFSS deals with anisotropic materials in waveports, the present simulations together with the Thru-Line calibration give more accurate results.

The third hypothesis was the presence of lateral conductivity. The simulated results are plotted below (Figure 149). For each simulation two variables were changed, the axial conductivity (density of the CNTs/m^2) and the lateral conductivity. The idea was to find the correct couple to fit both the measured propagation constants Beta and Alpha. However, it seems like the couples fitting the measurements before cutoff are different from the ones fitting measurements after cutoff. The reason is probably that the height used is not the correct one due to bending of the CNTs (c.f. Figure 145).

We can also note (Figure 151) that for higher values of lateral conductivity (100 S/m) the slow-wave effect is less present, the propagation constant increases less. This is coherent because the magnetic field is hindered by lateral conductivity.

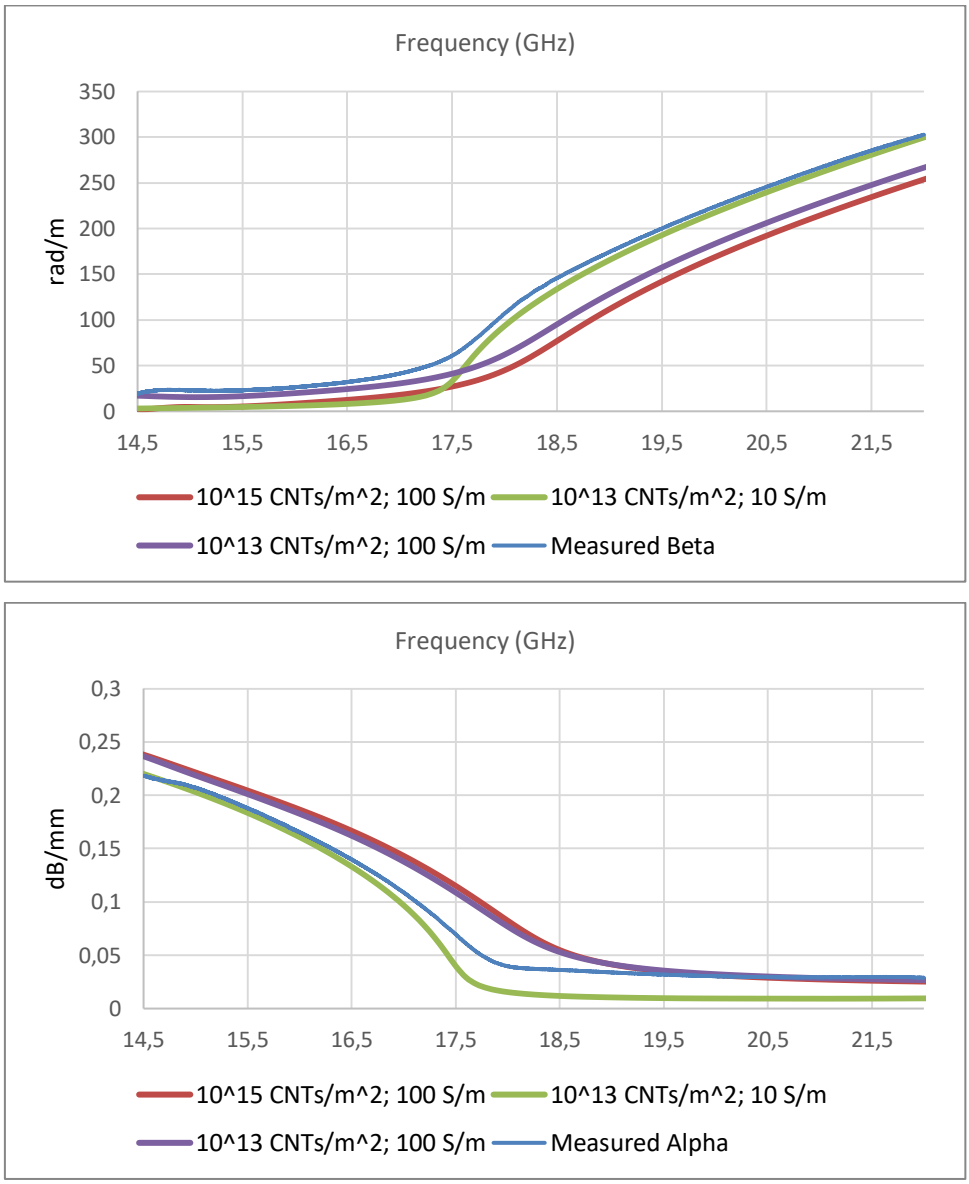

Figure 151 : Above, Beta, Simulated and Measured, Below, Alpha, Simulated and Measured

At this point it is interesting to compare our results with [218], from RFIC lab. The structure and measurements are shown in Figure 152 below.

The structure relies on the same principle as ours i.e. air-filled waveguide partially filled with an anisotropic conductive material. The measurements are made at a higher frequency (up to 70 GHz) than in our case (20 GHz). However, the same insertion losses are witnessed (Figure 152 b.). These losses are not explained in the article, their origin is under investigation.

In order to see if these losses are due to lateral conductivity (and not the fabrication process of the SIW), it would be interesting to replace the CNTs in our structure by this nanoporous membrane filled with metallic nanowires.

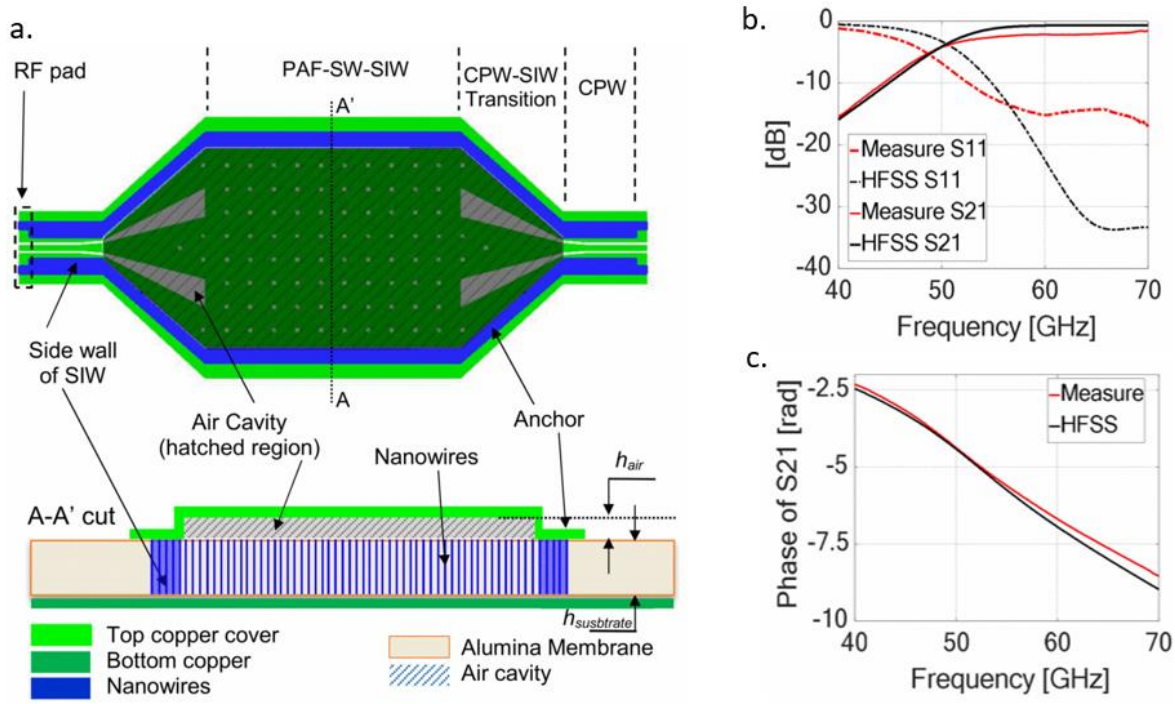

Figure 152 : a. Schematic of the structure, b. Simulated and Measured S11 and S21, c. Simulated and Measured S21 phase

3.5. Conclusion

We started this section with a brief state of the art of the existing miniaturization methods for SIW. We then had a particular focus on the slow-wave effect. The use of VACNTs for slow-wave effect was then simulated for our structures (air-filled SIW with VACNTs walls) and different parameters of the slow-wave pattern were studied (height, width, density, etc.).

We then decided to showcase the slow-wave effect at lower frequencies (20 GHz), for easier fabrication. A new type of design was simulated and measured, and the propagation constants were extracted. To the knowledge of the author, the slow-wave effect due to CNTs was demonstrated for the first time. We then tried to explain the high insertion losses.

As perspectives, it would be interesting to replace the VACNTs of our device with other anisotropic conductive materials: nanoporous membrane filled with metallic nanowires, PECVD VACNTs with lower density, VACNTs coated with Boron-Nitride (an insulator) [305], etc.

Chapter 4: Interconnections

This last chapter describes a complementary work to the functionalized interposer technology presented in the previous chapters. It is dedicated to a prospective approach applied to RF interconnects based on VACNTs. The main idea is to propose an alternative technology to the wire-bonding one.

Fortunately, CNTs is an ideal material for high frequency interconnects. Indeed, CNTs possess properties particularly interesting in the case of interconnects. CNTs are highly electrically conductive [44], highly flexible [49], and highly thermally conductive [56], have low CTE [306], and can withhold extremely high current densities [307]. These properties led to CNTs being intensely studied, in recent years, for high frequency interconnects [308]–[310]. Indeed, with higher frequencies, interconnects tend to get smaller, leading to certain technological issues (e.g. electro-migration [311]) for other more conventional materials (metal alloys).

In particular, VACNTs bundles as flip-chip bumps have been studied in the past [81], [87], [106]. However, the flip-chip technology has one major drawback; the “on wafer” measurements is not possible, due to the chip being face down. Furthermore, at higher frequencies (above 40 GHz), wire-bonds are usually not used the chip to the substrate carrier due to their high inductance behavior. That is why we propose an alternative approach (entirely compatible with the smart interposer) to connect chips on substrate carrier. The functionalized cover we propose is composed of CNT based RF and DC bridges respectively for RF and bias interconnects. The topology of the functionalized cover is described in Figure 153.

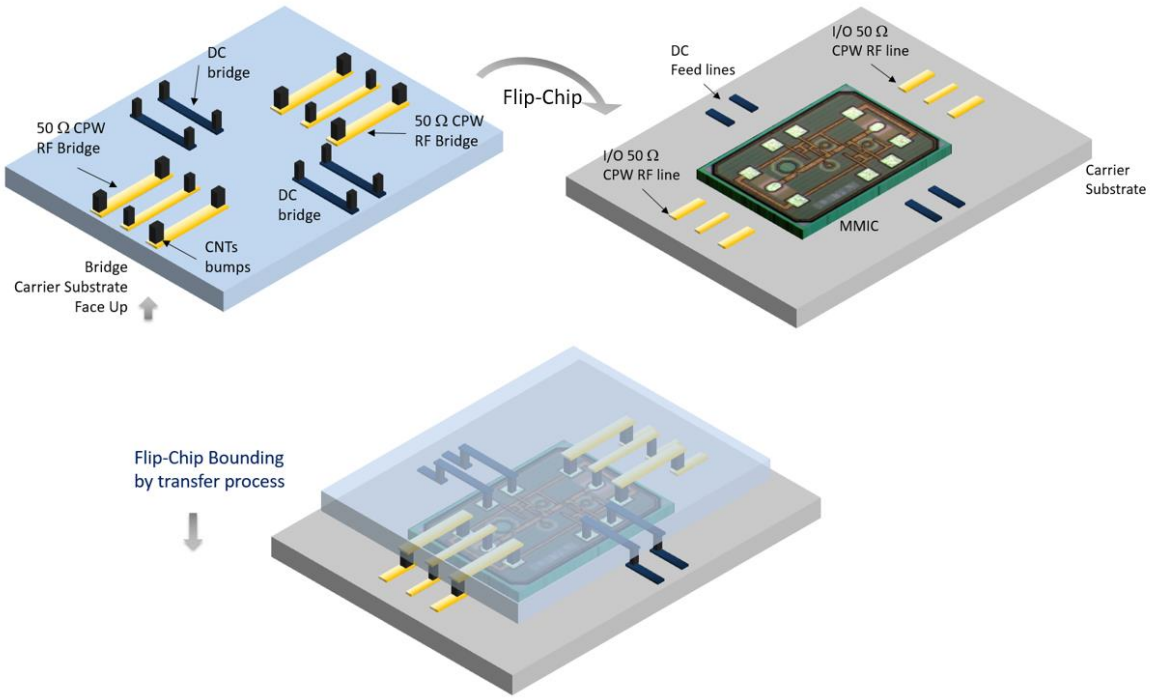

Figure 153 : Topology of the DC (black lines) and CPW (yellow lines) Interconnects on the functionalized cover (up left) for a MMIC facing upwards (up right)

In addition to the DC and RF interconnects, this cover allows the incorporation of other VACNTs packaging properties described in Chapter 1, such as EM shielding and thermal management of the MMIC. A schematic for such a structure is given below in Figure 154.

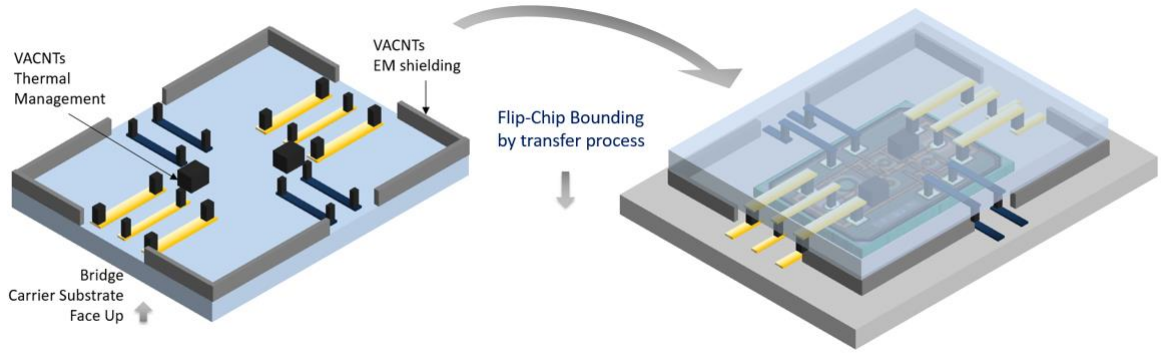

Figure 154 : Schematic of a fully functionalized cover with interconnects, EM shielding and Thermal management

This topology is particularly interesting because it has the advantage of the wire bonding process (MMIC chip facing upwards) while being transposable at higher frequency because the inductance of the VACNTs bridge (CNT bumps and line on the cover) is much lower.

In this chapter, we will start by a brief state of the art on interconnects technologies at high frequencies, we will then propose a test structure for the proof of concept of VACNTs bridges. This test structure will be simulated, the fabrication process will be slightly improved in order to be compatible with interconnects of a few microns, and measurements will be interpreted.

4.1. State of the art

In this section, we will go over the following different topics, in order:

- Problems of electro-migration in metallic interconnects
- Wire bonding compensation at high frequencies
- Previous results on VACNTs interconnects

4.1.1. Electro-migration in metallic interconnects

The use of higher frequencies in telecommunications implies smaller dimensions for passive devices. In particular, for interconnects, it means smaller diameter. Thus, it is possible that the electric field present in these interconnects creates very high current densities. For current densities above 10^6 A/cm^2, the electro-migration phenomenon can appear.

When the electric field is high enough, the force applied to the metallic cations is higher than the force due to the “electronic wind”. The resulting force (F) is given by:

$$\mathrm{F} = Z^* q \boldsymbol{E} = Z^* q \rho \boldsymbol{j_e}$$

With, Z^* the effective number of charges, q the elementary charge, and $\boldsymbol{E}$ the electric field given by product between the current density $\boldsymbol{j_e}$ and the resistivity of the material ρ. When this force is high enough the cations migrate toward the anode [312].

The cations diffusion caused by electro-migration usually happens at the grain boundaries[16] of the metallic interconnects [313]. The equation linking the mass flux (J) to this diffusion is given in [312] by:

$$J = -D^* \frac{dC}{dx} + \frac{CD^*F}{kT}$$

With, D^* the diffusion coefficient, C the atom concentration, k Boltzmann's constant, T the temperature, and F the generalized form of the moving force.

The moving force F results from three phenomenon, the force from the electronic wind, the gradient of temperature and the mechanical stress [314]. Inserting this in the previous equation we obtain:

$$J = -D^* \frac{dC}{dx} + \frac{CD^*}{kT}(-qZ^*E - K\frac{\partial T}{\partial x} + \Omega \frac{\partial \sigma}{\partial x})$$

With, K the thermal conductivity of the material, Ω the atomic volume, and σ the mechanical stress.

In the case of a homogenous material, the concentration gradient can be considered equal to zero, and for current densities around 10^6 A/cm^2, the gradient of temperature also. We obtain the following simplified equation:

$$J = -\frac{CD^*}{kT} qZ^*E + \frac{CD^*}{kT}\Omega \frac{\partial \sigma}{\partial x}$$

This equations shows that after a certain time the flux of cations due to the electric field is compensated by the flux due to compression, giving a critical length below which there is no resulting mass transfer [314]:

$$L_c = \frac{\Omega \sigma_c}{Z^* q \rho j_e}$$

As a result of the electro-migration effect, cracks can appear in the interconnect (as shown in Figure 154) leading to poor performances and even possible breakage.

Different solutions are proposed in the literature to palliate this problem, from changing the materials [311], [315] to changing the topologies [316].

[16] The interconnect is not monocrystalline but composed of multiple crystal grains.

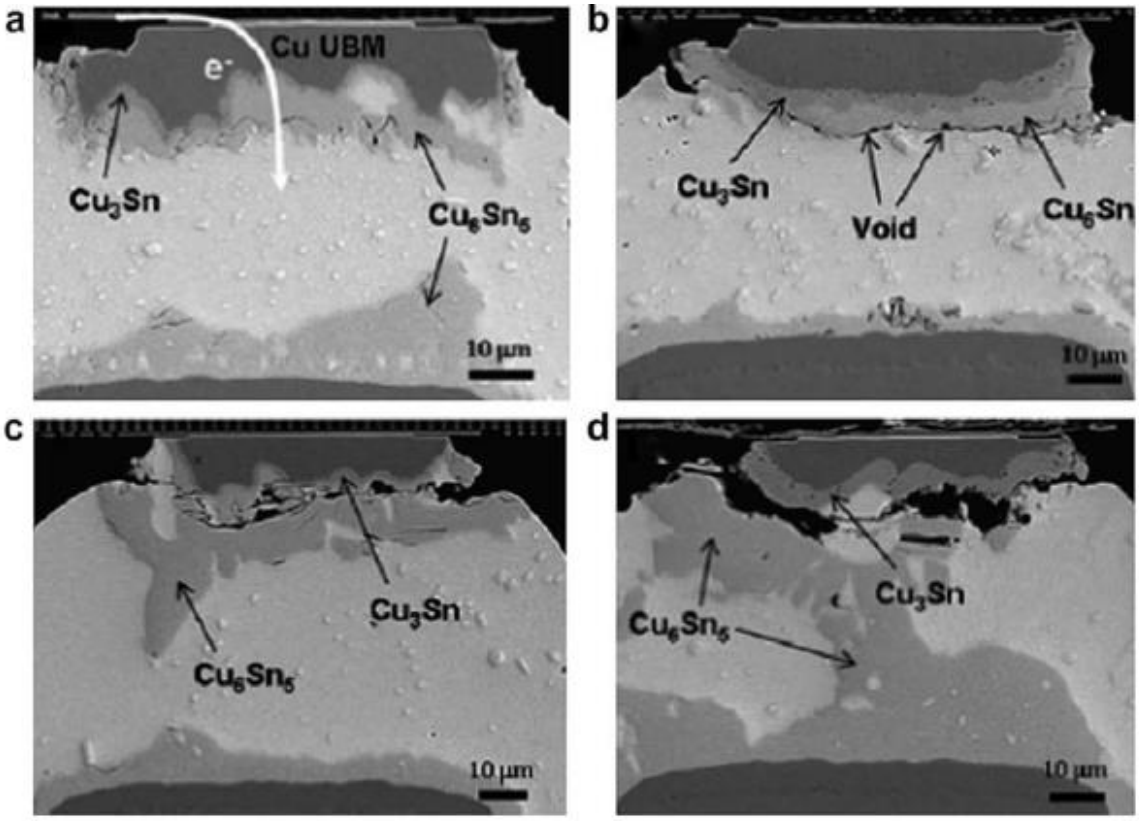

Figure 155 : (a) Initial Interconnect, (b), (c) and (d) Propagating crack in the interconnect until final open failure [317]

4.1.2. Wire bonding Compensation

At higher frequencies (above 40 GHz), the reactance of wire-bonds (equivalent to an inductance) becomes difficult to compensate, resulting in poor adaptation and performances of the bonded devices. In this section, we will present the existing solutions to either reduce this reactance or compensate for it.

The first way to decrease wire-bonds inductance is to double them. Indeed, by putting two wire-bonds in parallel instead of one, the resulting inductance (L_{eq}) is given by:

$$L_{eq} = \frac{L_1 L_2 - M^2}{L_1 + L_2 - 2M}$$

With, L_1 the inductance of the first wirebond, $L_2$the inductance of the second wire-bond, and M the mutual inductance. Because, we have $\mathrm{M} < \min(L_1, L_2)$, the resulting inductance is lower than $L_1$and L_2. We can also note that the mutual inductance is squared in the numerator and not in the denominator, meaning that decreasingM, will decrease the resulting inductance. In practice, the two wirebonds are placed as far to each other as possible. When the dimensions of the outgoing/ingoing pads, we have this typical V shape, shown in Figure 154.

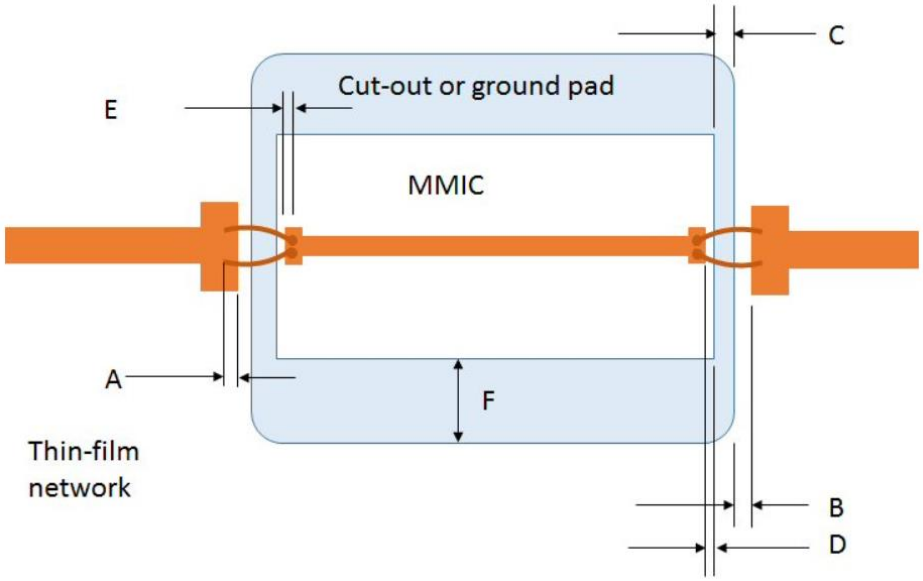

Figure 156 : V shape of the doubled wire-bonds [318]

Another similar way to reduce bonding reactance is to use bonding ribbons, for which the inductance is lower [319].

However, the reactance of the wire-bonds cannot always be reduced enough and sometimes need to be compensated.

The most common compensation method is the use of capacitive pads “before” and “after” the wire-bond in order to make a Π type filter and compensate the reactance (Figure 157).

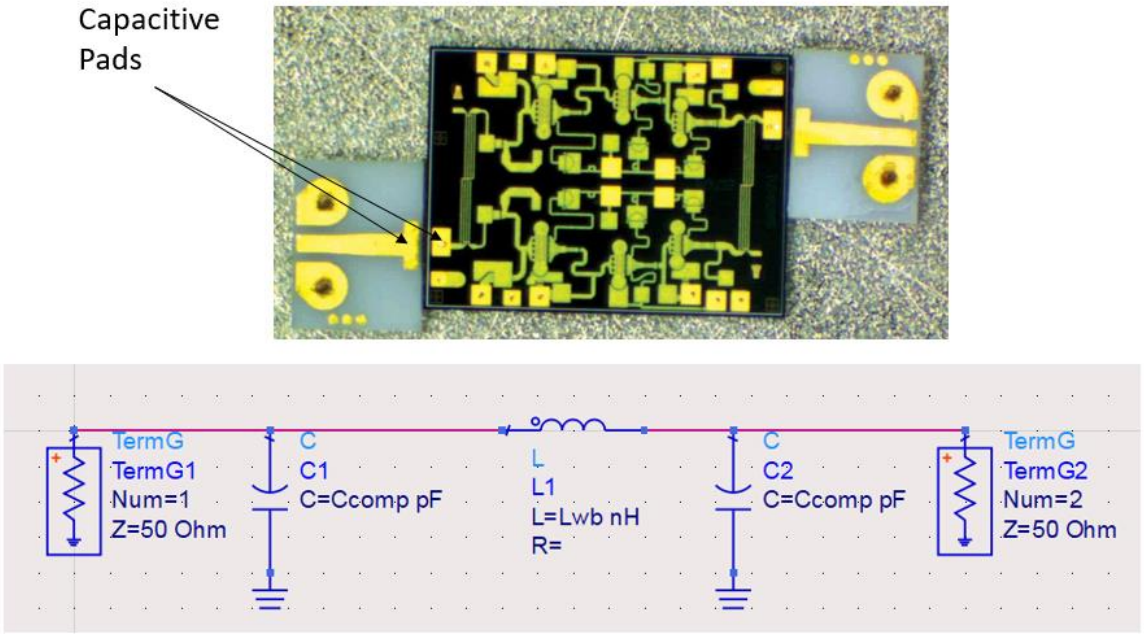

Figure 157 : Above, Photo of a device with capacitive pads for the wire-bond [320], Below, Equivalent Circuit model on ADS

Unfortunately, this simple structure does not allow to compensate for wire-bonds with important reactance at higher frequencies. Furthermore, the behavior of the capacitive pad is frequency dependent making this method narrowband.

In [321] the authors propose two solutions to compensate for the reactance, matching with a higher order filter, and self-matching half-wave wire-bonds. The two solutions are presented in Figure 158. There are different inherent problems to these two methods, but the main one is the quite narrow bands.

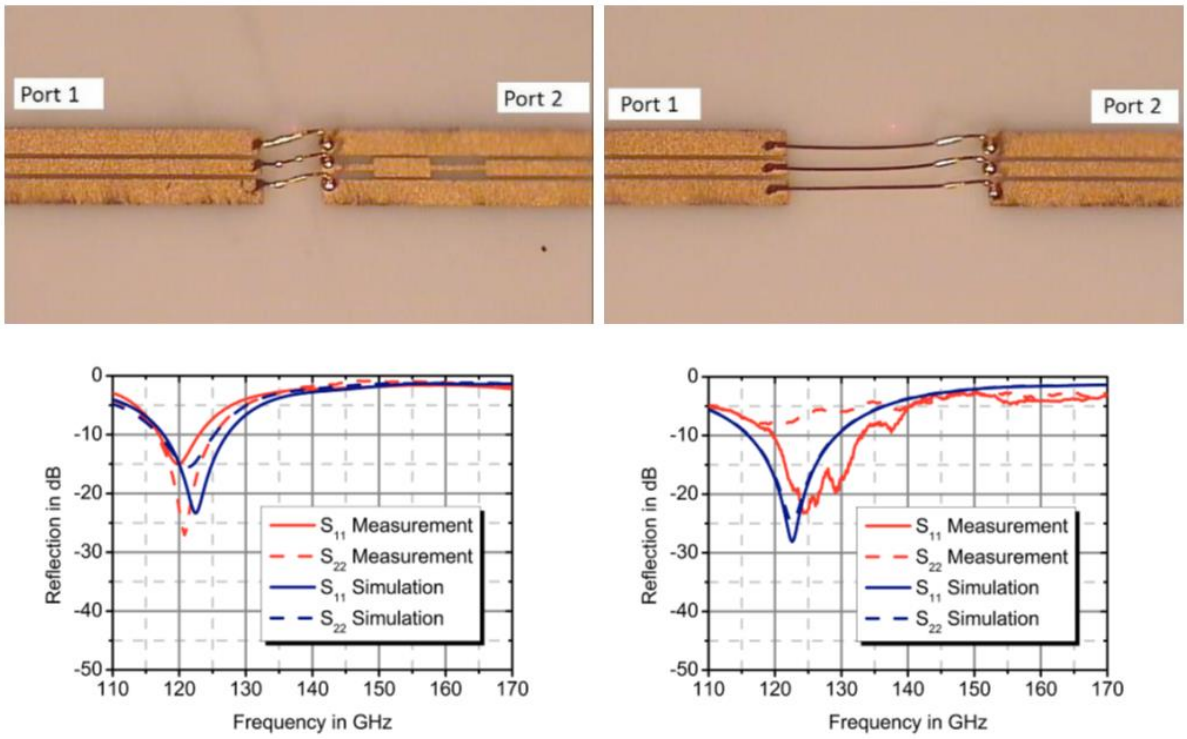

Figure 158 : Left, Photo and measurements of the higher order filter compensation, Right, Photo and measurements of the half-wave compensation

Finally, the authors in [322] manage to compensate for a 150 um long wire-bond from 10 GHz to 180 GHz (Figure 159). The idea comes from [323], where a symmetric higher order filter centered on the wire-bond is used to compensate for it. This method is more broadband than in [321] because the filter is symmetric.

The problem of this method is that it implies that both sides of the wire-bond can be designed, the motherboard and the MMIC, which is usually not the case. The MMIC is usually supplied by a third party.

That is why VACNTs bridges can be particularly interesting.

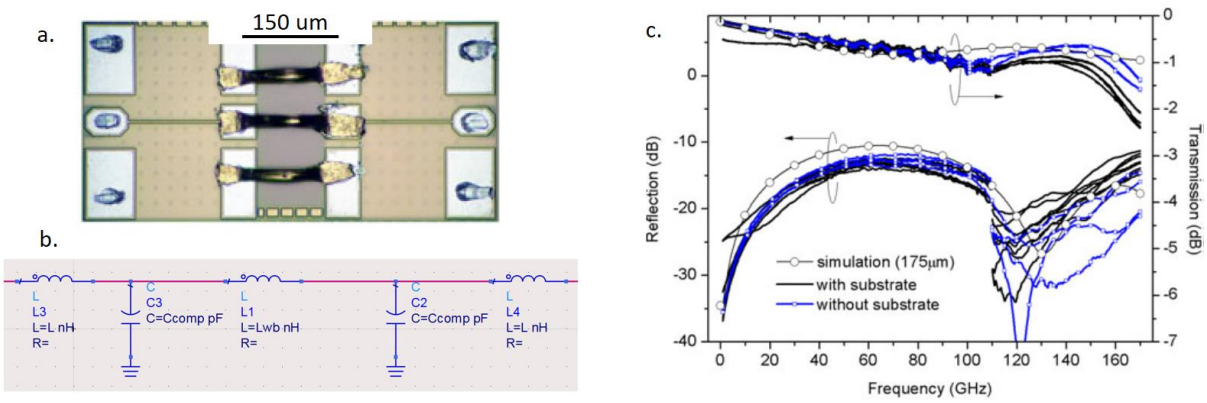

Figure 159 : a. Photo of the compensated wire-bond, b. Equivalent Circuit Model, c. Measurements

4.1.3. VACNT interconnects

The first millimeter-wave interconnect using VACNTs bundles was reported in [87]. The structure and measurements are presented in Figure 160.

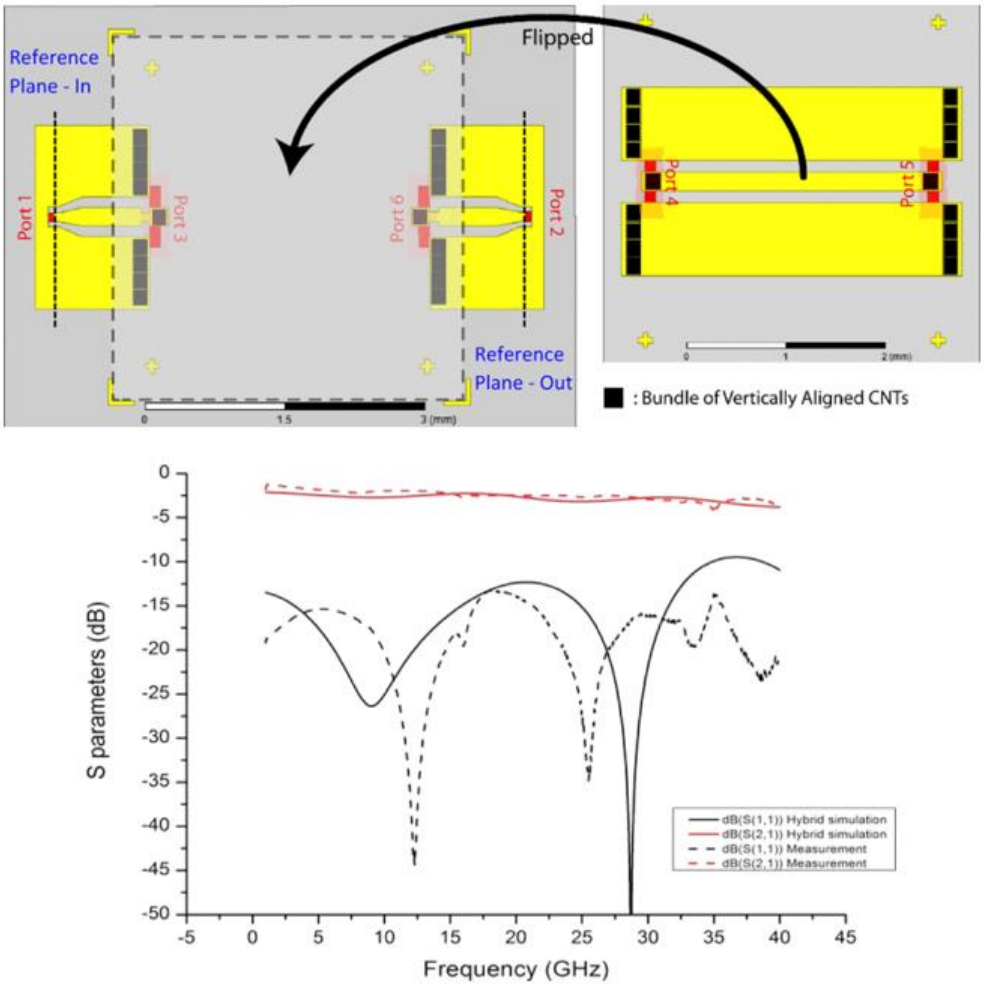

Figure 160 : Top, Design of the structure, Below, Measurements and Simulations

The structure is a flipped chip type structure. In this article, the chip consists in a CPW line. Measurements and simulations are in good adequation. The fabrication process is as follows: the bottom and top substrates are fabricated using classical photolithography processes, VACNTs are grown at the bumps locations directly on the substrates using PECVD, the “chip” (or CPW line) is flipped onto the bottom substrate and the CNTs from top and bottom bumps intertwine to make one unique interconnect.

A former PhD student in XLIM, Philippe Roux-Lévy, then transposed this result to higher frequencies (75 GHz-105 GHz) [81]. This was allowed by the introduction of VACNTs transfer in the fabrication process. The structure’s design and measurements are shown in Figure 161.

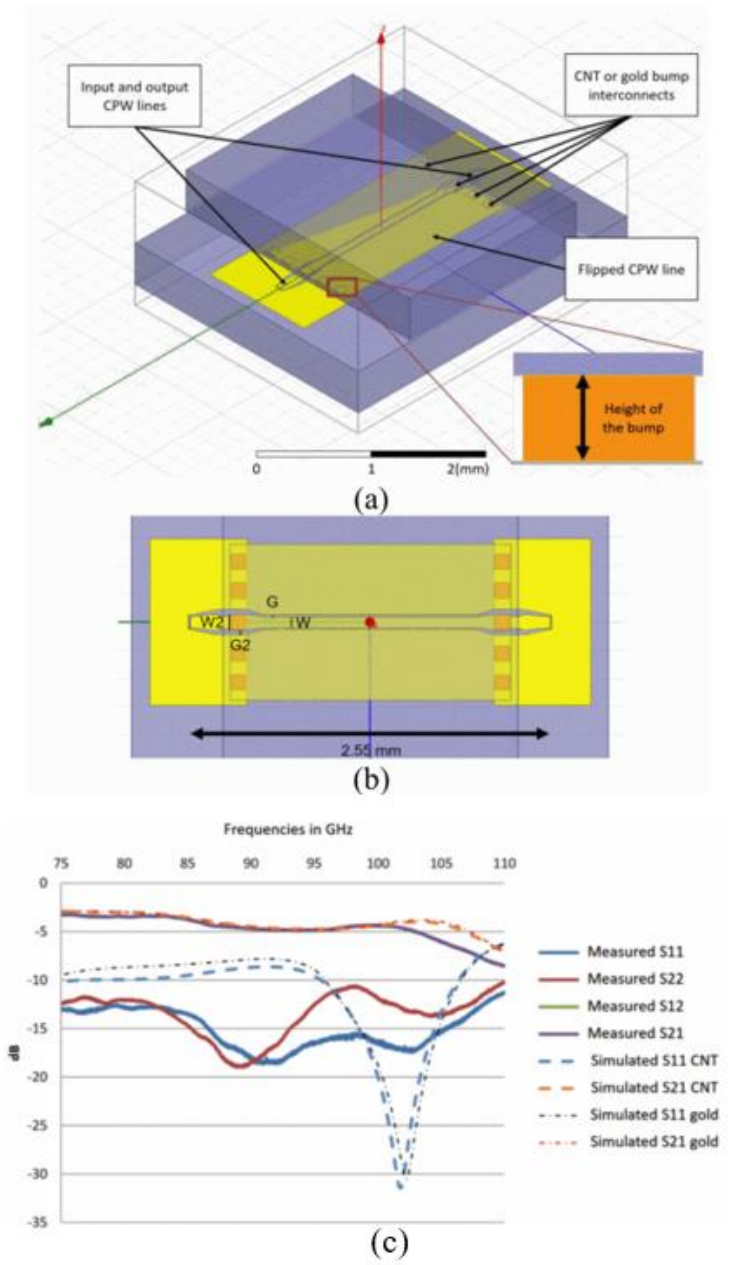

Figure 161 : (a) Isometric View of the structure, (b) Top view of the structure, (c), Simulated and Measured S-parameters

As we can see, good accordance is obtained between the simulated results and the measurements. The simulated performances of a gold bump of the same dimensions than the CNT bump are similar to what is measured. In [81] the losses due to the bumps are extracted and found to be around 1.8 dB, a lot of the losses in Figure 161 are due to the CPW lines.

However, further investigation showed that the CNTs were crushed during the fabrication process [81], changing slightly the interpretation of the results. The results are currently being further analyzed using different simulation methods combining 3D EM software and circuit simulation on ADS.

4.2. Functionalized Cover Proof of Concept

4.2.1. Design and Simulations

The design of the structure is shown in Figure 162. As in [81], [87], the “chip” consists in a CPW line. The CPW line is bonded to the input/output accesses through the VACNTs bridges when the cover is flipped.

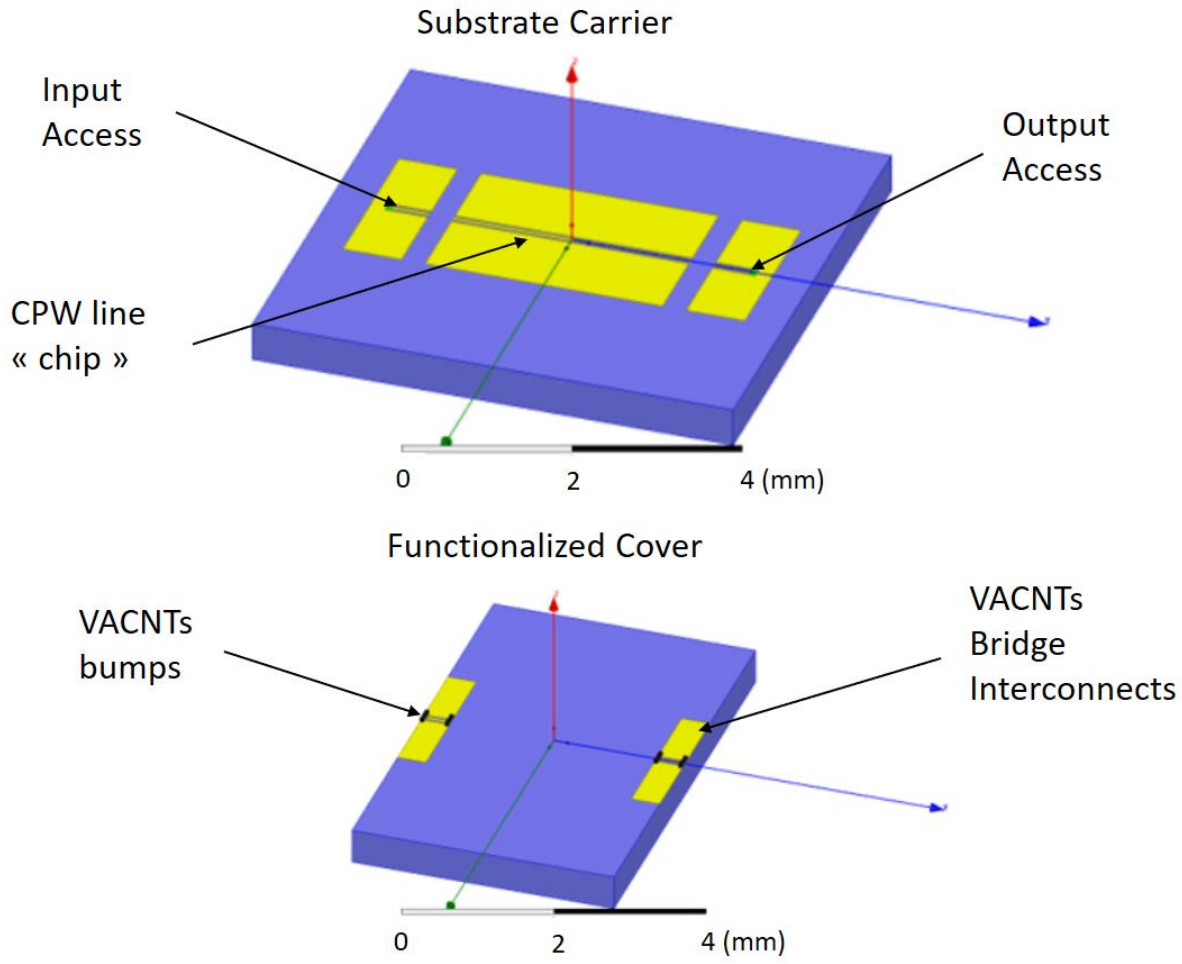

Figure 162 : Design of the structure, Top, Substrate Carrier with Input/Output lines and CPW line “chip”, Bottom, Functionalized Cover with VACNTs bridges

The CPW lines have a gap of 40 um and a signal line width of 50 um. The VACNTs bumps are 50 um x 50 um x 50 um cubes.

The simulated performances are plotted in Figure 163..

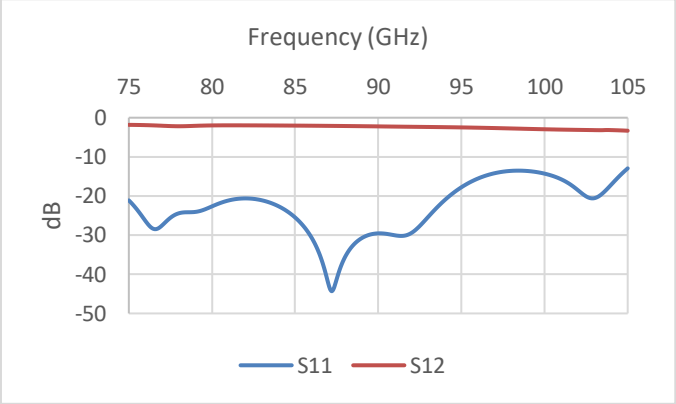

Figure 163 : Simulated performances of the VACNTs bridges

As we can see, the adaptation is below -10 dB on the whole 75 GHz to 105 GHz. We can notice that the performances are quite good on a large bandwidth, even though no optimization was done on the bridges geometry.

The same structure was simulated with wire-bonds of 25 um diameter (c.f. Figure 164). As we can see, the reactance of the wire-bonds does not allow for a good adaptation and good performances.

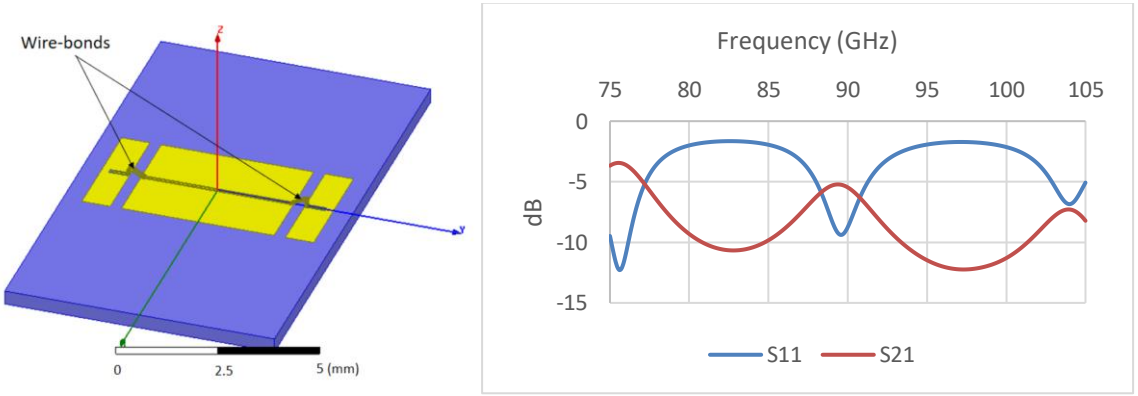

Figure 164 : Left, design with wire-bonds, Right, simulated performances of the design with wire-bonds

4.2.2. Fabrication Process

As we said earlier, the VACNTs bumps are 50 um x 50 um x 50 um cubes. Yet the fabrication process used for the previous interconnects [81], had a minimum size limitations of 200 um. The use of a shadow mask to deposit a gold layer on top of the CNT bumps did not allow for lower dimensions.

Here we propose a fabrication process (Figure 165) that allows us to have bumps as little as a few 100 nm^2 in section.

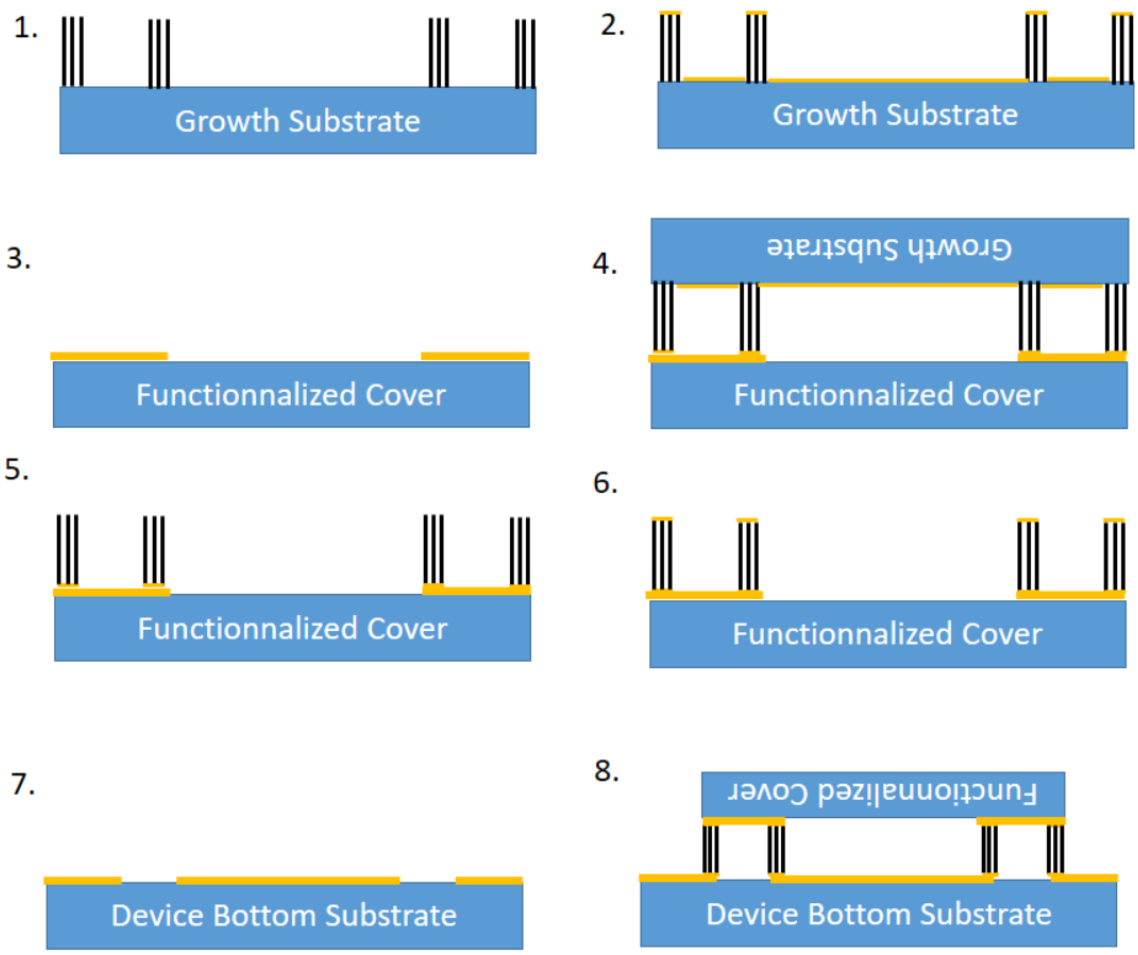

Figure 165 : Fabrication process of the VACNTs bridges

The steps of the fabrication process are as follows:

Step 1: Grow the VACNTs bumps on a separate substrate

Step 2: Deposit gold via evaporation on the whole substrate in order to cover the bumps with a gold layer

Step 3: Fabricate using classical lithography process the CPW lines on the cover

Step 4 and 5: Transfer the CNT bumps on the cover using the transfer process (gold-gold bonding)

Step 6: Deposit a gold layer on top of the CNT bumps using the ZEISS Crossbeam 550, deposition process (resolution as low as 100 nm x 100 nm)

Note: For Step 4, we cannot do the same as Step 2 in order to have a gold layer on top of our CNTs. If we evaporate gold all over the substrate we will short circuit our lines. For the waveguide fabrication, we could deposit gold through evaporation because there was no pattern on the cover.

Step 7: Fabricate using classical lithography process the Input/Output lines and the CPW on the bottom substrate

Step 8: Bond the functionalized cover to the bottom substrate through gold-gold bonding

The process in step 4 i.e. the deposition process in the Crossbeam 550 is described in Figure 165.

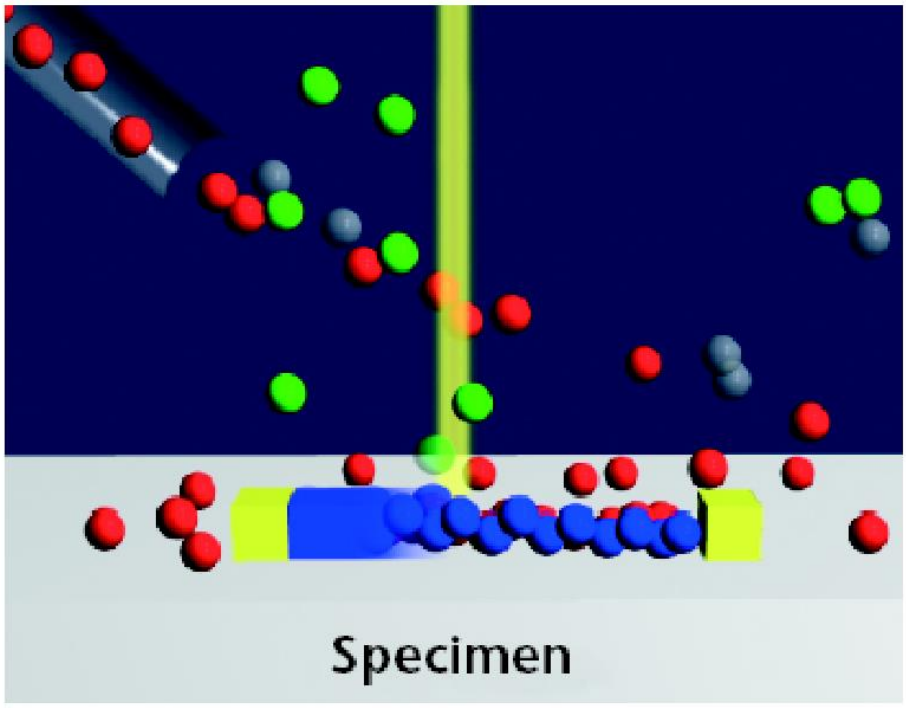

Figure 166 : Schematic display of the beam chemistry process of deposition. It shows the supply of precursor through the Gas Injection System (red). They (temporarily) stick to the surface and are decomposed by the beam into a volatile component (green) and a non-volatile component (blue) that deposits on the surface. Some neutral gas molecules in the vacuum chamber are shown in gray. [324]

4.2.3. Measurements

The devices are currently being fabricated, the measurements will be added to the manuscript for the defense.

4.3. Conclusion

In this brief chapter, we proposed to investigate the performances of VACNT interconnects. A new type of CNT bridge for the high frequency interconnects of RF chips was designed and simulated. This prospective approach is an alternative one to the current technology for RF interconnect which is based on wire-bonding technology. In addition, the proposed approach offers the possibility to manage the chip thermal behavior and its EM shielding by applying the same design and fabrication process. That could be of large interest for the 3D packaging of future millimeter and sub-millimeter wave devices.

A new fabrication process was established using cutting edge technology available in our lab, allowing for lower pattern dimensions in future devices. Measurements and interpretation will be added for the defense.

Conclusion

The research reported in this thesis was funded by the Agence Nationale de la Recherche (ANR) as part of the project TRiCOT (Emerging Technology for RF and Millimeter-wave Circuits based on Carbon Nanotubes). This project was in the context of ultra-compact millimeter-wave systems manufacturing and in particular we planned to develop E-band demonstrators (71-86 GHz). An original concept of functionalized interposer has been proposed, in particular by integrating a beamforming circuit (Butler matrix). In this PhD work we investigated this new type of nanopackaging based on VACNTs for mm-wave devices. The different aspects of a functionalized interposer based on VACNTs were investigated.

We started this manuscript by describing the properties of the material used (VACNTs). We began by giving the theoretical equations that govern CNTs behavior. We then gave the properties of VACNTs that arose from these properties. Different methods to investigate the structure of VACNTs (particularly density) were developed. These experimentations gave us useful insights on the material.

In the second chapter, the design of an air-filled SIW with lateral walls of CNTs was investigated. The structure was designed and simulated using an equivalent bulk model developed for VACNTs. Different fabrication processes were investigated. A characterization method of our fabrication process was established. A new design, more robust was developed and to the best of our knowledge, very encouraging experimental performances have been measured for the first time, with transmission level at -5dB around 81-86 GHz. These measurements contribute to validate both the design and fabrication approaches, even if future improvements are needed.

In the third chapter, the miniaturization of the air-filled SIW was investigated. The miniaturization was necessary because the device being air-filled, it had a bigger footprint. The theory of the slow-wave effect has been described and applied to a dedicated test structure based on a TE10 mode waveguide. This later has been design and fabricated in order to validate the possible use of the VACNTs to provide a slow-wave effect. And to the best of our knowledge, the slow-wave effect due to CNTs has been experimentally showcased for the first time.

In the fourth chapter, an alternative RF interconnect approach based on VACNTs has been briefly described. The potential electrical performances of the RF VACNTs bridge has been studied and a test structure has been designed. The fabrication process is mainly based on the CNT transfer process used in the previous chapters, and a specific step has been proposed to allow the fabrication of small CNTs based interconnect (around 50umx50um in section). Unfortunately, the test structure is still under fabrication and it is not possible to present measurements in this manuscript.

The perspectives are numerous, let us go through them chapter by chapter.

Regarding the air-filled SIW, the design needs to be optimized in order to have a better excitation that has less losses. Then the fabrication process needs to be improved. In order to characterize different fabrication processes tested one should use the resonant cavities designed for this. Once this is done, one should design the other base bricks of the 4x4 Butler matrix, the couplers and the crossover. Once this is done, the performances of the whole Butler matrix should be tested with an antenna array.

Regarding the slow-wave technology, the test structure should be used to characterize other anisotropic materials, such as nanowires or BN coated nanotubes. Once the problem of the lateral conductivity is solved. The slow wave effect needs to be integrated in the structures of chapter 2 in order to reduce the footprint of the Butler matrix. Again the performances with the slow wave should be tested with an antenna array.

In the fourth chapter, once the interconnects are validated. The EM shielding and thermal management need to be investigated. This prospective part of this PhD work is very promising in the context of 3D heterogeneous integration for millimeter and submillimeter devices. It can offer numerous perspectives and impacts for a better management of RF interconnects and thermal behaviors and EM shielding.

Bibliography

List of publications of the author

Joseph de Saxcé, Philippe Roux-Lévy, Chun Fei Siah, Jianxiong Wang, Beng Kang Tay, Philippe Coquet, Dominique Baillargeat,

"Millimeter-wave CNT Based Resonant Cavity,"

2019 IEEE MTT-S International Microwave Workshop Series on Advanced Materials and Processes for RF and THz Applications (IMWS-AMP), 2019, pp. 124-126.

Joseph de Saxcé, Philippe Roux-Lévy, Chun Fei Siah, Jianxiong Wang, Beng Kang Tay, Philippe Coquet, Dominique Baillargeat,

"Millimeter Wave Carbon Nanotube Based Flip Chip Coplanar Interconnects,"

2020 IEEE 22nd Electronics Packaging Technology Conference (EPTC), 2020, pp. 81-84.

Philippe Roux-Lévy, Joseph de Saxcé, Chun Fei Siah, Jianxiong Wang, Beng Kang Tay, Philippe Coquet, Dominique Baillargeat,

"W Band Carbon Nanotubes Interconnects Compatible with CMOS Technology,"

2020 IEEE/MTT-S International Microwave Symposium (IMS), 2020, pp. 1047-1050.

Phi Long Doan, Emmanuel Pistono, Philippe Coquet, Jianxiong Wang, Dominique Baillargeat, Joseph de Saxcé, Stéphane Bila, Florence Podevin

"Potentialities of Air-Filled Substrate Integrated Waveguides based on Carbon Nanotubes in E-band,"

2020 IEEE MTT-S International Conference on Microwaves for Intelligent Mobility (ICMIM), 2020, pp. 1-4.

Bibliography

[1] “Internet users in the world 2021,” *Statista*. https://www.statista.com/statistics/617136/digital-population-worldwide/ (accessed Nov. 12, 2021).

[2] G. Alain, “L’ÉPUISEMENT DES MÉTAUX ET MINÉRAUX : FAUT-IL S’INQUIÉTER ?,” p. 23.

[3] R. P. Feynman, “There’s Plenty of Room at the Bottom,” California Institute of Technology, 1960.

[4] “IBM Unveils World’s First 2 Nanometer Chip Technology, Opening a New Frontier for Semiconductors,” *IBM Newsroom*, Aug. 05, 2021. https://newsroom.ibm.com/2021-05-06-IBM-Unveils-Worlds-First-2-Nanometer-Chip-Technology,-Opening-a-New-Frontier-for-Semiconductors (accessed Aug. 06, 2021).

[5] F. Fang *et al.*, “Towards atomic and close-to-atomic scale manufacturing,” *Int. J. Extreme Manuf.*, vol. 1, no. 1, p. 012001, Apr. 2019, doi: 10.1088/2631-7990/ab0dfc.

[6] F. Arute *et al.*, “Hartree-Fock on a superconducting qubit quantum computer,” *Science*, vol. 369, no. 6507, pp. 1084–1089, Aug. 2020, doi: 10.1126/science.abb9811.

[7] F. Arute *et al.*, “Quantum supremacy using a programmable superconducting processor,” *Nature*, vol. 574, no. 7779, pp. 505–510, Oct. 2019, doi: 10.1038/s41586-019-1666-5.

[8] I. Aprahamian, “The Future of Molecular Machines,” *ACS Cent. Sci.*, vol. 6, no. 3, pp. 347–358, Mar. 2020, doi: 10.1021/acscentsci.0c00064.

[9] C. Joachim, “Nanopackaging Requests for Atomic Scale Circuits and Molecule-Machines,” 2015. Accessed: Aug. 06, 2021. [Online]. Available: https://www.springerprofessional.de/en/nanopackaging-requests-for-atomic-scale-circuits-and-molecule-ma/2497284

[10] P. M. Raj and R. Mahajan, “Foreword Special Section on Nanopackaging,” *IEEE Trans. Compon. Packag. Manuf. Technol.*, vol. 6, no. 12, pp. 1731–1732, Dec. 2016, doi: 10.1109/TCPMT.2016.2635499.

[11] C. Brun *et al.*, “Deoxyribonucleic Acid for Nanopackaging: A promising bottom-up approach,” *IEEE Nanotechnol. Mag.*, vol. 11, no. 1, pp. 12–19, Mar. 2017, doi: 10.1109/MNANO.2016.2633679.

[12] A. Filoramo, “DNA Metallization Processes and Nanoelectronics,” in *Nanopackaging: From Nanomaterials to the Atomic Scale*, Cham, 2015, pp. 17–32. doi: 10.1007/978-3-319-21194-7_2.

[13] H. Jiang, X. Zhang, J. Gao, and N. Guo, “Dielectric Properties of SiO2/MMT/LDPE Micro-nano Composites,” in *2020 IEEE International Conference on High Voltage Engineering and Application (ICHVE)*, Sep. 2020, pp. 1–4. doi: 10.1109/ICHVE49031.2020.9279624.

[14] L. Del Carro, J. Zürcher, U. Drechsler, I. E. Clark, G. Ramos, and T. Brunschwiler, “Low-Temperature Dip-Based All-Copper Interconnects Formed by Pressure-Assisted Sintering of Copper Nanoparticles,” *IEEE Trans. Compon. Packag. Manuf. Technol.*, vol. 9, no. 8, pp. 1613–1622, Aug. 2019, doi: 10.1109/TCPMT.2019.2891111.

[15] S. Bistarelli, S. Sun, L. Pierantoni, S. Bellucci, D. Mencarelli, and J. Lui, “Evaluating CNT-Based Interconnects : A Nummerical Tool to Characterize Hybrid CNT-Copper Interconnects,” *IEEE Microw. Mag.*, vol. 18, no. 4, pp. 124–129, Jun. 2017, doi: 10.1109/MMM.2017.2680038.

[16] S. Das, S. Bhattacharya, D. Das, and H. Rahaman, “A Short Review on Graphene Nanoribbon Interconnect,” in *2020 International Symposium on Devices, Circuits and Systems (ISDCS)*, Mar. 2020, pp. 1–7. doi: 10.1109/ISDCS49393.2020.9263018.

[17] S. Agrawal, A. Srivastava, and G. Kaushal, “N-Doped Zigzag Graphene Nanoribbons For Nanoscale Interconnects,” in *2020 IEEE 10th International Conference Nanomaterials: Applications Properties (NAP)*, Nov. 2020, pp. 01TPNS03-1-01TPNS03-5. doi: 10.1109/NAP51477.2020.9309690.

[18] PRFI, *Technical Discussion on mmWave Packaging*. Accessed: Aug. 06, 2021. [Online]. Available: https://www.youtube.com/watch?v=AGLH3lto3i4

[19] M. Monthioux and V. L. Kuznetsov, “Who should be given the credit for the discovery of carbon nanotubes?,” *Carbon*, vol. 44, no. 9, pp. 1621–1623, Aug. 2006, doi: 10.1016/j.carbon.2006.03.019.

[20] S. Iijima, “Helical microtubules of graphitic carbon,” *Nature*, vol. 354, no. 6348, pp. 56–58, Nov. 1991, doi: 10.1038/354056a0.

[21] “Allotropes of carbon,” *Wikipedia*. Jul. 21, 2021. Accessed: Aug. 08, 2021. [Online]. Available: https://en.wikipedia.org/w/index.php?title=Allotropes_of_carbon&oldid=1034778539

[22] Ponor, *English: Sigma and pi bonds in graphene. Sigma bonds result from an overlap of sp2 hybrid orbitals, whereas pi bonds emerge from tunneling between the protruding pz orbitals. For clarity, only a few neighboring pz orbitals are shown.* 2020. Accessed: Aug. 08, 2021. [Online]. Available: https://commons.wikimedia.org/wiki/File:Graphene_-_sigma_and_pi_bonds.svg

[23] A. H. Castro Neto, F. Guinea, N. M. R. Peres, K. S. Novoselov, and A. K. Geim, "The electronic properties of graphene," *Rev. Mod. Phys.*, vol. 81, no. 1, pp. 109–162, Jan. 2009, doi: 10.1103/RevModPhys.81.109.

[24] A. J. Leggett and B. Coish, "Lecture 5: Graphene: Electronic band structure and Dirac fermions," p. 12.

[25] A. Cresti *et al.*, "Charge transport in disordered graphene-based low dimensional materials," *Nano Res.*, vol. 1, no. 5, pp. 361–394, Nov. 2008, doi: 10.1007/s12274-008-8043-2.

[26] J.-M. Poumirol, "Étude des propriétés électroniques du graphène et des matériaux à base de graphène sous champs magnétiques intenses," p. 166.

[27] P. R. Wallace, "The Band Theory of Graphite," *Phys. Rev.*, vol. 71, no. 9, pp. 622–634, May 1947, doi: 10.1103/PhysRev.71.622.

[28] S. Das Sarma, E. H. Hwang, and E. Rossi, "Theory of carrier transport in bilayer graphene," *Phys. Rev. B*, vol. 81, no. 16, p. 161407, Apr. 2010, doi: 10.1103/PhysRevB.81.161407.

[29] Y. Kinoshita, Y. Yamayose, Y. Doi, A. Nakatani, and T. Kitamura, "Selective excitations of intrinsic localized modes of atomic scales in carbon nanotubes," *Phys. Rev. B*, vol. 77, Jan. 2008, doi: 10.1103/PhysRevB.77.024307.

[30] M. Terrones, "Science and Technology of the Twenty-First Century: Synthesis, Properties, and Applications of Carbon Nanotubes," *Annu. Rev. Mater. Res.*, vol. 33, no. 1, pp. 419–501, Aug. 2003, doi: 10.1146/annurev.matsci.33.012802.100255.

[31] B. Liu, F. Wu, H. Gui, M. Zheng, and C. Zhou, "Chirality-Controlled Synthesis and Applications of Single-Wall Carbon Nanotubes," *ACS Nano*, vol. 11, no. 1, pp. 31–53, Jan. 2017, doi: 10.1021/acsnano.6b06900.

[32] J. R. Sanchez-Valencia *et al.*, "Controlled synthesis of single-chirality carbon nanotubes," *Nature*, vol. 512, no. 7512, pp. 61–64, Aug. 2014, doi: 10.1038/nature13607.

[33] "Nanotube & Carbon Fiber Overview - The World of Nanoscience." https://worldofnanoscience.weebly.com/nanotube--carbon-fiber-overview.html (accessed Aug. 08, 2021).

[34] C. T. White and J. W. Mintmire, "Fundamental Properties of Single-Wall Carbon Nanotubes," p. 14.

[35] E. Malic, M. Hirtschulz, F. Milde, A. Knorr, and S. Reich, "Analytical approach to optical absorption in carbon nanotubes," *Phys. Rev. B - PHYS REV B*, vol. 74, Nov. 2006, doi: 10.1103/PhysRevB.74.195431.

[36] G. Dresselhaus, M. S. Dresselhaus, and R. Saito, *Physical Properties Of Carbon Nanotubes*. World Scientific, 1998.

[37] A. G. Perri and R. Marani, *CNTFET Electronics: Design Principles*, Editor Progedit. Italy, 2017.

[38] G. Gelao, R. Marani, and A. G. Perri, "A Formula to Determine Energy Band Gap in Semiconducting Carbon Nanotubes," *ECS J. Solid State Sci. Technol.*, vol. 8, no. 2, pp. M19–M21, 2019, doi: 10.1149/2.0201902jss.

[39] P. T. Araujo *et al.*, “Third and Fourth Optical Transitions in Semiconducting Carbon Nanotubes,” *Phys. Rev. Lett.*, vol. 98, no. 6, p. 067401, Feb. 2007, doi: 10.1103/PhysRevLett.98.067401.

[40] J.-P. Cleuziou, “Propriétés de transport électronique de nanotubes de carbone: des nanotubes hybrides au nano-SQUID,” phdthesis, Université Paul Sabatier - Toulouse III, 2007. Accessed: Aug. 09, 2021. [Online]. Available: https://tel.archives-ouvertes.fr/tel-00342549

[41] C. T. White and T. N. Todorov, “Carbon nanotubes as long ballistic conductors,” *Nature*, vol. 393, no. 6682, pp. 240–242, May 1998, doi: 10.1038/30420.

[42] J. W. G. Wilder, L. C. Venema, A. G. Rinzler, R. E. Smalley, and C. Dekker, “Electronic structure of atomically resolved carbon nanotubes,” *Nature*, vol. 391, no. 6662, pp. 59–62, Jan. 1998, doi: 10.1038/34139.

[43] A. Naeemi and J. D. Meindl, “Compact physical models for multiwall carbon-nanotube interconnects,” *IEEE Electron Device Lett.*, vol. 27, no. 5, pp. 338–340, May 2006, doi: 10.1109/LED.2006.873765.

[44] H. J. Li, W. G. Lu, J. J. Li, X. D. Bai, and C. Z. Gu, “Multichannel Ballistic Transport in Multiwall Carbon Nanotubes,” *Phys. Rev. Lett.*, vol. 95, no. 8, p. 086601, Aug. 2005, doi: 10.1103/PhysRevLett.95.086601.

[45] J. Jiang, J. Dong, H. T. Yang, and D. Y. Xing, “Universal expression for localization length in metallic carbon nanotubes,” *Phys. Rev. B*, vol. 64, no. 4, p. 045409, Jul. 2001, doi: 10.1103/PhysRevB.64.045409.

[46] R. Zhang, Y. Zhang, Q. Zhang, H. Xie, W. Qian, and F. Wei, “Growth of Half-Meter Long Carbon Nanotubes Based on Schulz–Flory Distribution,” *ACS Nano*, vol. 7, no. 7, pp. 6156–6161, Jul. 2013, doi: 10.1021/nn401995z.

[47] X. Wang *et al.*, “Fabrication of Ultralong and Electrically Uniform Single-Walled Carbon Nanotubes on Clean Substrates,” *Nano Lett.*, vol. 9, no. 9, pp. 3137–3141, Sep. 2009, doi: 10.1021/nl901260b.

[48] X. Zhang *et al.*, “Ultrastrong, Stiff, and Lightweight Carbon-Nanotube Fibers,” *Adv. Mater.*, vol. 19, no. 23, pp. 4198–4201, Dec. 2007, doi: 10.1002/adma.200700776.

[49] M. Yu, “Strength and Breaking Mechanism of Multiwalled Carbon Nanotubes Under Tensile Load,” *Science*, vol. 287, no. 5453, pp. 637–640, Jan. 2000, doi: 10.1126/science.287.5453.637.

[50] B. Ruelle, S. Peeterbroeck, T. Godfroid, C. Bittencourt, R. Snyders, and P. Dubois, “FUNCTIONALIZATION OF CARBON NANOTUBES VIA PLASMA POST-DISCHARGE SURFACE TREATMENT: IMPLICATION AS NANOFILLER IN POLYMERIC MATRICES,” p. 2.

[51] Y. Saito, “Preparation and properties of carbon nanotubes,” in *MHS’99. Proceedings of 1999 International Symposium on Micromechatronics and Human Science (Cat. No.99TH8478)*, Nagoya, Japan, 1999, pp. 43–49. doi: 10.1109/MHS.1999.819980.

[52] M. K. Samani, N. Khosravian, G. C. K. Chen, M. Shakerzadeh, D. Baillargeat, and B. K. Tay, “Thermal conductivity of individual multiwalled carbon nanotubes,” *Int. J. Therm. Sci.*, vol. 62, pp. 40–43, Dec. 2012, doi: 10.1016/j.ijthermalsci.2012.03.003.

[53] A. A. Balandin, “Thermal properties of graphene and nanostructured carbon materials,” *Nat. Mater.*, vol. 10, no. 8, pp. 569–581, Aug. 2011, doi: 10.1038/nmat3064.

[54] C. Ren, W. Zhang, Z. Xu, Z. Zhu, and P. Huai, “Thermal Conductivity of Single-Walled Carbon Nanotubes under Axial Stress,” *J. Phys. Chem. C*, vol. 114, no. 13, pp. 5786–5791, Apr. 2010, doi: 10.1021/jp910339h.

[55] T. Yamamoto, K. Watanabe, and E. R. Hernández, “Mechanical Properties, Thermal Stability and Heat Transport in Carbon Nanotubes,” in *Carbon Nanotubes*, vol. 111, A. Jorio, G. Dresselhaus, and M. S. Dresselhaus, Eds. Berlin, Heidelberg: Springer Berlin Heidelberg, 2007, pp. 165–195. doi: 10.1007/978-3-540-72865-8_5.

[56] E. Pop, D. Mann, Q. Wang, K. Goodson, and H. Dai, “Thermal Conductance of an Individual Single-Wall Carbon Nanotube above Room Temperature,” *Nano Lett.*, vol. 6, no. 1, pp. 96–100, Jan. 2006, doi: 10.1021/nl052145f.

[57] Y.-K. Kwon and P. Kim, “Unusually High Thermal Conductivity in Carbon Nanotubes,” in *High Thermal Conductivity Materials*, S. L. Shindé and J. S. Goela, Eds. New York: Springer-Verlag, 2006, pp. 227–265. doi: 10.1007/0-387-25100-6_8.

[58] P. Kim, L. Shi, A. Majumdar, and P. L. McEuen, “Thermal Transport Measurements of Individual Multiwalled Nanotubes,” *Phys. Rev. Lett.*, vol. 87, no. 21, p. 215502, Oct. 2001, doi: 10.1103/PhysRevLett.87.215502.

[59] M. F. L. De Volder, S. H. Tawfick, R. H. Baughman, and A. J. Hart, “Carbon Nanotubes: Present and Future Commercial Applications,” *Science*, vol. 339, no. 6119, pp. 535–539, Feb. 2013, doi: 10.1126/science.1222453.

[60] K. Banerjee, H. Li, and N. Srivastava, “Current Status and Future Perspectives of Carbon Nanotube Interconnects,” in *2008 8th IEEE Conference on Nanotechnology*, Aug. 2008, pp. 432–436. doi: 10.1109/NANO.2008.132.

[61] “Carbon nanotube,” *Wikipedia*. Jul. 23, 2021. Accessed: Aug. 10, 2021. [Online]. Available: https://en.wikipedia.org/w/index.php?title=Carbon_nanotube&oldid=1035053686

[62] P. Franck, “Mesoscopic electromagnetic model of carbon-nanotube arrays and scalable technological processes : Application to the fabrication of novel antennas.”

[63] J. A. Misewich, R. Martel, P. Avouris, J. C. Tsang, S. Heinze, and J. Tersoff, “Electrically Induced Optical Emission from a Carbon Nanotube FET,” *Science*, vol. 300, no. 5620, pp. 783–786, May 2003, doi: 10.1126/science.1081294.

[64] M. Freitag, Y. Martin, J. A. Misewich, R. Martel, and Ph. Avouris, “Photoconductivity of Single Carbon Nanotubes,” *Nano Lett.*, vol. 3, no. 8, pp. 1067–1071, Aug. 2003, doi: 10.1021/nl034313e.

[65] C. Kingston and B. Simard, “Fabrication of Carbon Nanotubes,” *Anal. Lett.*, vol. 36, pp. 3119–3145, Dec. 2003, doi: 10.1081/AL-120026564.

[66] C. Journet *et al.*, “Large-scale production of single-walled carbon nanotubes by the electric-arc technique,” *Nature*, vol. 388, no. 6644, pp. 756–758, Aug. 1997, doi: 10.1038/41972.

[67] T. Guo, P. Nikolaev, A. Thess, D. T. Colbert, and R. E. Smalley, “Catalytic growth of single-walled manotubes by laser vaporization,” *Chem. Phys. Lett.*, vol. 243, no. 1, pp. 49–54, Sep. 1995, doi: 10.1016/0009-2614(95)00825-O.

[68] V. Choudhary, B. P. Singh, and R. B. Mathur, “Carbon Nanotubes and Their Composites,” 2013, pp. 193–222. doi: 10.5772/52897.

[69] C. D. Scott, S. Arepalli, P. Nikolaev, and R. E. Smalley, “Growth mechanisms for single-wall carbon nanotubes in a laser-ablation process,” *Appl. Phys. A*, vol. 72, no. 5, pp. 573–580, May 2001, doi: 10.1007/s003390100761.

[70] R. S. Wagner and W. C. Ellis, “VAPOR-LIQUID-SOLID MECHANISM OF SINGLE CRYSTAL GROWTH,” *Appl. Phys. Lett.*, vol. 4, no. 5, pp. 89–90, Mar. 1964, doi: 10.1063/1.1753975.

[71] V. Balakrishnan *et al.*, “Real-Time Imaging of Self-Organization and Mechanical Competition in Carbon Nanotube Forest Growth,” *ACS Nano*, vol. 10, no. 12, pp. 11496–11504, Dec. 2016, doi: 10.1021/acsnano.6b07251.

[72] M. Kumar and Y. Ando, “Chemical Vapor Deposition of Carbon Nanotubes: A Review on Growth Mechanism and Mass Production,” *J. Nanosci. Nanotechnol.*, vol. 10, no. 6, pp. 3739–3758, Jun. 2010, doi: 10.1166/jnn.2010.2939.

[73] V. A. Nebol’sin *et al.*, “Development of lateral faces during vapor-liquid-solid growth of silicon whiskers,” *Inorg. Mater.*, vol. 42, no. 4, pp. 339–345, Apr. 2006, doi: 10.1134/S0020168506040017.

[74] V. A. Nebol’sin and A. A. Shchetinin, “Role of Surface Energy in the Vapor–Liquid–Solid Growth of Silicon,” vol. 39, no. 9, p. 5, 2003.

[75] K. Hernadi, A. Fonseca, J. B. Nagy, D. Bernaerts, and A. A. Lucas, “Fe-catalyzed carbon nanotube formation,” *Carbon*, vol. 34, no. 10, pp. 1249–1257, Jan. 1996, doi: 10.1016/0008-6223(96)00074-7.

[76] W. Z. Li *et al.*, “Large-Scale Synthesis of Aligned Carbon Nanotubes,” *Science*, vol. 274, no. 5293, pp. 1701–1703, Dec. 1996, doi: 10.1126/science.274.5293.1701.

[77] R. Sen, A. Govindaraj, and C. N. R. Rao, “Carbon nanotubes by the metallocene route,” *Chem. Phys. Lett.*, vol. 267, no. 3, pp. 276–280, Mar. 1997, doi: 10.1016/S0009-2614(97)00080-8.

[78] P. Nikolaev *et al.*, “Gas-phase catalytic growth of single-walled carbon nanotubes from carbon monoxide,” *Chem. Phys. Lett.*, vol. 313, no. 1, pp. 91–97, Nov. 1999, doi: 10.1016/S0009-2614(99)01029-5.

[79] Z.-J. Liu, R. Che, Z. Xu, and L.-M. Peng, “Preparation of Fe-filled carbon nanotubes by catalytic decomposition of cyclohexane,” *Synth. Met.*, vol. 128, no. 2, pp. 191–195, Apr. 2002, doi: 10.1016/S0379-6779(02)00005-X.

[80] O. A. Nerushev, S. Dittmar, R.-E. Morjan, F. Rohmund, and E. E. B. Campbell, “Particle size dependence and model for iron-catalyzed growth of carbon nanotubes by thermal chemical vapor deposition,” *J. Appl. Phys.*, vol. 93, no. 7, pp. 4185–4190, Apr. 2003, doi: 10.1063/1.1559433.

[81] P. Roux-Levy, “Nanostructures de carbone dédiées aux interconnexions hautes fréquences,” 2018.

[82] K. Hata, D. N. Futaba, K. Mizuno, T. Namai, M. Yumura, and S. Iijima, “Water-Assisted Highly Efficient Synthesis of Impurity-Free Single-Walled Carbon Nanotubes,” *Science*, vol. 306, no. 5700, pp. 1362–1364, Nov. 2004, doi: 10.1126/science.1104962.

[83] S. P. Patole, J. H. Park, T. Y. Lee, J. H. Lee, A. S. Patole, and J. B. Yoo, “Growth interruption studies on vertically aligned 2-3 wall carbon nanotubes by water assisted chemical vapor deposition,” *Appl. Phys. Lett.*, vol. 93, no. 11, p. 114101, Sep. 2008, doi: 10.1063/1.2976328.

[84] C. Brun, “Carbon nanotubes based nanopackaging dedicated to innovative high frequency interconnections,” 2014. Accessed: Aug. 04, 2021. [Online]. Available: https://ieeexplore.ieee.org/document/7460443/

[85] M. Meyyappan, L. Delzeit, A. Cassell, and D. Hash, “Carbon nanotube growth by PECVD: a review,” *Plasma Sources Sci. Technol.*, vol. 12, no. 2, pp. 205–216, May 2003, doi: 10.1088/0963-0252/12/2/312.

[86] M. Cometto, “Use of carbon nanotubes for passive radio-frequency devices,” Nanyang Technological University, 2018. doi: 10.32657/10220/46256.

[87] C. Brun *et al.*, “Carbon Nanostructures Dedicated to Millimeter-Wave to THz Interconnects,” *IEEE Trans. Terahertz Sci. Technol.*, vol. 5, no. 3, pp. 383–390, May 2015, doi: 10.1109/TTHZ.2015.2407859.

[88] P. Bondavalli, M. B. Martin, L. Hamidouche, A. Montanaro, A.-F. Trompeta, and C. A. Charitidis, “Nano-Graphitic based Non-Volatile Memories Fabricated by the Dynamic Spray-Gun Deposition Method,” *Micromachines*, vol. 10, no. 2, Art. no. 2, Feb. 2019, doi: 10.3390/mi10020095.

[89] “Air-brush deposition for high performance graphene based supercaps,” *IDTechEx*, Jul. 20, 2015. https://www.idtechex.com/fr/research-article/air-brush-deposition-for-high-performance-graphene-based-supercaps/8052 (accessed Aug. 11, 2021).

[90] R. P. Tortorich and J.-W. Choi, “Inkjet Printing of Carbon Nanotubes,” *Nanomaterials*, vol. 3, no. 3, Art. no. 3, Sep. 2013, doi: 10.3390/nano3030453.

[91] A. Kumar, V. L. Pushparaj, S. Kar, O. Nalamasu, P. M. Ajayan, and R. Baskaran, “Contact transfer of aligned carbon nanotube arrays onto conducting substrates,” *Appl. Phys. Lett.*, vol. 89, no. 16, p. 163120, Oct. 2006, doi: 10.1063/1.2356899.

[92] Y. Fu, Y. Qin, T. Wang, S. Chen, and J. Liu, “Ultrafast Transfer of Metal-Enhanced Carbon Nanotubes at Low Temperature for Large-Scale Electronics Assembly,” *Adv. Mater.*, vol. 22, no. 44, pp. 5039–5042, 2010, doi: 10.1002/adma.201002415.

[93] L. Zhu, Y. Sun, D. W. Hess, and C.-P. Wong, “Well-Aligned Open-Ended Carbon Nanotube Architectures: An Approach for Device Assembly,” *Nano Lett.*, vol. 6, no. 2, pp. 243–247, Feb. 2006, doi: 10.1021/nl052183z.

[94] G.-H. Jeong, N. Olofsson, L. K. L. Falk, and E. E. B. Campbell, “Effect of catalyst pattern geometry on the growth of vertically aligned carbon nanotube arrays,” *Carbon*, vol. 47, no. 3, pp. 696–704, Mar. 2009, doi: 10.1016/j.carbon.2008.11.003.

[95] P. Franck, D. Baillargeat, and B. K. Tay, “Mesoscopic Model for the Electromagnetic Properties of Arrays of Nanotubes and Nanowires: A Bulk Equivalent Approach,” *IEEE Trans. Nanotechnol.*, vol. 11, no. 5, pp. 964–974, Sep. 2012, doi: 10.1109/TNANO.2012.2209457.

[96] F. Wakaya, K. Katayama, and K. Gamo, “Contact resistance of multiwall carbon nanotubes,” *Microelectron. Eng.*, vol. 67–68, pp. 853–857, Jun. 2003, doi: 10.1016/S0167-9317(03)00147-3.

[97] S. C. Lim *et al.*, “Contact resistance between metal and carbon nanotube interconnects: Effect of work function and wettability,” *Appl. Phys. Lett.*, vol. 95, no. 26, p. 264103, Dec. 2009, doi: 10.1063/1.3255016.

[98] A. I. Vorob’eva, “Fabrication techniques of electrode arrays for carbon nanotubes,” *Phys.-Uspekhi*, vol. 52, no. 3, p. 225, Mar. 2009, doi: 10.3367/UFNe.0179.200903b.0243.

[99] X. Sun, K. Li, R. Wu, P. Wilhite, and C. Y. Yang, “Contact resistances of carbon nanotubes grown under various conditions,” in *2010 IEEE Nanotechnology Materials and Devices Conference*, Oct. 2010, pp. 332–333. doi: 10.1109/NMDC.2010.5652354.

[100] K. Asaka, M. Karita, and Y. Saito, “Modification of interface structure and contact resistance between a carbon nanotube and a gold electrode by local melting,” *Appl. Surf. Sci.*, vol. 257, no. 7, pp. 2850–2853, Jan. 2011, doi: 10.1016/j.apsusc.2010.10.079.

[101] X. Sun, K. Li, W. Wu, P. Wilhite, T. Saito, and C. Y. Yang, “Contact resistances of carbon nanotube via interconnects,” in *2009 IEEE International Conference of Electron Devices and Solid-State Circuits (EDSSC)*, Dec. 2009, pp. 131–135. doi: 10.1109/EDSSC.2009.5394173.

[102] C. Lan, P. Srisungsitthisunti, P. B. Amama, T. S. Fisher, X. Xu, and R. G. Reifenberger, “Measurement of metal/carbon nanotube contact resistance by adjusting contact length

using laser ablation," *Nanotechnology*, vol. 19, no. 12, p. 125703, Feb. 2008, doi: 10.1088/0957-4484/19/12/125703.

[103] E. Suhir, Y. C. Lee, and C. P. Wong, Eds., *Micro- and Opto-Electronic Materials and Structures: Physics, Mechanics, Design, Reliability, Packaging*. Boston, MA: Springer US, 2007. doi: 10.1007/0-387-32989-7.

[104] J.-Y. Park *et al.*, "Electron−Phonon Scattering in Metallic Single-Walled Carbon Nanotubes," *Nano Lett.*, vol. 4, no. 3, pp. 517–520, Mar. 2004, doi: 10.1021/nl035258c.

[105] M. S. Sarto and A. Tamburrano, "Single-Conductor Transmission-Line Model of Multiwall Carbon Nanotubes," *IEEE Trans. Nanotechnol.*, vol. 9, no. 1, pp. 82–92, Jan. 2010, doi: 10.1109/TNANO.2009.2023516.

[106] H. Li, W.-Y. Yin, K. Banerjee, and J.-F. Mao, "Circuit Modeling and Performance Analysis of Multi-Walled Carbon Nanotube Interconnects," *IEEE Trans. Electron Devices*, vol. 55, no. 6, pp. 1328–1337, Jun. 2008, doi: 10.1109/TED.2008.922855.

[107] P. J. Burke, "Luttinger liquid theory as a model of the gigahertz electrical properties of carbon nanotubes," *IEEE Trans. Nanotechnol.*, vol. 1, no. 3, pp. 129–144, Sep. 2002, doi: 10.1109/TNANO.2002.806823.

[108] A. Stetter, J. Vancea, and C. H. Back, "Determination of the intershell conductance in a multiwall carbon nanotube," *Appl. Phys. Lett.*, vol. 93, no. 17, p. 172103, Oct. 2008, doi: 10.1063/1.3006426.

[109] P. G. Collins and Ph. Avouris, "Multishell conduction in multiwalled carbon nanotubes," *Appl. Phys. A*, vol. 74, no. 3, pp. 329–332, Mar. 2002, doi: 10.1007/s003390201280.

[110] G. Ya. Slepyan, S. A. Maksimenko, A. Lakhtakia, O. Yevtushenko, and A. V. Gusakov, "Electrodynamics of carbon nanotubes: Dynamic conductivity, impedance boundary conditions, and surface wave propagation," *Phys. Rev. B*, vol. 60, no. 24, pp. 17136–17149, Dec. 1999, doi: 10.1103/PhysRevB.60.17136.

[111] G. W. Hanson, "Dyadic Green's functions and guided surface waves for a surface conductivity model of graphene," *J. Appl. Phys.*, vol. 103, no. 6, p. 064302, Mar. 2008, doi: 10.1063/1.2891452.

[112] S. M. Mikki and A. A. Kishk, "Mean-Field Electrodynamic Theory of Aligned Carbon Nanotube Composites," *IEEE Trans. Antennas Propag.*, vol. 57, no. 5, pp. 1412–1419, May 2009, doi: 10.1109/TAP.2009.2016687.

[113] Z. Liu *et al.*, "Densification of Carbon Nanotube Bundles for Interconnect Application," in *2007 IEEE International Interconnect Technology Conferencee*, Jun. 2007, pp. 201–203. doi: 10.1109/IITC.2007.382389.

[114] G. F. Zhong, T. Iwasaki, and H. Kawarada, "Semi-quantitative study on the fabrication of densely packed and vertically aligned single-walled carbon nanotubes," *Carbon*, vol. 44, no. 10, pp. 2009–2014, Aug. 2006, doi: 10.1016/j.carbon.2006.01.027.

[115] M. Bedewy and A. J. Hart, "Mechanical coupling limits the density and quality of self-organized carbon nanotube growth," *Nanoscale*, vol. 5, no. 7, p. 2928, 2013, doi: 10.1039/c3nr34067h.

[116] M. Bedewy, E. R. Meshot, M. J. Reinker, and A. J. Hart, "Population Growth Dynamics of Carbon Nanotubes," *ACS Nano*, vol. 5, no. 11, pp. 8974–8989, Nov. 2011, doi: 10.1021/nn203144f.

[117] B. N. Wang, R. D. Bennett, E. Verploegen, A. J. Hart, and R. E. Cohen, "Characterizing the Morphologies of Mechanically Manipulated Multiwall Carbon Nanotube Films by Small-Angle X-ray Scattering," *J. Phys. Chem. C*, vol. 111, no. 48, pp. 17933–17940, Dec. 2007, doi: 10.1021/jp071798c.

[118] D. N. Futaba *et al.*, “Shape-engineerable and highly densely packed single-walled carbon nanotubes and their application as super-capacitor electrodes,” *Nat. Mater.*, vol. 5, no. 12, pp. 987–994, Dec. 2006, doi: 10.1038/nmat1782.

[119] T. Wang, D. Jiang, S. Chen, K. Jeppson, L. Ye, and J. Liu, “Formation of three-dimensional carbon nanotube structures by controllable vapor densification,” *Mater. Lett.*, vol. 78, pp. 184–187, Jul. 2012, doi: 10.1016/j.matlet.2012.03.059.

[120] W. Feuray *et al.*, “Evaluation of metal coating techniques up to 66 GHz and their application to additively manufactured bandpass filters,” in *2017 47th European Microwave Conference (EuMC)*, Oct. 2017, pp. 512–515. doi: 10.23919/EuMC.2017.8230902.

[121] S. M. Sri-Jayantha, G. McVicker, K. Bernstein, and J. U. Knickerbocker, “Thermomechanical modeling of 3D electronic packages,” *IBM J. Res. Dev.*, vol. 52, no. 6, pp. 623–634, Nov. 2008, doi: 10.1147/JRD.2008.5388568.

[122] S. Faraji, K. L. Stano, O. Yildiz, A. Li, Y. Zhu, and P. D. Bradford, “Ultralight anisotropic foams from layered aligned carbon nanotube sheets,” *Nanoscale*, vol. 7, no. 40, pp. 17038–17047, Oct. 2015, doi: 10.1039/C5NR03899E.

[123] G. Yuan, H. Li, B. Shan, and J. Liu, “Thermal Interface Materials Based on Vertically Aligned Carbon Nanotube Arrays: A Review,” *Micro Nanosyst.*, vol. 11, no. 1, pp. 3–10, Apr. 2019, doi: 10.2174/1876402911666181218143608.

[124] T. Tong, Y. Zhao, L. Delzeit, A. Kashani, M. Meyyappan, and A. Majumdar, “Dense Vertically Aligned Multiwalled Carbon Nanotube Arrays as Thermal Interface Materials,” *IEEE Trans. Compon. Packag. Technol.*, vol. 30, no. 1, pp. 92–100, Mar. 2007, doi: 10.1109/TCAPT.2007.892079.

[125] Y. T. Lee, S. Shanmugan, and D. Mutharasu, “Thermal resistance of CNTs-based thermal interface material for high power solid state device packages,” *Appl. Phys. A*, vol. 114, no. 4, pp. 1145–1152, Mar. 2014, doi: 10.1007/s00339-013-7676-5.

[126] M. Wang *et al.*, “Crack-Free and Scalable Transfer of Carbon Nanotube Arrays into Flexible and Highly Thermal Conductive Composite Film,” *ACS Appl. Mater. Interfaces*, vol. 6, no. 1, pp. 539–544, Jan. 2014, doi: 10.1021/am404594m.

[127] H. Huang, C. H. Liu, Y. Wu, and S. Fan, “Aligned Carbon Nanotube Composite Films for Thermal Management,” *Adv. Mater.*, vol. 17, no. 13, pp. 1652–1656, 2005, doi: 10.1002/adma.200500467.

[128] T. Borca-Tasciuc, M. Mazumder, Y. Son, S. K. Pal, L. S. Schadler, and P. M. Ajayan, “Anisotropic Thermal Diffusivity Characterization of Aligned Carbon Nanotube-Polymer Composites,” *J. Nanosci. Nanotechnol.*, vol. 7, no. 4–5, pp. 1581–1588, Apr. 2007, doi: 10.1166/jnn.2007.657.

[129] K. Kordás *et al.*, “Chip cooling with integrated carbon nanotube microfin architectures,” *Appl. Phys. Lett.*, vol. 90, no. 12, p. 123105, Mar. 2007, doi: 10.1063/1.2714281.

[130] P. Mahajan and S. P. Agnihotri, “Analyzing Two Stage CMOS LNA for Wireless Interconnect,” in *2019 IEEE 5th International Conference for Convergence in Technology (I2CT)*, Mar. 2019, pp. 1–4. doi: 10.1109/I2CT45611.2019.9033629.

[131] S. Laha, S. Kaya, D. W. Matolak, W. Rayess, D. DiTomaso, and A. Kodi, “A New Frontier in Ultralow Power Wireless Links: Network-on-Chip and Chip-to-Chip Interconnects,” *IEEE Trans. Comput.-Aided Des. Integr. Circuits Syst.*, vol. 34, no. 2, pp. 186–198, Feb. 2015, doi: 10.1109/TCAD.2014.2379640.

[132] L. Yan and G. Hanson, “Wave propagation channels for intra-chip wireless communication systems,” in *2009 IEEE Antennas and Propagation Society International Symposium*, Jun. 2009, pp. 1–4. doi: 10.1109/APS.2009.5172085.

[133] P. J. Burke, S. Li, and Z. Yu, “Quantitative theory of nanowire and nanotube antenna performance,” *IEEE Trans. Nanotechnol.*, vol. 5, no. 4, pp. 314–334, Jul. 2006, doi: 10.1109/TNANO.2006.877430.

[134] Y. Wang, Q. Wu, W. Shi, X. He, X. Sun, and T. Gui, “Radiation Properties of Carbon Nanotubes Antenna at Terahertz/Infrared Range,” *Int. J. Infrared Millim. Waves*, vol. 29, no. 1, pp. 35–42, Jan. 2008, doi: 10.1007/s10762-007-9306-9.

[135] S. A. Maksimenko, G. Ya. Slepyan, A. M. Nemilentsau, and M. V. Shuba, “Carbon nanotube antenna: Far-field, near-field and thermal-noise properties,” *Phys. E Low-Dimens. Syst. Nanostructures*, vol. 40, no. 7, pp. 2360–2364, May 2008, doi: 10.1016/j.physe.2007.09.196.

[136] K. Kempa *et al.*, “Carbon Nanotubes as Optical Antennae,” *Adv. Mater.*, vol. 19, no. 3, pp. 421–426, Feb. 2007, doi: 10.1002/adma.200601187.

[137] Y. Wang *et al.*, “Receiving and transmitting light-like radio waves: Antenna effect in arrays of aligned carbon nanotubes,” *Appl. Phys. Lett.*, vol. 85, no. 13, pp. 2607–2609, Sep. 2004, doi: 10.1063/1.1797559.

[138] G. W. Hanson, “A Common Electromagnetic Framework for Carbon Nanotubes and Solid Nanowires—Spatially Dispersive Conductivity, Generalized Ohm’s Law, Distributed Impedance, and Transmission Line Model,” *IEEE Trans. Microw. Theory Tech.*, vol. 59, no. 1, pp. 9–20, Jan. 2011, doi: 10.1109/TMTT.2010.2090693.

[139] G. W. Hanson, “Fundamental transmitting properties of carbon nanotube antennas,” *IEEE Trans. Antennas Propag.*, vol. 53, no. 11, pp. 3426–3435, Nov. 2005, doi: 10.1109/TAP.2005.858865.

[140] G. W. Hanson, “Current on an infinitely-long carbon nanotube antenna excited by a gap generator,” *IEEE Trans. Antennas Propag.*, vol. 54, no. 1, pp. 76–81, Jan. 2006, doi: 10.1109/TAP.2005.861550.

[141] C. Brun, P. Franck, P. Coquet, D. Baillargeat, and B. K. Tay, “Monopole antenna based on carbon nanotubes,” in *2013 IEEE MTT-S International Microwave Symposium Digest (MTT)*, Jun. 2013, pp. 1–4. doi: 10.1109/MWSYM.2013.6697482.

[142] J. Gipprich and D. Stevens, “A new via fence structure for crosstalk reduction in high density stripline packages,” in *2001 IEEE MTT-S International Microwave Sympsoium Digest (Cat. No.01CH37157)*, May 2001, vol. 3, pp. 1719–1722 vol.3. doi: 10.1109/MWSYM.2001.967237.

[143] M. Kazerooni, M. A. Salari, and A. Cheldavi, “A novel method for crosstalk reduction in coupled pair microstrip lines,” *Int. J. RF Microw. Comput.-Aided Eng.*, vol. 22, no. 2, pp. 167–174, 2012, doi: 10.1002/mmce.20573.

[144] A. Suntives, A. Khajooeizadeh, and R. Abhari, “Using via fences for crosstalk reduction in PCB circuits,” in *2006 IEEE International Symposium on Electromagnetic Compatibility, 2006. EMC 2006.*, Aug. 2006, vol. 1, pp. 34–37. doi: 10.1109/ISEMC.2006.1706258.

[145] M. H. Al-Saleh and U. Sundararaj, “Electromagnetic interference shielding mechanisms of CNT/polymer composites,” *Carbon*, vol. 47, no. 7, pp. 1738–1746, Jun. 2009, doi: 10.1016/j.carbon.2009.02.030.

[146] A. Kumar *et al.*, “EM shielding effectiveness of Pd-CNT-Cu nanocomposite buckypaper,” *J. Mater. Chem. A*, vol. 3, no. 26, pp. 13986–13993, Jun. 2015, doi: 10.1039/C4TA05749J.

[147] J.-S. Roh, Y.-S. Chi, T. J. Kang, and S. Nam, “Electromagnetic Shielding Effectiveness of Multifunctional Metal Composite Fabrics,” *Text. Res. J.*, vol. 78, no. 9, pp. 825–835, Sep. 2008, doi: 10.1177/0040517507089748.

[148] L. Kong *et al.*, “Powerful absorbing and lightweight electromagnetic shielding CNTs/RGO composite,” *Carbon*, vol. 145, pp. 61–66, Apr. 2019, doi: 10.1016/j.carbon.2019.01.009.

[149] D. Tan *et al.*, “A light-weight electromagnetic shield using high density carbon nanotube fence-wall for RF packaging,” in *2015 IEEE MTT-S International Microwave Symposium*, May 2015, pp. 1–4. doi: 10.1109/MWSYM.2015.7166849.

[150] D. Tan, M. Cometto, P. Roux-Levy, P. Coquet, T. B. Kang, and D. Baillargeat, “Carbon nanotubes based RF packaging solutions,” in *2018 IEEE 18th International Conference on Nanotechnology (IEEE-NANO)*, Jul. 2018, pp. 1–4. doi: 10.1109/NANO.2018.8626279.

[151] T. Dunlin, “CARBON NANOTUBE FENCE-WALL FOR RADIO FREQUENCY ISOLATION.”

[152] J. U. Knickerbocker *et al.*, “3D silicon integration,” in *2008 58th Electronic Components and Technology Conference*, May 2008, pp. 538–543. doi: 10.1109/ECTC.2008.4550025.

[153] A. Usman *et al.*, “Interposer Technologies for High-Performance Applications,” *IEEE Trans. Compon. Packag. Manuf. Technol.*, vol. 7, no. 6, pp. 819–828, Jun. 2017, doi: 10.1109/TCPMT.2017.2674686.

[154] Z. Du, K. Aronkytö, J. Putkonen, J. Kapanen, E. Ohlmer, and D. Swist, “5G E-band backhaul system evaluations: Focus on moving objects and outdoor to indoor transmission,” in *2017 European Conference on Networks and Communications (EuCNC)*, Jun. 2017, pp. 1–5. doi: 10.1109/EuCNC.2017.7980764.

[155] S. Peleg, “The Advantages of E-Band Wireless Systems in Mobile Backhaul Applications, March 2009,” p. 15, 2009.

[156] M. V. Pelegrini *et al.*, “Interposer based on metallic-nanowire-membrane (MnM) for mm-wave applications,” in *2016 46th European Microwave Conference (EuMC)*, Oct. 2016, pp. 1461–1464. doi: 10.1109/EuMC.2016.7824630.

[157] M. Bertrand *et al.*, “Integrated Waveguides in Nanoporous Alumina Membrane for Millimeter-Wave Interposer,” *IEEE Microw. Wirel. Compon. Lett.*, vol. 29, no. 2, pp. 83–85, Feb. 2019, doi: 10.1109/LMWC.2018.2887193.

[158] M. Bertrand *et al.*, “Substrate Integrated Waveguides for mm-wave Functionalized Silicon Interposer,” in *2018 IEEE/MTT-S International Microwave Symposium - IMS*, Jun. 2018, pp. 875–878. doi: 10.1109/MWSYM.2018.8439287.

[159] G. Prigent, A.-L. Franc, M. Wietstruck, and M. Keynak, “Substrate Integrated Waveguide Bandpass Filters implemented on Silicon Interposer for Terahertz Applications,” in *2020 IEEE/MTT-S International Microwave Symposium (IMS)*, Aug. 2020, pp. 595–598. doi: 10.1109/IMS30576.2020.9223781.

[160] P. L. Doan, “Emerging Technology for RF and Millimeter-wave Circuits based on Carbone Nanotubes.”

[161] J. G. Andrews *et al.*, “What Will 5G Be?,” *ArXiv14052957 Cs Math*, May 2014, Accessed: Aug. 15, 2021. [Online]. Available: http://arxiv.org/abs/1405.2957

[162] T. E. Bogale and L. B. Le, “Massive MIMO and mmWave for 5G Wireless HetNet: Potential Benefits and Challenges,” *IEEE Veh. Technol. Mag.*, vol. 11, no. 1, pp. 64–75, Mar. 2016, doi: 10.1109/MVT.2015.2496240.

[163] V. Obukhovets, “Some New Trends in Phased Antenna Array Designing,” in *2019 Radiation and Scattering of Electromagnetic Waves (RSEMW)*, Jun. 2019, pp. 20–23. doi: 10.1109/RSEMW.2019.8792760.

[164] F. Casini, R. V. Gatti, L. Marcaccioli, and R. Sorrentino, “A novel design method for Blass matrix beam-forming networks,” in *2007 European Radar Conference*, Oct. 2007, pp. 232–235. doi: 10.1109/EURAD.2007.4404979.

[165] H. Ren, H. Zhang, Y. Jin, Y. Gu, and B. Arigong, “A Novel 2-D 3×3 Nolen Matrix for 2-D Beamforming Applications,” *IEEE Trans. Microw. Theory Tech.*, vol. 67, no. 11, pp. 4622–4631, Nov. 2019, doi: 10.1109/TMTT.2019.2917211.

[166] R. Wang, F. Yang, P. Yang, and Y. Yan, “Design of a Rotman lens antenna array for wide-scan and beam uniformity applications,” in *2019 IEEE International Symposium on Antennas and Propagation and USNC-URSI Radio Science Meeting*, Jul. 2019, pp. 1877–1878. doi: 10.1109/APUSNCURSINRSM.2019.8888825.

[167] W. Li, S. Liu, J. Deng, Z. Hu, and Z. Zhou, “A Compact SIW Monopulse Antenna Array Based on Microstrip Feed,” *IEEE Antennas Wirel. Propag. Lett.*, vol. 20, no. 1, pp. 93–97, Jan. 2021, doi: 10.1109/LAWP.2020.3041485.

[168] S. Vashist, M. Soni, and P. K. Singhal, “A Review on the Development of Rotman Lens Antenna,” *Chin. J. Eng.*, vol. 2014, pp. 1–9, Jul. 2014, doi: 10.1155/2014/385385.

[169] A. Tajik, A. Shafiei Alavijeh, and M. Fakharzadeh, “Asymmetrical 4×4 Butler Matrix and its Application for Single Layer 8×8 Butler Matrix,” *IEEE Trans. Antennas Propag.*, vol. 67, no. 8, pp. 5372–5379, Aug. 2019, doi: 10.1109/TAP.2019.2916695.

[170] M. Nedil, T. A. Denidni, and L. Talbi, “Novel Butler matrix using CPW multi-layer technology,” in *2005 IEEE Antennas and Propagation Society International Symposium*, Jul. 2005, vol. 3A, pp. 299–302 vol. 3A. doi: 10.1109/APS.2005.1552240.

[171] T. Djerafi, N. J. G. Fonseca, and K. Wu, “Design and implementation of a planar 4×4 butler matrix in SIW technology for wideband applications,” in *The 40th European Microwave Conference*, Sep. 2010, pp. 910–913. doi: 10.23919/EUMC.2010.5616642.

[172] J. Butler, “Beam-forming matrix simplifies design of electronically scanned antennas,” *undefined*, 1961, Accessed: Aug. 15, 2021. [Online]. Available: https://www.semanticscholar.org/paper/Beam-forming-matrix-simplifies-design-of-scanned-Butler/887b6e44c0421637def86a8fdfc1677b19c894af

[173] J. Hirokawa, T. Tomura, K. Nishimori, and T. Hiraguri, “A $64\mathrmx64$-way Two-dimensional Beam-switching Butler Matrix for Multi-beam Massive MIMO,” in *2019 IEEE International Symposium on Phased Array System Technology (PAST)*, Oct. 2019, pp. 1–4. doi: 10.1109/PAST43306.2019.9020759.

[174] Zulfi, A. Dewantari, and A. Munir, “Implementation of Meander Line Structure for Size Miniaturization of 4×4 Butler Matrix,” in *2020 27th International Conference on Telecommunications (ICT)*, Oct. 2020, pp. 1–4. doi: 10.1109/ICT49546.2020.9239448.

[175] Y. Zhai, X. Fang, K. Ding, and F. He, “Miniaturization Design for 8 × 8 Butler Matrix Based on Back-to-Back Bilayer Microstrip,” *Int. J. Antennas Propag.*, vol. 2014, p. e583903, Mar. 2014, doi: 10.1155/2014/583903.

[176] W. Nie, Y. Fan, S. Luo, and Y. Guo, “A switched-beam microstrip antenna array with miniaturized butler matrix network,” *Microw. Opt. Technol. Lett.*, vol. 57, no. 4, pp. 841–845, 2015, doi: 10.1002/mop.28972.

[177] F. Wu and L. Sun, “Miniaturization of 4×4 Butler matrix using high slow-wave factor structure,” in *2017 IEEE 2nd Advanced Information Technology, Electronic and Automation Control Conference (IAEAC)*, Mar. 2017, pp. 1772–1775. doi: 10.1109/IAEAC.2017.8054317.

[178] K. Wincza and K. Sachse, “Broadband 4×4 Butler matrix in microstrip multilayer technology designed with the use of three-section directional couplers and phase

correction Networks," in *18-th INTERNATIONAL CONFERENCE ON MICROWAVES, RADAR AND WIRELESS COMMUNICATIONS*, Jun. 2010, pp. 1–4.

[179] K. Wincza, S. Gruszczynski, and K. Sachse, "Broadband Planar Fully Integrated 8 $\, \times \,$8 Butler Matrix Using Coupled-Line Directional Couplers," *IEEE Trans. Microw. Theory Tech.*, vol. 59, no. 10, pp. 2441–2446, Oct. 2011, doi: 10.1109/TMTT.2011.2164092.

[180] K. Wincza and S. Gruszczynski, "Broadband Integrated 8×8 Butler Matrix Utilizing Quadrature Couplers and Schiffman Phase Shifters for Multibeam Antennas With Broadside Beam," *IEEE Trans. Microw. Theory Tech.*, vol. 64, no. 8, pp. 2596–2604, Aug. 2016, doi: 10.1109/TMTT.2016.2582877.

[181] K. Ding, J. Bai, and A. Kishk, "A quasi butler matrix with 6×6 beam-forming capacity using 3×3 hybrid couplers," in *2017 XXXIInd General Assembly and Scientific Symposium of the International Union of Radio Science (URSI GASS)*, Aug. 2017, pp. 1–4. doi: 10.23919/URSIGASS.2017.8120341.

[182] H. N. Chu and T.-G. Ma, "An Extended 4×4 Butler Matrix With Enhanced Beam Controllability and Widened Spatial Coverage," *IEEE Trans. Microw. Theory Tech.*, vol. 66, no. 3, pp. 1301–1311, Mar. 2018, doi: 10.1109/TMTT.2017.2772815.

[183] C.-H. Chen, X.-P. Zhang, and J. Xu, "Implementation of a low-loss wide-band flat-topped beam-forming network based on butler martix," in *2015 Asia-Pacific Microwave Conference (APMC)*, Dec. 2015, vol. 3, pp. 1–3. doi: 10.1109/APMC.2015.7413400.

[184] S. Trinh-Van, J. M. Lee, Y. Yang, K.-Y. Lee, and K. C. Hwang, "A Sidelobe-Reduced, Four-Beam Array Antenna Fed by a Modified 4×4 Butler Matrix for 5G Applications," *IEEE Trans. Antennas Propag.*, vol. 67, no. 7, pp. 4528–4536, Jul. 2019, doi: 10.1109/TAP.2019.2905783.

[185] K. Wincza, A. Rydosz, I. Slomian, and S. Gruszczynski, "Reduced sidelobe multibeam antenna array with broadside beam fed by 4×8 Butler matrix," in *2015 International Symposium on Antennas and Propagation (ISAP)*, Nov. 2015, pp. 1–3.

[186] S. Gruszczynski, K. Wincza, and K. Sachse, "Reduced Sidelobe Four-Beam N-Element Antenna Arrays Fed by $4\times N$ Butler Matrices," *IEEE Antennas Wirel. Propag. Lett.*, vol. 5, pp. 430–434, 2006, doi: 10.1109/LAWP.2006.885015.

[187] N. Ashraf, A. A. Kishk, and A.-R. Sebak, "AMC Packaged - Butler Matrix for Millimeter Wave Beamforming," in *2018 IEEE International Symposium on Antennas and Propagation USNC/URSI National Radio Science Meeting*, Jul. 2018, pp. 417–418. doi: 10.1109/APUSNCURSINRSM.2018.8608299.

[188] X. Zhang, F. Qin, and H. Zhang, "A Compact Dual-Polarized Millimeter-Wave Multi-Beam Antenna for 5G Applications," in *2020 International Conference on Microwave and Millimeter Wave Technology (ICMMT)*, Sep. 2020, pp. 1–3. doi: 10.1109/ICMMT49418.2020.9386662.

[189] Y. Liu, O. Bshara, I. Tekin, and K. R. Dandekar, "A 4 by 10 series 60 GHz microstrip array antenna fed by butler matrix for 5G applications," in *2018 IEEE 19th Wireless and Microwave Technology Conference (WAMICON)*, Apr. 2018, pp. 1–4. doi: 10.1109/WAMICON.2018.8363899.

[190] A. J. Fenn, "A Review of Adaptive Microwave and RF Phased Arrays for Thermotherapy Treatment of Cancer," in *2018 IEEE International Symposium on Antennas and Propagation USNC/URSI National Radio Science Meeting*, Jul. 2018, pp. 17–18. doi: 10.1109/APUSNCURSINRSM.2018.8608815.

[191] P. Chen and W. Hong, "Research advances in phased array antennas for satellite communications," in *12th European Conference on Antennas and Propagation (EuCAP 2018)*, Apr. 2018, pp. 1–3. doi: 10.1049/cp.2018.0981.

[192] Q. Sun, Y.-L. Ban, X.-Y. Zhao, X.-F. Li, and J.-W. Zheng, “Folded C-Type SIW Butler Matrix,” in *2019 IEEE MTT-S International Wireless Symposium (IWS)*, May 2019, pp. 1–2. doi: 10.1109/IEEE-IWS.2019.8804128.

[193] Y. Cao, K.-S. Chin, W. Che, W. Yang, and E. S. Li, “A Compact 38 GHz Multibeam Antenna Array With Multifolded Butler Matrix for 5G Applications,” *IEEE Antennas Wirel. Propag. Lett.*, vol. 16, pp. 2996–2999, 2017, doi: 10.1109/LAWP.2017.2757045.

[194] J.-W. Lian, Y.-L. Ban, Y.-Q. Wu, and L.-H. Zhong, “Miniaturized Multibeam Array Antenna Based on E-Plane Butler Matrix for 5G Application,” in *2018 IEEE International Symposium on Antennas and Propagation USNC/URSI National Radio Science Meeting*, Jul. 2018, pp. 1031–1032. doi: 10.1109/APUSNCURSINRSM.2018.8609010.

[195] Y. Li, J. Wang, and K.-M. Luk, “Millimeter-Wave MultiBeam Aperture-Coupled Magnetoelectric Dipole Array With Planar Substrate Integrated Beamforming Network for 5G Applications,” *IEEE Trans. Antennas Propag.*, vol. 65, no. 12, pp. 6422–6431, Dec. 2017, doi: 10.1109/TAP.2017.2681429.

[196] Y. Yang, W. Luo, and C. Zhang, “A Novel Millimeter Wave Multiple Beam Antenna with SIW Butler Matrix,” in *2019 IEEE International Conference on Computational Electromagnetics (ICCEM)*, Mar. 2019, pp. 1–3. doi: 10.1109/COMPEM.2019.8779056.

[197] T. Djerafi and K. Wu, “A Low-Cost Wideband 77-GHz Planar Butler Matrix in SIW Technology,” *IEEE Trans. Antennas Propag.*, vol. 60, no. 10, pp. 4949–4954, Oct. 2012, doi: 10.1109/TAP.2012.2207309.

[198] G. Namgung, C. Lee, H. Park, Y. Seo, S. Kahng, and D. Lim, “Design of Wideband SIW Beamforming Circularly Polarized Antennas for 5G-band,” in *2019 8th Asia-Pacific Conference on Antennas and Propagation (APCAP)*, Aug. 2019, pp. 297–298. doi: 10.1109/APCAP47827.2019.9471979.

[199] Z. Zhang, X. Cao, J. Gao, S. Li, and J. Han, “Broadband SIW Cavity-Backed Slot Antenna for Endfire Applications,” *IEEE Antennas Wirel. Propag. Lett.*, vol. 17, no. 7, pp. 1271–1275, Jul. 2018, doi: 10.1109/LAWP.2018.2842046.

[200] S. Mukherjee, A. Biswas, and K. V. Srivastava, “Broadband Substrate Integrated Waveguide Cavity-Backed Bow-Tie Slot Antenna,” *IEEE Antennas Wirel. Propag. Lett.*, vol. 13, pp. 1152–1155, 2014, doi: 10.1109/LAWP.2014.2330743.

[201] G. Q. Luo, Z. F. Hu, W. J. Li, X. H. Zhang, L. L. Sun, and J. F. Zheng, “Bandwidth-Enhanced Low-Profile Cavity-Backed Slot Antenna by Using Hybrid SIW Cavity Modes,” *IEEE Trans. Antennas Propag.*, vol. 60, no. 4, pp. 1698–1704, Apr. 2012, doi: 10.1109/TAP.2012.2186226.

[202] M. Ohira, A. Miura, and M. Ueba, “60-GHz Wideband Substrate-Integrated-Waveguide Slot Array Using Closely Spaced Elements for Planar Multisector Antenna,” *IEEE Trans. Antennas Propag.*, vol. 58, no. 3, pp. 993–998, Mar. 2010, doi: 10.1109/TAP.2009.2039329.

[203] M. V. Varnoosfaderani, J. Lu, and B. Zhu, “Matching slot role in bandwidth enhancement of SIW cavity-backed slot antenna,” in *Proceedings of 2014 3rd Asia-Pacific Conference on Antennas and Propagation*, Jul. 2014, pp. 244–247. doi: 10.1109/APCAP.2014.6992464.

[204] Z. Chen and Z. Shen, “A Compact Cavity-Backed Endfire Slot Antenna,” *IEEE Antennas Wirel. Propag. Lett.*, vol. 13, pp. 281–284, 2014, doi: 10.1109/LAWP.2014.2304731.

[205] S. Yun, D.-Y. Kim, and S. Nam, “Bandwidth Enhancement of Cavity-Backed Slot Antenna Using a Via-Hole Above the Slot,” *IEEE Antennas Wirel. Propag. Lett.*, vol. 11, pp. 1092–1095, 2012, doi: 10.1109/LAWP.2012.2215911.

[206] P. N. Choubey, W. Hong, Z.-C. Hao, P. Chen, T.-V. Duong, and J. Mei, “A Wideband Dual-Mode SIW Cavity-Backed Triangular-Complimentary-Split-Ring-Slot (TCSRS) Antenna,” *IEEE Trans. Antennas Propag.*, vol. 64, no. 6, pp. 2541–2545, Jun. 2016, doi: 10.1109/TAP.2016.2550036.

[207] H. Yang, J. Lu, C. Lin, C. Song, and G. Gao, “Design of Wideband Cavity-Backed Slot Antenna With Multilayer Dielectric Cover,” *IEEE Antennas Wirel. Propag. Lett.*, vol. 15, pp. 861–864, 2016, doi: 10.1109/LAWP.2015.2477605.

[208] J.-W. Lian, Y.-L. Ban, C. Xiao, and Z.-F. Yu, “Compact Substrate-Integrated 4 × 8 Butler Matrix With Sidelobe Suppression for Millimeter-Wave Multibeam Application,” *IEEE Antennas Wirel. Propag. Lett.*, vol. 17, no. 5, pp. 928–932, May 2018, doi: 10.1109/LAWP.2018.2825367.

[209] P.-S. Kildal, E. Alfonso, A. Valero-Nogueira, and E. Rajo-Iglesias, “Local Metamaterial-Based Waveguides in Gaps Between Parallel Metal Plates,” *IEEE Antennas Wirel. Propag. Lett.*, vol. 8, pp. 84–87, 2009, doi: 10.1109/LAWP.2008.2011147.

[210] F. J. Gutierrez Bernal and E. Rajo-Iglesias, “Design of a wide band Butler matrix in groove gap waveguide technology,” in *2017 International Symposium on Antennas and Propagation (ISAP)*, Oct. 2017, pp. 1–2. doi: 10.1109/ISANP.2017.8228890.

[211] J. Cao, H. Wang, R. Gao, Y. Wang, and S. Mou, “2-Dimensional Beam Scanning Gap Waveguide Leaky Wave Antenna Array Based on Butler Matrix in Metallic 3D Printed Technology,” in *2019 13th European Conference on Antennas and Propagation (EuCAP)*, Mar. 2019, pp. 1–4.

[212] A. Tamayo-Domínguez, J.-M. Fernández-González, and M. Sierra-Castañer, “3-D-Printed Modified Butler Matrix Based on Gap Waveguide at W-Band for Monopulse Radar,” *IEEE Trans. Microw. Theory Tech.*, vol. 68, no. 3, pp. 926–938, Mar. 2020, doi: 10.1109/TMTT.2019.2953164.

[213] A. Vosoogh, A. A. Brazález, and P.-S. Kildal, “A V-Band Inverted Microstrip Gap Waveguide End-Coupled Bandpass Filter,” *IEEE Microw. Wirel. Compon. Lett.*, vol. 26, no. 4, pp. 261–263, Apr. 2016, doi: 10.1109/LMWC.2016.2538598.

[214] J.-Y. Deng *et al.*, “Slow-Wave Substrate Integrated Groove Gap Waveguide,” *IEEE Microw. Wirel. Compon. Lett.*, vol. 30, no. 5, pp. 461–464, May 2020, doi: 10.1109/LMWC.2020.2983017.

[215] F. Parment, A. Ghiotto, T.-P. Vuong, J.-M. Duchamp, and K. Wu, “Broadband transition from dielectric-filled to air-filled Substrate Integrated Waveguide for low loss and high power handling millimeter-wave Substrate Integrated Circuits,” in *2014 IEEE MTT-S International Microwave Symposium (IMS2014)*, Jun. 2014, pp. 1–3. doi: 10.1109/MWSYM.2014.6848524.

[216] T. Martin, A. Ghiotto, T.-P. Vuong, and F. Lotz, “Configurable Perforated Air-Filled Substrate Integrated Waveguide (AFSIW) For Generic High-Performance Systems on Substrate,” *IEEE Trans. Microw. Theory Tech.*, vol. 67, no. 11, pp. 4308–4321, Nov. 2019, doi: 10.1109/TMTT.2019.2940193.

[217] F. Parment, A. Ghiotto, T.-P. Vuong, J.-M. Duchamp, and K. Wu, “Low-loss air-filled Substrate Integrated Waveguide (SIW) band-pass filter with inductive posts,” in *2015 European Microwave Conference (EuMC)*, Sep. 2015, pp. 761–764. doi: 10.1109/EuMC.2015.7345875.

[218] J. Corsi *et al.*, “Partially-Air-Filled Slow-Wave Substrate Integrated Waveguide in Metallic Nanowire Membrane Technology,” in *2020 IEEE/MTT-S International Microwave Symposium (IMS)*, Aug. 2020, pp. 9–12. doi: 10.1109/IMS30576.2020.9223955.

[219] F. David *et al.*, “3D micro-fabricated high-Q 140 GHz filter,” in *2017 IEEE MTT-S International Microwave Symposium (IMS)*, Jun. 2017, pp. 1297–1299. doi: 10.1109/MWSYM.2017.8058848.

[220] N. Jguirim, D. Passerieux, N. Parou, C. Dalmay, and P. Blondy, “Design and Additive Microfabrication of a Two-Pole 287-GHz Waveguide Bandpass Filter,” *IEEE Microw. Wirel. Compon. Lett.*, vol. 30, no. 1, pp. 20–22, Jan. 2020, doi: 10.1109/LMWC.2019.2955595.

[221] Y. Jin, H. Sun, Y. Xiao, W. Tan, and Z. Song, “A 340GHz Cross-coupled Waveguide Filter Based on MEMS Process,” in *2021 IEEE 4th International Conference on Electronics Technology (ICET)*, May 2021, pp. 289–293. doi: 10.1109/ICET51757.2021.9450939.

[222] J. Ye, H. Zhang, and R. Chu, “Analysis of a New Method to Design a Coaxial-to-Rectangular Waveguide Transition,” in *2019 International Applied Computational Electromagnetics Society Symposium - China (ACES)*, Aug. 2019, vol. 1, pp. 1–2. doi: 10.23919/ACES48530.2019.9060514.

[223] I. Mohamed and A. Sebak, “Broadband Transition of Substrate-Integrated Waveguide-to-Air-Filled Rectangular Waveguide,” *IEEE Microw. Wirel. Compon. Lett.*, vol. 28, no. 11, pp. 966–968, Nov. 2018, doi: 10.1109/LMWC.2018.2871330.

[224] R. Kazemi, A. E. Fathy, S. Yang, and R. A. Sadeghzadeh, “Development of an ultra wide band GCPW to SIW transition,” in *2012 IEEE Radio and Wireless Symposium*, Jan. 2012, pp. 171–174. doi: 10.1109/RWS.2012.6175308.

[225] P. Souzangar and M. Shahabadi, “Numerical Multimode Thru-Line (TL) Calibration Technique for Substrate Integrated Waveguide Circuits,” *J. Electromagn. Waves Appl.*, vol. 23, no. 13, pp. 1785–1793, Jan. 2009, doi: 10.1163/156939309789566969.

[226] D. M. Pozar, “Microstrip antenna aperture-coupled to a microstripline,” *Electron. Lett.*, vol. 21, p. 49, Jan. 1985, doi: 10.1049/el:19850034.

[227] U. Rafique, S. A. Ali, M. A. Khan, and M. M. Ahmed, “A wideband slot-coupled inverted microstrip patch antenna for wireless communications,” in *2012 International Conference on Emerging Technologies*, Islamabad, Pakistan, Oct. 2012, pp. 1–4. doi: 10.1109/ICET.2012.6375492.

[228] N. Ghassemi, J. Rashed-Mohassel, M. H. Neshati, and M. Ghassemi, “SLOT COUPLED MICROSTRIP ANTENNA FOR ULTRA WIDEBAND APPLICATIONS IN C AND X BANDS,” *Prog. Electromagn. Res. M*, vol. 3, pp. 15–25, 2008, doi: 10.2528/PIERM08051202.

[229] Cristina Arenas Buendia, “Enhanced fluid characterization in the millimeter-wave band using Gap Waveguide Technology,” Universitat Politècnica de València, 2015.

[230] A. M. E. Safwata, K. A. Zaki, W. Johnson, and C. H. Lee, “Novel design for coplanar waveguide to microstrip transition,” in *2001 IEEE MTT-S International Microwave Sympsoium Digest (Cat. No.01CH37157)*, Phoenix, AZ, USA, 2001, vol. 2, pp. 607–610. doi: 10.1109/MWSYM.2001.966968.

[231] Guizhen Zheng, J. Papapolymerou, and M. M. Tentzeris, “Wideband coplanar waveguide RF probe pad to microstrip transitions without via holes,” *IEEE Microw. Wirel. Compon. Lett.*, vol. 13, no. 12, pp. 544–546, Dec. 2003, doi: 10.1109/LMWC.2003.820638.

[232] L. Zhu and W. Menzel, “Broad-Band Microstrip-to-CPW Transition via Frequency-Dependent Electromagnetic Coupling,” *IEEE Trans. Microw. Theory Tech.*, vol. 52, no. 5, pp. 1517–1522, May 2004, doi: 10.1109/TMTT.2004.827034.

[233] R. S. Beeresha, A. M. Khan, and H. V. M. Reddy, “CPW to microstrip transition using different CPW ground plane structures,” in *2016 IEEE International Conference on*

Recent Trends in Electronics, Information & Communication Technology (RTEICT), Bangalore, India, May 2016, pp. 667–671. doi: 10.1109/RTEICT.2016.7807907.

[234] Shi-Chang Gao, Le-Wei Li, Mook-Seng Leong, and Tat-Soon Yeo, "Dual-polarized slot-coupled planar antenna with wide bandwidth," *IEEE Trans. Antennas Propag.*, vol. 51, no. 3, pp. 441–448, Mar. 2003, doi: 10.1109/TAP.2003.809842.

[235] T. Hozen, S. Saito, and Y. Kimura, "Measurement of a microstrip antenna array fed by longitudinal slots on a narrow wall of the rectangular waveguide with standing-wave excitation for linear polarization perpendicular to the axis," in *2020 International Symposium on Antennas and Propagation (ISAP)*, Jan. 2021, pp. 433–434. doi: 10.23919/ISAP47053.2021.9391513.

[236] P. F. Zhang, L. Zhu, and S. Sun, "Study of Microstrip Slotted EH2-Mode Leaky Wave Antenna from Circuit Perspective," in *2019 IEEE Asia-Pacific Microwave Conference (APMC)*, Dec. 2019, pp. 1277–1279. doi: 10.1109/APMC46564.2019.9038681.

[237] P. F. Combes, *Micro-Ondes T2. Circuits passifs, propagation, antennes*, Dunod.

[238] H. Meier, T. Baier, and G. Riha, "Miniaturization and advanced functionalities of SAW devices," *IEEE Trans. Microw. Theory Tech.*, vol. 49, no. 4, pp. 743–748, Apr. 2001, doi: 10.1109/22.915458.

[239] J. Zuo, X. Chen, G. Han, L. Li, and W. Zhang, "An Integrated Approach to RF Antenna-Filter Co-Design," *IEEE Antennas Wirel. Propag. Lett.*, vol. 8, pp. 141–144, 2009, doi: 10.1109/LAWP.2009.2012732.

[240] C. Ni, W. Wu, Q. Liu, and H. Li, "A co-designed quasi Yagi antenna with coupled line filter," in *2017 7th IEEE International Symposium on Microwave, Antenna, Propagation, and EMC Technologies (MAPE)*, Oct. 2017, pp. 61–62. doi: 10.1109/MAPE.2017.8250797.

[241] Y. Sato *et al.*, "Ultra-miniaturized and surface-mountable glass-based 3D IPAC packages for RF modules," in *2013 IEEE 63rd Electronic Components and Technology Conference*, May 2013, pp. 1656–1661. doi: 10.1109/ECTC.2013.6575795.

[242] M. Le Coq *et al.*, "Miniature microstrip filter using high-permittivity ceramic substrates (er = 90)," in *2011 IEEE MTT-S International Microwave Symposium*, Jun. 2011, pp. 1–4. doi: 10.1109/MWSYM.2011.5972807.

[243] S. Jarchi, M. Khalily, and R. Tafazolli, "Effects of Metamaterial Loading on Miniaturization of Loop and Open Loop Microstrip Filters," in *2020 International Conference on UK-China Emerging Technologies (UCET)*, Aug. 2020, pp. 1–4. doi: 10.1109/UCET51115.2020.9205325.

[244] A. Delage *et al.*, "Aerosol jet printing of millimeter wave transmission lines on 3D ceramic substrates made by additive manufacturing," in *2018 IEEE/MTT-S International Microwave Symposium - IMS*, Jun. 2018, pp. 1557–1560. doi: 10.1109/MWSYM.2018.8439498.

[245] D. Deslandes and K. Wu, "Integrated transition of coplanar to rectangular waveguides," in *2001 IEEE MTT-S International Microwave Sympsoium Digest (Cat. No.01CH37157)*, May 2001, vol. 2, pp. 619–622 vol.2. doi: 10.1109/MWSYM.2001.966971.

[246] K. Wu, D. Deslandes, and Y. Cassivi, "The substrate integrated circuits - a new concept for high-frequency electronics and optoelectronics," in *6th International Conference on Telecommunications in Modern Satellite, Cable and Broadcasting Service, 2003. TELSIKS 2003.*, Oct. 2003, vol. 1, p. P-III. doi: 10.1109/TELSKS.2003.1246173.

[247] A. Iqbal, J. J. Tiang, S. K. Wong, M. Alibakhshikenari, F. Falcone, and E. Limiti, "Miniaturization Trends in Substrate Integrated Waveguide (SIW) Filters: A Review," *IEEE Access*, vol. 8, pp. 223287–223305, 2020, doi: 10.1109/ACCESS.2020.3044088.

[248] Y. Ding and K. Wu, “Miniaturization Techniques of Substrate Integrated Waveguide Circuits,” in *2008 IEEE MTT-S International Microwave Workshop Series on Art of Miniaturizing RF and Microwave Passive Components*, Dec. 2008, pp. 63–66. doi: 10.1109/IMWS.2008.4782262.

[249] M. Khalil, M. Kamarei, J. Jomaah, and H. Ayad, “Substrate Integrated Waveguide miniaturization using Slow Wave and Half Mode techniques,” in *2015 IEEE MTT-S International Microwave and RF Conference (IMaRC)*, Dec. 2015, pp. 173–176. doi: 10.1109/IMaRC.2015.7411390.

[250] S. B. Cohn, “Properties of Ridge Wave Guide,” *Proc. IRE*, vol. 35, no. 8, pp. 783–788, Aug. 1947, doi: 10.1109/JRPROC.1947.226277.

[251] W. Che, C. Li, P. Russer, and Y. L. Chow, “Propagation and band broadening effect of planar integrated ridged waveguide in multilayer dielectric substrates,” in *2008 IEEE MTT-S International Microwave Symposium Digest*, Jun. 2008, pp. 217–220. doi: 10.1109/MWSYM.2008.4633142.

[252] L. Sun, Y. Zhang, Z. Qian, D. Guan, and X. Zhong, “A compact broadband hybrid ridged SIW and GCPW coupler,” in *2016 IEEE MTT-S International Microwave Workshop Series on Advanced Materials and Processes for RF and THz Applications (IMWS-AMP)*, Jul. 2016, pp. 1–3. doi: 10.1109/IMWS-AMP.2016.7588451.

[253] M. Bozzi, S. Winkler, and K. Wu, “Broadband and compact ridge substrate-integrated waveguides,” *Microw. Antennas Propag. IET*, vol. 4, pp. 1965–1973, Dec. 2010, doi: 10.1049/iet-map.2009.0529.

[254] W. L. Barrow and H. Schaevitz, “Hollow Pipes of Relatively Small Dimensions,” *Trans. Am. Inst. Electr. Eng.*, vol. 60, no. 3, pp. 119–122, Mar. 1941, doi: 10.1109/T-AIEE.1941.5058293.

[255] N. Grigoropoulos and P. R. Young, “Compact folded waveguides,” in *34th European Microwave Conference, 2004.*, Oct. 2004, vol. 2, pp. 973–976.

[256] N. Nguyen-Trong, T. Kaufmann, L. Hall, and C. Fumeaux, “Variational Analysis of Folded Substrate-Integrated Waveguides,” *IEEE Microw. Wirel. Compon. Lett.*, vol. 25, no. 6, pp. 352–354, Jun. 2015, doi: 10.1109/LMWC.2015.2421251.

[257] W. Che, L. Geng, K. Wu, and Y. L. Chow, “Theoretical investigation and experimental verification of compact folded substrate integrated waveguide,” in *2007 European Microwave Conference*, Oct. 2007, pp. 380–383. doi: 10.1109/EUMC.2007.4405206.

[258] W. Che, L. Geng, K. Deng, and Y. L. Chow, “Analysis and Experiments of Compact Folded Substrate-Integrated Waveguide,” *IEEE Trans. Microw. Theory Tech.*, vol. 56, no. 1, pp. 88–93, Jan. 2008, doi: 10.1109/TMTT.2007.911955.

[259] C. A. Zhang, Y. J. Cheng, and and Y. Fan, “Quadri-Folded Substrate Integrated Waveguide Cavity and its Miniaturized Bandpass Filter Applications,” *Prog. Electromagn. Res. C*, vol. 23, pp. 1–14, 2011, doi: 10.2528/PIERC11052401.

[260] M. Shahidzadeh Mahani and G. W. Roberts, “A mmWave Folded Substrate Integrated Waveguide in a 130-nm CMOS Process,” *IEEE Trans. Microw. Theory Tech.*, vol. 65, no. 8, pp. 2775–2788, Aug. 2017, doi: 10.1109/TMTT.2017.2661259.

[261] Y. Ding and K. Wu, “Miniaturized hybrid ring circuits using T-type folded substrate integrated waveguide (TFSIW),” in *2009 IEEE MTT-S International Microwave Symposium Digest*, Jun. 2009, pp. 705–708. doi: 10.1109/MWSYM.2009.5165794.

[262] W. Hong *et al.*, “Half Mode Substrate Integrated Waveguide: A New Guided Wave Structure for Microwave and Millimeter Wave Application,” in *2006 Joint 31st International Conference on Infrared Millimeter Waves and 14th International Conference on Teraherz Electronics*, Sep. 2006, pp. 219–219. doi: 10.1109/ICIMW.2006.368427.

[263] B. Liu, W. Hong, Y.-Q. Wang, Q.-H. Lai, and K. Wu, “Half Mode Substrate Integrated Waveguide (HMSIW) 3-dB Coupler,” *IEEE Microw. Wirel. Compon. Lett.*, vol. 17, no. 1, pp. 22–24, Jan. 2007, doi: 10.1109/LMWC.2006.887244.

[264] J. Chen, W. Hong, P. Yan, B. Liu, Y. Wang, and K. Wu, “Design of a Six-Port Junction Using Half-Mode Substrate Integrated Waveguide,” in *2007 Asia-Pacific Microwave Conference*, Dec. 2007, pp. 1–4. doi: 10.1109/APMC.2007.4554870.

[265] O. Caytan *et al.*, “Half-Mode Substrate-Integrated-Waveguide Cavity-Backed Slot Antenna on Cork Substrate,” *IEEE Antennas Wirel. Propag. Lett.*, vol. 15, pp. 162–165, 2016, doi: 10.1109/LAWP.2015.2435891.

[266] S. Nam, B. Lee, and J. Lee, “Constant-absolute-bandwidth frequency-tunable half-mode SIW filter containing no tunable coupling structures,” in *2017 IEEE MTT-S International Microwave Symposium (IMS)*, Jun. 2017, pp. 267–270. doi: 10.1109/MWSYM.2017.8059093.

[267] G. Sangamithra, Y. V. S. Koushik, P. B. Sai, K. R. Subhash, and S. Natarajamani, “Design of Half Mode Substrate Integrated Waveguide based Dual-Band Bandpass Filter,” in *2020 Third International Conference on Smart Systems and Inventive Technology (ICSSIT)*, Aug. 2020, pp. 13–15. doi: 10.1109/ICSSIT48917.2020.9214299.

[268] R. Camdoo, S. M. Lau, and H. T. Su, “Compact cross-coupled half-mode substrate integrated waveguide bandpass filter,” in *2017 IEEE Asia Pacific Microwave Conference (APMC)*, Nov. 2017, pp. 706–709. doi: 10.1109/APMC.2017.8251544.

[269] S. Pelluri, M. Fasil, and M. Kartikeyan, “Miniaturized Wide Stopband Half-Mode SIW Bandpass Filter,” in *2019 IEEE MTT-S International Microwave and RF Conference (IMARC)*, Dec. 2019, pp. 1–5. doi: 10.1109/IMaRC45935.2019.9118655.

[270] Y.-N. Yang, G. H. Li, L. Sun, W. Yang, and and X. Yang, “Design of Compact Bandpass Filters Using Sixteenth Mode and Thirty-Second Mode SIW Cavities,” *Prog. Electromagn. Res. Lett.*, vol. 75, pp. 61–66, 2018, doi: 10.2528/PIERL18021002.

[271] S. Moitra and P. S. Bhowmik, “Modelling and analysis of Substrate Integrated Waveguide (SIW) and half-mode SIW (HMSIW) band-pass filter using reactive longitudinal periodic structures,” *AEU - Int. J. Electron. Commun.*, vol. 70, no. 12, pp. 1593–1600, Dec. 2016, doi: 10.1016/j.aeue.2016.09.005.

[272] L. Riaz, U. Naeem, and M. F. Shafique, “Miniaturization of SIW Cavity Filters Through Stub Loading,” *IEEE Microw. Wirel. Compon. Lett.*, vol. 26, no. 12, pp. 981–983, Dec. 2016, doi: 10.1109/LMWC.2016.2623242.

[273] A. Iqbal, A. W. Ahmad, A. Smida, and N. K. Mallat, “Tunable SIW Bandpass Filters With Improved Upper Stopband Performance,” *IEEE Trans. Circuits Syst. II Express Briefs*, vol. 67, no. 7, pp. 1194–1198, Jul. 2020, doi: 10.1109/TCSII.2019.2936495.

[274] L.-N. Chen, Y.-C. Jiao, Z. Zhang, F.-S. Zhang, and and Y.-Y. Chen, “Miniaturized Dual-Mode Substrate Integrated Waveguide (SIW) Band-Pass Filters Loaded by Double/Single T-Shaped Structures,” *Prog. Electromagn. Res. Lett.*, vol. 29, pp. 65–74, 2012, doi: 10.2528/PIERL11112602.

[275] A. N. Alkhafaji, A. J. Salim, and J. K. Ali, “Compact Substrate Integrated Waveguide BPF for Wideband Communication Applications,” p. 6, 2015.

[276] H. Jin, K. Wang, J. Guo, S. Ding, and K. Wu, “Slow-Wave Effect of Substrate Integrated Waveguide Patterned With Microstrip Polyline,” *IEEE Trans. Microw. Theory Tech.*, vol. 64, no. 6, pp. 1717–1726, Jun. 2016, doi: 10.1109/TMTT.2016.2559479.

[277] H. Jin, Y. Zhou, Y. M. Huang, and K. Wu, “Slow-Wave Propagation Properties of Substrate Integrated Waveguide Based on Anisotropic Artificial Material,” *IEEE Trans.*

Antennas Propag., vol. 65, no. 9, pp. 4676–4683, Sep. 2017, doi: 10.1109/TAP.2017.2726688.

[278] V. G. Veselago, “The electrodynamics of substances with simultaneously negative values of epsilon and mu,” 1968.

[279] R. Marqués, F. Martín, and M. Sorolla, *Metamaterials with Negative Parameters: Theory, Design, and Microwave Applications*. John Wiley & Sons, 2011.

[280] M. Danaeian, K. Afrooz, and A. Hakimi, “Miniaturization of substrate integrated waveguide filters using novel compact metamaterial unit-cells based on SIR technique,” *AEU - Int. J. Electron. Commun.*, vol. 84, pp. 62–73, Feb. 2018, doi: 10.1016/j.aeue.2017.11.008.

[281] B. Zarghooni, A. Dadgarpour, and T. A. Denidni, “Effect of stepped-impedance resonators on rectangular metamaterial unit cells,” *Int. J. RF Microw. Comput.-Aided Eng.*, vol. 25, no. 7, pp. 582–590, 2015, doi: 10.1002/mmce.20896.

[282] T. R. Jones and M. Daneshmand, “Miniaturized folded ridged half-mode substrate integrated waveguide,” in *2017 47th European Microwave Conference (EuMC)*, Oct. 2017, pp. 528–531. doi: 10.23919/EuMC.2017.8230906.

[283] M. Danaeian and K. Afrooz, “Compact metamaterial unit-cell based on stepped-impedance resonator technique and its application to miniaturize substrate integrated waveguide filter and diplexer,” *Int. J. RF Microw. Comput.-Aided Eng.*, vol. 29, no. 2, p. e21537, 2019, doi: 10.1002/mmce.21537.

[284] “Miniaturized HMSIW Bandpass Filter Based on the Coupling of Dual-Iris with Nested Stepped-Impedance CSRRs.” https://www.jpier.org/PIERL/pier.php?paper=19022604 (accessed Aug. 30, 2021).

[285] T. Yang, P.-L. Chi, R. Xu, and W. Lin, “Folded Substrate Integrated Waveguide Based Composite Right/Left-Handed Transmission Line and Its Application to Partial H -Plane Filters,” *IEEE Trans. Microw. Theory Tech.*, vol. 61, no. 2, pp. 789–799, Feb. 2013, doi: 10.1109/TMTT.2012.2231431.

[286] Y. Dong and T. Itoh, “Substrate integrated waveguide negativeorder resonances and their applications,” 2010, doi: 10.1049/IET-MAP.2009.0592.

[287] “Design of a Compact 5.7-5.9 GHz Filter Based on CRLH Resonator Units.” https://www.jpier.org/PIERL/view/19110502/ (accessed Aug. 30, 2021).

[288] S. Hu, Y. Hu, H. Zheng, W. Zhu, Y. Gao, and X. Zhang, “A Compact 3.3–3.5 GHz Filter Based on Modified Composite Right-/Left-Handed Resonator Units,” *Electronics*, vol. 9, no. 1, p. 1, Dec. 2019, doi: 10.3390/electronics9010001.

[289] Z. Troudi and L. Osman, “Design of Miniaturized Half Mode SIW BandPass Filter Using Metamaterial Unit Cell,” in *2019 IEEE 19th Mediterranean Microwave Symposium (MMS)*, Oct. 2019, pp. 1–4. doi: 10.1109/MMS48040.2019.9157268.

[290] H. Kirino and K. Ogawa, “A fast and slow wave combined-mode metamaterial ridged waveguide for array antenna applications,” in *2013 7th European Conference on Antennas and Propagation (EuCAP)*, Apr. 2013, pp. 2878–2882.

[291] E. A. Torrero, “Circuits and devices: High-frequency components play catch-up: From RF to mm waves, improved circuit and packaging techniques have increased the density and performance of the latest components,” *IEEE Spectr.*, vol. 13, no. 11, pp. 31–36, Nov. 1976, doi: 10.1109/MSPEC.1976.6330466.

[292] H. Hasegawa and H. Okizaki, “M.I.S. and Schottky slow-wave coplanar striplines on GaAs substrates,” *Electron. Lett.*, vol. 13, no. 22, p. 663, 1977, doi: 10.1049/el:19770471.

[293] S. Seki and H. Hasegawa, “Cross-tie slow-wave coplanar waveguide on semi-insulating GaAs substrates,” *Electron. Lett.*, vol. 17, no. 25–26, p. 940, 1981, doi: 10.1049/el:19810657.

[294] H. Hasegawa, M. Furukawa, and H. Yanai, “Properties of Microstrip Line on Si-SiO2 System,” *IEEE Trans. Microw. Theory Tech.*, vol. 19, no. 11, pp. 869–881, Nov. 1971, doi: 10.1109/TMTT.1971.1127658.

[295] H. Guckel, P. A. Brennan, and I. Palocz, “A Parallel-Plate Waveguide Approach to Microminiaturized, Planar Transmission Lines for Integrated Circuits,” *IEEE Trans. Microw. Theory Tech.*, vol. 15, no. 8, pp. 468–476, Aug. 1967, doi: 10.1109/TMTT.1967.1126505.

[296] T. S. D. Cheung and J. R. Long, “Shielded Passive Devices for Silicon-Based Monolithic Microwave and Millimeter-Wave Integrated Circuits,” *IEEE J. Solid-State Circuits*, vol. 41, no. 5, pp. 1183–1200, May 2006, doi: 10.1109/JSSC.2006.872737.

[297] D. Kaddour *et al.*, “High-Q Slow-Wave Coplanar Transmission Lines on 0.35 µm CMOS Process,” *IEEE Microw. Wirel. Compon. Lett.*, vol. 19, no. 9, pp. 542–544, Sep. 2009, doi: 10.1109/LMWC.2009.2027053.

[298] A.-L. Franc, E. Pistono, N. Corrao, D. Gloria, and P. Ferrari, “Compact high-Q, low-loss mmW transmission lines and power splitters in RF CMOS technology,” in *2011 IEEE MTT-S International Microwave Symposium*, Jun. 2011, pp. 1–4. doi: 10.1109/MWSYM.2011.5972820.

[299] A. L. C. Serrano *et al.*, “Modeling and Characterization of Slow-Wave Microstrip Lines on Metallic-Nanowire- Filled-Membrane Substrate,” *IEEE Trans. Microw. Theory Tech.*, vol. 62, no. 12, pp. 3249–3254, Dec. 2014, doi: 10.1109/TMTT.2014.2366108.

[300] D. Wang *et al.*, “Slow Wave Inverted Microstrip Line Based on Metallic Nanowire Filled Alumina Membrane,” in *2020 German Microwave Conference (GeMiC)*, Mar. 2020, pp. 160–163.

[301] D. Wang *et al.*, “A Compact Butler Matrix Design Based on Metallic Nanowire Filled Membrane Technology and Tunable Phase Shifter at 160 GHz,” in *2019 44th International Conference on Infrared, Millimeter, and Terahertz Waves (IRMMW-THz)*, Sep. 2019, pp. 1–2. doi: 10.1109/IRMMW-THz.2019.8873696.

[302] A. Niembro-Martín *et al.*, “Slow-Wave Substrate Integrated Waveguide,” *IEEE Trans. Microw. Theory Tech.*, vol. 62, no. 8, pp. 1625–1633, Aug. 2014, doi: 10.1109/TMTT.2014.2328974.

[303] X. Li, K. Dhwaj, and T. Itoh, “Single-Layer Slow-Wave Substrate Integrated Waveguide with Enhanced Capacitance,” in *2018 IEEE/MTT-S International Microwave Symposium - IMS*, Jun. 2018, pp. 316–318. doi: 10.1109/MWSYM.2018.8439214.

[304] Y. Zhang *et al.*, “Slow Wave Substrate-Integrated Waveguide With Miniaturized Dimensions and Broadened Bandwidth,” *IEEE Trans. Microw. Theory Tech.*, vol. 69, no. 8, pp. 3675–3683, Aug. 2021, doi: 10.1109/TMTT.2021.3074170.

[305] M. Wang *et al.*, “Facile fabrication of Hildewintera-colademonis-like hexagonal boron nitride/carbon nanotube composite having light weight and enhanced microwave absorption,” *J. Colloid Interface Sci.*, vol. 564, pp. 454–466, Mar. 2020, doi: 10.1016/j.jcis.2019.12.124.

[306] A. Sinha, J. A. Mihailovic, J. E. Morris, H. Lu, and C. Bailey, “Modeling thermal conductivity and CTE for CNT-Cu composites for 3-D TSV application,” in *2010 IEEE Nanotechnology Materials and Devices Conference*, Oct. 2010, pp. 262–266. doi: 10.1109/NMDC.2010.5652157.

[307] S. Hong and S. Myung, “A flexible approach to mobility,” *Nat. Nanotechnol.*, vol. 2, no. 4, pp. 207–208, Apr. 2007, doi: 10.1038/nnano.2007.89.

[308] A. Pacheco-Sanchez, I. Larruz-Castillo, D. Sangani, and D. Valdez-Pérez, “Comprehensive review on high-frequency CNT-based interconnects,” in *2019 IEEE International Conference on Applied Science and Advanced Technology (iCASAT)*, Nov. 2019, pp. 1–7. doi: 10.1109/iCASAT48251.2019.9069515.

[309] A. Singh and R. Dhiman, “Proposal and Analysis of Mixed CNT Bundle for Sub-Threshold Interconnects,” *IEEE Trans. Nanotechnol.*, vol. 18, pp. 584–588, 2019, doi: 10.1109/TNANO.2019.2919445.

[310] P. U. Sathyakam, A. Banerjee, and P. S. Mallick, “On the Applicability of Triangular Carbon Nanotube Bundles as VLSI interconnects,” in *2019 IEEE 21st Electronics Packaging Technology Conference (EPTC)*, Dec. 2019, pp. 578–581. doi: 10.1109/EPTC47984.2019.9026693.

[311] L. Li, Z. Zhu, A. Yoon, and H.-S. P. Wong, “In-Situ Grown Graphene Enabled Copper Interconnects With Improved Electromigration Reliability,” *IEEE Electron Device Lett.*, vol. 40, no. 5, pp. 815–817, May 2019, doi: 10.1109/LED.2019.2908426.

[312] M. Ohring, *Reliability and Failure of Electronic Materials and Devices*. Elsevier, 1998.

[313] R. Rosenberg, “Inhibition of Electromigration Damage in Thin Films,” *J. Vac. Sci. Technol.*, vol. 9, no. 1, pp. 263–270, Jan. 1972, doi: 10.1116/1.1316576.

[314] D. Young and A. Christou, “Failure mechanism models for electromigration,” *IEEE Trans. Reliab.*, vol. 43, no. 2, pp. 186–192, Jun. 1994, doi: 10.1109/24.294986.

[315] Z. Zhu, Y. Chan, F. Wu, C. L. Gan, and Z. Chen, “Review on test vehicles for electromigration (EM) study in solder interconnects,” in *2017 IEEE 19th Electronics Packaging Technology Conference (EPTC)*, Dec. 2017, pp. 1–5. doi: 10.1109/EPTC.2017.8277478.

[316] X. Chen, G. Gao, B. Geng, and S. Li, “Impact of side reservoir on electromigration of copper interconnects,” in *2017 International Conference on Electron Devices and Solid-State Circuits (EDSSC)*, Oct. 2017, pp. 1–2. doi: 10.1109/EDSSC.2017.8126452.

[317] B. H.-L. Chao, X. Zhang, S.-H. Chae, and P. S. Ho, “Recent advances on kinetic analysis of electromigration enhanced intermetallic growth and damage formation in Pb-free solder joints,” *Microelectron. Reliab.*, vol. 49, no. 3, pp. 253–263, Mar. 2009, doi: 10.1016/j.microrel.2009.01.006.

[318] “V-bonds.” https://www.microwaves101.com/encyclopedias/v-bonds (accessed Nov. 20, 2021).

[319] F. Lim, L. Wo, C. Lee, and B. Rizal, “Process characterization of aluminum ribbon bond,” in *2007 International Conference on Electronic Materials and Packaging*, Nov. 2007, pp. 1–5. doi: 10.1109/EMAP.2007.4510320.

[320] “RF wirebond compensation.” https://www.microwaves101.com/encyclopedias/rf-wirebond-compensation (accessed Nov. 20, 2021).

[321] S. Beer *et al.*, “Design and measurement of matched wire bond and flip chip interconnects for D-band system-in-package applications,” in *2011 IEEE MTT-S International Microwave Symposium*, Jun. 2011, pp. 1–4. doi: 10.1109/MWSYM.2011.5972851.

[322] V. Valenta *et al.*, “Design and experimental evaluation of compensated bondwire interconnects above 100 GHz,” *Int. J. Microw. Wirel. Technol.*, vol. 7, no. 3–4, pp. 261–270, Jun. 2015, doi: 10.1017/S1759078715000070.

[323] T. P. Budka, “Wide-bandwidth millimeter-wave bond-wire interconnects,” *IEEE Trans. Microw. Theory Tech.*, vol. 49, no. 4, pp. 715–718, Apr. 2001, doi: 10.1109/22.915447.

[324] ThermoFischer, “Chemical Surface Modification with SEM, FIB and DualBeam.” [Online]. Available: https://assets.thermofisher.com/TFS-Assets/MSD/Application-Notes/gis-beam-chemistries-appnote.pdf

Appendices

Appendix 1. The resonant cavity characterization method for conductivity

In order to characterize the conductivity of a material the process is as follows.

Let us consider a resonating cavity with a removable cover made of the same material, as shown below.

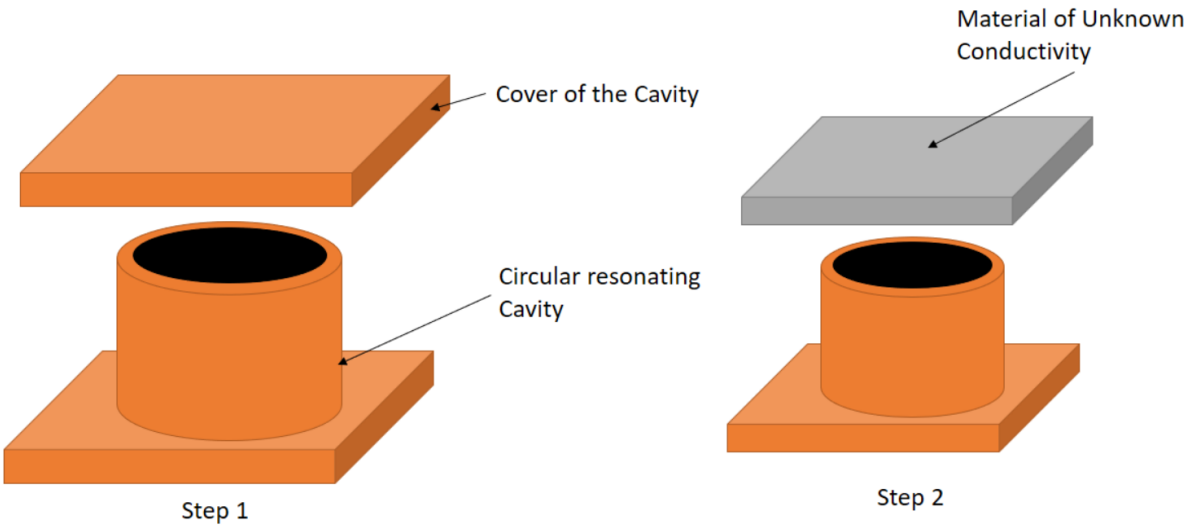

Step 1: The resonating frequencies of the TE011 and TE012 modes are measured. The dimensions of the cavity can be extracted from these measurements. The quality factor of the resonant mode TE01p (with p an integer different from 0) is measured. We can deduce analytically the conductivity of the material in which the cavity is made. Indeed, we know the analytical expression of the fields in the cavity for the TE01p modes, and the quality factor (Q) is directly linked to the conductivity by the following equations:

$$Q = 2\pi \frac{W_a}{W}$$

With, W_a the stored energy and W the energy lost in a period (T).

We have,

$$W_a = \frac{1}{2}\mu \iiint \mathbf{H}.\mathbf{H}^* dv = \frac{1}{2}\varepsilon \iiint \mathbf{E}.\mathbf{E}^* dv$$

With $\mathbf{H}$ and $\mathbf{E}$ the magnetic and electric fields in the cavity, μ the permeability of the media in the cavity (usually air) and ε the permittivity of the media in the cavity.

W or the energy lost in a period is linked to the power lost in a period (P) by

$$W = \mathrm{PT}$$

The power lost in a period can be written as the sum of, the power lost through coupling (P_{ex}), the power lost through dielectric losses in the media (P_d) and the losses through the Joule effect in the walls.

P_{ex} and P_d are usually considered equal to zero if the cavity is weak coupled and the loss tangent of the media is low, respectively.

P_j is directly linked to the conductivity by:

$$P_j = \frac{1}{2} R_s \oiint \mathbf{H}.\mathbf{H}^* dS$$

With, $R_s = \frac{1}{\sigma_1 \delta_s} = \frac{\sqrt{\pi \mu_1 f}}{\sqrt{\sigma_1}}$ the superficial resitance of the walls of conductivity and permeability σ_1 and μ_1 respectively.

At the end of Step 1, the conductivity of the material consisting the cavity is known and the dimensions of the cavity also.

Step 2: In this step, the cover of the cavity is changed with the material of unknown conductivity.

The quality factors vary because the losses due to the Joule effect in the cover depend on its conductivity.

A decrease in the quality factor corresponds to an increase in P_j. This increase in P_j can directly be linked to the conductivity variation of the cover through the analytical expression of P_j. Indeed, P_j is the sum of the losses in the lateral walls, the bottom plane and the cover.

Note: The TE01p modes are used because the quality factor does not depend on the quality of the contact between the cover and the cavity. There is no leakage because there is no current at the interface.

Unfortunately, if we suppose we transferred CNTs on a metallic cover to close the cavity with, the fields would go through the CNTs, as the electric field is perpendicular to the direction of the CNTs. The CNTs would not be characterized.

Appendix 2. Thru Line calibration

The Thru-Line calibration principle is as follows.

Let us suppose we are trying to extract the S-parameters of a device named DUT (Device Under Test) and that this DUT is not directly measurable. Transitions (e.g. from CPW to SIW) are needed to excite the structure. Let us name these transitions X_1 and X_2. A schematic is given below:

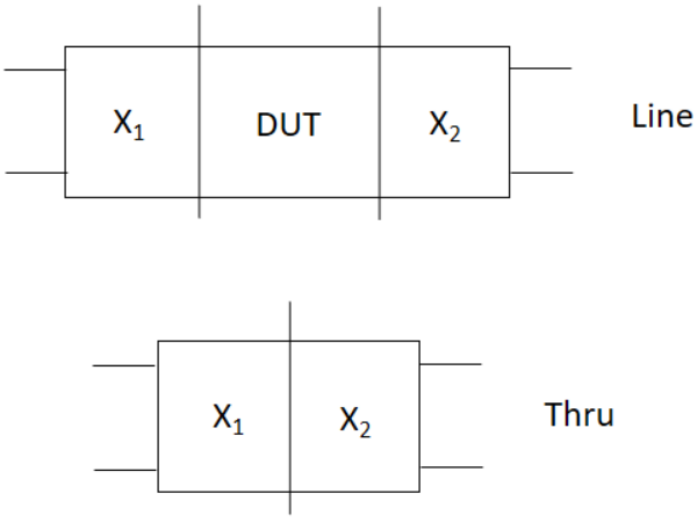

If we have two devices of different lengths, the shorter one can be considered to be the Thru and the bigger one the Line.

The transfer matrices of these two devices are given by:

$$T_{Line} = T_{X1} T_{DUT} T_{X2}$$

$$T_{Thru} = T_{X1} T_{X2}$$

With, T_{X1} and T_{X2} the transfer matrices of the transitions X_1 and X_2 respectively, and T_{DUT} the transfer matrix of the DUT.

Let us define the matrix Q by:

$$\mathrm{Q} = T_{Line} {T_{Thru}}^{-1}$$

All the matrixes are invertible because the devices are supposed passive.

We have,

$$\mathrm{Q} = T_{X1} T_{DUT} T_{X2} {T_{X2}}^{-1} {T_{X1}}^{-1} = T_{X1} T_{DUT} {T_{X1}}^{-1}$$

Meaning that Q and T_{DUT} are similar.

Thus Q and T_{DUT} have the same eigenvalues.

If we suppose that a single mode is propagating in the DUT (a good approximation if the adaptation is good enough), we have:

$$T_{DUT} = \begin{bmatrix} e^{-\gamma l} & 0 \\ 0 & e^{\gamma l} \end{bmatrix}$$

With, γ the propagation constant of the mode and l the length of the DUT.

Hence, if we measure T_{Thru} and T_{Line} (obtained from the S-parameters) we can calculate the eigenvalues of Q that will give us the propagation constant in our DUT.

Appendix 3. Data sheet MF-117 absorbent

The electromagnetic constants of the MF-117 high frequency absorbent were given by the manufacturer (EMERSON & CUMMING Microwaves Products). They are presented below:

Physical Properties :

	MF
Colour	Dark Grey
Service Temperature, °C	<180
Density, g/cc	3,6 - 4,9
Hardness (Shore D)	85
Tensile Strength, kg/cm^2	560
Thermal Expansion per °C	~30 x 10^{-6}
Water Absorption, % 24 hours	<0,3
Thermal Conductivity, (W/mK)	0,98
Volume Resistivity (Ohm.cm)	>10^{11}
Outgassing : TML (%) CVCM (%)	0,51(MF110) 0,01(MF110)

Typical Electrical Properties Legend

K'	Real part of the permittivity (dielectric constant)
tan δ_d	Dielectric loss tangent
K"	Imaginary part of the permittivity (loss)
M'	Real part of the magnetic permeability
tan δ_m	Magnetic loss tangent
M"	Imaginary part of the magnetic permeability (loss)
dB/cm	Attenuation per unit distance
dB/in	Attenuation per unit distance
$\lvert Z\rvert/Z_0$	Normalized impedance magnitude ratio

		Frequency (Hz)							Frequency (GHz)				
		10^2	10^3	10^4	10^5	10^6	10^7	10^8	1	3	8.6	10	18
	dB/cm	0	0	0	0	0	0	0,09	1,3	5,0	21	32	57
	$\lvert Z\rvert/Z_0$	0,32	0,32	0,34	0,35	0,37	0,39	0,47	0,42	0,42	0,33	0,33	0,33
MF-117	K'	195	158	120	85	62	48	38	28	22,9	21,4	21	20,6
	Tan	0,18	0,21	0,23	0,24	0,22	0,18	0,12	0,09	0,06	0,02	0,02	0,02
	K''	35	33	28	20	14	8,6	4,6	2,5	1,4	0,42	0,42	0,41
	'	5,0	5,0	5,0	5,0	5,0	5,0	4,8	4,1	3,4	1,2	1,1	1,0
	Tan	0	0	0	0	0	0	0,1	0,20	0,39	1,36	1,5	2,00
	"	0	0	0	0	0	0	0,48	0,82	1,33	1,63	1,7	2,00
	dB/cm	0	0	0	0	0	0,03	0,27	2,8	11,0	46	56	119
	$\lvert Z\rvert/Z_0$	0,16	0,18	0,20	0,24	0,28	0,32	0,36	0,39	0,40	0,30	0,31	0,33
	K'	260	205	145	95	70	52	40	32	25,8	23,8	23,6	23,0
	Tan	0,40	0,39	0,36	0,31	0,26	0,20	0,14	0,08	0,07	0,05	0,03	0,04
	K''	104	80	52	30	18	10	5,6	2,6	1,8	1,10	0,71	0,92

Développement de Solutions Originales pour l'Intégration 3D de Dispositifs RF et Millimétriques à base de Nanotubes de Carbone

La montée en fréquence des dispositifs de télécommunication est intéressante pour plusieurs raisons. En effet, le nombre croissant de dispositifs connectés ces dernières années a fait que les bandes de fréquences plus basses, généralement utilisées, sont devenues surchargées. De plus, afin d'augmenter le débit des connexions sans fils (afin de pouvoir atteindre des niveaux comparables à ceux de la fibre optique) il est nécessaire d'augmenter les fréquences de fonctionnement. Toutefois, la montée en fréquence pose de réels défis technologiques au niveau de l'équipement à cause des dimensions plus petites, du comportement des matériaux traditionnels à hautes fréquences, d'effets parasites, etc. Nous étudions dans ce manuscrit les possibilités apportées par les nanomatériaux (en particulier les Nanotubes de Carbone (NTC)) dans le domaine du packaging pour les dispositifs millimétriques. Nous proposons dans un premier temps de décrire les propriétés physiques du matériau que nous utilisons, à savoir les paquets des NTC alignés verticalement. Dans un deuxième temps, une topologie innovante d'interposeur fonctionnalisé à base de NTC est proposé et une preuve de concept est fabriquée et mesurée. Dans un troisième temps, les effets de miniaturisation possibles grâce aux NTC sont étudiés et mis en évidence. Finalement, l'apport des NTC dans le domaine des interconnections est abordé.

Mots-clés : dispositifs millimétriques, nano-packaging, interposeur, NTC

Development of Original Solutions for the 3D Integration of RF and Millimeter-wave Devices Based on Carbon Nanotubes

The shift to higher frequencies of wireless communications is interesting for several reasons. Indeed, the increasing number of connected devices these last years has made the lower frequency bands (traditionally used) overcrowded. Furthermore, in order to increase the data rates of wireless communications (to match the ones of the fiber optics) it is necessary to increase the used frequencies. However, higher frequencies come with lower dimensions and more difficult fabrication processes, lossy behavior of the traditionally used materials, and parasitic effects that become no more negligible, etc. In this manuscript, we study the possibilities that nanomaterials (in particular Carbon Nanotubes (CNTs)) in the domain of packaging for millimeter-wave devices. In a first chapter, we describe the physical properties of the material we use, namely bundles of vertically aligned CNTs. In the second chapter, an innovative topology of a functionnalized interposer based on CNTs is presented, and a proof of concept device is fabricated and measured. In a third chapter, the miniaturization effects due to the use of CNTs are investigated and highlighted. Finally, the contribution of CNTs in the domain of high frequency interconnects is approached.

Keywords: Millimeter-wavedevices, nano-packaging, interposer, CNT